ENGINEERED THERAPEUTIC PLASMIDS AND NANOPARTICLE DELIVERY VEHICLES FOR TARGETED TREATMENT OF HEPATOCELLULAR CARCINOMA

by
Hannah Vaughan

A dissertation submitted to Johns Hopkins University in conformity with the requirements for the degree of Doctor of Philosophy

Baltimore, Maryland
June 2021

Abstract

Nucleic acid-based therapies can be used to target the genetic basis of a disease and have been explored for the treatment of wide range of medical conditions, including cancer. However, many of these therapies have largely been ineffective in the clinic due to off-target toxicities and poor targeting properties, resulting in poor safety and efficacy outcomes. To address these challenges, there has been a strong effort over the past decades to develop delivery vehicles for targeted nucleic acid delivery. A high degree of targeting is particularly critical when delivering cytotoxic therapies for cancer cell killing, as off-target toxicities can lead to dangerous or deadly adverse events. In the case of liver cancer, off-target toxicity has a high risk of liver failure due to the prevalence of severe underlying liver disease in these patients.

The aim of this thesis is to investigate multiple methods for targeted DNA delivery to hepatocellular carcinoma, the most common form of liver cancer. Polyplex nanoparticles (NPs) synthesized using poly(beta-amino ester) (PBAE) serve as a delivery vehicle to deliver plasmid DNA to target cells. This thesis uses PBAE NPs to explore multimodal targeting using (1) anatomical targeting of tissues, specifically HCC tumor vasculature, (2) optimization of delivery vehicle biomaterials for HCC cell-specific transfection, and (3) an HCC-specific promoter to restrict therapeutic gene expression. These methodologies are explored independently and in combination to specifically deliver DNA to HCC cells *in vitro* and *in vivo.* Importantly, these targeting principles are applied to develop two targeted therapeutics for HCC, which show therapeutic efficacy in preclinical rodent models of HCC. Altogether, these results highlight the clinical potential of PBAE NPs for targeted therapy for HCC.

Thesis Committee

Jordan J. Green, Ph.D. *(Advisor, reader)*

Professor, Department of Biomedical Engineering,

Johns Hopkins University School of Medicine

Martin G. Pomper, M.D., Ph.D. *(Reader)*

Professor, Department of Radiology

Johns Hopkins University School of Medicine

Hai-Quan Mao, Ph.D. *(Thesis Committee Chair)*

Professor, Department of Materials Science and Engineering

Johns Hopkins University School of Medicine

Joshua C. Doloff, Ph.D.

Professor, Department of Biomedical Engineering,

Johns Hopkins University School of Medicine

Acknowledgements

The success of these projects would not have been possible without the personal and professional support I have received from my collaborators, mentors, and colleagues. I would first like to thank Dr. Jordan Green for his mentorship and guidance over the past five years. His influence during my summer as an undergraduate researcher sparked my interest in gene delivery, inspiring me to pursue my PhD in the field. I appreciate the freedom that he granted me over the past five years to explore new areas and take on challenging projects. Without his perspectives, guidance, and advice, this research would not have been possible. I was also fortunate to have worked with many collaborators who broadened my perspectives and challenged me to place clinical translation at the forefront of my work. Dr. Martin Pomper was a significant mentor to me from my first day at Johns Hopkins, and I am grateful to him for his encouragement and insight. Other important collaborators include Dr. Florin Selaru, Dr. Ling Li, Dr. Mark Donowitz, Dr. Nicholas Zachos, Dr. Ruxian Lin, Dr. Rafiq Sarker, Dr. Kathleen Gabrielson, Dr. Xin Guo, Dr. Khalid Shah, Dr. Ron Mease, Dr. Catherine Foss, and Dr. Il Minn. I am grateful to them for their endless generosity with their time and knowledge as we pursued projects together. I also thank all of the faculty, staff, and students in the Translational Tissue Engineering Center, the Institute for Nanobiotechnology, and the Department of Biomedical Engineering for their support. I would especially like to thank my thesis committee, Dr. Jordan Green, Dr. Martin Pomper, Dr. Joshua Doloff, Dr. Hai-Quan Mao for their invaluable guidance throughout the process of developing and communicating my thesis work.

I would also like to thank my lab mates in the Green Group, Dr. Stephany Tzeng, Dr. Camila Gadens Zamboni, Dr. Johan Karlsson, Dr. Maziar Mohammadi, Dr. Kristen Kozielski, Dr. Jayoung Kim, Dr. Randall Meyer, Dr. David Wilson, Dr. Yuan Rui, Elana Ben-Akiva, Kelly

Rhodes, Savannah Est Witte, Kathryn Luly, Sarah Neshat, Hongzhe Yu, Sydney Shannon, and Erin Kavanaugh. Every day I felt surrounded by the brightest possible group, and I'm so grateful for everything I've learned from them. They also made lab a place I looked forward to coming to every day, despite the many challenges we all faced in our work, especially during this year's COVID-19 pandemic. In particular, I owe much of my success to Camila, who trained me for my first few years in the lab and launched many of the projects that comprise this thesis. Her intelligence and tenacity are unparalleled, and I am thankful for our continued friendship. I would also like to thank the undergraduate students that I worked with over the past years: Pranshu Bhardwaj, Nicholas Radant, David Francisco, Laboni Hassan, and Ann Jiang. They showed tremendous enthusiasm and eagerness to learn, and they contributed immensely to the projects described in this thesis. They were a joy to work with an learn from, and I am eager to watch their future success.

I would like to thank my friends and family for their unconditional support which made this work possible. My parents have been my relentless supporters in everything I do, and I have been lucky to have their love and encouragement during this journey. I am also grateful to have the love and support of my brothers Alec and Erik and to watch them grow and develop in their own careers. My fiancé Brian has offered endless encouragement and has made many sacrifices to support me in this pursuit over the past five years. I also feel lucky to have had an amazing extended family who has always supported my education, and a network of incredible friends. You all made this chapter unforgettable.

Table of Contents

List of Tables

List of Figures

Chapter 1: Introduction to the thesis

1.1 DNA Delivery

Many important cancer-associated genes have been identified in recent years, underpinning new molecular therapeutics, including recent cancer gene therapy efforts[1]. The delivery of DNA and other types of nucleic acid allows cells to be altered at the genetic level, allowing for sequence-specific regulation of disease-associated gene expression[2]. By changing the gene expression profile of target cells, researchers can directly address the cause of diseases that have a genetic component, including cancer. Malignant cells with dysregulated gene expression patterns can be treated by inducing overexpression of genes that induce apoptosis or by decreasing the expression of genes that promote cancer cell survival. However, effective and safe intracellular delivery of nucleic acids to cancer cells remains a challenge. The ability to target cancer cells is crucial to maximize the efficiency of anti-cancer treatment as well as to avoid causing unwanted toxicity to healthy tissues.

1.1.1 Barriers to Nucleic Acid Delivery

A major challenge in developing nucleic acid-based therapeutics is achieving successful delivery to target tissues and cells (**Figure 1.1**). Nucleic acids on their own are vulnerable to degradation and various mechanisms of clearance. In order to reach cells intact, they must be loaded or condensed into nano-sized structures that can protect them from the environment and

---

This chapter contains material modified from the following published articles.

Vaughan, H. J., Green, J. J., & Tzeng, S. Y. (2020). Cancer-targeting nanoparticles for combinatorial nucleic acid delivery. *Advanced Materials*, *32*(13), 1901081.

Karlsson, J.*, Vaughan, H. J.*, & Green, J. J. (2018). Biodegradable polymeric nanoparticles for therapeutic cancer treatments. *Annual review of chemical and biomolecular engineering*, *9*, 105-127. (* These authors contributed equally)

facilitate their trafficking to target sites. Polymer nanoparticles can be engineered into a variety of formulations, such as solid nanoparticles, core-shell structures, polymeric micelles, and polyplexes (**Figure 1.2**). The preferred nanoparticle formulation and synthesis method depends on the properties of the chosen polymer and cargo, and they are generally formed by either self-assembly or an emulsion polymerization method. Self-assembly methods involve inter- and intramolecular interactions between the polymer itself and its cargo, such as complexation of cationic polymers with anionic nucleic acids to form polyplexes, as well as spontaneous micelle assembly when amphiphilic block copolymers reach a critical micelle and form particles owing to hydrophobic interactions. For emulsification synthesis methods, nanoparticles are formed as droplets of one phase dispersed in a second phase. Typically, the polymer is dissolved in an organic phase that is then mixed with a surfactant and sonicated in an aqueous phase with high intensity to form nanodroplets[3]. The emulsion is stirred until the solvent evaporates, leaving behind hardened polymer nanoparticles. These hard nanoparticles can also be coated with another material to form core-shell nanoparticles with favorable surface properties[4,5].

Nanoparticles administered intravenously must avoid rapid clearance by the mononuclear phagocyte system[6,7]. Macrophages in the liver and spleen phagocytose and degrade nanoparticles in the 10-200 nm size range, reducing circulation time and minimizing nanoparticle accumulation in the tumor. This process can be slowed by reducing interactions between nanoparticles and macrophages. One common method is to shield the surface of the nanoparticles by coating them with poly(ethylene glycol) (PEG), a hydrophilic molecule that prevents adsorption of serum proteins and non-specific binding to cells[8].

Nanoparticles must be internalized by target cells to deliver the nucleic acid payload to the cytoplasm. Because the glycocalyx and lipid bilayer cell membrane have a net negative charge

on the extracellular surface, cationic nanoparticles facilitate cellular binding and uptake via electrostatic interactions[9–12]. Surface modification with certain moieties, such as cell-penetrating peptides (CPPs) or active targeting ligands, can be used to further improve overall cellular uptake of nanoparticles[13–17]. Nanoparticles are taken up by endocytic vesicles, then the endosomal pH is lowered as the vesicle progresses to the late endosome stage. Polymeric nanoparticles often incorporate H^+ buffering polyamines into the polymer to promote the endosomal rupture through the proton sponge effect[18,19]. The amines of the cationic polymer are protonated as the pH decreases, causing accumulation of Cl^- and osmotic swelling within the endosome, which generates a 140% increase in endosome volume in a process known as the proton sponge effect[18]. This volume increase facilitates endosomal rupture, releasing the nanoparticle cargo into the cytoplasm. Additionally, cationic or fusogenic components can interact with the anionic endosomal membrane and destabilize the compartment, causing release of the cargo into the cytoplasm[20].

Once nanoparticles are released from the endosome, the nucleic acid cargo must be released from the nanoparticle, which can occur by a decrease in binding between cargo and delivery material and/or degradation of the material itself[21,22]. Plasmid DNA must enter the nucleus, and diffusion of large biomacromolecules like plasmid DNA through the cytoplasm to the nucleus is very slow This can be improved upon by the attachment of a nuclear localization signal (NLS) to the plasmid or the nanocarrier[23], promoting the binding of the DNA cargo to import proteins that can actively facilitate nuclear transport and entry[24]. It is therefore unsurprising that plasmid DNA delivery by non-viral nanocarriers has often been found to be much more efficient in dividing cells[25–27]. While non-mitotic mechanisms of nuclear entry have been demonstrated[28], nuclear transport remains a key challenge for non-viral delivery of plasmid DNA. Given the long history

of using uncontrolled cell division as a method of targeting cancer cells while they are in mitosis[29], however, this nuclear barrier to plasmid DNA delivery could in fact serve as an avenue to improving the selectivity of an anti-cancer gene therapy.

Because of the complex sequential barriers that nucleic acid delivery nanoparticles must overcome, the properties described here should be considered together. For example, while cationic materials are convenient for encapsulation or complexation of anionic cargo, positively charged materials can also cause toxicity by disrupting the cell membrane[30]. On the other hand, decreasing the molecular weight[31] or introducing biodegradable functional groups[32] into the polymer materials has been shown to increase the safety of the nanomaterial[33–35]. Further, different types of nucleic acid cargos have distinct delivery challenges, so their delivery vehicles require different properties (**Table 1.1**). Thus, a combination of optimized parameters should be used to design an ideal nanoparticle delivery vehicle.

1.1.2 Biomaterials

Many types of materials exist as constituent building blocks of nanocarriers, including both natural and synthetic materials (**Figure 1.3**). Synthetic strategies include inorganic nanoparticles, such as those composed of gold[36,37] or iron oxide[38], which have intrinsic ability for imaging, sensing, and diagnostic applications[39,40] but can have significant limitations for drug loading and drug release for therapeutic applications[41]. Organic materials such as lipids have had a relatively long history of use for delivering biomolecules for therapeutic purposes. These include therapeutics such as DOXIL®, liposomal doxorubicin surface-coated with PEG, which has been used to treat multiple cancers, including breast and ovarian cancers[42–44]. Many types of polymer materials have also been developed for drug delivery and have multiple benefits, including the ability to tailor the physical, chemical, and biological properties of the nanocarrier.

Biodegradable polymers are especially appealing because they break down in physiological conditions, which generally both reduces the toxicity of the carrier and facilitates drug release[45,46].

1.1.3 Natural Polymers

Many naturally derived polysaccharide and protein-based polymers (**Figure 1.4**) have already been approved for diverse food, cosmetic, and medical applications[47]. They show excellent biocompatibility since they are broken down by enzymatic degradation into easily metabolized peptides or polysaccharides in the body, and this degradation rate can be tuned for a desired release profile[48]. However, these polymers are more variable batch to batch, often require chemical modification to act as efficient nanocarriers, and must be extensively purified to avoid immunogenicity.

Chitosan is a linear polysaccharide derived from chitin, an abundant natural biopolymer found in the exoskeleton of insects and crustaceans[49]. Chitosan is synthesized by the deacetylation of chitin, which forms primary amine groups, making the polymer cationic in dilute acidic solutions. As a result, chitosan electrostatically binds to and complexes with negatively charged macromolecules such as nucleic acids to form polyplexes[50,51]. Chitosan's positive charge increases cell uptake and adhesion to negatively charged mucosal surfaces, making it well-suited for oral drug delivery[52]. Degradation is highly tunable and can be optimized for biomedical applications by varying molecular weight, degree of deacetylation, and chemical modifications[53].

Dextran is a branched polysaccharide composed of simple repeat units of α-D-glucose joined by glycosidic bonds[54]. Dextran is hydrophilic and water soluble but can be acetylated to create a hydrophobic polysaccharide (AcDex)[55]. For drug delivery, it is typically combined with

crosslinkers to form a hydrogel or coating. Further, dextran can be linked to a hydrophilic polymer such as PEG, poly(ε-caprolactone) (PCL), or polylactide (PLA) as a block copolymer to form amphiphilic micelles, which can be loaded with hydrophobic therapeutic agents[56].

Alginate is an inexpensive, naturally derived hydrophobic polymer purified from algae. It is linear and unbranched, consisting of blocks of β-1,4-linked mannuronic acid and α-(1–4)-linked guluronic acid residues[57]. Alginate is anionic, and introducing divalent cations such as calcium induces gelation[58]. It is easily functionalized owing to hydroxyl and carboxyl groups on the backbone, so its chemical and biological properties can be tuned[59]. Alginate is biocompatible and nonimmunogenic and is used in a range of Food and Drug Administration–approved products, from food additives to wound dressings[59].

Gelatin is a mixture of peptides and proteins derived from partial hydrolysis of animal collagen. It is biocompatible, nonimmunogenic, and widely used in food and cosmetic products. Gelatin nanoparticles have been investigated for both nucleic acid and small-molecule drug delivery to tumors[60,61]. However, natural gelatin generally binds therapeutic cargos too loosely, so it is thereby chemically modified for drug delivery applications. Carboxyl and hydroxyl groups allow for modification, including the introduction of thiol for direct conjugation of gelatin to the therapeutic cargo and redox-responsive degradation and release[60,61]. The isoelectric point of gelatin can be modified to optimize loading of charged drugs, and gelatin molecular weight and crosslinking density can be altered to control drug release[62].

Poly(L-lysine) (PLL) is the polymerized form of lysine, a cationic amino acid, with L stereochemistry for natural enzymatic degradability. High positive charge density of the polymer allows PLL to efficiently condense negatively charged molecules into nanoparticles. Further, its positive charge improves particle uptake, so PLL is often used as a coating on core-shell

nanoparticles. PLL can be synthesized in linear and dendritic forms, with dendritic PLL exhibiting enhanced buffering capability and improved nucleic acid delivery[63].

1.1.4 Synthetic Polymers

Synthetic polymers (**Figure 1.4**) are engineered with desirable properties, such as charge, hydrophobicity, and degradation profile, which are optimized for particular cargos, delivery routes, and disease targets. Synthesis is controlled for low batch-to-batch variability, and production is typically scalable for large-scale manufacturing. However, unintended degradation products or metabolites can cause synthetic polymers to be cytotoxic or immunogenic.

PLA exists in two optically active forms, because the lactide molecule is chiral: L-lactide and D-lactide. The degradation of poly(L-lactide) is too slow for drug delivery systems; hence, poly(DL-lactide) is the preferred candidate owing to its faster degradation rate[64]. PLA undergoes hydrolytic degradation as random scission of the ester bonds occurs, releasing the particle cargo. To improve its use for gene delivery, tertiary amines are grafted onto the PLA backbone and serve as a source of positive charge to promote electrostatic interactions with nucleic acids[65]. The charge density can hence be adjusted through varied degrees of functional groups to the polymer structure.

Poly(lactide-*co*-glycolide) (PLGA) is a copolymer of lactic acid and glycolic acid. PLGA is an attractive delivery material because of its high stability and low toxicity and a degradation rate that is easily tuned by varying the ratios of the constituent monomers. PLGA nanoparticles are typically synthesized by emulsion methods and are used to encapsulate small-molecule drugs. Surface modification with the addition of cationic ligands promotes efficacy of gene delivery, for example, using cationic lipids for small interfering RNA (siRNA) delivery[66].

PCL is a hydrophobic, semicrystalline biodegradable polymer with a high capacity for drug

binding and biodegradable properties due to the fact that ester bonds break under physiological conditions[67]. PCL is a hydrophobic, semicrystalline biodegradable polymer with a high capacity for drug binding and biodegradable properties because ester bonds in the polymer backbone are hydrolyzed under physiological conditions[67]. PCL exhibits high colloidal stability in a biological fluid, facile cellular uptake by endocytosis, low toxicity in vitro and in vivo, and controlled cargo release[68]. Thus, this polymer has been used in tissue engineering scaffolds, biomedical devices, and drug delivery devices, such as the implantable contraceptive Capronor®[69]. PCL is often blended with other biodegradable polymers to speed degradation rate. In cancer nanomedicine, PEG–PCL block copolymers have been used to form micelles encapsulating chemotherapeutics[70,71].

Cyclodextrins are water-soluble synthetic carbohydrates composed of six to eight glucose units in a ring structure. Cyclodextrins form an amphiphilic cup shape with a hydrophilic exterior and hydrophobic interior. Adamantine-PEG (AD-PEG) functionalization is used for nanoparticle stabilization without disturbing the electrostatic interactions to anionic cargos. Functionalized cyclodextrins have thereby been shown to form stable complexes with DNA and high transfection efficiency with low cytotoxicity[72,73].

1.1.5 Poly(β-amino ester) (PBAE)

Poly(β-amino ester) (PBAE) libraries are synthesized by reacting diacrylates with amine monomers, including different structures of backbone, side-chain, and endcapping monomers, to form polymers with diverse properties, including size, charge, and hydrophobicity[74,75]. By using high-throughput screening, PBAE formulations have been selected for high transfection efficacy, low toxicity, and cell-type specificity for targeted gene delivery to cancer cells[76,77]. For example, specific PBAE structures can provide a preferential DNA and siRNA delivery to patient-derived

glioblastoma cells over healthy human progenitor neural cells[78,79].

PBAEs are cationic, contain ester bonds that are hydrolytically cleavable, and can be engineered with primary, secondary, and tertiary amines[80]. These properties enable the polymers to bind anionic cargos and facilitate endocytosis, endosomal escape, and intracellular release of cargo, enabling efficient gene delivery[77]. To further promote cytoplasmic degradation, bioreducible disulfide linkages have been introduced into the polymer structure, enabling more efficient, triggered siRNA release in the reducing environment of the cytosol compared with release from ester bond hydrolysis alone[79,81].

1.2 Approaches for Tumor Targeting

An overarching challenge in cancer therapeutics, including in nanomedicine, is achieving sufficient concentrations of an anti-cancer agent in the tumor while minimizing off-target toxicities in healthy tissues. Targeting methods take advantage of features that differentiate cancer from healthy tissue, including properties of the tumor microenvironment, overexpressed molecules on the cancer cell surface, and dysregulated gene expression. Nano-scale delivery vehicles are uniquely capable of passive targeting, active targeting via ligand functionalization, and controlled or triggered release. Additionally, nucleic acid cargos can themselves be engineered to take advantage of aberrant gene expression in cancer cells and achieve cancer specificity through their mechanism of action. Tumor targeting must be carefully considered when developing these delivery vehicles to maximize cargo delivery to cancer cells while avoiding dangerous off-target effects.

1.2.1 Passive Targeting

Hypervasculature, enhanced vascular permeability, and decreased lymphatic drainage are all hallmarks of rapidly growing tumors. The abnormal architecture of angiogenic tumor blood

vessels underlies the enhanced permeability and retention (EPR) effect, which describes the tendency for systemically administered macromolecules within a 10-200 nm size range to accumulate in solid tumors[82]. Nanoparticle formulations of chemotherapies, such as Doxil® (for doxorubicin) and Abraxane (for paclitaxel), were developed in response to this phenomenon and have improved pharmacokinetics, an increased maximum tolerated dose, less systemic toxicity, and improved therapeutic efficacy compared to their free drug counterparts[43]. Nanoparticle size is a key predictor of passive targeting because size affects clearance rate and route, extravasation into tumor tissue, cellular uptake, and interactions with the immune system. The range for passive targeting by the EPR effect is around 10-200 nm, although tumor accumulation has been described for slightly smaller or larger particles. Particle accumulation in the tumor compartment is in competition with clearance, either by the renal system or the MPS, which is comprised of macrophages predominately in the liver and spleen. Particles smaller than 10 nm are rapidly cleared by the renal system and tend to accumulate in the kidney, while larger particles accumulate in the liver and spleen[83]. Both clearance routes compete with accumulation in tumor tissue, so developing particles with low clearance rate and high circulation time is the primary goal for passive targeting by EPR.

Inspired by the cylindrical or filamentous shapes of many viruses, non-spherical geometries have been explored for therapeutic drug and nucleic acid delivery. Long cylindrical, rod-like, disk-shaped, or filamentous particles have been shown to evade phagocytosis by resident macrophages. There is evidence that the contact angle between macrophages and particles affects phagocytic uptake; contact with a flatter surface such as a rod or disk causes macrophage spreading rather than phagocytosis[84]. Additionally, in dynamic fluid flow, filamentous particles elongate and align with flow, and hydrodynamic shear forces pull particles off of

macrophages[85].These effects slow the uptake of filamentous particles by the MPS and can dramatically increase circulation times. For example, Geng et al. developed filamentous micelles (filomicelles) which remains in circulation 1 week after injection, while spherical versions are cleared within 2 days **(Figure 1.5)**[86]**.** Increased circulation time is correlated with enhanced therapeutic efficacy of paclitaxel-loaded filomicelles in a subcutaneous xenograft model. Micelle length appears to be a critical factor: an eight-fold increase in filomicelle length had the same therapeutic benefit as an eight-fold increase in paclitaxel dose.

Along with size and shape, surface properties are a key parameter affecting biodistribution and cellular uptake. For example, nanoparticles with a strong charge or a hydrophobic surface attract serum proteins, which adsorb to the surface and form a protein corona. Adsorption of opsonins, such as IgG or complement factor, tag the protein for clearance by the immune system. A protein corona can also block targeting ligands that have been conjugated to the particle surface. Therefore, a neutral hydrophilic charge is typically desirable for systemically administered nanocarriers. PEGylation of particles is often used to reduce non-specific protein adsorption[87,88]. PEG can be incorporated into block co-polymers, conjugated to the surface of inorganic particles, or incorporated into liposomal formulations, making it an attractive option for a variety of delivery applications. PEGylation reduces uptake by the MPS and dramatically extends circulation time, particularly when particles are coated with high-molecular weight PEG at a high density[45,89]. Thus, many nanocarriers for cancer targeting are coated with PEG to increase blood circulation half-life and enhance passive targeting. However, bioinert hydrophilic carriers, due to their reduced binding to proteins and cellular components, also tend to have poor intracellular uptake and endosomal escape, and this related but unintended consequence is known as the PEG dilemma[90].

While EPR has been a significant discovery in preclinical models, passive targeting is a complex and highly variable process that depends on the size, degree of vascularization, and location or the tumor[91,92].There is also often a high degree of heterogeneity within tumors, with changes in cell density, interstitial pressure, and extracellular matrix composition affecting how nanoparticles move through different regions of tumor tissue[93]. These parameters are not easily recapitulated in vitro, and screening nanoparticles for in vivo delivery is traditionally low throughput and expensive.

1.2.2. Active Targeting

The large surface-to-volume ratio inherent to nanocarriers facilitates their interactions with biomolecules and cells. While methods described above have been employed to minimize this, thus extending the circulation time of nanocarriers, such interactions can also be leveraged as an advantage. Particles may be functionalized with active-targeting molecules that will specifically interact with the target and enrich particle accumulation in that site[94–96]. Nanoparticles have been functionalized to target various surface macromolecules on cancer cells, including overexpressed or mutated proteins, altered glycoproteins or glycolipids, and cancer-associated fetal proteins. Particles can also target molecules overexpressed in the tumor microenvironment, such as integrins, which are overexpressed on tumor vasculature[97,98]. Optimizing active molecular targeting of nanocarriers requires careful selection of a conjugation chemistry by which to attach targeting molecules to the particle surface. Different conjugation strategies can be selected depending on the bulk particle material, targeting ligand, and desired application. It is possible to harness hydrophobic or electrostatic interactions to functionalize nanoparticles by nonspecific adsorption, which enables functionalization without chemical modifications or complex reactions[99]. However, this requires the use of large amounts of targeting molecule and targeting

ligands may be displaced by other biological molecules in a physiological environment. Thus, covalent conjugation is commonly used for irreversible attachment of targeting ligands. Biological molecules such as proteins or peptides contain primary amines, which react with activated carboxylic acid groups on a nanocarrier to form an amide bond[100]. Common carboxylic acid-activating compounds include carbodiimidazole (CDI), as well as carbodiimide compounds, such as 1-ethyl-3-(3-dimethylaminopropyl)carbodiimide (EDC), often in combination with N-hydroxysuccinimide (NHS), or dicyclohexylcarbodiimide (DCC)[101]. Alternatively, cysteine residues in proteins or peptides contain thiol groups that can be reacted with maleimide-containing particles[102]. Proteins can also be functionalized with biotin for reaction with streptavidin-coated particles. To control ligand orientation on the particle surface, these reactive groups can be introduced at specific locations on the protein, either during synthesis or after protein purification[96,103]. Particles can also be coated with Protein A or Protein G, which bind the Fc region of antibodies and facilitates properly oriented conjugation. Conjugating targeting molecules via a flexible linker, such as PEG, allows the conjugated ligand or antibody to rotate and move freely in space for optimal binding with a target[104].

Conjugation methods can also dictate ligand density on the particle surface, which has proven an important parameter for optimization. For example, using various ratios of ligand-functionalized and unfunctionalized PEG for particle coating can significantly affect uptake by target cells[105]. While enriching the targeting ligand can lead to multivalent complexation and enhanced affinity, a saturation effect or even reduced binding has been reported[106,107]. This effect has been attributed to multiple factors, including steric hindrance or suboptimal receptor clustering. Nanoparticle size and shape also dictates surface curvature and contact surface area, which can affect interactions between particles and target cells[108]. Therefore, although ligand

density has been optimized in detail for particular nanocarriers[109], optimal parameters vary greatly depending on the size, shape, and material composition of the particle as well as size, chemistry, and avidity of the particular targeting ligand[110,111]. These parameters are summarized in (**Figure 1.6**).

A. Antibodies and Fragments

Antibodies have been extensively explored as therapeutics because they can be engineered to target almost any antigen with a high degree of specificity[112]. Monoclonal antibodies have been used in cancer therapy for over 20 years, and patient responses are well-understood, so they are a natural choice for nanoparticle targeting[113]. While antibody therapies work by blocking or binding a receptor on a cancer cell, nanoparticles harness the specificity of antibodies while incorporating additional therapeutic modes of action by encapsulating a drug or imaging agent or acting as a therapeutic itself. For example, trastuzumab is a monoclonal antibody for HER2 that is used clinically for breast cancer, and conjugating this antibody to gold nanoparticles showed promise as a photodynamic therapy, a strategy to ablate tumor tissue with a high degree of precision[114]. Antibodies can also bind to endocytic receptors on target cells and facilitate cellular uptake, which is necessary for functional nucleic acid delivery[115,116]. However, antibodies are bulky and significantly increase the size of conjugated nanoparticles. Safety concerns have also been raised, even with clinically approved monoclonal antibodies, regarding their immunogenicity[117].

With the clinical success of antibody therapies came interest in developing molecules with the same specificity but smaller size. That initiative sparked the invention of next-generation antibodies, including single chain antibodies, domain antibodies, and nanobodies[118–120]. Single-chain antibody fragments have been extensively explored for active targeting, since they

maintain the antigen-binding capability, are one fifth the size of full antibodies, and are considered safer than antibodies[121]. Antibodies and fragments are developed through display libraries, which preferentially and rapidly select for candidates which bind target cells and are internalized[122,123]. Because fragments can be screened for intracellular uptake, functionalized particles have been explored for nucleic acid delivery. For instance, liposomes surface-conjugated to a melanoma-targeted antibody fragment showed a significant therapeutic benefit in melanoma lung metastases, while non-targeted control particles had no significant effect[124]. Because of their small size, antibody fragments targeting EGFR have been conjugated to very small particles (quantum dots and 10-nm iron oxide nanoparticles) for high-sensitivity diagnostic imaging[125].

B. Ligands

Another approach to cancer cell targeting is functionalizing nanocarriers with ligands for overexpressed receptors, such as epidermal growth factor receptor (EGFR) and transferrin receptor. Many of these surface receptors are well-characterized cancer biomarkers, and ligands for these receptors have been identified and studied, which has led to their extensive development for active targeting. The natural ligands for overexpressed receptors range from proteins to carbohydrates to small molecules, such as vitamins[126]. Alternative small molecule ligands may also be developed using computational modeling and binding experiments, which expands targeting possibilities beyond the native ligand for a receptor[127].

Cancer-specific receptors can have a variety of functions, but nucleic acid delivery benefits from active targeting to endocytic receptors, which facilitate cancer-specific uptake and intracellular delivery. The transferrin receptor is a commonly overexpressed endocytic receptor on cancer cells and can be targeted by transferrin (Tf) protein-coated particles[128]. In another

example, hyaluronic acid (HA) functionalization facilitates uptake via overexpressed CD44 receptors. HA can serve as a bulk scaffold material for self-assembled nanoparticles or as a coating to functionalize particles composed of alternate materials, such as mesoporous silica[129].

Small molecule ligands also offer specificity to overexpressed receptors with minimal increase in particle size. Folic acid has been extensively studied as a targeting ligand due to its high affinity of the folate receptor, which is overexpressed in approximately 40% of cancer types, including breast, lung, ovarian, and colorectal cancers[130,131]. Small molecule 2-[3-[5-amino-1-carboxypentyl]-ureido] pentanedioic acid (ACUPA) is a high-affinity small molecule ligand of PSMA which has shown targeting properties in vivo and in vitro[132,133]. BIND-14, a PEG-PLGA nanoparticle with ACUPA active targeting for docetaxel developed by BIND Therapeutics, was evaluated in clinical trials for PSMA-targeted docetaxel delivery to prostate cancer[111]. ACUPA has recently been employed for PSMA-targeted delivery of siRNA to prostate cancer cells. For example, Xu et al. developed a nanocarrier comprised of a pH-responsive polymer blend coated with PEG-ACUPA for PSMA targeting to deliver siRNA targeting prohibitin (**Figure 1.7**)[134]. ACUPA-targeted NPs significantly suppressed tumor growth over non-targeted NPs after 30 days, showing the benefit of active targeting in this case[134].

Diseased or cancerous cells often display a different array of surface glycans compared to healthy cells, offering another targetable feature[135,136]. Lectins can be used to target drugs or nanoparticles specifically to cells displaying these abnormal features[137]. One useful example is targeting asialoglycoprotein receptors on liver cancer cells with galactosamine-conjugated nanoparticles[138–140]. Lectin conjugation can also facilitate transport across the blood-brain barrier, which typically serves a major hurdle for delivery to brain tumors. For example, nanoparticles modified with wheat germ agglutinin enhanced delivery to the brain two-fold over

unmodified nanocarriers[141].

An alternative to direct ligand conjugation is coating nanocarriers with cancer cell membranes. Recent research describes homotypic cancer cell binding—a phenomenon where cancer cells preferentially bind to membranes which carry the same surface antigens[142]. To harness this feature, researchers have coated nanoparticles with modified and unmodified cancer cell membranes, which provides a stealth coating as well as tumor homing properties[143]. This straightforward approach enables particle functionalization with the complete range of tumor ligands in a biomimetic manner and facilitates cancer-specific accumulation and uptake.

C. Aptamers

As discussed, many ligand-based active targeting systems are restricted to a biological ligand binding its natural target receptor. Aptamers are single-stranded DNA or RNA oligos that serve as attractive targeting alternatives. These nucleic acid molecules form sequence-specific three-dimensional structures and can be engineered to bind virtually any target, from small molecules and single amino acids to proteins, carbohydrates, and whole tumor cells. Aptamers are attractive for nanoparticle targeting because they have low molecular weight and can include chemical modifications for particle conjugation.[144]. Targeted aptamers are selected from a large library of random sequences using systematic evolution of ligands by exponential enrichment (SELEX)[145]. In each round of this process, the aptamer library is exposed to the desired target, unbound sequences are washed away, and bound sequences are selectively eluted and amplified using PCR. The process is repeated in subsequent selection rounds with more stringent binding conditions to generate tightly binding aptamers with antibody-like affinity and specificity.

Aptamers have been extensively explored in the past decade and have yielded novel selection methods for cancer targeting. Cell SELEX selects for aptamers that bind to a monolayer of

cultured cancer cells, rather than purified antigen[146]. This selection method generates a diverse pool of targeting aptamers that bind to or are internalized by the target cell population (**Figure 1.8**)[146–148] Methods have also been developed for in vivo SELEX, where aptamers are selected by binding tumors in situ in animal models[149]. This has resulted in aptamers with minimal off-target binding to healthy tissues that can bind multiple cell types in heterogeneous tumors[150]. Because aptamers can be generated for a range of molecules expressed in tumors, this targeting approach circumvents the problem of resistance, which is common when targeting a single receptor[151].

D. Integrins

The integrin profile of tumors is distinct from that of healthy tissues, and several integrins are upregulated on tumor endothelial cells and cancer cells[152,153]. The αVβ3 integrin is significantly upregulated in many cancers and can be targeted with a simple RGD peptide motif. RGD-targeted nanoparticles bind selectively to αVβ3 integrins, and this interaction facilitates selective endocytosis into angiogenic endothelial cells and cancer cells[154]. This approach has been used to efficiently deliver nucleic acids to tumor vasculature, for example to deliver siRNA against VEGF-R2 and inhibit both angiogenesis and tumor growth[155]. Because αVβ3 is expressed on both endothelial cells and cancer cells, RGD facilitates cancer cell targeting in addition to endothelial targeting. This dual targeting is a major advantage of RGD-functionalized nanocarriers. RGD-targeted chitosan nanoparticles containing siRNA have been used to successfully downregulate drug efflux transporter P-glycoprotein expression and reverse multidrug resistance in a breast cancer model[156]. Other integrins can serve as therapeutic targets, including arresten (α1β1), canstatin (αvβ3 and αvβ5), angiostatin (αvβ3), tumstatin (αvβ3), endostatin (αvβ3, αvβ5, and α5β1), and endorepellin (α2β1)[157]. Nanoparticles have been used to deliver these anti-angiogenic agents[158] or the genes that encode them[159].

Despite promising preclinical data for active targeting in nanomedicine, no FDA-approved nanocarriers have employed active targeting strategies. Active targeting increases the complexity and potential immunogenicity of a drug delivery system, which makes it more difficult, time consuming, and expensive to develop. Further complicating their optimization is the binding site barrier effect, where antibodies or nanoparticles bind target cells with high affinity and cannot penetrate throughout the tumor[160,161]. BIND-014 was an early targeted nanocarrier to enter clinical trials, and it benefitted from rigorous and systematic optimization of particle properties (size, surface properties, drug loading etc.) in preclinical studies and biodistribution validation in multiple animal models (mouse, rat, and monkey)[111]. This rigor is essential when increasing the complexity of a platform and should be a model for active targeting in the future.

Target identification remains a major hurdle, and even well-characterized targets are almost always heterogeneously expressed within tumors. Additionally, many of the receptors overexpressed on cancer cells, including transferrin and folate receptors, are also expressed on proliferating healthy cells, so targeting these receptors can lead to off-target side effects and systemic cytotoxicity[162]. Thus, efforts should be focused on developing companion diagnostic methods to characterize target expression and predict patient response. Radiolabeled tracers based on the RGD peptide sequence are already in clinical development for monitoring αVβ3 integrin expression in patients[163]. Such advanced diagnostic tools are needed to study biomarker distribution within patient populations and assess the feasibility of actively targeted nanocarriers for personalized medicine.

1.2.3 Stimulus-Responsive Targeting

As tumors grow and develop, cancer cells exist in a constantly changing environment, influenced by high cell density and low blood supply. Solid tumors have an abnormally acidic

pH, are subjected to low oxygen, and have a high concentration of certain enzymes[164]. These properties of the tumor microenvironment are targetable features that can be exploited for nanoparticle targeting and controlled release (**Figure 1.9**). To respond to an environmental stimulus, nanocarriers must include responsive chemistries that change the properties of the particle when it encounters a trigger. This triggered response can expose binding domains, dismantle a protective coating, or change particle surface properties to facilitate cancer-specific uptake.

Zwitterionic polymer nanoparticles are neutrally charged in physiological conditions, which confers stability, resists serum protein adhesion, and prevents clearance[164]. In the slightly acidic tumor microenvironment, the zwitterionic polymer becomes protonated and switches to cationic, facilitating uptake into cancer cells[165]. Cleavable PEG linkers can similarly be used to facilitate tumor cell uptake. Inert PEG coatings are commonly used in drug and gene delivery to enhance particle stability in circulation and increases the circulation half-life. However, as mentioned above, PEG coating also tends to decrease cellular uptake of particles[90]. To address this, researchers have coated particles with cleavable PEG, which is released in response to a trigger. For example, matrix metalloproteinases (MMPs), enzymes associated with angiogenesis and tumor growth, have been explored for triggered PEG de-shielding in a tumor-specific manner[166]. A multifunctional envelope-type nano-device (MEND) functionalized with MMP-cleavable PEG maintained the prolonged serum stability characteristic of PEG functionalized particles. Further, carriers conjugated with cleavable PEG exhibited superior in vitro and in vivo tumor transfection over carriers with non-cleavable PEG[167,168].

Responsive vehicles can also facilitate cytosolic release of nucleic acid cargo, which is particularly important for an efficient therapeutic response from RNA, since these molecules act

in the cytoplasm. Polymer nanoparticles often incorporate disulfide bonds, which degrade in the reducing environment of the cytoplasm and release their cargo. Using a bioreducible polymer reduces the toxicity of the nanocarrier while ensuring full protection of the easily degraded RNA cargo. pH can also trigger release in the acidic endosomal environment for site-specific cellular delivery. Acidic pH can trigger a shape change or expansion which disrupts the endosome and releases nucleic acid directly in the cytosol. Lipid-based liquid crystalline nanoparticles, termed nano-transformers, expand in a pH 5 environment from needle-like structures to nanospheres[169]. This shape transformation was proposed to have improved endosomal escape by promoting membrane fusion with the endosome. In another approach, Luo et al used miRNA-catalyzed release to specifically trigger payload release in the presence of miRNA-21, which is overexpressed in many cancers[170]. Similarly, the DNA "nanosuitcase" developed by Bujold et al. opens conditionally in the presence of a miRNA or mRNA and releases its therapeutic oligo cargo[171]. This approach allows triggered intracellular release in response to a genetic biomarker, limiting its effects to cancer cells. Responsive vehicles for intracellular delivery ensure efficient and specific cargo release to allow all components in a combinatorial system to act simultaneously, which is likely important to achieve synergistic effects.

Systemically administered nanocarriers can also be triggered by an external stimulus to enhance gene delivery at the tumor site. The properties of thermoresponsive polymer particles change in response to externally applied heat or cold, which can be harnessed for tumor-specific gene delivery[172]. Poly(N-isopropylacrylamide) (PNIPAM)-based polymer nanocarriers undergo a hydrophilic to hydrophobic transition when temperature is raised from 37° C to 42°C, which causes the particles to aggregate and enhances endosomal escape, resulting in 2 orders of magnitude enhanced transfection at hyperthermic sites[173]. Light-responsive particles have also

been used to enhance endosomal escape in a spatially controlled manner[174]. To harness this for siRNA delivery, a photosensitizer was combined with siRNA and encapsulated using the Lipofectamine commercial transfection reagent, and cells stimulated with light showed 10-fold higher silencing than non-stimulated cells[175]. Though this strategy has shown efficacy in vitro, photodynamic therapy in vivo is limited by the penetration depth of visible light through tissue. Magnetic coating or encapsulation of magnetic material can be used for magnetically guided nucleic acid delivery to a targeted site[176,177]. An applied magnetic field is used to concentrate or retain gene delivery particles at the tumor site, which has been used to enhance the delivery of DNA and siRNA in a process termed magnetofection[176,178].

Ultrasound has been extensively used in combination with microbubbles for regio-specific delivery of anticancer agents. Briefly, a nucleic acid nanocarrier is co-delivered with gas microbubbles, which are clinically approved for use as a contrast agent[179]. Co-localization of microbubbles and nanocarriers is essential for successful transfection, so the nanocarriers must be coupled to the surface of the bubble using covalent conjugation. Then, ultrasound is applied to the target area, and passage of ultrasound through tissue creates pressure waves, which cause the microbubbles to undergo cavitation and release energy that opens transient pores in surrounding cells. The co-delivered nanocarrier enters the cell through these sub-micron pores, which leads to significantly enhanced transfection at the site where ultrasound was applied. DNA-containing PEI polyplexes conjugated to microbubbles combined with ultrasound stimulation enabled gene delivery to implanted tumors in a mouse kidney with 40-fold higher expression in tumor tissue than control non-sonicated tissue[180]. In a similar approach, liposome-bearing microbubbles enhanced the delivery of an anti-fibrotic miRNA to diseased liver in rats[181]. Microbubble cavitation can also be used to open the blood-brain barrier and allow systemically administered

nanocarriers to reach tumors in the brain[182]. Because nanocarriers enter through pores in the cell membrane, they bypass endosomal uptake and are delivered directly to the cytosol[183]. The method is also non-invasive and provides precise spatial and temporal control over nucleic acid delivery. However, the precise location of the tumor must be known to effectively apply the ultrasound to the target site. Image-guided focused ultrasound has been used to localize ultrasound signal more precisely, particularly for opening the blood brain barrier[184,185]. Still, this approach is limited to primary tumor sites rather than dispersed metastases.

1.2.4 Local Administration

When possible, local administration can increase particle concentrations at the target site while decreasing healthy tissue exposure. Direct intratumoral administration is not an option in most cases, as accessing the tumor would involve an invasive procedure. Surgical tumor resection can be used as an opportunity to deliver a therapeutic directly to the site, where any remaining cancer cells can be treated to prevent recurrence. Implanted drug delivery depots can deliver a therapeutic at a controlled dose over the course of weeks or months with a single implantation surgery[186]. Nucleic acid therapeutics have been encapsulated in hydrogel depots for local delivery and reduced systemic toxicity. Naked DNA can be incorporated in hydrogels for regenerative medicine and anti-cancer applications, but only low levels of gene transfer have been observed due to the absence of a carrier[187,188]. DNA/PEI polyplexes have been successfully encapsulated in hydrogels and show effective gene transfer in vitro and in choriallantoic membrane assays[189,190]. siRNA-loaded micelles have similarly been encapsulated in injectable polyurethane scaffolds for sustained local gene silencing[191]. The bulk hydrogel can be tuned to achieve the desired release kinetics, including varying material, molecular weight, crosslinking density, size, and geometry. Another advantage of hydrogels is the ability to encapsulate multiple

separate agents in a single gel and simultaneously target cancer by multiple modes of action. Locally implanted hydrogel patches have been used to simultaneously deliver chemotherapy, siRNA, and gold nanoparticles for photothermal therapy[192]. This strategy can also be applied to deliver nucleic acid cargos with different properties, for example RNA and DNA, at the same site with particles optimized for each particular cargo. Nanocarrier properties can be independently tuned for efficient and targeted nucleic acid delivery, but maintaining stability and bioactivity of encapsulated particles is a significant hurdle to successful transfection.

Certain tumors can be accessed with non-surgical and non-invasive delivery routes, which reduces the potential for complications and enables frequent repeated particle dosing. Aerosol delivery provides direct access to lung tissue and can be used as a delivery route for lung cancer[193,194]. An inhalable cationic liposome formulation for plasmid DNA is in clinical trials to treat cystic fibrosis, and a hyperbranched PBAE nanoparticle recently was used for mRNA delivery to lung epithelium (**Figure 1.10**)[195,196]. Patel et al. reported that hDD90-118 polyplexes remained stable after aerosolizing with a vibrating mesh nebulizer, which produced micro-sized droplets ideal for distribution throughout lung tissue[195]. They were able to transfect 24.6% of lung epithelial cells after a single dose, with transfection seen in all five lobes of the lung[195]. Delivery to other tissues, including the liver, spleen, and heart, was negligible, and there was no observed local or systemic toxicity[195].While this platform has not been employed in lung cancer models, cancer treatment is an obvious potential application of these new inhalable technologies. The skin is uniquely accessible for local delivery, so topical applications are being explored for nanoparticle gene delivery to skin cancer[197]. Nanocarriers can be used to control permeation through the skin, and transport properties can be controlled independently of the cargo[198]. Chitosan nanoparticles have been used for antisense oligonucleotide and plasmid DNA delivery

to skin, with reporter gene effects persisting on rat skin for 6-7 days[199,200]. Free nucleic acid had no measurable transfection, indicating that a drug silvery system is required to effectively protect and deliver topically applied nucleic acids. Finally, oral delivery of nanoparticles allows direct access to tumors of the gastrointestinal tract[201,202]. Chitosan nanoparticles have also been explored for this purpose, as they are stable upon oral administration, can encapsulate nucleic acid cargos, facilitate transport across the intestinal wall, and can be functionalized for active tumor targeting[203]. Delivery to different tissues requires overcoming different barriers, which can be physical (surfactant, mucous, stratum corneum), biological (enzymes, resident immune cells, blood brain barrier), and chemical (harsh pH of the GI tract). Future work in this area must focus on enhancing particle stability, controlling release kinetics, and improving transport and permeability across these tissue-specific barriers in orthotopic tumor models.

1.2.5 Nucleic Acid Targeting

Cancer is fundamentally a condition caused by dysregulated gene expression, and nucleic acid therapies can treat the genetic basis of the disease by counteracting observed genetic changes. Advances in high throughput sequencing, microarray technologies, and novel computational models have resulted in a rapidly growing understanding of the genetic basis of cancer. We are now beginning to understand how particular genetic mutations and expression profiles correlate with disease stage, drug resistance, and potential for metastasis. Therefore, selecting certain nucleic acid cargos can target disease that is more aggressive, drug resistant, or likely to metastasize. Combinatorial strategies greatly increase the number of possible nucleic acid combinations that may be used to target a heterogeneous tumor population. Additionally, as illustrated thus far, combinatorial approaches have been successful in slowing tumor growth in these aggressive and difficult to treat cases.

One common approach is restoring the function of a mutated tumor suppressor with exogenous nucleic acids. Mutations in tumor suppressors have been associated with resistance to chemotherapy and radiation[204,205]. Tumor suppressor function can be restored by introducing nucleic acids, including DNA and mRNA, that encode for the wild-type protein[206]. For example, systemic delivery of PTEN mRNA using polymer-lipid hybrid nanoparticles was shown to slow tumor growth in multiple models of prostate cancer[207]. Modified mRNA shows enhanced stability compared to plasmid DNA therapies in systemic circulation with more predictable and desirable protein kinetics. P53 is another tumor suppressor that has been targeted in many clinical and preclinical trials[208,209]. Studies have shown that introducing p53 induces apoptosis in many cancer cells, but healthy cells only experience cell cycle arrest, which suggests inherent cancer-specificity to p53 gene therapy[210,211]. However, certain healthy cell types, including epithelial and hemopoietic cells, are sensitive to p53-induced apoptosis[212,213]. Also, p53 is part of a complex interconnected web of factors, and the efficacy of these therapies is limited by mutations in downstream factors and epigenetic changes, as well as heterogeneous p53 expression throughout tumors[213]. While p53 mutations have been explored most extensively due to their prevalence, other tumor suppressors (e.g., Rb7, PTEN, or mda-7) have also been targeted[214].

An alternative approach is silencing of overexpressed oncogenes using RNAi. Many strategies involving siRNA or miRNA have been developed to target oncogenes for cancer therapy. Ideal targets are upregulated in cancer cells, are vital for cancer progression, and do not have a rapid turnover rate. Examples of targeted pathways include angiogenesis (VEGF), proliferation (FAK), survival (Bcl-2, survivin), cell cycle (PLK1, cyclin B1), and resistance to chemotherapy or radiation (c-myc)[215]. Knocking down these pathways can have a potent anti-

cancer effect but can also affect the viability of healthy cells and tissues, leading to systemic toxicity. Brummelkamp et al. approached this problem by developing siRNA that specifically targets the oncogenic K-RASV12 allele without any effect on wild-type K-RAS expression, which is required for normal cell survival[216]. They showed that knocking down K-RASV12 with a viral vector completely prevented CAPAN-1 pancreatic cancer cell growth in vitro as well as in a subcutaneous tumor model. This approach is promising for specifically targeting cancers with mutations or chromosomal translocations that produce mRNA transcripts distinct from those expressed in healthy cells.

Cancer cells are also more vulnerable to cell death through certain proapoptotic pathways, including TNF[217], Fas[218], and Bcl[219]. Tumor necrosis factor (TNF)-related apoptosis-inducing ligand (TRAIL) induces apoptosis with a strong cancer selectivity, due to overexpression of TRAIL-binding death receptors on cancer cells[220]. Because recombinant TRAIL proteins have poor pharmacokinetics and a short circulation half-life, nucleic acid therapies are a promising approach to achieve sustained TRAIL expression. Co-delivery with small molecule sensitizers, including clinically approved chemotherapies, has been shown to reverse TRAIL-resistance and improve antitumor efficacy in a synergistic manner. A dendrimer nanocarrier co-encapsulating doxorubicin and a plasmid DNA expressing human TRAIL induced synergistic growth inhibition in U87 glioma cells[221]. This treatment administered intravenously induced observable apoptosis in an orthotopic murine glioma model, and the co-delivery vehicle extended median survival to 57 days, compared to 34 days with doxorubicin alone. Another strategy for TRAIL therapy is to transfect or transduce tumor-homing stem cells ex vivo to secrete TRAIL in the vicinity of the tumor[222]. This strategy combines regio-selective delivery of the stem cells with the cancer-specific TRAIL therapy and shows significant survival benefit in an aggressive brainstem glioma

model[223]. A secretable TRAIL construct has also been developed to enhance the bystander effect to neighboring cancer cells and further potentiate the antitumor effect[224].

Gene expression in cancer cells is modulated by differential expression of transcription factors, which can be exploited to restrict the expression of therapeutic genes to tumor cells. By placing transgenes under the control of certain promoters, it is possible to achieve tissue-specific, cell-specific, or exogenously stimulated expression[225]. For example, hTR and hTERT promoters drive telomerase activity, which is a common feature of most cancers and can activate genes in a cancer-targeted manner[226]. Tumor-specific promoters ideally have strong expression in cancer cells and little to no expression in healthy cells. For example, alpha fetoprotein (AFP) is transcriptionally silent in adult liver but is expressed in 70-80% of hepatocellular carcinoma cases[227]. When potent pro-apoptotic genes are placed under the control of the AFP-promoter, cell death is restricted to AFP-producing HCC cells, and no acute systemic toxicity is observed[228]. Transcriptionally targeted BikDD DNA delivered by DOPC-cholesterol liposomes prolonged survival in multiple xenograft and syngeneic orthotopic murine HCC models (**Figure 1.11**)[228]. Histological staining indicated that treatment-induced apoptosis was restricted to liver tumor cells, and cell death was not observed in healthy liver[228]. Many other tumor-specific promoters have been identified for particular cancer types, each with a different prevalence, expression profile, promoter strength, and tumor target. Another approach is to use promoters that respond to the tumor microenvironment. Hypoxia response elements (HREs) can be used to drive gene expression in hypoxic tumor environments, where cells are typically resistant to chemotherapy and radiation. Glucose-responsive promoters, such as hexokinase 2 and GRP78, respond to low glucose and high catabolism in tumors[229–231]. Finally, inducible promoters have been developed to respond to exogenous stimulation. Examples of stimuli include radiation, hyperthermia, and

small molecule drugs[232–234]. These promoters do not depend on the expression profile of the tumor, so the strength and duration of activation can be controlled. Ultimately, transcriptional targeting offers an opportunity to control expression at the cellular level, which can dramatically reduce off-target toxicity.

Combinatorial delivery can also be used to counteract phenotypic changes in a particular subset of cancer cells, such as drug resistant or stem-like cells. A combination of miRNAs can be used to target multiple pathways involved in the stem-like phenotype of brain tumor initiating cells. This minor population of glioblastoma cells has been associated with tumor reoccurrence and drug resistance. Using pooled miRNAs to revert the stem-like traits in these cells has proven successful in inhibiting growth, neurosphere formation, and shrinking orthotopic xenografts in mouse glioblastoma models[235,236]. Therefore, particular combinations of nucleic acids can target certain phenotypes associated with aggressive or reoccurring disease. Pooled siRNAs have also been used as a treatment strategy to overcome multiple drug resistance. In one example, two siRNAs (anti-Pgp and anti-Bcl-2) were combined with epirubicin in a calcium phosphate inorganic nanoparticle as a treatment for drug-resistant liver cancer cells and tumors[237]. The study concluded that the combination therapy was effective due to simultaneous targeting of two drug resistance mechanisms: pump (anti-Pgp) and non-pump (anti-Bcl-2)[237]. Therefore, pooled nucleic acid combination therapies can act synergistically and address tumor heterogeneity by acting on multiple pathways with spatial and temporal synchronization.

1.2.6 Multifunctional Targeted Nanocarriers

The use of a cancer-specific cargo reduces the burden of developing a perfectly targeted nanocarrier, since off-target delivery will have minimal effect in normal cells. Further, combinatorial nucleic acid therapies can be selected to address tumor heterogeneity or to target a

particular cancer cell subtype. The targeting methods described here work at different levels: local delivery to the tissue of interest, responsive uptake in the tumor microenvironment, active targeting to certain cell types, and genetic targeting to particular expression profiles. Thus, these orthogonal targeting mechanisms can be combined into highly targeted multifunctional nanocarriers. The multifunctional envelope-type nano-device (MEND) developed by Hatakeyama et al. integrates multiple strategies for successful cancer-specific nucleic acid delivery[168]. MEND is a nanocarrier comprised of nucleic acid condensed by a cationic polymer coated with a lipid envelope, which has been functionalized with various combinations of responsive and targeting features. For example, one iteration of the platform combines MMP-cleavable PEG and pH-sensitive fusogenic peptides to overcome the PEG dilemma and specifically enhance cellular uptake of siRNA in solid tumors[20]. Combining transcriptional targeting with particle targeting is another promising dual-targeting strategy, demonstrated by Cocco et al.[238] They developed a PLGA-PBAE blend nanoparticle functionalized with tumor targeting c-CPE peptides and used these particles to deliver a diphtheria toxin subunit A (DT-A) gene under the control of the cancer-specific p16 promoter. The dual-targeted particles efficiently transfected primary patient cells and significantly slowed tumor growth in chemotherapy-resistant ovarian cancer models.

Multifunctional particles also have the potential to achieve stepwise release of therapeutic agents. For example, core-shell particles can release siRNA molecules from an outer polymer layer in a glutathione-responsive manner followed by slow release of a chemotherapy to overcome multi-drug resistance[239]. While multifunctional targeted particles show promise in preclinical studies, the lack of targeted particles in clinical trials for nucleic acid delivery is a testament to the complexity of implementing active targeting in a translational and scalable way.

Developing targeted nanocarriers requires additional testing, time, and expense, and the resulting product is often expensive to manufacture. Despite these hurdles, several next-generation actively targeted nanomedicines for nucleic acid delivery have entered clinical trials. As more potent nucleic acid therapies are developed, particularly immunotherapies, a high degree of specificity will be essential to avoid dangerous off-target effects. Thus, these targeting strategies may serve as enabling technologies to bring nucleic therapies to patients.

1.2.7 Clinical Results

In recent years, several polymer nanoparticle formulations have been tested in the clinic with promising results, as outlined in **Table 1.2**.

CALAA-01 (Calando Pharmaceuticals) was the first nanocarrier for siRNA delivery to reach clinical development in 2008[82]. CALAA-01 is a cyclodextrin particle decorated with PEG for biological stability and transferrin ligands to target transferrin receptors overexpressed on cancer cells[240]. This carrier is used to deliver siRNA targeting the M2 subunit of ribonucleotide reductase. Tumor biopsies showed evidence of gene silencing by RNA interference, suggesting that targeted cyclodextrin nanoparticles are promising delivery vehicles for nucleic acids[241]. The therapy was shown to be safe in phase I trials, with minimal liver and kidney toxicity[242]. In the phase I trial, the most promising response was stable disease in one melanoma patient for four months[242].

Dr. Robert Langer of the Massachusetts Institute of Technology and Dr. Omid Farokhzad of Harvard Medical School developed a promising targeted and controlled release polymeric nanoparticle tested in humans. Their company, BIND Therapeutics, was founded around BIND-014, a prostate-specific membrane antigen (PSMA)-targeted PLGA nanoparticle containing docetaxel[111]. The treatment was well tolerated with no unanticipated toxicities in phase 1 clinical

trials, and 6 of 52 patients responded to the treatment, one with a complete response[243]. Responses occurred in both PSMA-expressing and non-expressing tumors, indicating that passive targeting played a significant role.

NanoCarrier Co. has completed phase I clinical trials with NC-6004, a polymeric micelle made of PEG-poly(amino acid) block copolymers. These particles have been tested in clinical trials to deliver cisplatin for lung, bladder, bile duct, pancreatic, and head and neck cancers. In phase I trials, the use of the nanocarrier increased the dose-limiting toxicity of cisplatin 34-fold, and stable disease was observed for longer than 4 weeks in 7 of 17 patients with solid tumors treated with NC-6004[244].

CRLX101 (NewLink Genetics Corporation) particles are formed with alternating units of cyclodextrin and PEG, which improves circulation time, and camptothecin is chemically linked to the polymer for pH-dependent release[245]. Phase I clinical trials showed acceptable safety and pharmacokinetics[246]. In phase II clinical trials, a measurable reduction in tumor size was observed in 74% of 22 patients with platinum-resistant ovarian cancer, and most recent results report a 16% response rate according to internationally recognized Response Evaluation Criteria in Solid Tumors (RECIST) criteria[247]. Preclinical and preliminary clinical studies suggest a synergistic effect with anti–vascular endothelial growth factor therapy bevacizumab, which will be further evaluated in future trials[247,248].

NK105, developed by Nippon Kayaku Co., is a micellar form of paclitaxel formulated from PEG-polyaspartate block copolymers. This nanoparticle formulation demonstrated preclinical success in increasing circulation time, reducing off-target toxicity, and improving the antitumor effect of paclitaxel[249]. Phase I trials showed a maximum tolerated dose 15 times higher than that of free paclitaxel[250]. In phase II trials, two full responses and 12 partial responses were observed

for a 25% overall response rate[251].

1.3 Specific Aims

The goal of this thesis is to explore several methods for targeting DNA delivery. The thesis begins by evaluating PBAE NPs for targeted delivery *in vivo*, exploring both systemic delivery of DNA (Chapter 1) and local delivery via the hepatic artery (Chapter 2). Then, biomaterial targeting is employed to deliver a pro-apoptotic cDNA to HCC cells (Chapter 3). Finally, transcriptional targeting is employed to restrict theranostic gene expression to HCC cells (Chapter 4).

Specific Aim 1: Analyze and optimize tissue-specific DNA delivery by systemically and locally administered nanoparticles

a) Develop a barcode DNA system as an enabling technology for high throughput analysis of biodistribution and transfection by systemically administered nanoparticles.

b) Evaluate tumor-specific gene delivery by loco-regional delivery via the hepatic artery.

Specific Aim 2: Apply cancer specific PBAE nanoparticles to deliver a novel secretable TRAIL (sTRAIL) therapy to human hepatocellular carcinoma

a) Construct and characterize a vector and nanoparticle non-viral delivery vehicle for secretable TRAIL therapy

b) Characterize cancer-specific apoptosis *in vitro* with combination sTRAIL nanoparticles and small molecule sensitizer treatment

c) Assess tumor killing properties of sTRAIL therapy *in vivo* in a xenograft tumor model of human HCC

Specific Aim 3: Engineer cancer specific PBAE nanoparticles to deliver theranostic transcriptionally targeted DNA to human hepatocellular carcinoma and achieve targeted cancer

cell killing and PET imaging

a) Construct a clinically compatible theranostic vector harboring a cancer-specific promoter and SR39 suicide gene

b) Evaluate transcriptional HCC targeting via *in vitro* delivery of SR39 for AFP-specific cancer cell killing and radiotracer uptake

c) Deliver theranostic vector to orthotopic hepatocellular carcinoma, followed by systemic administration of a radiotracer and prodrug GCV to enable simultaneous PET/MRI imaging and tumor killing

1.4 References

1. Vogelstein, B and Kinzler, KW (2004). Cancer genes and the pathways they control. *Nat. Med.* **10**: 789–799.
2. Leung, RKM and Whittaker, PA (2005). RNA interference: from gene silencing to gene-specific therapeutics. *Pharmacol. Ther.* **107**: 222–239.
3. McCall, RL and Sirianni, RW (2013). PLGA nanoparticles formed by single-or double-emulsion with vitamin E-TPGS. *J. Vis. Exp. JoVE*.
4. Chan, JM, Zhang, L, Yuet, KP, Liao, G, Rhee, J-W, Langer, R, *et al.* (2009). PLGA–lecithin–PEG core–shell nanoparticles for controlled drug delivery. *Biomaterials* **30**: 1627–1634.
5. Wang, Y, Gao, S, Ye, W-H, Yoon, HS and Yang, Y-Y (2006). Co-delivery of drugs and DNA from cationic core–shell nanoparticles self-assembled from a biodegradable copolymer. *Nat. Mater.* **5**: 791–796.
6. Wightman, L, Kircheis, R, Rössler, V, Carotta, S, Ruzicka, R, Kursa, M, *et al.* (2001). Different behavior of branched and linear polyethylenimine for gene delivery in vitro and

in vivo. *J. Gene Med. A cross-disciplinary J. Res. Sci. gene Transf. its Clin. Appl.* **3**: 362–372.

7. Ogris, M, Steinlein, P, Kursa, M, Mechtler, K, Kircheis, R and Wagner, E (1998). The size of DNA/transferrin-PEI complexes is an important factor for gene expression in cultured cells. *Gene Ther.* **5**: 1425–1433.

8. Ogris, M, Brunner, S, Schüller, S, Kircheis, R and Wagner, E (1999). PEGylated DNA/transferrin–PEI complexes: reduced interaction with blood components, extended circulation in blood and potential for systemic gene delivery. *Gene Ther.* **6**: 595–605.

9. Hafez, IM, Maurer, N and Cullis, PR (2001). On the mechanism whereby cationic lipids promote intracellular delivery of polynucleic acids. *Gene Ther.* **8**: 1188–1196.

10. Xu, Y and Szoka, FC (1996). Mechanism of DNA release from cationic liposome/DNA complexes used in cell transfection. *Biochemistry* **35**: 5616–5623.

11. Zelphati, O and Szoka, FC (1996). Mechanism of oligonucleotide release from cationic liposomes. *Proc. Natl. Acad. Sci.* **93**: 11493–11498.

12. Verma, A and Stellacci, F (2010). Effect of surface properties on nanoparticle–cell interactions. *small* **6**: 12–21.

13. Heitz, F, Morris, MC and Divita, G (2009). Twenty years of cell-penetrating peptides: from molecular mechanisms to therapeutics. *Br. J. Pharmacol.* **157**: 195–206.

14. Niidome, T, Ohmori, N, Ichinose, A, Wada, A, Mihara, H, Hirayama, T, *et al.* (1997). Binding of cationic α-helical peptides to plasmid DNA and their gene transfer abilities into cells. *J. Biol. Chem.* **272**: 15307–15312.

15. Plank, C, Oberhauser, B, Mechtler, K, Koch, C and Wagner, E (1994). The influence of endosome-disruptive peptides on gene transfer using synthetic virus-like gene transfer

systems. *J. Biol. Chem.* **269**: 12918–12924.

16. Frankel, AD and Pabo, CO (1988). Cellular uptake of the tat protein from human immunodeficiency virus. *Cell* **55**: 1189–1193.

17. Green, M and Loewenstein, PM (1988). Autonomous functional domains of chemically synthesized human immunodeficiency virus tat trans-activator protein. *Cell* **55**: 1179–1188.

18. Sonawane, ND, Szoka Jr, FC and Verkman, AS (2003). Chloride accumulation and swelling in endosomes enhances DNA transfer by polyamine-DNA polyplexes. *J. Biol. Chem.* **278**: 44826–44831.

19. Shim, MS and Kwon, YJ (2012). Stimuli-responsive polymers and nanomaterials for gene delivery and imaging applications. *Adv. Drug Deliv. Rev.* **64**: 1046–1059.

20. Hatakeyama, H, Ito, E, Akita, H, Oishi, M, Nagasaki, Y, Futaki, S, *et al.* (2009). A pH-sensitive fusogenic peptide facilitates endosomal escape and greatly enhances the gene silencing of siRNA-containing nanoparticles in vitro and in vivo. *J. Control. Release* **139**: 127–132.

21. Gary, DJ, Puri, N and Won, Y-Y (2007). Polymer-based siRNA delivery: perspectives on the fundamental and phenomenological distinctions from polymer-based DNA delivery. *J. Control. Release* **121**: 64–73.

22. Luo, D and Saltzman, WM (2000). Synthetic DNA delivery systems. *Nat. Biotechnol.* **18**: 33–37.

23. Xu, Y, Liang, W, Qiu, Y, Cespi, M, Palmieri, GF, Mason, AJ, *et al.* (2016). Incorporation of a nuclear localization signal in pH responsive LAH4-L1 peptide enhances transfection and nuclear uptake of plasmid DNA. *Mol. Pharm.* **13**: 3141–3152.

24. Lechardeur, D and Lukacs, GL (2006). Nucleocytoplasmic transport of plasmid DNA: a perilous journey from the cytoplasm to the nucleus. *Hum. Gene Ther.* **17**: 882–889.

25. Kirchenbuechler, I, Kirchenbuechler, D and Elbaum, M (2016). Correlation between cationic lipid-based transfection and cell division. *Exp. Cell Res.* **345**: 1–5.

26. Grosse, S, Thévenot, G, Monsigny, M and Fajac, I (2006). Which mechanism for nuclear import of plasmid DNA complexed with polyethylenimine derivatives? *J. Gene Med. A cross-disciplinary J. Res. Sci. gene Transf. its Clin. Appl.* **8**: 845–851.

27. Ross, NL and Sullivan, MO (2016). Overexpression of caveolin-1 in inflammatory breast cancer cells enables IBC-specific gene delivery and prodrug conversion using histone-targeted polyplexes. *Biotechnol. Bioeng.* **113**: 2686–2697.

28. Matz, RL, Erickson, B, Vaidyanathan, S, Kukowska-Latallo, JF, Baker Jr, JR, Orr, BG, *et al.* (2013). Polyplex exposure inhibits cell cycle, increases inflammatory response, and can cause protein expression without cell division. *Mol. Pharm.* **10**: 1306–1317.

29. Chan, KS, Koh, CG and Li, HY (2012). Mitosis-targeted anti-cancer therapies: where they stand. *Cell Death Dis.* **3**: e411–e411.

30. Spagnou, S, Miller, AD and Keller, M (2004). Lipidic carriers of siRNA: differences in the formulation, cellular uptake, and delivery with plasmid DNA. *Biochemistry* **43**: 13348–13356.

31. Hill, IRC, Garnett, MC, Bignotti, F and Davis, SS (1999). In vitro cytotoxicity of poly(amidoamine)s: relevance to DNA delivery. *Biochim. Biophys. Acta - Gen. Subj.* **1427**: 161–174.

32. Lim, Y-B, Han, S-O, Kong, H-U, Lee, Y, Park, J-S, Jeong, B, *et al.* (2000). Biodegradable Polyester, Poly[α-(4-Aminobutyl)-l-Glycolic Acid], as a Non-Toxic Gene Carrier. *Pharm.*

Res. **17**: 811–816.

33. Forrest, ML, Koerber, JT and Pack, DW (2003). A Degradable Polyethylenimine Derivative with Low Toxicity for Highly Efficient Gene Delivery. *Bioconjug. Chem.* **14**: 934–940.

34. Sutton, D, Kim, S, Shuai, X, Leskov, K, Marques, JT, Williams, BRG, *et al.* (2006). Efficient suppression of secretory clusterin levels by polymer-siRNA nanocomplexes enhances ionizing radiation lethality in human MCF-7 breast cancer cells in vitro. *Int. J. Nanomedicine* **1**: 155–162.

35. Richards Grayson, AC, Doody, AM and Putnam, D (2006). Biophysical and Structural Characterization of Polyethylenimine-Mediated siRNA Delivery in Vitro. *Pharm. Res.* **23**: 1868–1876.

36. Ekin, A, Karatas, OF, Culha, M and Ozen, M (2014). Designing a gold nanoparticle-based nanocarrier for microRNA transfection into the prostate and breast cancer cells. *J. Gene Med.* **16**: 331–335.

37. Madhusudhan, A, Reddy, GB, Venkatesham, M, Veerabhadram, G, Kumar, DA, Natarajan, S, *et al.* (2014). Efficient pH dependent drug delivery to target cancer cells by gold nanoparticles capped with carboxymethyl chitosan. *Int. J. Mol. Sci.* **15**: 8216–8234.

38. Zhou, J, Zhang, J and Gao, W (2014). Enhanced and selective delivery of enzyme therapy to 9L-glioma tumor via magnetic targeting of PEG-modified, β-glucosidase-conjugated iron oxide nanoparticles. *Int. J. Nanomedicine* **9**: 2905.

39. Zhu, J, Zheng, L, Wen, S, Tang, Y, Shen, M, Zhang, G, *et al.* (2014). Targeted cancer theranostics using alpha-tocopheryl succinate-conjugated multifunctional dendrimer-entrapped gold nanoparticles. *Biomaterials* **35**: 7635–7646.

40. Iv, M, Telischak, N, Feng, D, Holdsworth, SJ, Yeom, KW and Daldrup-Link, HE (2015). Clinical applications of iron oxide nanoparticles for magnetic resonance imaging of brain tumors. *Nanomedicine* **10**: 993–1018.

41. Gilleron, J, Querbes, W, Zeigerer, A, Borodovsky, A, Marsico, G, Schubert, U, *et al.* (2013). Image-based analysis of lipid nanoparticle–mediated siRNA delivery, intracellular trafficking and endosomal escape. *Nat. Biotechnol.* **31**: 638–646.

42. Xing, M, Yan, F, Yu, S and Shen, P (2015). Efficacy and cardiotoxicity of liposomal doxorubicin-based chemotherapy in advanced breast cancer: a meta-analysis of ten randomized controlled trials. *PLoS One* **10**: e0133569.

43. O'Brien, MER, Wigler, N, Inbar, M, Rosso, R, Grischke, E, Santoro, A, *et al.* (2004). Reduced cardiotoxicity and comparable efficacy in a phase III trial of pegylated liposomal doxorubicin HCl (CAELYX™/Doxil®) versus conventional doxorubicin for first-line treatment of metastatic breast cancer. *Ann. Oncol.* **15**: 440–449.

44. Muggia, FM, Hainsworth, JD, Jeffers, S, Miller, P, Groshen, S, Tan, M, *et al.* (1997). Phase II study of liposomal doxorubicin in refractory ovarian cancer: antitumor activity and toxicity modification by liposomal encapsulation. *J. Clin. Oncol.* **15**: 987–993.

45. Gref, R, Minamitake, Y, Peracchia, MT, Trubetskoy, V, Torchilin, V and Langer, R (1994). Biodegradable long-circulating polymeric nanospheres. *Science (80-.).* **263**: 1600–1603.

46. Song, CX, Labhasetwar, V, Murphy, H, Qu, X, Humphrey, WR, Shebuski, RJ, *et al.* (1997). Formulation and characterization of biodegradable nanoparticles for intravascular local drug delivery. *J. Control. Release* **43**: 197–212.

47. Dang, JM and Leong, KW (2006). Natural polymers for gene delivery and tissue

engineering. *Adv. Drug Deliv. Rev.* **58**: 487–499.

48. Nair, LS and Laurencin, CT (2007). Biodegradable polymers as biomaterials. *Prog. Polym. Sci.* **32**: 762–798.

49. Rampino, A, Borgogna, M, Blasi, P, Bellich, B and Cesàro, A (2013). Chitosan nanoparticles: preparation, size evolution and stability. *Int. J. Pharm.* **455**: 219–228.

50. Hong, S-C, Yoo, S-Y, Kim, H and Lee, J (2017). Chitosan-based multifunctional platforms for local delivery of therapeutics. *Mar. Drugs* **15**: 60.

51. Carrillo, C, Suñé, JM, Pérez-Lozano, P, García-Montoya, E, Sarrate, R, Fàbregas, A, *et al.* (2014). Chitosan nanoparticles as non-viral gene delivery systems: determination of loading efficiency. *Biomed. Pharmacother.* **68**: 775–783.

52. Luo, Y, Teng, Z, Li, Y and Wang, Q (2015). Solid lipid nanoparticles for oral drug delivery: Chitosan coating improves stability, controlled delivery, mucoadhesion and cellular uptake. *Carbohydr. Polym.* **122**: 221–229.

53. Kean, T and Thanou, M (2010). Biodegradation, biodistribution and toxicity of chitosan. *Adv. Drug Deliv. Rev.* **62**: 3–11.

54. Fonte, P, Araújo, F, Silva, C, Pereira, C, Reis, S, Santos, HA, *et al.* (2015). Polymer-based nanoparticles for oral insulin delivery: Revisited approaches. *Biotechnol. Adv.* **33**: 1342–1354.

55. Breitenbach, BB, Schmid, I and Wich, PR (2017). Amphiphilic polysaccharide block copolymers for pH-responsive micellar nanoparticles. *Biomacromolecules* **18**: 2839–2848.

56. Banerjee, A and Bandopadhyay, R (2016). Use of dextran nanoparticle: A paradigm shift in bacterial exopolysaccharide based biomedical applications. *Int. J. Biol. Macromol.* **87**: 295–301.

57. Hudson, D and Margaritis, A (2014). Biopolymer nanoparticle production for controlled release of biopharmaceuticals. *Crit. Rev. Biotechnol.* **34**: 161–179.

58. Jana, S, Kumar Sen, K and Gandhi, A (2016). Alginate based nanocarriers for drug delivery applications. *Curr. Pharm. Des.* **22**: 3399–3410.

59. Jain, D and Bar-Shalom, D (2014). Alginate drug delivery systems: application in context of pharmaceutical and biomedical research. *Drug Dev. Ind. Pharm.* **40**: 1576–1584.

60. Lee, SJ, Yhee, JY, Kim, SH, Kwon, IC and Kim, K (2013). Biocompatible gelatin nanoparticles for tumor-targeted delivery of polymerized siRNA in tumor-bearing mice. *J. Control. release* **172**: 358–366.

61. Singh, A, Xu, J, Mattheolabakis, G and Amiji, M (2016). EGFR-targeted gelatin nanoparticles for systemic administration of gemcitabine in an orthotopic pancreatic cancer model. *Nanomedicine Nanotechnology, Biol. Med.* **12**: 589–600.

62. Santoro, M, Tatara, AM and Mikos, AG (2014). Gelatin carriers for drug and cell delivery in tissue engineering. *J. Control. release* **190**: 210–218.

63. Yamagata, M, Kawano, T, Shiba, K, Mori, T, Katayama, Y and Niidome, T (2007). Structural advantage of dendritic poly (L-lysine) for gene delivery into cells. *Bioorg. Med. Chem.* **15**: 526–532.

64. Acharya, S and Sahoo, SK (2011). PLGA nanoparticles containing various anticancer agents and tumour delivery by EPR effect. *Adv. Drug Deliv. Rev.* **63**: 170–183.

65. Chen, C, Law, W, Aalinkeel, R, Nair, B, Kopwitthaya, A, Mahajan, SD, *et al.* (2012). Well-defined degradable cationic polylactide as nanocarrier for the delivery of siRNA to silence angiogenesis in prostate cancer. *Adv. Healthc. Mater.* **1**: 751–761.

66. Hasan, W, Chu, K, Gullapalli, A, Dunn, SS, Enlow, EM, Luft, JC, *et al.* (2012). Delivery

of multiple siRNAs using lipid-coated PLGA nanoparticles for treatment of prostate cancer. *Nano Lett.* **12**: 287–292.

67. Grossen, P, Witzigmann, D, Sieber, S and Huwyler, J (2017). PEG-PCL-based nanomedicines: A biodegradable drug delivery system and its application. *J. Control. Release* **260**: 46–60.

68. Palamà, IE, Cortese, B, D'Amone, S and Gigli, G (2015). mRNA delivery using non-viral PCL nanoparticles. *Biomater. Sci.* **3**: 144–151.

69. Ulery, BD, Nair, LS and Laurencin, CT (2011). Biomedical applications of biodegradable polymers. *J. Polym. Sci. Part B Polym. Phys.* **49**: 832–864.

70. Loverde, SM, Klein, ML and Discher, DE (2012). Nanoparticle shape improves delivery: rational coarse grain molecular dynamics (rCG-MD) of taxol in worm-like PEG-PCL micelles. *Adv. Mater.* **24**: 3823–3830.

71. Tu, Y, Peng, F, André, AAM, Men, Y, Srinivas, M and Wilson, DA (2017). Biodegradable hybrid stomatocyte nanomotors for drug delivery. *ACS Nano* **11**: 1957–1963.

72. Davis, ME, Pun, SH, Bellocq, NC, Reineke, TM, Popielarski, SR, Mishra, S, *et al.* (2004). Self-assembling nucleic acid delivery vehicles via linear, water-soluble, cyclodextrin-containing polymers. *Curr. Med. Chem.* **11**: 179–197.

73. Gonzalez, H, Hwang, SJ and Davis, ME (1999). New class of polymers for the delivery of macromolecular therapeutics. *Bioconjug. Chem.* **10**: 1068–1074.

74. Tzeng, SY and Green, JJ (2013). Subtle changes to polymer structure and degradation mechanism enable highly effective nanoparticles for siRNA and DNA delivery to human brain cancer. *Adv. Healthc. Mater.* **2**: 468–480.

75. Sunshine, JC, Akanda, MI, Li, D, Kozielski, KL and Green, JJ (2011). Effects of base polymer hydrophobicity and end-group modification on polymeric gene delivery. *Biomacromolecules* **12**: 3592–3600.

76. Sunshine, J, Green, JJ, Mahon, KP, Yang, F, Eltoukhy, AA, Nguyen, DN, *et al.* (2009). Small-molecule end-groups of linear polymer determine cell-type gene-delivery efficacy. *Adv. Mater.* **21**: 4947–4951.

77. Green, JJ, Langer, R and Anderson, DG (2008). A combinatorial polymer library approach yields insight into nonviral gene delivery. *Acc. Chem. Res.* **41**: 749–759.

78. Guerrero-Cázares, H, Tzeng, SY, Young, NP, Abutaleb, AO, Quiñones-Hinojosa, A and Green, JJ (2014). Biodegradable Polymeric Nanoparticles Show High Efficacy and Specificity at DNA Delivery to Human Glioblastoma in Vitro and in Vivo. *ACS Nano* **8**: 5141–5153.

79. Kozielski, KL, Tzeng, SY, Hurtado De Mendoza, BA and Green, JJ (2014). Bioreducible cationic polymer-based nanoparticles for efficient and environmentally triggered cytoplasmic siRNA delivery to primary human brain cancer cells. *ACS Nano* **8**: 3232–3241.

80. Lynn, DM and Langer, R (2000). Degradable poly (β-amino esters): synthesis, characterization, and self-assembly with plasmid DNA. *J. Am. Chem. Soc.* **122**: 10761–10768.

81. Sunshine, JC, Peng, DY and Green, JJ (2012). Uptake and transfection with polymeric nanoparticles are dependent on polymer end-group structure, but largely independent of nanoparticle physical and chemical properties. *Mol. Pharm.* **9**: 3375–3383.

82. Matsumura, Y and Maeda, H (1986). A new concept for macromolecular therapeutics in

cancer chemotherapy: mechanism of tumoritropic accumulation of proteins and the antitumor agent smancs. *Cancer Res.* **46**: 6387–6392.

83. Steichen, SD, Caldorera-Moore, M and Peppas, NA (2013). A review of current nanoparticle and targeting moieties for the delivery of cancer therapeutics. *Eur. J. Pharm. Sci.* **48**: 416–427.

84. Champion, JA and Mitragotri, S (2006). Role of target geometry in phagocytosis. *Proc. Natl. Acad. Sci.* **103**: 4930–4934.

85. Truong, NP, Whittaker, MR, Mak, CW and Davis, TP (2015). The importance of nanoparticle shape in cancer drug delivery. *Expert Opin. Drug Deliv.* **12**: 129–142.

86. Geng, Y, Dalhaimer, P, Cai, S, Tsai, R, Tewari, M, Minko, T, *et al.* (2007). Shape effects of filaments versus spherical particles in flow and drug delivery. *Nat. Nanotechnol.* **2**: 249.

87. Peracchia, MT, Harnisch, S, Pinto-Alphandary, H, Gulik, A, Dedieu, JC, Desmaële, D, *et al.* (1999). Visualization of in vitro protein-rejecting properties of PEGylated stealth® polycyanoacrylate nanoparticles. *Biomaterials* **20**: 1269–1275.

88. Gref, R, Lück, M, Quellec, P, Marchand, M, Dellacherie, E, Harnisch, S, *et al.* (2000). 'Stealth' corona-core nanoparticles surface modified by polyethylene glycol (PEG): influences of the corona (PEG chain length and surface density) and of the core composition on phagocytic uptake and plasma protein adsorption. *Colloids Surfaces B Biointerfaces* **18**: 301–313.

89. Bazile, D, Prud'homme, C, Bassoullet, M, Marlard, M, Spenlehauer, G and Veillard, M (1995). Stealth Me. PEG-PLA nanoparticles avoid uptake by the mononuclear phagocytes system. *J. Pharm. Sci.* **84**: 493–498.

90. Hatakeyama, H, Akita, H and Harashima, H (2013). The polyethyleneglycol dilemma: advantage and disadvantage of PEGylation of liposomes for systemic genes and nucleic acids delivery to tumors. *Biol. Pharm. Bull.* **36**: 892–899.

91. Prabhakar, U, Maeda, H, Jain, RK, Sevick-Muraca, EM, Zamboni, W, Farokhzad, OC, *et al.* (2013). Challenges and key considerations of the enhanced permeability and retention effect for nanomedicine drug delivery in oncology.

92. Maeda, H (2015). Toward a full understanding of the EPR effect in primary and metastatic tumors as well as issues related to its heterogeneity. *Adv. Drug Deliv. Rev.* **91**: 3–6.

93. Jain, RK and Stylianopoulos, T (2010). Delivering nanomedicine to solid tumors. *Nat. Rev. Clin. Oncol.* **7**: 653.

94. Bazak, R, Houri, M, El Achy, S, Kamel, S and Refaat, T (2015). Cancer active targeting by nanoparticles: a comprehensive review of literature. *J. Cancer Res. Clin. Oncol.* **141**: 769–784.

95. Zhong, Y, Meng, F, Deng, C and Zhong, Z (2014). Ligand-directed active tumor-targeting polymeric nanoparticles for cancer chemotherapy. *Biomacromolecules* **15**: 1955–1969.

96. Byrne, JD, Betancourt, T and Brannon-Peppas, L (2008). Active targeting schemes for nanoparticle systems in cancer therapeutics. *Adv. Drug Deliv. Rev.* **60**: 1615–1626.

97. Weis, SM and Cheresh, DA (2011). αV integrins in angiogenesis and cancer. *Cold Spring Harb. Perspect. Med.* **1**: a006478.

98. Desgrosellier, JS and Cheresh, DA (2010). Integrins in cancer: biological implications and therapeutic opportunities. *Nat. Rev. Cancer* **10**: 9.

99. Harris, TJ, Green, JJ, Fung, PW, Langer, R, Anderson, DG and Bhatia, SN (2010). Tissue-specific gene delivery via nanoparticle coating. *Biomaterials* **31**: 998–1006.

100. Noga, DE, Petrie, TA, Kumar, A, Weck, M, García, AJ and Collard, DM (2008). Synthesis and modification of functional poly (lactide) copolymers: toward biofunctional materials. *Biomacromolecules* **9**: 2056–2062.

101. Nicolas, J, Mura, S, Brambilla, D, Mackiewicz, N and Couvreur, P (2013). Design, functionalization strategies and biomedical applications of targeted biodegradable/biocompatible polymer-based nanocarriers for drug delivery. *Chem. Soc. Rev.* **42**: 1147–1235.

102. Li, J, Feng, L, Fan, L, Zha, Y, Guo, L, Zhang, Q, *et al.* (2011). Targeting the brain with PEG–PLGA nanoparticles modified with phage-displayed peptides. *Biomaterials* **32**: 4943–4950.

103. Kumar, S, Aaron, J and Sokolov, K (2008). Directional conjugation of antibodies to nanoparticles for synthesis of multiplexed optical contrast agents with both delivery and targeting moieties. *Nat. Protoc.* **3**: 314.

104. Kawano, K and Maitani, Y (2011). Effects of polyethylene glycol spacer length and ligand density on folate receptor targeting of liposomal Doxorubicin in vitro. *J. Drug Deliv.* **2011**.

105. Nasongkla, N, Shuai, X, Ai, H, Weinberg, BD, Pink, J, Boothman, DA, *et al.* (2004). cRGD-Functionalized Polymer Micelles for Targeted Doxorubicin Delivery. *Angew. Chemie Int. Ed.* **43**: 6323–6327.

106. Elias, DR, Poloukhtine, A, Popik, V and Tsourkas, A (2013). Effect of ligand density, receptor density, and nanoparticle size on cell targeting. *Nanomedicine Nanotechnology, Biol. Med.* **9**: 194–201.

107. Haun, JB and Hammer, DA (2008). Quantifying Nanoparticle Adhesion Mediated by

Specific Molecular Interactions. *Langmuir* **24**: 8821–8832.

108. Chithrani, BD, Ghazani, AA and Chan, WCW (2006). Determining the size and shape dependence of gold nanoparticle uptake into mammalian cells. *Nano Lett.* **6**: 662–668.

109. Choi, CHJ, Alabi, CA, Webster, P and Davis, ME (2010). Mechanism of active targeting in solid tumors with transferrin-containing gold nanoparticles. *Proc. Natl. Acad. Sci.* **107**: 1235 LP – 1240.

110. Nel, AE, Mädler, L, Velegol, D, Xia, T, Hoek, EM V, Somasundaran, P, *et al.* (2009). Understanding biophysicochemical interactions at the nano–bio interface. *Nat. Mater.* **8**: 543.

111. Hrkach, J, Von Hoff, D, Ali, MM, Andrianova, E, Auer, J, Campbell, T, *et al.* (2012). Preclinical Development and Clinical Translation of a PSMA-Targeted Docetaxel Nanoparticle with a Differentiated Pharmacological Profile. *Sci. Transl. Med.* **4**: 128ra39 LP-128ra39.

112. Reichert, JM (2008). Monoclonal antibodies as innovative therapeutics. *Curr. Pharm. Biotechnol.* **9**: 423–430.

113. Scott, AM, Wolchok, JD and Old, LJ (2012). Antibody therapy of cancer. *Nat. Rev. Cancer* **12**: 278.

114. Stuchinskaya, T, Moreno, M, Cook, MJ, Edwards, DR and Russell, DA (2011). Targeted photodynamic therapy of breast cancer cells using antibody–phthalocyanine–gold nanoparticle conjugates. *Photochem. Photobiol. Sci.* **10**: 822–831.

115. Kirpotin, DB, Drummond, DC, Shao, Y, Shalaby, MR, Hong, K, Nielsen, UB, *et al.* (2006). Antibody Targeting of Long-Circulating Lipidic Nanoparticles Does Not Increase Tumor Localization but Does Increase Internalization in Animal Models. *Cancer Res.* **66**:

6732 LP – 6740.

116. Mamot, C, Drummond, DC, Noble, CO, Kallab, V, Guo, Z, Hong, K, *et al.* (2005). Epidermal Growth Factor Receptor–Targeted Immunoliposomes Significantly Enhance the Efficacy of Multiple Anticancer Drugs In vivo *Cancer Res.* **65**: 11631 LP – 11638.

117. Hansel, TT, Kropshofer, H, Singer, T, Mitchell, JA and George, AJT (2010). The safety and side effects of monoclonal antibodies. *Nat. Rev. Drug Discov.* **9**: 325.

118. Kijanka, M, Dorresteijn, B, Oliveira, S and van Bergen en Henegouwen, PMP (2015). Nanobody-based cancer therapy of solid tumors. *Nanomedicine* **10**: 161–174.

119. Muyldermans, S (2013). Nanobodies: natural single-domain antibodies. *Annu. Rev. Biochem.* **82**: 775–797.

120. Lipovšek, D (2011). Adnectins: engineered target-binding protein therapeutics. *Protein Eng. Des. Sel.* **24**: 3–9.

121. Holliger, P and Hudson, PJ (2005). Engineered antibody fragments and the rise of single domains. *Nat. Biotechnol.* **23**: 1126.

122. Winter, G, Griffiths, AD, Hawkins, RE and Hoogenboom, HR (1994). Making antibodies by phage display technology. *Annu. Rev. Immunol.* **12**: 433–455.

123. Kretzschmar, T and Von Rüden, T (2002). Antibody discovery: phage display. *Curr. Opin. Biotechnol.* **13**: 598–602.

124. Chen, Y, Zhu, X, Zhang, X, Liu, B and Huang, L (2010). Nanoparticles modified with tumor-targeting scFv deliver siRNA and miRNA for cancer therapy. *Mol. Ther.* **18**: 1650–1656.

125. Yang, L, Mao, H, Wang, YA, Cao, Z, Peng, X, Wang, X, *et al.* (2009). Single Chain

Epidermal Growth Factor Receptor Antibody Conjugated Nanoparticles for in vivo Tumor Targeting and Imaging. *Small* **5**: 235–243.

126. Saha, RN, Vasanthakumar, S, Bende, G and Snehalatha, M (2010). Nanoparticulate drug delivery systems for cancer chemotherapy. *Mol. Membr. Biol.* **27**: 215–231.

127. Hornick, JR, Xu, J, Vangveravong, S, Tu, Z, Mitchem, JB, Spitzer, D, *et al.* (2010). The novel sigma-2 receptor ligand SW43 stabilizes pancreas cancer progression in combination with gemcitabine. *Mol. Cancer* **9**: 1–11.

128. Bartlett, DW, Su, H, Hildebrandt, IJ, Weber, WA and Davis, ME (2007). Impact of tumor-specific targeting on the biodistribution and efficacy of siRNA nanoparticles measured by multimodality in vivo imaging. *Proc. Natl. Acad. Sci.* **104**: 15549 LP – 15554.

129. Ganesh, S, Iyer, AK, Morrissey, D V and Amiji, MM (2013). Hyaluronic acid based self-assembling nanosystems for CD44 target mediated siRNA delivery to solid tumors. *Biomaterials* **34**: 3489–3502.

130. Low, PS and Kularatne, SA (2009). Folate-targeted therapeutic and imaging agents for cancer. *Curr. Opin. Chem. Biol.* **13**: 256–262.

131. Zwicke, GL, Ali Mansoori, G and Jeffery, CJ (2012). Utilizing the folate receptor for active targeting of cancer nanotherapeutics. *Nano Rev.* **3**: 18496.

132. Maresca, KP, Hillier, SM, Femia, FJ, Keith, D, Barone, C, Joyal, JL, *et al.* (2009). A Series of Halogenated Heterodimeric Inhibitors of Prostate Specific Membrane Antigen (PSMA) as Radiolabeled Probes for Targeting Prostate Cancer. *J. Med. Chem.* **52**: 347–357.

133. Hillier, SM, Maresca, KP, Femia, FJ, Marquis, JC, Foss, CA, Nguyen, N, *et al.* (2009).

Preclinical Evaluation of Novel Glutamate-Urea-Lysine Analogues That Target Prostate-Specific Membrane Antigen as Molecular Imaging Pharmaceuticals for Prostate Cancer. *Cancer Res.* **69**: 6932 LP – 6940.

134. Xu, X, Wu, J, Liu, Y, Saw, PE, Tao, W, Yu, M, *et al.* (2017). Multifunctional Envelope-Type siRNA Delivery Nanoparticle Platform for Prostate Cancer Therapy. *ACS Nano* **11**: 2618–2627.

135. Adamczyk, B, Tharmalingam, T and Rudd, PM (2012). Glycans as cancer biomarkers. *Biochim. Biophys. Acta (BBA)-General Subj.* **1820**: 1347–1353.

136. Dube, DH and Bertozzi, CR (2005). Glycans in cancer and inflammation — potential for therapeutics and diagnostics. *Nat. Rev. Drug Discov.* **4**: 477.

137. Bies, C, Lehr, C-M and Woodley, JF (2004). Lectin-mediated drug targeting: history and applications. *Adv. Drug Deliv. Rev.* **56**: 425–435.

138. Zhu, D, Tao, W, Zhang, H, Liu, G, Wang, T, Zhang, L, *et al.* (2016). Docetaxel (DTX)-loaded polydopamine-modified TPGS-PLA nanoparticles as a targeted drug delivery system for the treatment of liver cancer. *Acta Biomater.* **30**: 144–154.

139. Liang, H-F, Chen, S-C, Chen, M-C, Lee, P-W, Chen, C-T and Sung, H-W (2006). Paclitaxel-loaded poly (γ-glutamic acid)-poly (lactide) nanoparticles as a targeted drug delivery system against cultured HepG2 cells. *Bioconjug. Chem.* **17**: 291–299.

140. Seymour, LW, Ferry, DR, Anderson, D, Hesslewood, S, Julyan, PJ, Poyner, R, *et al.* (2002). Hepatic drug targeting: phase I evaluation of polymer-bound doxorubicin. *J. Clin. Oncol.* **20**: 1668–1676.

141. Gao, X, Tao, W, Lu, W, Zhang, Q, Zhang, Y, Jiang, X, *et al.* (2006). Lectin-conjugated PEG–PLA nanoparticles: Preparation and brain delivery after intranasal administration.

Biomaterials **27**: 3482–3490.

142. Fang, RH, Hu, C-MJ, Luk, BT, Gao, W, Copp, JA, Tai, Y, *et al.* (2014). Cancer cell membrane-coated nanoparticles for anticancer vaccination and drug delivery. *Nano Lett.* **14**: 2181–2188.

143. Sun, H, Su, J, Meng, Q, Yin, Q, Chen, L, Gu, W, *et al.* (2016). Cancer-cell-biomimetic nanoparticles for targeted therapy of homotypic tumors. *Adv. Mater.* **28**: 9581–9588.

144. Levy-Nissenbaum, E, Radovic-Moreno, AF, Wang, AZ, Langer, R and Farokhzad, OC (2008). Nanotechnology and aptamers: applications in drug delivery. *Trends Biotechnol.* **26**: 442–449.

145. Tuerk, C and Gold, L (1990). Systematic evolution of ligands by exponential enrichment: RNA ligands to bacteriophage T4 DNA polymerase. *Science (80-.).* **249**: 505–510.

146. Daniels, DA, Chen, H, Hicke, BJ, Swiderek, KM and Gold, L (2003). A tenascin-C aptamer identified by tumor cell SELEX: systematic evolution of ligands by exponential enrichment. *Proc. Natl. Acad. Sci.* **100**: 15416–15421.

147. Xiao, Z, Shangguan, D, Cao, Z, Fang, X and Tan, W (2008). Cell-specific internalization study of an aptamer from whole cell selection. *Chem. Eur. J.* **14**: 1769–1775.

148. Xiao, Z, Levy-Nissenbaum, E, Alexis, F, Lupták, A, Teply, BA, Chan, JM, *et al.* (2012). Engineering of targeted nanoparticles for cancer therapy using internalizing aptamers isolated by cell-uptake selection. *ACS Nano* **6**: 696–704.

149. Mi, J, Liu, Y, Rabbani, ZN, Yang, Z, Urban, JH, Sullenger, BA, *et al.* (2010). In vivo selection of tumor-targeting RNA motifs. *Nat. Chem. Biol.* **6**: 22–24.

150. Liu, H, Mai, J, Shen, J, Wolfram, J, Li, Z, Zhang, G, *et al.* (2018). A Novel DNA Aptamer for Dual Targeting of Polymorphonuclear Myeloid-derived Suppressor Cells and Tumor

Cells. *Theranostics* **8**: 31–44.

151. Kaur, J and Tikoo, K (2015). Ets1 identified as a novel molecular target of RNA aptamer selected against metastatic cells for targeted delivery of nano-formulation. *Oncogene* **34**: 5216.

152. Guo, W and Giancotti, FG (2004). Integrin signalling during tumour progression. *Nat. Rev. Mol. Cell Biol.* **5**: 816.

153. Mbeunkui, F and Johann, DJ (2009). Cancer and the tumor microenvironment: a review of an essential relationship. *Cancer Chemother. Pharmacol.* **63**: 571–582.

154. Danhier, F, Le Breton, A and Préat, V (2012). RGD-Based Strategies To Target Alpha(v) Beta(3) Integrin in Cancer Therapy and Diagnosis. *Mol. Pharm.* **9**: 2961–2973.

155. Schiffelers, RM, Ansari, A, Xu, J, Zhou, Q, Tang, Q, Storm, G, *et al.* (2004). Cancer siRNA therapy by tumor selective delivery with ligand-targeted sterically stabilized nanoparticle. *Nucleic Acids Res.* **32**: e149–e149.

156. Jiang, J, Yang, S, Wang, J, Yang, L, Xu, Z, Yang, T, *et al.* (2010). Sequential treatment of drug-resistant tumors with RGD-modified liposomes containing siRNA or doxorubicin. *Eur. J. Pharm. Biopharm.* **76**: 170–178.

157. Kim, J, Mirando, AC, Popel, AS and Green, JJ (2017). Gene delivery nanoparticles to modulate angiogenesis. *Adv. Drug Deliv. Rev.* **119**: 20–43.

158. Li, W, Zhao, X, Du, B, Li, X, Liu, S, Yang, X-Y, *et al.* (2016). Gold nanoparticle–mediated targeted delivery of recombinant human endostatin normalizes tumour vasculature and improves cancer therapy. *Sci. Rep.* **6**: 1–11.

159. Zheng, Y, Chen, H, Zeng, X, Liu, Z, Xiao, X, Zhu, Y, *et al.* (2013). Surface modification of TPGS-b-(PCL-ran-PGA) nanoparticles with polyethyleneimine as a co-delivery system

of TRAIL and endostatin for cervical cancer gene therapy. *Nanoscale Res. Lett.* **8**: 1–12.

160. Juweid, M, Neumann, R, Paik, C, Perez-Bacete, MJ, Sato, J, van Osdol, W, *et al.* (1992). Micropharmacology of monoclonal antibodies in solid tumors: direct experimental evidence for a binding site barrier. *Cancer Res.* **52**: 5144–5153.

161. Allen, TM (2002). Ligand-targeted therapeutics in anticancer therapy. *Nat. Rev. Cancer* **2**: 750.

162. Cheng, Z, Al Zaki, A, Hui, JZ, Muzykantov, VR and Tsourkas, A (2012). Multifunctional nanoparticles: cost versus benefit of adding targeting and imaging capabilities. *Science (80-.).* **338**: 903–910.

163. Gaertner, FC, Kessler, H, Wester, H-J, Schwaiger, M and Beer, AJ (2012). Radiolabelled RGD peptides for imaging and therapy. *Eur. J. Nucl. Med. Mol. Imaging* **39**: 126–138.

164. Whiteside, TL (2008). The tumor microenvironment and its role in promoting tumor growth. *Oncogene* **27**: 5904–5912.

165. Yuan, Y-Y, Mao, C-Q, Du, X-J, Du, J-Z, Wang, F and Wang, J (2012). Surface Charge Switchable Nanoparticles Based on Zwitterionic Polymer for Enhanced Drug Delivery to Tumor. *Adv. Mater.* **24**: 5476–5480.

166. Coussens, LM, Fingleton, B and Matrisian, LM (2002). Matrix metalloproteinase inhibitors and cancer—trials and tribulations. *Science (80-.).* **295**: 2387–2392.

167. Hatakeyama, H, Akita, H, Kogure, K, Oishi, M, Nagasaki, Y, Kihira, Y, *et al.* (2007). Development of a novel systemic gene delivery system for cancer therapy with a tumor-specific cleavable PEG-lipid. *Gene Ther.* **14**: 68–77.

168. Hatakeyama, H, Akita, H and Harashima, H (2011). A multifunctional envelope type nano device (MEND) for gene delivery to tumours based on the EPR effect: A strategy for

overcoming the PEG dilemma. *Adv. Drug Deliv. Rev.* **63**: 152–160.

169. He, S, Fan, W, Wu, N, Zhu, J, Miao, Y, Miao, X, *et al.* (2018). Lipid-based liquid crystalline nanoparticles facilitate cytosolic delivery of siRNA via structural transformation. *Nano Lett.* **18**: 2411–2419.

170. Luo, X, Li, Z, Wang, G, He, X, Shen, X, Sun, Q, *et al.* (2017). MicroRNA-catalyzed cancer therapeutics based on DNA-programmed nanoparticle complex. *ACS Appl. Mater. Interfaces* **9**: 33624–33631.

171. Bujold, KE, Hsu, JCC and Sleiman, HF (2016). Optimized DNA "nanosuitcases" for encapsulation and conditional release of siRNA. *J. Am. Chem. Soc.* **138**: 14030–14038.

172. Du, F-S, Wang, Y, Zhang, R and Li, Z-C (2010). Intelligent nucleic acid delivery systems based on stimuli-responsive polymers. *Soft Matter* **6**: 835–848.

173. Zintchenko, A, Ogris, M and Wagner, E (2006). Temperature Dependent Gene Expression Induced by PNIPAM-Based Copolymers: Potential of Hyperthermia in Gene Transfer. *Bioconjug. Chem.* **17**: 766–772.

174. Oliveira, S, Hogset, A and Storm, G (2008). Delivery of siRNA to the target cell cytoplasm: photochemical internalization facilitates endosomal escape and improves silencing efficiency, in vitro and in vivo. *Curr. Pharm. Des.* **14**: 3686–3697.

175. Oliveira, S, Fretz, MM, Høgset, A, Storm, G and Schiffelers, RM (2007). Photochemical internalization enhances silencing of epidermal growth factor receptor through improved endosomal escape of siRNA. *Biochim. Biophys. Acta - Biomembr.* **1768**: 1211–1217.

176. Mykhaylyk, O, Zelphati, O, Rosenecker, J and Plank, C (2008). siRNA delivery by magnetofection. *Curr. Opin. Mol. Ther.* **10**: 493–505.

177. Schillinger, U, Brill, T, Rudolph, C, Huth, S, Gersting, S, Krötz, F, *et al.* (2005).

Advances in magnetofection—magnetically guided nucleic acid delivery. *J. Magn. Magn. Mater.* **293**: 501–508.

178. Scherer, F, Anton, M, Schillinger, U, Henke, J, Bergemann, C, Krüger, A, *et al.* (2002). Magnetofection: enhancing and targeting gene delivery by magnetic force in vitro and in vivo. *Gene Ther.* **9**: 102–109.

179. Hernot, S and Klibanov, AL (2008). Microbubbles in ultrasound-triggered drug and gene delivery. *Adv. Drug Deliv. Rev.* **60**: 1153–1166.

180. Sirsi, SR, Hernandez, SL, Zielinski, L, Blomback, H, Koubaa, A, Synder, M, *et al.* (2012). Polyplex-microbubble hybrids for ultrasound-guided plasmid DNA delivery to solid tumors. *J. Control. Release* **157**: 224–234.

181. Yang, D, Gao, Y-H, Tan, K-B, Zuo, Z-X, Yang, W-X, Hua, X, *et al.* (2013). Inhibition of hepatic fibrosis with artificial microRNA using ultrasound and cationic liposome-bearing microbubbles. *Gene Ther.* **20**: 1140.

182. McDannold, N, Vykhodtseva, N and Hynynen, K (2006). Targeted disruption of the blood–brain barrier with focused ultrasound: association with cavitation activity. *Phys. Med. Biol.* **51**: 793.

183. Mura, S, Nicolas, J and Couvreur, P (2013). Stimuli-responsive nanocarriers for drug delivery. *Nat. Mater.* **12**: 991.

184. Fan, C-H, Ting, C-Y, Lin, H-J, Wang, C-H, Liu, H-L, Yen, T-C, *et al.* (2013). SPIO-conjugated, doxorubicin-loaded microbubbles for concurrent MRI and focused-ultrasound enhanced brain-tumor drug delivery. *Biomaterials* **34**: 3706–3715.

185. Kinoshita, M, McDannold, N, Jolesz, FA and Hynynen, K (2006). Noninvasive localized delivery of Herceptin to the mouse brain by MRI-guided focused ultrasound-induced

blood–brain barrier disruption. *Proc. Natl. Acad. Sci.* **103**: 11719–11723.

186. Wolinsky, JB, Colson, YL and Grinstaff, MW (2012). Local drug delivery strategies for cancer treatment: Gels, nanoparticles, polymeric films, rods, and wafers. *J. Control. Release* **159**: 14–26.

187. Megeed, Z, Haider, M, Li, D, O'Malley, BW, Cappello, J and Ghandehari, H (2004). In vitro and in vivo evaluation of recombinant silk-elastinlike hydrogels for cancer gene therapy. *J. Control. Release* **94**: 433–445.

188. Jang, J-H, Rives, CB and Shea, LD (2005). Plasmid Delivery in Vivo from Porous Tissue-Engineering Scaffolds: Transgene Expression and Cellular Transfection. *Mol. Ther.* **12**: 475–483.

189. Lei, Y, Huang, S, Sharif-Kashani, P, Chen, Y, Kavehpour, P and Segura, T (2010). Incorporation of active DNA/cationic polymer polyplexes into hydrogel scaffolds. *Biomaterials* **31**: 9106–9116.

190. Lei, Y, Rahim, M, Ng, Q and Segura, T (2011). Hyaluronic acid and fibrin hydrogels with concentrated DNA/PEI polyplexes for local gene delivery. *J. Control. Release* **153**: 255–261.

191. Nelson, CE, Gupta, MK, Adolph, EJ, Shannon, JM, Guelcher, SA and Duvall, CL (2012). Sustained local delivery of siRNA from an injectable scaffold. *Biomaterials* **33**: 1154–1161.

192. Conde, J, Oliva, N, Zhang, Y and Artzi, N (2016). Local triple-combination therapy results in tumour regression and prevents recurrence in a colon cancer model. *Nat. Mater.* **15**: 1128–1138.

193. Sung, JC, Pulliam, BL and Edwards, DA (2007). Nanoparticles for drug delivery to the

lungs. *Trends Biotechnol.* **25**: 563–570.

194. Koshkina, N V, Knight, V, Gilbert, BE, Golunski, E, Roberts, L and Waldrep, JC (2001). Improved respiratory delivery of the anticancer drugs, camptothecin and paclitaxel, with 5% CO 2-enriched air: pharmacokinetic studies. *Cancer Chemother. Pharmacol.* **47**: 451–456.

195. Patel, AK, Kaczmarek, JC, Bose, S, Kauffman, KJ, Mir, F, Heartlein, MW, *et al.* (2019). Inhaled Nanoformulated mRNA Polyplexes for Protein Production in Lung Epithelium. *Adv. Mater.* **0**: 1805116.

196. Alton, EWFW, Armstrong, DK, Ashby, D, Bayfield, KJ, Bilton, D, Bloomfield, E V, *et al.* (2015). Repeated nebulisation of non-viral CFTR gene therapy in patients with cystic fibrosis: a randomised, double-blind, placebo-controlled, phase 2b trial. *Lancet Respir. Med.* **3**: 684–691.

197. Zhang, Z, Tsai, P-C, Ramezanli, T and Michniak-Kohn, BB (2013). Polymeric nanoparticles-based topical delivery systems for the treatment of dermatological diseases. *Wiley Interdiscip. Rev. Nanomedicine Nanobiotechnology* **5**: 205–218.

198. Guterres, SS, Alves, MP and Pohlmann, AR (2007). Polymeric Nanoparticles, Nanospheres and Nanocapsules, for Cutaneous Applications. *Drug Target Insights* **2**: 117739280700200000.

199. Özbaş-Turan, S and Akbuğa, J (2011). Plasmid DNA-loaded chitosan/TPP nanoparticles for topical gene delivery. *Drug Deliv.* **18**: 215–222.

200. Özbaş-Turan, S, Akbuğa, J and Sezer, AD (2010). Topical Application of Antisense Oligonucleotide-Loaded Chitosan Nanoparticles to Rats. *Oligonucleotides* **20**: 147–153.

201. Yang, S-J, Lin, F-H, Tsai, K-C, Wei, M-F, Tsai, H-M, Wong, J-M, *et al.* (2010). Folic

Acid-Conjugated Chitosan Nanoparticles Enhanced Protoporphyrin IX Accumulation in Colorectal Cancer Cells. *Bioconjug. Chem.* **21**: 679–689.

202. Jain, A, Jain, SK, Ganesh, N, Barve, J and Beg, AM (2010). Design and development of ligand-appended polysaccharidic nanoparticles for the delivery of oxaliplatin in colorectal cancer. *Nanomedicine Nanotechnology, Biol. Med.* **6**: 179–190.

203. Bowman, K and Leong, KW (2006). Chitosan nanoparticles for oral drug and gene delivery. *Int. J. Nanomedicine* **1**: 117–128.

204. Tsai, C-M, Chang, K-T, Wu, L-H, Chen, J-Y, Gazdar, AF, Mitsudomi, T, *et al.* (1996). Correlations between intrinsic chemoresistance and HER-2/neu gene expression, p53 gene mutations, and cell proliferation characteristics in non-small cell lung cancer cell lines. *Cancer Res.* **56**: 206–209.

205. Buttitta, F, Marchetti, A, Gadducci, A, Pellegrini, S, Morganti, M, Carnicelli, V, *et al.* (1997). p53 alterations are predictive of chemoresistance and aggressiveness in ovarian carcinomas: a molecular and immunohistochemical study. *Br. J. Cancer* **75**: 230.

206. Wang, K, Huang, Q, Qiu, F and Sui, M (2015). Non-viral delivery systems for the application in p53 cancer gene therapy. *Curr. Med. Chem.* **22**: 4118–4136.

207. Islam, MA, Xu, Y, Tao, W, Ubellacker, JM, Lim, M, Aum, D, *et al.* (2018). Restoration of tumour-growth suppression in vivo via systemic nanoparticle-mediated delivery of PTEN mRNA. *Nat. Biomed. Eng.* **2**: 850–864.

208. Zhang, SW, Xiao, SW, Liu, CQ, Sun, Y, Su, X, Li, DM, *et al.* (2003). Treatment of head and neck squamous cell carcinoma by recombinant adenovirus-p53 combined with radiotherapy: a phase II clinical trial of 42 cases. *Zhonghua Yi Xue Za Zhi* **83**: 2023–2028.

209. Lang, FF, Bruner, JM, Fuller, GN, Aldape, K, Prados, MD, Chang, S, *et al.* (2003). Phase

I trial of adenovirus-mediated p53 gene therapy for recurrent glioma: biological and clinical results. *J. Clin. Oncol.* **21**: 2508–2518.

210. Vousden, KH (2002). Switching from life to death: The Miz-ing link between Myc and p53. *Cancer Cell* **2**: 351–352.

211. Seoane, J, Le, H-V and Massagué, J (2002). Myc suppression of the p21 Cip1 Cdk inhibitor influences the outcome of the p53 response to DNA damage. *Nature* **419**: 729.

212. Yang, L, Zheng, H, Ratnakar, JS, Adebesin, BY, Do, QN, Kovacs, Z, *et al.* (2018). Engineering a pH-sensitive liposomal MRI agent by modification of a bacterial channel. *Small* **14**: 1704256.

213. Zeimet, AG and Marth, C (2003). Why did p53 gene therapy fail in ovarian cancer? *Lancet Oncol.* **4**: 415–422.

214. Gottesman, MM (2003). Cancer gene therapy: an awkward adolescence. *Cancer Gene Ther.* **10**: 501.

215. Resnier, P, Montier, T, Mathieu, V, Benoit, J-P and Passirani, C (2013). A review of the current status of siRNA nanomedicines in the treatment of cancer. *Biomaterials* **34**: 6429–6443.

216. Brummelkamp, TR, Bernards, R and Agami, R (2002). Stable suppression of tumorigenicity by virus-mediated RNA interference. *Cancer Cell* **2**: 243–247.

217. Wu, Y and Zhou, BP (2010). TNF-α/NF-κB/Snail pathway in cancer cell migration and invasion. *Br. J. Cancer* **102**: 639.

218. O'Brien, DI, Nally, K, Kelly, RG, O'Connor, TM, Shanahan, F and O'Connell, J (2005). Targeting the Fas/Fas ligand pathway in cancer. *Expert Opin. Ther. Targets* **9**: 1031–1044.

219. Adams, JM and Cory, S (2007). The Bcl-2 apoptotic switch in cancer development and

therapy. *Oncogene* **26**: 1324.

220. Stuckey, DW and Shah, K (2013). TRAIL on trial: preclinical advances in cancer therapy. *Trends Mol. Med.* **19**: 685–694.

221. Liu, S, Guo, Y, Huang, R, Li, J, Huang, S, Kuang, Y, *et al.* (2012). Gene and doxorubicin co-delivery system for targeting therapy of glioma. *Biomaterials* **33**: 4907–4916.

222. Jiang, X, Fitch, S, Wang, C, Wilson, C, Li, J, Grant, GA, *et al.* (2016). Nanoparticle engineered TRAIL-overexpressing adipose-derived stem cells target and eradicate glioblastoma via intracranial delivery. *Proc. Natl. Acad. Sci.* **113**: 13857–13862.

223. Choi, SA, Hwang, S-K, Wang, K-C, Cho, B-K, Phi, JH, Lee, JY, *et al.* (2011). Therapeutic efficacy and safety of TRAIL-producing human adipose tissue–derived mesenchymal stem cells against experimental brainstem glioma. *Neuro. Oncol.* **13**: 61–69.

224. Kim, CY, Jeong, M, Mushiake, H, Kim, BM, Kim, WB, Ko, JP, *et al.* (2006). Cancer gene therapy using a novel secretable trimeric TRAIL. *Gene Ther.* **13**: 330–338.

225. Robson, T and Hirst, DG (2003). Transcriptional targeting in cancer gene therapy. *Biomed Res. Int.* **2003**: 110–137.

226. De Cian, A, Lacroix, L, Douarre, C, Temime-Smaali, N, Trentesaux, C, Riou, J-F, *et al.* (2008). Targeting telomeres and telomerase. *Biochimie* **90**: 131–155.

227. Hallenbeck, PL, Chang, Y-N, Hay, C, Golightly, D, Stewart, D, Lin, J, *et al.* (1999). A novel tumor-specific replication-restricted adenoviral vector for gene therapy of hepatocellular carcinoma. *Hum. Gene Ther.* **10**: 1721–1733.

228. Li, LY, Dai, HY, Yeh, FL, Kan, SF, Lang, J, Hsu, JL, *et al.* (2011). Targeted hepatocellular carcinoma proapoptotic BikDD gene therapy. *Oncogene* **30**: 1773–1783.

229. Little, E, Ramakrishnan, M, Roy, B, Gazit, G and Lee, AS (1994). The glucose-regulated

proteins (GRP78 and GRP94): functions, gene regulation, and applications. *Crit. Rev. Eukaryot. Gene Expr.* **4**: 1–18.

230. Lee, AS (2001). The glucose-regulated proteins: stress induction and clinical applications. *Trends Biochem. Sci.* **26**: 504–510.

231. Katabi, MM, Chan, HLB, Karp, SE and Batist, G (1999). Hexokinase type II: a novel tumor-specific promoter for gene-targeted therapy differentially expressed and regulated in human cancer cells. *Hum. Gene Ther.* **10**: 155–164.

232. Kawashita, Y, Ohtsuru, A, Kaneda, Y, Nagayama, Y, Kawazoe, Y, Eguchi, S, *et al.* (1999). Regression of hepatocellular carcinoma in vitro and in vivo by radiosensitizing suicide gene therapy under the inducible and spatial control of radiation. *Hum. Gene Ther.* **10**: 1509–1519.

233. Braiden, V, Ohtsuru, A, Kawashita, Y, Miki, F, Sawada, T, Ito, M, *et al.* (2000). Eradication of breast cancer xenografts by hyperthermic suicide gene therapy under the control of the heat shock protein promoter. *Hum. Gene Ther.* **11**: 2453–2463.

234. Orth, P, Schnappinger, D, Hillen, W, Saenger, W and Hinrichs, W (2000). Structural basis of gene regulation by the tetracycline inducible Tet repressor–operator system. *Nat. Struct. Biol.* **7**: 215–219.

235. Esposito, CL, Nuzzo, S, Kumar, SA, Rienzo, A, Lawrence, CL, Pallini, R, *et al.* (2016). A combined microRNA-based targeted therapeutic approach to eradicate glioblastoma stem-like cells. *J. Control. Release* **238**: 43–57.

236. Lopez-Bertoni, H, Kozielski, KL, Rui, Y, Lal, B, Vaughan, H, Wilson, DR, *et al.* (2018). Bioreducible polymeric nanoparticles containing multiplexed cancer stem cell regulating miRNAs inhibit glioblastoma growth and prolong survival. *Nano Lett.* **18**: 4086–4094.

237. Chen, W, Liu, X, Xiao, Y and Tang, R (2015). Overcoming Multiple Drug Resistance by Spatial–Temporal Synchronization of Epirubicin and Pooled siRNAs. *Small* **11**: 1775–1781.

238. Cocco, E, Deng, Y, Shapiro, EM, Bortolomai, I, Lopez, S, Lin, K, *et al.* (2017). Dual-Targeting Nanoparticles for In Vivo Delivery of Suicide Genes to Chemotherapy-Resistant Ovarian Cancer Cells. *Mol. Cancer Ther.* **16**: 323 LP – 333.

239. Sun, L, Wang, D, Chen, Y, Wang, L, Huang, P, Li, Y, *et al.* (2017). Core-shell hierarchical mesostructured silica nanoparticles for gene/chemo-synergetic stepwise therapy of multidrug-resistant cancer. *Biomaterials* **133**: 219–228.

240. Davis, ME (2009). The First Targeted Delivery of siRNA in Humans via a Self-Assembling, Cyclodextrin Polymer-Based Nanoparticle: From Concept to Clinic. *Mol. Pharm.* **6**: 659–668.

241. Davis, ME, Zuckerman, JE, Choi, CHJ, Seligson, D, Tolcher, A, Alabi, CA, *et al.* (2010). Evidence of RNAi in humans from systemically administered siRNA via targeted nanoparticles. *Nature* **464**: 1067.

242. Zuckerman, JE, Gritli, I, Tolcher, A, Heidel, JD, Lim, D, Morgan, R, *et al.* (2014). Correlating animal and human phase Ia/Ib clinical data with CALAA-01, a targeted, polymer-based nanoparticle containing siRNA. *Proc. Natl. Acad. Sci.* **111**: 11449 LP – 11454.

243. Von Hoff, D, Mita, MM, Ramanathan, RK, Weiss, GJ, Mita, AC, LoRusso, PM, *et al.* (2016). Phase 1 study of PSMA-targeted docetaxel-containing nanoparticle BIND-014 in patients with advanced solid tumors. *Clin. Cancer Res.*: clincanres-2548.

244. Plummer, R, Wilson, RH, Calvert, H, Boddy, A V, Griffin, M, Sludden, J, *et al.* (2011). A

Phase I clinical study of cisplatin-incorporated polymeric micelles (NC-6004) in patients with solid tumours. *Br. J. Cancer* **104**: 593–598.

245. Gaur, S, Chen, L, Yen, T, Wang, Y, Zhou, B, Davis, M, *et al.* (2012). Preclinical study of the cyclodextrin-polymer conjugate of camptothecin CRLX101 for the treatment of gastric cancer. *Nanomedicine Nanotechnology, Biol. Med.* **8**: 721–730.

246. Weiss, GJ, Chao, J, Neidhart, JD, Ramanathan, RK, Bassett, D, Neidhart, JA, *et al.* (2013). First-in-human phase 1/2a trial of CRLX101, a cyclodextrin-containing polymer-camptothecin nanopharmaceutical in patients with advanced solid tumor malignancies. *Invest. New Drugs* **31**: 986–1000.

247. Pham, E, Birrer, MJ, Eliasof, S, Garmey, EG, Lazarus, D, Lee, CR, *et al.* (2015). Translational Impact of Nanoparticle–Drug Conjugate CRLX101 with or without Bevacizumab in Advanced Ovarian Cancer. *Clin. Cancer Res.* **21**: 808 LP – 818.

248. Zou, Y, Fang, Y, Meng, H, Meng, F, Deng, C, Zhang, J, *et al.* (2016). Self-crosslinkable and intracellularly decrosslinkable biodegradable micellar nanoparticles: A robust, simple and multifunctional nanoplatform for high-efficiency targeted cancer chemotherapy. *J. Control. Release* **244**: 326–335.

249. Hamaguchi, T, Matsumura, Y, Suzuki, M, Shimizu, K, Goda, R, Nakamura, I, *et al.* (2005). NK105, a paclitaxel-incorporating micellar nanoparticle formulation, can extend in vivo antitumour activity and reduce the neurotoxicity of paclitaxel. *Br. J. Cancer* **92**: 1240–1246.

250. Hamaguchi, T, Kato, K, Yasui, H, Morizane, C, Ikeda, M, Ueno, H, *et al.* (2007). A phase I and pharmacokinetic study of NK105, a paclitaxel-incorporating micellar nanoparticle formulation. *Br. J. Cancer* **97**: 170–176.

251. Kato, K, Chin, K, Yoshikawa, T, Yamaguchi, K, Tsuji, Y, Esaki, T, *et al.* (2012). Phase II study of NK105, a paclitaxel-incorporating micellar nanoparticle, for previously treated advanced or recurrent gastric cancer. *Invest. New Drugs* **30**: 1621–1627.

252. Doye, JPK, Ouldridge, TE, Louis, AA, Romano, F, Šulc, P, Matek, C, *et al.* (2013). Coarse-graining DNA for simulations of DNA nanotechnology. *Phys. Chem. Chem. Phys.* **15**: 20395–20414.

1.5 Figures and Tables

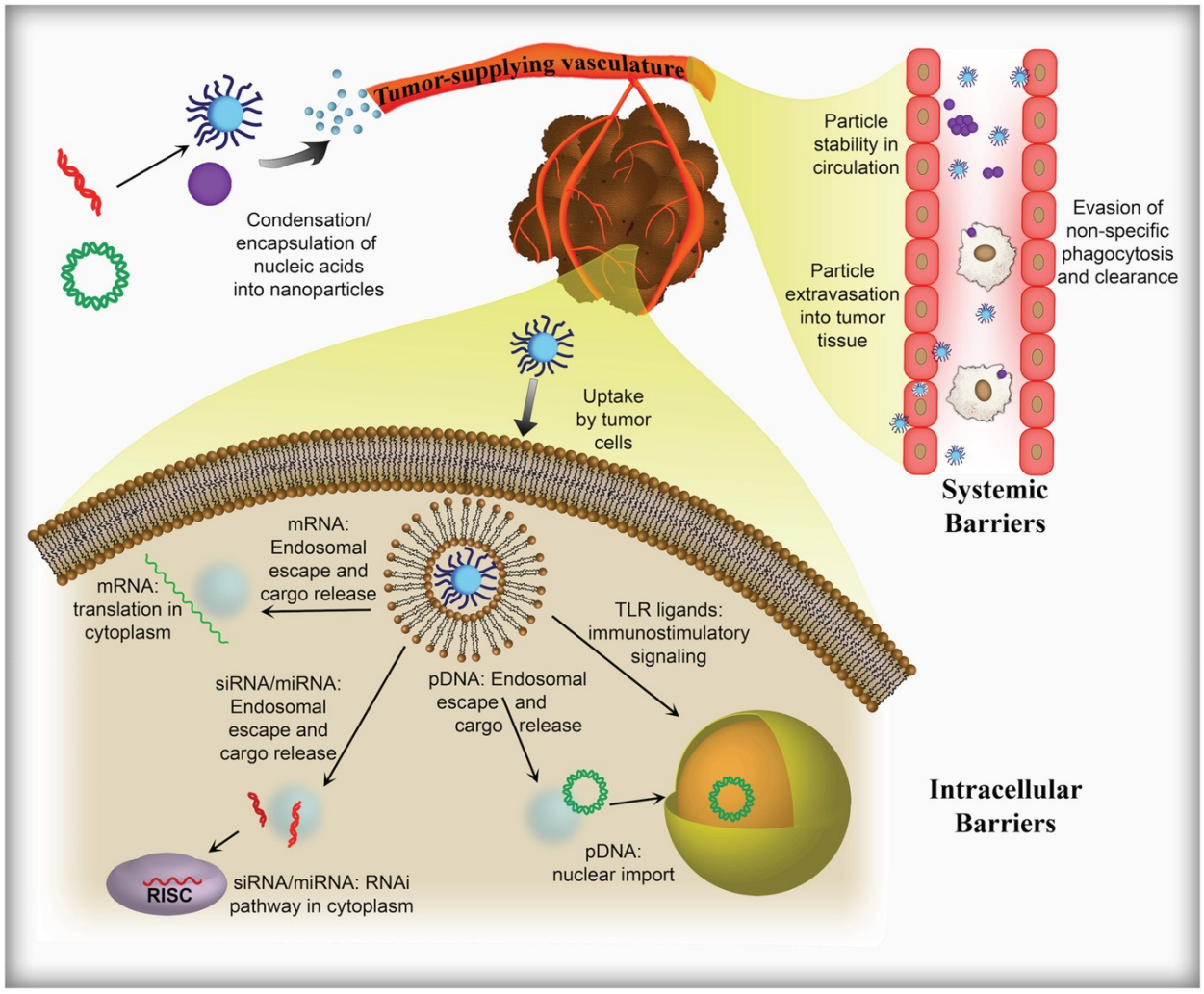

Figure 1.1 Challenges of nucleic acid delivery to tumors. Effective and specific delivery of nucleic acids to tumors requires encapsulation or condensation of the cargo into nanoparticles. Nanoparticles must then remain stable in circulation, evading clearance and avoiding aggregation with other particles, and then leave the circulation to accumulate at the tumor site. Once there, particles must enter cells, and various intracellular barriers must be overcome depending on the type of nucleic acid cargo being delivered.

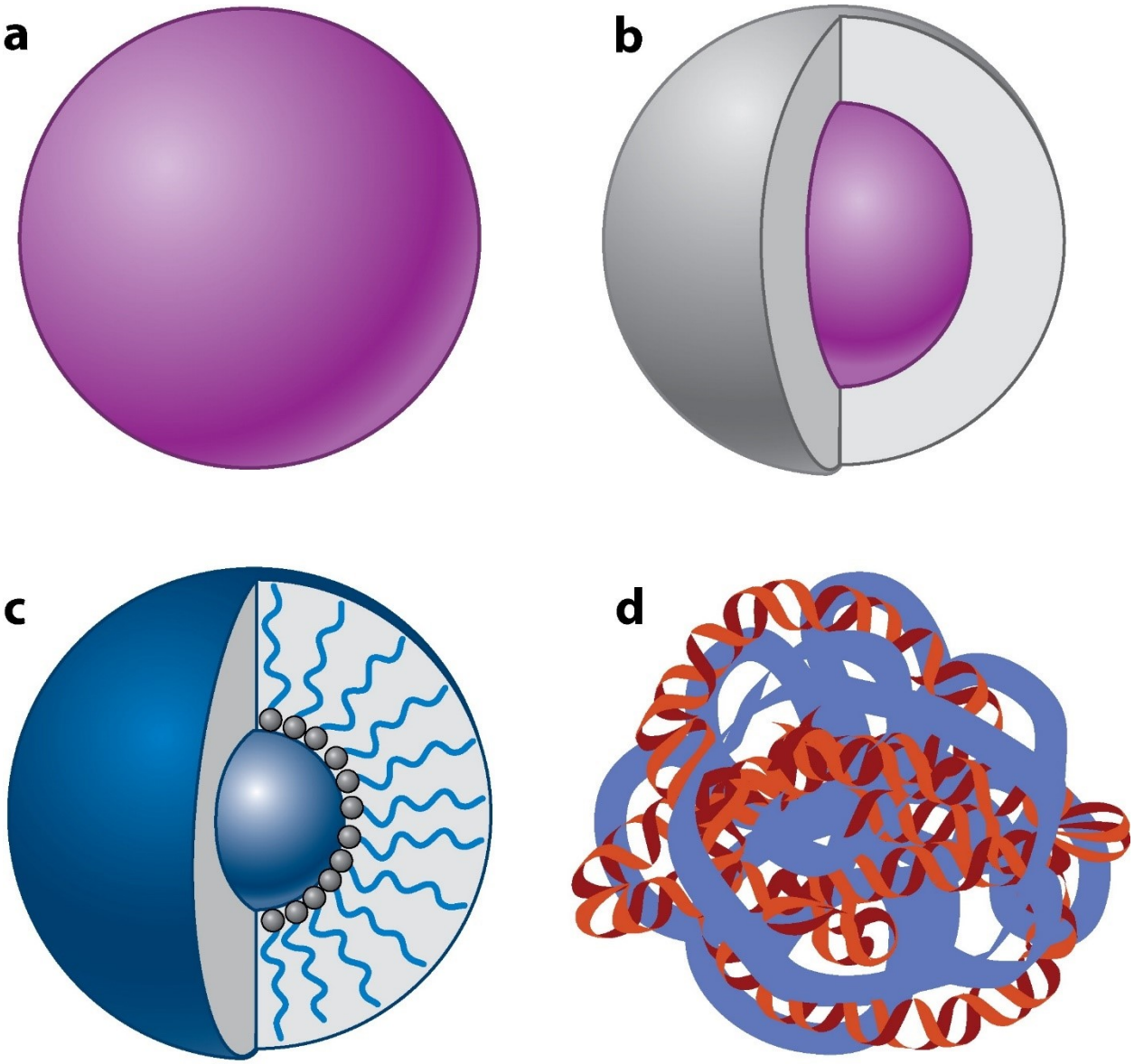

Figure 1.2 Schematic of various polymer nanoparticle formulation types. A. solid nanoparticles B. core-shell nanoparticles C. polymeric micelles D. polyplex nanoparticles

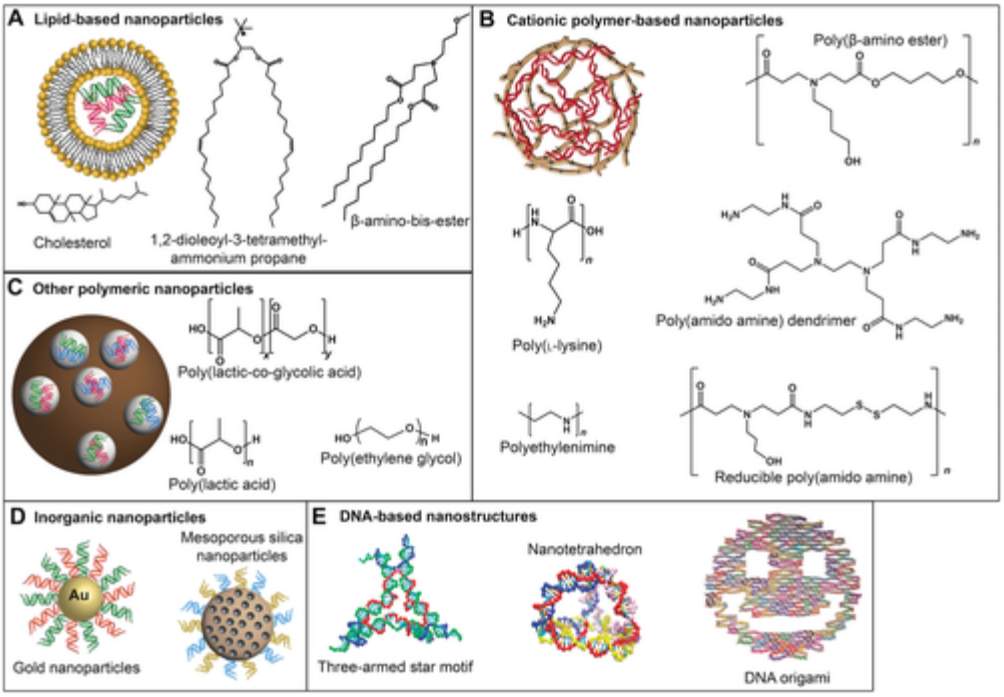

Figure 1.3 Types of nanomaterials used for nucleic acid delivery Broad classes of materials and nanostructures used as nucleic acid delivery vehicles are summarized, including A. lipid-based nanoparticles B. cationic polymer-based nanoparticles, C. nanoparticles based on other polymer types, D. inorganic nanoparticles, and E. nanostructures that use DNA itself as a structural component. Part E reproduced with permission[252]. Copyright 2013, Royal Society of Chemistry.

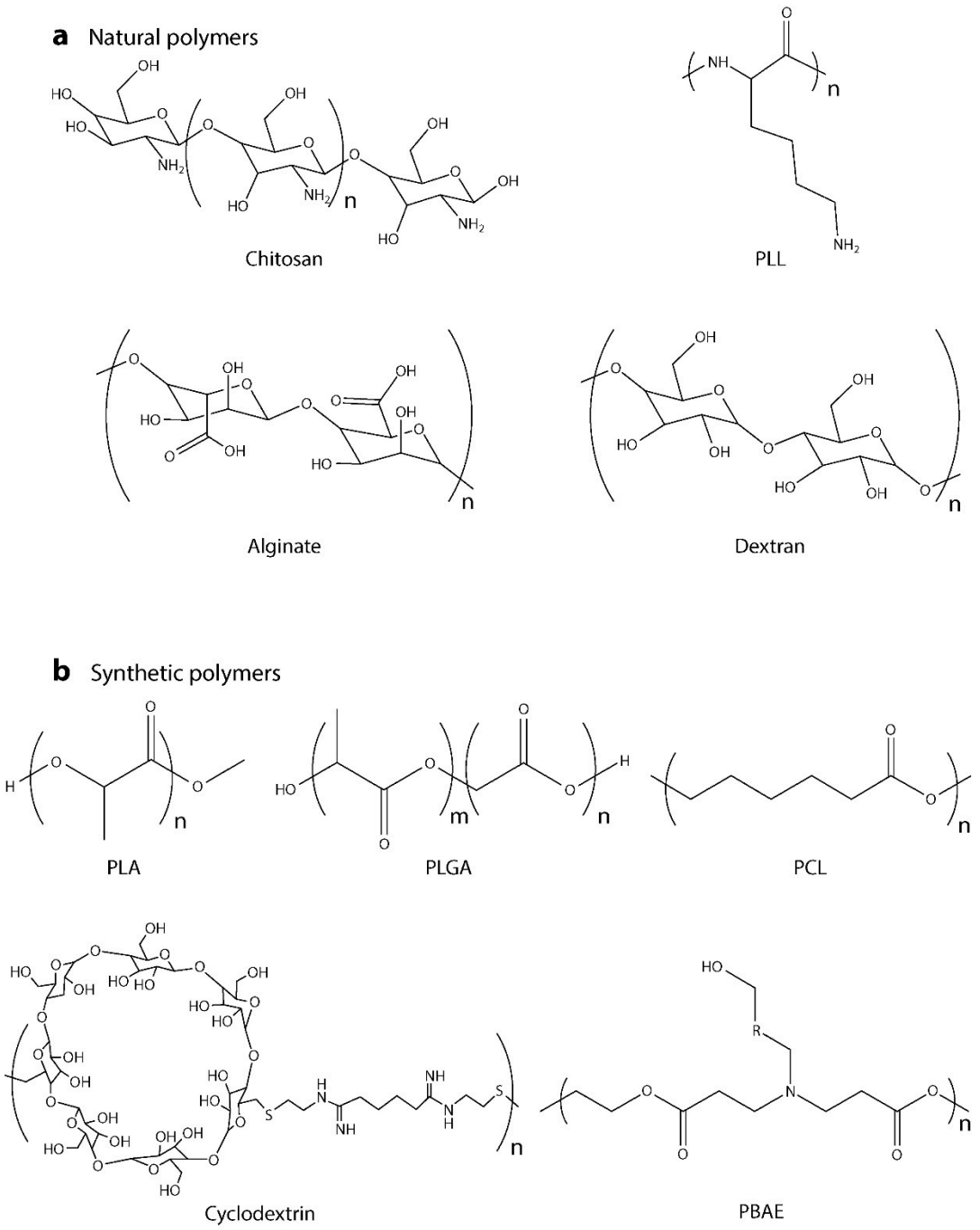

Figure 1.4 Chemical structures for natural and synthetic polymers used as drug delivery materials for anticancer drugs. Abbreviations: PBAE, poly(beta-amino ester); PCL, polycaprolactone; PLA, polylactide; PLGA, poly(lactide-*co*-glycolide); PLL, poly(l-lysine).

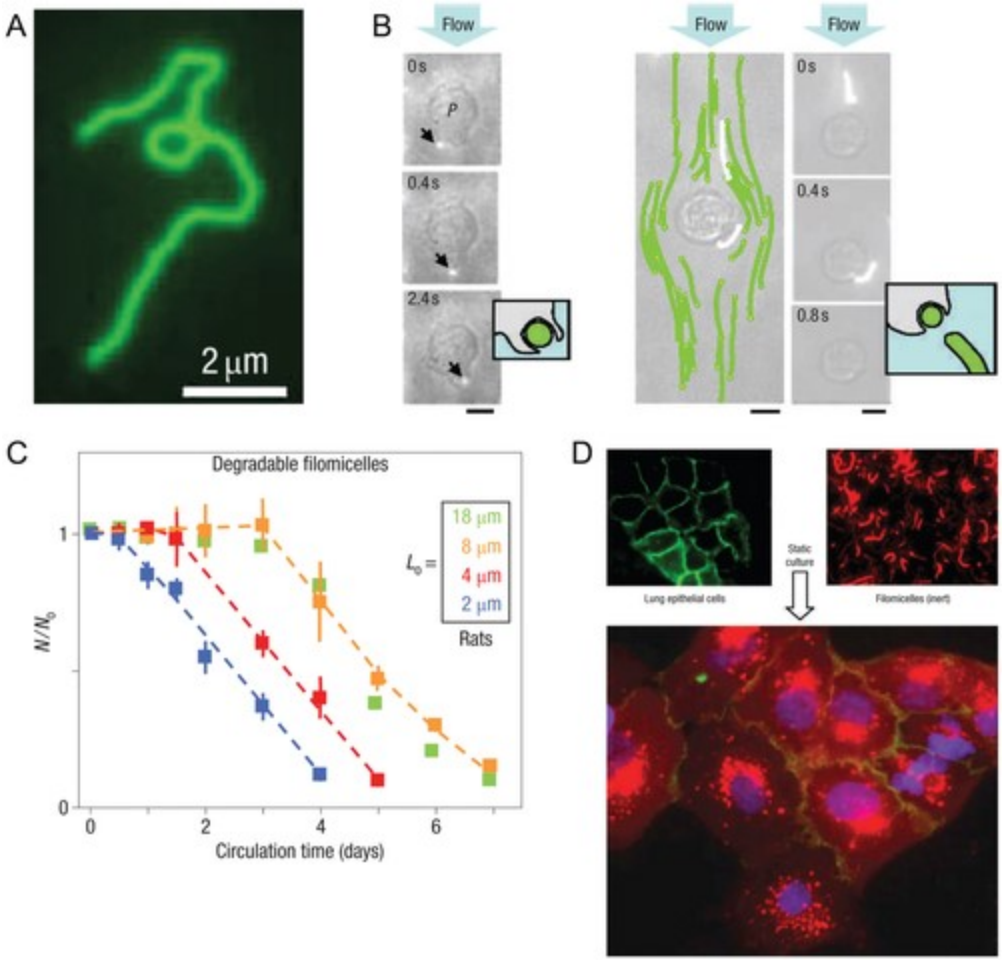

Figure 1.5 Shape effects of spherical vs filamentous micelles. Filomicelles are self-assembled from diblock co-polymers (a) with nano-scale diameter and micro-scale length. The filomicelles extend in flow (b) and evade phagocytosis while spherical micelles in flow are internalized. When the micelles are injected systemically in mice, they persist in circulation for days, and longer micelles have a longer circulation half-life than shorter micelles. Filomicelles are efficiently internalized (d) by lung epithelial cells in static culture. Reproduced from Geng et al., "Shape effects of filaments versus spherical particles in flow and drug delivery" *Nature Nanotechnology* 2 249-255, 2007, with permission from Springer Nature.

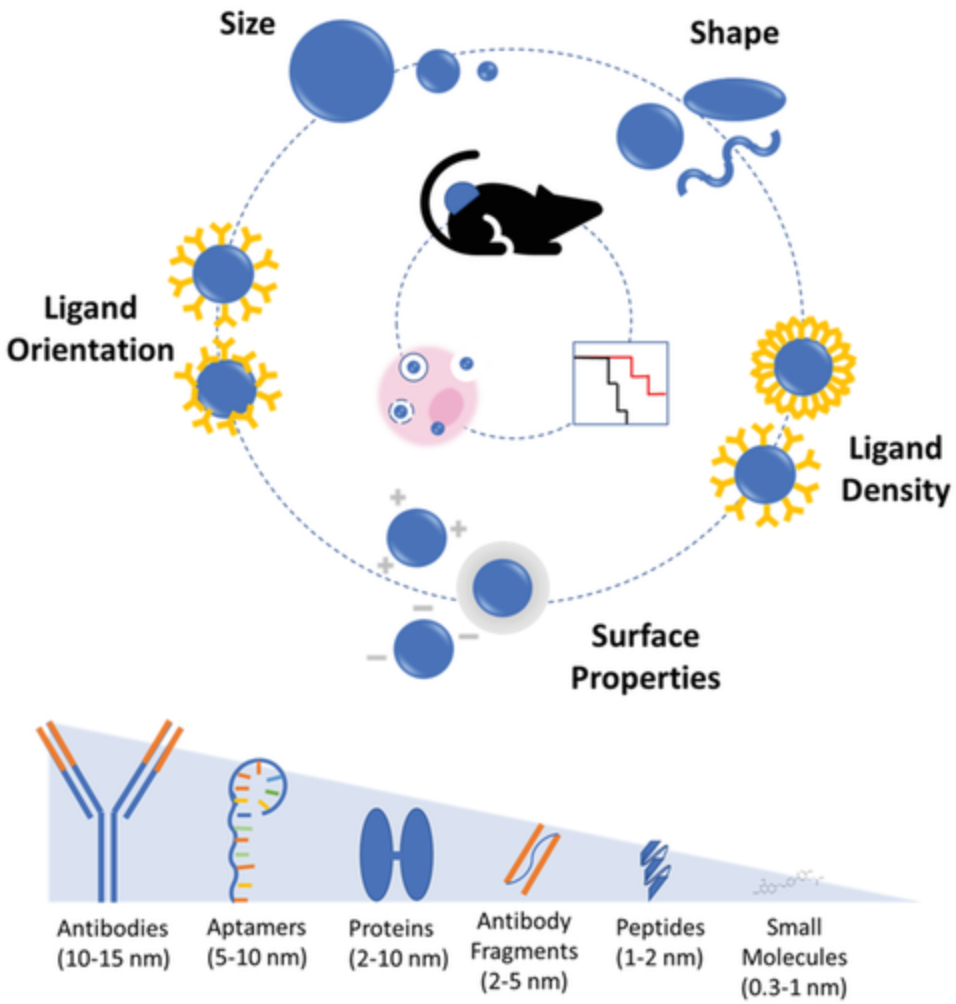

Figure 1.6 Optimization parameters for cancer-specific nanocarriers. Physical and chemical properties of delivery vehicles affect tumor accumulation, particle internalization and cargo delivery, and ultimately the therapeutic outcome. Classes of targeting moieties and their sizes are also summarized.

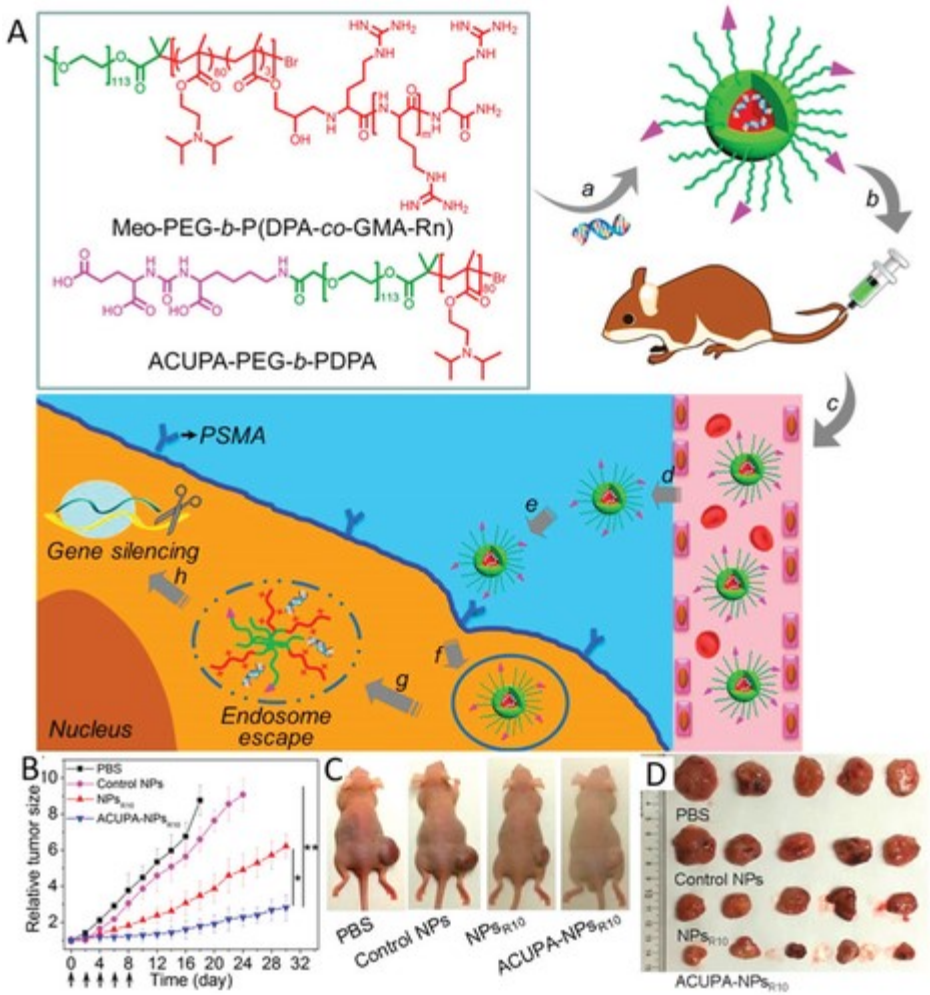

Figure 1.7 A prostate cancer ligand-targeted multifunctional envelope-like nanodevice (MEND) A. The nanocarrier is synthesized by siRNA self-assembly with two block copolymers: sharp oligoarginine functionalized pH responsive Meo-PEG-*b*-P(DPA-*co*-GMA-Rn) and PSMA targeted ACUPA-PEG-*b*-PDPA. Schematic shows targeted intracellular siRNA delivery after IV administration of MENDs. B. This strategy enables efficient gene silencing and significantly slows LNCaP tumor growth compared with control and nontargeted NPs. C. Representative images of tumor bearing mice on day 18 and D. photographs of harvested LNCaP tumors after 30 days. Reproduced with permission[134]. Copyright 2017, American Chemical Society.

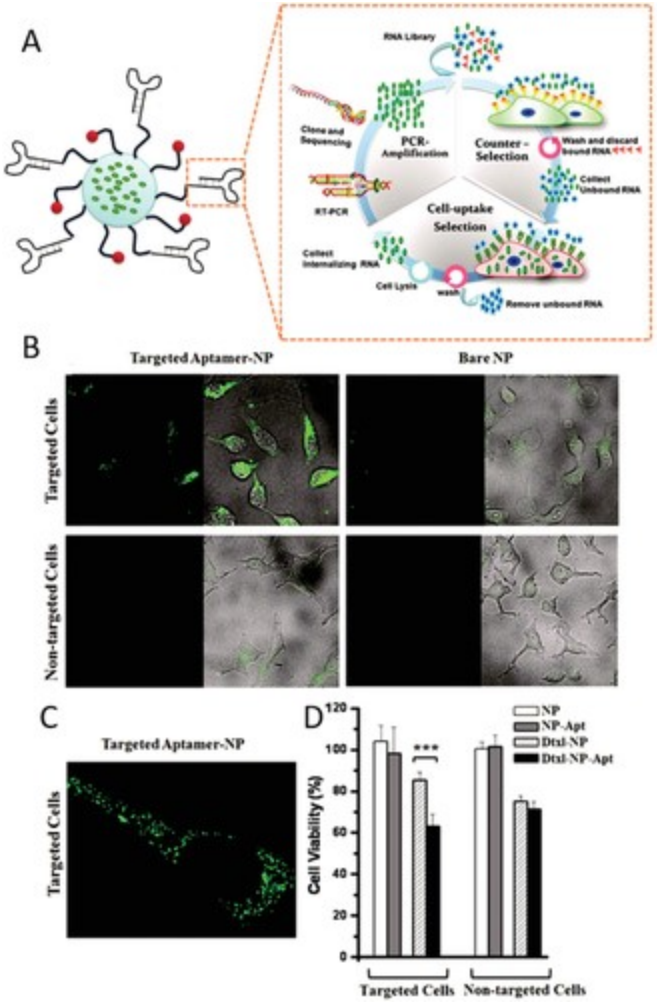

Figure 1.8 Aptamer-conjugated nanoparticles for prostate cancer cell targeting. A. Schematic illustrating the selection process for prostate cancer-specific internalizing RNA aptamers. B. Nanoparticles coated with prostate cancer-specific internalizing aptamers are specifically taken up in target PC3 cells to a higher degree than in nontarget HeLa cells. Bare particles without aptamer are taken up at low levels in both target and nontarget cells, so aptamer conjugation is necessary for target-specific uptake. C. Uptake is distributed throughout the cytosol of targeted cells. D. When particles are loaded with docetaxel, the aptamer conjugated particles (Dtxl-NP-Apt) are significantly more potent nontargeted particles (Dtxl-NP) at killing target cells. Reproduced with permission[148]. Copyright 2012, American Chemical Society.

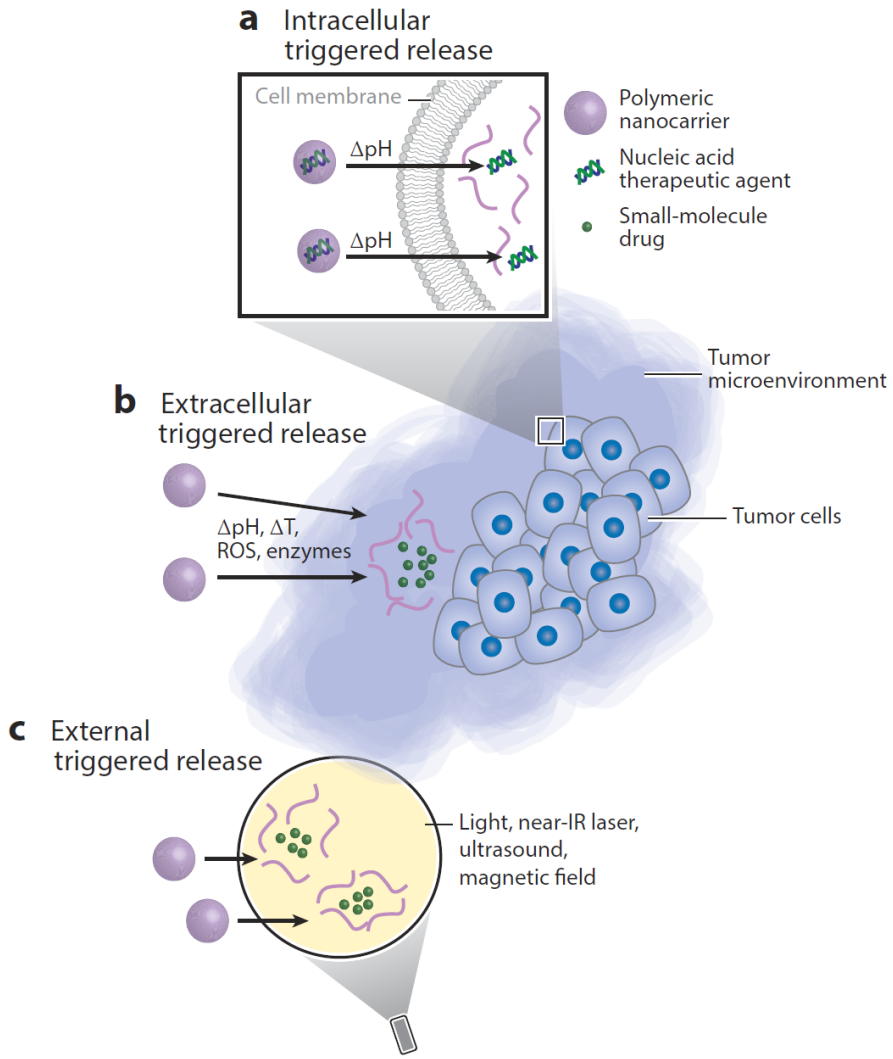

Figure 1.9 Tumor targeting by stimuli-responsive biomaterials. Polymeric materials can be engineered to transform their properties in response to intracellular stimulus, extracellular stimulus, or external triggers to provide release of the active agent at the desired site. A. Delivery materials for nucleic acid therapeutic agents are designed to protect the cargo during transport and subsequently provide an efficient intracellular release upon cell entry, often using pH responsiveness to enable endosomal escape to the cytosol. B. The nanocarrier can be designed to enable an environmentally sensitive stimuli-responsive release of therapeutic agents based on local changes to pH, temperature (T), concentration of reactive oxygen species (ROS), and concentration of enzymes in the tumor microenvironment. C. To obtain selective release at a specific site, external triggers, such as light, near infrared (IR) laser, ultrasound, and magnetic field, can be applied to achieve spatial and temporal controlled release of anticancer agents from the engineered nanoparticles.

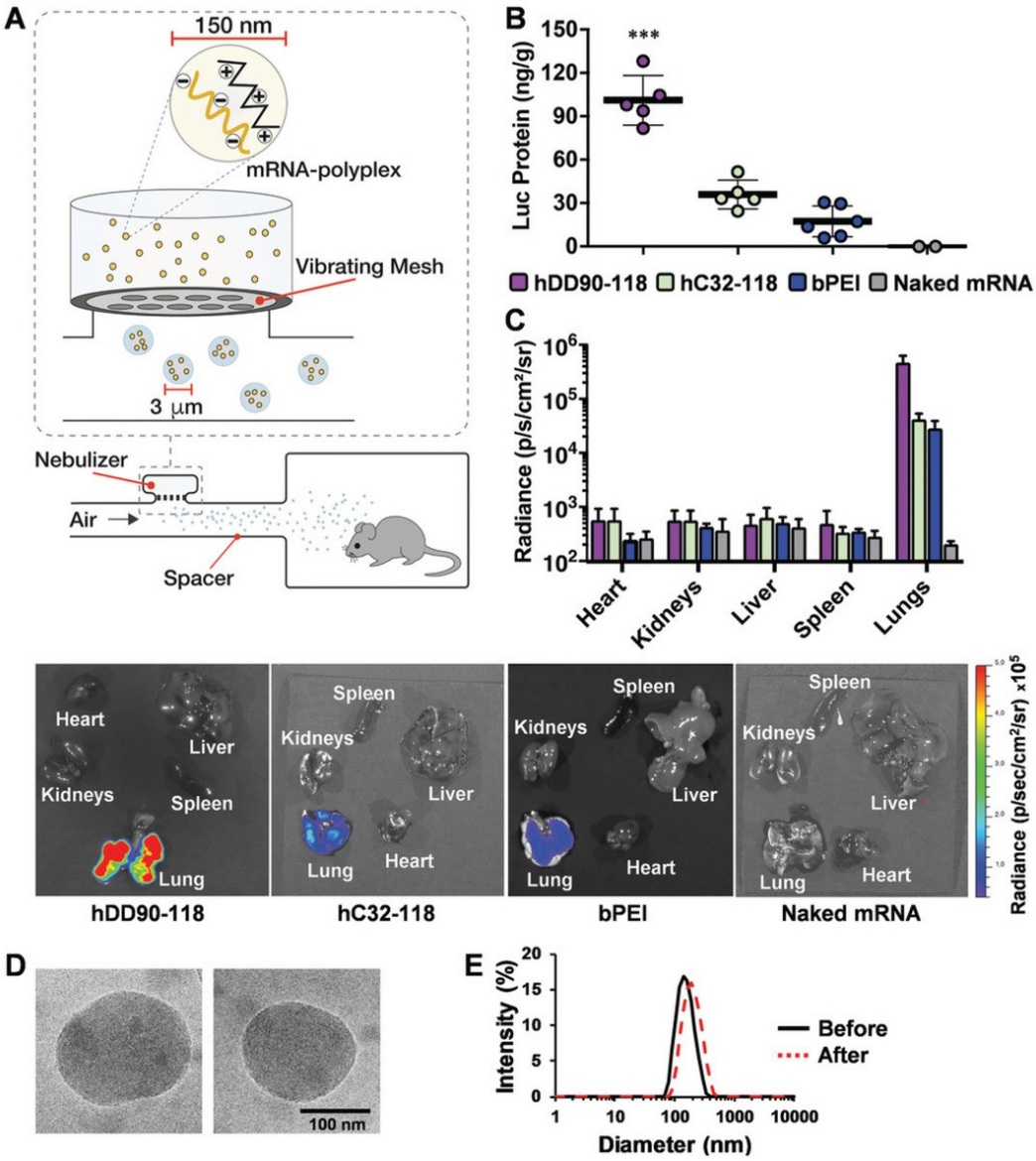

Figure 1.10 Aerosol administration of polyplex nanoparticles for mRNA delivery to the lungs. A. A vibrating mesh nebulizer was used to prepare luciferase mRNA delivery vectors for aerosol administration. Nanoscale polyplexes were encapsulated in micrometer-sized droplets and administered to a whole-body chamber. B. Hyperbranched PBAE hDD90-118 polyplexes enabled high levels of luciferase delivery in the lungs after 24 h. C. Local delivery by inhalation resulted in highly specific delivery to lung tissue and negligible off-target luciferase measured by bioluminescence. D. Particles maintained a similar size and morphology before and after nebulization, characterized by electron microscopy. E. Particles also have a narrow size distribution before and after nebulization. Reproduced with permission[195]. Copyright 2019, Wiley-VCH Verlag GmbH & Co. KGaA.

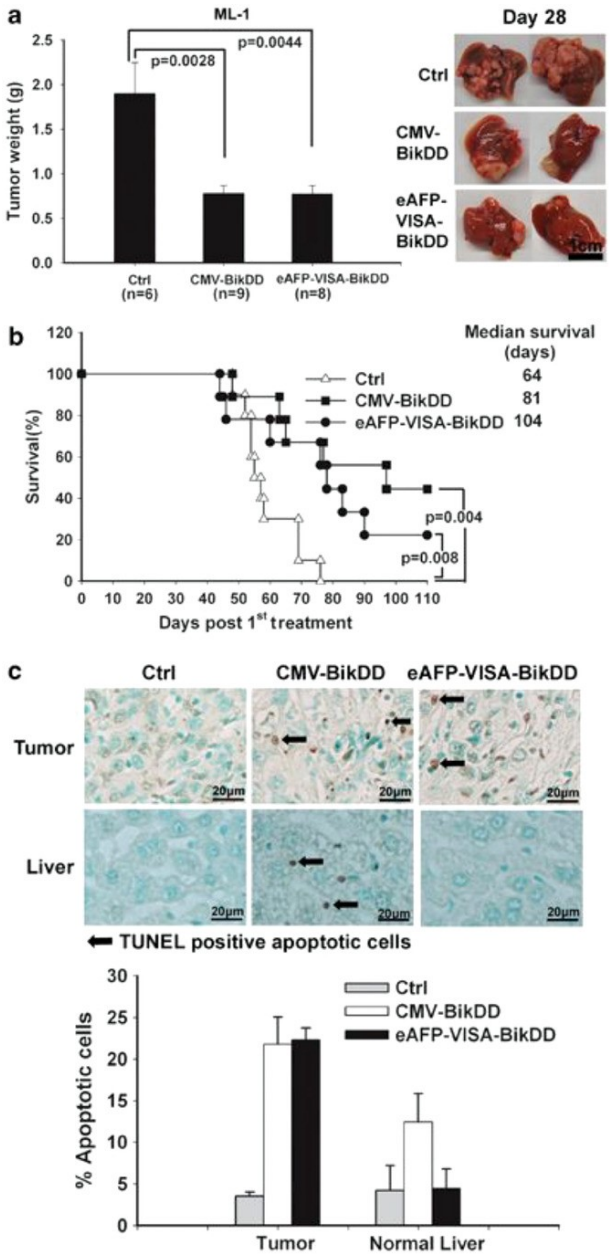

Figure 1.11 Transcriptionally targeted DNA restricts therapeutic gene expression to HCC cells DOTAP-cholesterol liposomes loaded with transcriptionally targeted eAFP-VISA-BikDD or nontargeted CMV-BikDD were I.V. injected in orthotopic ML-1 tumor-bearing mice. A. Both particles significantly reduced tumor burden, and representative photos are shown from 1 week after the last treatment. B. Mouse survival was significant on treatment groups, and the transcriptionally targeted DNA therapy extended survival significantly compared with the nontargeted DNA. C. Tissue samples were fixed and stained for apoptosis using a TUNEL assay. The percentage of apoptotic cells were quantified in random fields from both tumor and healthy liver. While the targeted and nontargeted therapies induced similar numbers of apoptotic cells in

the tumor, the transcriptionally targeted DNA induced less apoptosis in the healthy liver tissue. Reproduced with permission[228]. Copyright 2011, Nature Research.

Nucleic acid cargo	Intended action	Site of action	Chemical properties	Delivery challenges
Plasmid DNA (pDNA)	Gene overexpression	Transcription to mRNA in nucleus	– Double-stranded – Circular – Varying size (10^3–10^5 bp)	– Large size – Endosomal escape – Entry into nucleus – Off-target immune stimulation (CpG sequences)
Messenger RNA (mRNA)	Gene overexpression	Translation to protein in cytoplasm	– Single-stranded – Linear – 10^2–10^4 bases	– Endosomal escape – Release into cytoplasm – High susceptibility to RNAses (ssRNA in endosomes)
Small interfering RNA (siRNA)	Gene knockdown (affects specific gene)	RNAi pathway in cytoplasm	– Double-stranded – Linear – ≈20 bp	– Endosomal escape – Release into cytoplasm – Susceptibility to RNAses – Off-target immune stimulation (dsRNA)
Micro RNA (miRNA)	Gene regulation (affects pool of genes)	RNAi pathway in cytoplasm	– Double-stranded – Linear – ≈20 bp	– Endosomal escape – Release into cytoplasm – Susceptibility to RNAses – Off-target immune stimulation (dsRNA) – Nonspecific gene effects
CpG oligodeoxynucleotides (ODNs)	Immune stimulation	Endosome	– Single-stranded – Linear – ≈10–30 bases	– Off-target/excessive immune stimulation
Cyclic dinucleotides (CDNs)	Immune stimulation	Cytoplasm	– Heterocyclic – 2 nucleotides	– Endosomal escape – Off-target/excessive immune stimulation

Table 1.1 Examples of types of nucleic acid cargo, their properties, and delivery challenges

Name	Company	Material	Cargo	Phase	Cancer	Result	Reference
CALAA-01	Calando Pharmaceuticals	PEG-cyclodextrin	siRNA	I	Solid tumors	Significant toxicity was not observed	151
BIND-014	BIND Therapeutics	PLGA with PSMA targeting ligand	Docetaxel	I	Prostate	Significant toxicity was not observed, 12% overall response rate	153
NC-6004	Nanocarrier	PEG-poly(amino acid) block copolymer	Cisplatin	I	Pancreatic, head and neck, solid tumors	Significant toxicity was not observed	154
CRLX101	Newlink Genetics Corporation	PEG-cyclodextrin	Camptothecin	II	Lung, ovarian, solid tumors	Significant toxicity was not observed, 16% overall response rate	156, 157
NK105	Nippon Kayaku Co.	PEG-polyaspartate	Paclitaxel	II	Breast, gastric	Significant toxicity was not observed, 25% overall response rate	159, 160

Table 1.2 Select polymeric nucleic acid delivery vehicles for cancer therapy investigated in clinical trial

Chapter 2: High-throughput evaluation of polymeric nanoparticles for tissue-targeted gene expression using barcoded plasmid DNA

2.1 Introduction

Gene therapy using exogenous DNA or RNAi is a powerful tool with the potential to address and even cure the underlying genetic origin of disease. However, efficient delivery of the genetic cargo across biological barriers remains a major bottleneck to successful gene therapy[1]. Multiple sequential obstacles exist from the formulation of delivery vehicle for injection to the expression of a target protein in cells[2,3]. At the systemic level, delivery vehicles must protect the genetic cargo from enzymatic degradation in biological fluid, circumvent clearance by the renal and mononuclear phagocyte system (MPS), and efficiently accumulate in the target tissue. At the cellular level, barriers include cell-specific targeting, cellular uptake, endosomal escape, and cargo release[4].

Non-viral nanoparticle (NP) delivery systems can be engineered to overcome these specific challenges of delivery, while avoiding the design constraints and safety concerns of viral vectors[5–7]. Cellular uptake and endosomal escape can be tuned by modulating the vector's chemical structure and buffering capacity, among other factors[8–10]. Cell and tissue level active targeting is possible through conjugation targeting ligands, including peptides or small molecules[11]. Passive tissue targeting modification is enhanced by coating NPs with polyethylene glycol (PEG), but PEG may simultaneously prevent cellular uptake[12,13]. Multifunctional NPs

---

This chapter contains material modified from the following article in press

Kim, J.*, Vaughan, H.J.*, Zamboni, C.G., Sunshine, J.C., Green, J.J., High-throughput Screening of Polymer Structure on Tissue-targeted Gene Expression In Vivo Using Barcoded Plasmid DNA. (2021) *Journal of Controlled Release. In Press.*(* These authors contributed equally)

may be designed to sequentially overcome delivery barriers, but they are complex to develop, have interactive effects that are difficult to predict, and are challenging and costly to manufacture. Further, a vector optimized for cellular transfection *in vitro* may not show efficacy *in vivo* due to systemic factors, such as non-specific protein adsorption, that change the physical and chemical properties of the carriers[14]. For these reasons, rational design of NPs to overcome all *in vivo* delivery barriers is a major challenge.

An alternative approach is to screen large libraries of biomaterials for transfection in the target cell or tissue type. This approach has been used broadly, resulting in large libraries of polymer and lipid biomaterials for nucleic acid delivery[15–18]. Poly(beta-amino ester) (PBAE) is a class of biodegradable ionizable polymer that electrostatically complexes with negatively charged nucleic acids to form NPs[19]. Monomer units with distinct structures may be combined during synthesis to create a library of polymers with differential structures and properties, which have been used to successfully transfect multiple types of cells *in vitro* and *in vivo*[20–25]. Our group has previously performed high-throughput *in vitro* screening to demonstrate structure-function relationship of PBAE polymer at the cellular level, including the effect of monomer and end-group structures on cell-type specificity, cellular uptake, and endosomal escape[8,10,20,26,27]. While ligand- or PEG-modified PBAE NPs have been developed for enhanced tissue targeting[28–30] or penetration[13,21,31], respectively, the significance of differential molecular changes to PBAE chemical structure on biodistribution and transfection *in vivo* is still unclear.

Screening a wide range of biomaterials for tissue-specific *in vivo* transfection within the context of the entire gene delivery process requires high throughput methods, as *in vivo* study of multiple vectors is cost- and time-ineffective. Recently, high-throughput *in vivo* screening methods have been developed to study biodistribution of mRNA-loaded lipid NPs in major

organs using "genetic barcode"[32–34]. In this approach, NPs with distinct lipid compositions are used to encapsulate a unique, secondary nucleotide barcode sequence in addition to the siRNA or mRNA payload. This barcode technology enables sensitive quantification of each nanoparticle biodistribution *in vivo* by deep sequencing methods. However, unlike the previously reported methods that measure the accumulation of the oligonucleotide cargo, a DNA barcode system enables quantification of both plasmid DNA (pDNA) accumulation and its transcribed mRNA expression levels as an elegant way to screen multiple NP formulations, within the same animal, for *in vivo* transfection to a target tissue. Moreover, by using the actual pDNA cargo as the barcode sequence, the N/P ratio of barcoded NP remains unaltered in comparison to the non-barcoded NP with pDNA of interest, thereby minimizing potential change in NP's physicochemical properties.

In this study, we develop a high-throughput method for screening *in vivo* gene delivery efficiency of a library of PBAE NPs using a single pDNA that harbors a barcode sequence. Both biodistribution and transfection can be analyzed by detecting the primary barcode and the transcribed mRNA of the barcode through qPCR and RT-qPCR analysis, respectively. Also, by inserting the barcode sequence in the pDNA, we eliminate any potential change to the nanoparticle's physicochemical properties from the addition of a secondary barcode payload. Using the platform, we evaluate specific structures of PBAE polymers and their accumulation and transfection of pDNA in major organs following systemic administration.

2.2 Materials and methods

Materials

1,4-butanediol diacrylate (B4) (Alfa Aesar, Ward Hill, MA), 1,5-pentanediol diacrylate (B5) (Monomer Polymer & Dajac Labs), 3-amino-1-propanol (S3) (Alfa Aesar) ,4-amino-1-

pentanol (S4) (Alfa Aesar), 5-amino-1-pentanol (S5) (Alfa Aesar), 2-methylpentane-1,5-diamine (E4) (TCI America, Portland, OR), 2-(3-aminopropylamino)ethanol (E6) (Sigma-Aldrich, St. Louis, MO), and 1-(3-aminopropyl)-4-methylpiperazine (E7) (Alfa Aesar) were purchased and used as received. pEGFP-N1 was purchased from Elim Biopharmaceuticals and amplified by Aldevron (Fargo, ND). pfLuc Luciferase-pcDNA3 was a gift from William Kaelin (Addgene plasmid # 18964) and amplified by Aldevron (Fargo, ND). Purelink Genomic DNA Extraction kit (Thermo Fisher Scientific), PowerUp SYBR Green Master Mix (Applied Biosystems, Foster City, CA), Label IT®-Tracker™ Cy™3 and Cy™5 kit (Mirus Bio LLC, Madison, WI) were obtained from commercial vendors and used per manufacturer's instructions.

Polymer synthesis

PBAE polymers are synthesized via a two-step Michael addition reaction as previously described (**Figure 2.1A**). First, acrylate-terminated base polymer is created by reacting a diacrylate monomer with a primary amine-containing side chain monomer at a stoichiometric molar ratio of 1.2:1 for 24 h at 90 °C. Then, the base polymer is reacted with 20-fold excess molar amount of primary amine-containing end-capping molecule in THF for 3 h at room temperature. The final polymer is ether-precipitated and stored in DMSO at 100 mg/mL in -20 °C. For this study, a total of 8 PBAE polymers were synthesized using 2 different diacrylate monomers, 1,4-butanediol-diacrylate (B4) and 1,5-pentanediol-diacrylate (B5), 3 side chain monomers, 3-amino-1-propanol (S3), 4-amino-1-butanol (S4), and 5-amino-1-pentanol (S5), and 3 end-capping molecules, 2-methylpentane-1,5-diamine (E4), 2-(3-aminopropylamino)ethanol (E6), and 1-(3-aminopropyl)-4-methylpiperazine (E7) (**Figure 2.1B**). Nomenclature for the final polymer follows the label of each monomer used. For example, a polymer synthesized with B5, S3, and E6 is named 536. The molecular weights of the 8 PBAE polymers were determined by

gel permeation chromatography (GPC) on a high-performance liquid chromatography (HPLC) system (Agilent) equipped with UV-Vis (Agilent), refractive index (RI) (Wyatt Technology), and Multi-Angle Light Scattering (Wyatt Technology) detectors. Molecular weight information (Mn, Mw, and PDI) was determined for each polymer using a specific refractive index (dn/dc) of 0.06, which was calculated by injecting a known polymer mass, assuming 100% recovery (**Table 2.1**).

Plasmid preparation

A total of five plasmids were used, three encoding for fluorescent proteins and two encoding random nucleotide sequences. In order to ensure that all plasmids were similar in size and had the same backbone, pEGFP-N1 was used as the base plasmid and genes encoding other fluorescent proteins, mOrange and iRFP, or two random sequences were cloned in to replace EGFP gene. The two random plasmids were designed as a proof-of-concept that more plasmids with unique random barcode sequences can be used in a similar high-throughput study. These five plasmids are referred to as pDNA A (GFP), B (mOrange), C (iRFP), D (Noncoding 1), and E (Noncoding 2). All gene sequences can be found in **Table 2.2**.

For two plasmids with random noncoding sequences, two random 1500–base pair sequences with 25% fraction each of A, C, G, and T nucleotides were generated using the Aarhus University, Bioinformatics Research Centre, Denmark online tool (URL - http://users-birc.au.dk/~palle/php/fabox/random_sequence_generator.php) Sequences for mOrange and iRFP genes were acquired from Addgene. Restriction cloning sites for NheI and HindIII were encoded on the 5' and 3' ends of the DNA fragments, respectively. The double-stranded linear DNAs were custom ordered using gBlock Gene Fragments (IDT, Inc, Skokie, IL). Plasmids were cloned into the pN3 backbone using restriction digestion by NheI-HF and HindIII-HF restriction

enzymes (New England Biolabs, Ipswitch, MA), following the manufacturer's instructions. Purification of DNA fragments was performed by gel electrophoresis and extraction using the QIAquick Gel Extraction Kit (Qiagen, Hilden, Germany), following the manufacturer's instructions. DNA ligation was performed by combining 100 ng of digested backbone DNA with 700 ng of digested insert, then performing an overnight ligation at 16 °C with T4 DNA ligase (New England Biolabs). Ligated cloned were selected for and amplified using 5-alpha Competent E. coli (New England Biolabs) and Qiagen Maxi Kits. mOrange and iRFP plasmids were also amplified by Aldevron. All plasmids were stored at 1 mg/mL in sterile water at 4 °C.

Primer optimization

In order to generate forward and reverse primers specific to each pDNA and avoid non-specific amplification of other plasmids or murine genomic DNA, Basic Local Alignment Search Tool (BLAST) from the National Institute of Health's National Center for Biotechnology Information was used to extensively check for homology. First, Primer-BLAST was used to generate 50 primer candidates for each plasmid that match the conditions listed in **Figure 2.2A**. Then, the primer candidates for each plasmid were used as the input query sequence in BLASTn to check for homology against other plasmids as well as the mouse genome (**Figure 2.2B**). Primer candidates that showed undesired homology (matching sequence) in the last 6 base pairs or in more than 10 base pairs total were excluded (**Figure 2.2C**). Lastly, the top-scoring candidate for each plasmid was checked for hairpin, self-dimerization and hetero-dimerization using IDT OligoAnalyzer 3.1. The final primer sequences were custom ordered (IDT, Inc, Skokie, IL), and stored as 3 μM aliquots in -20 °C. All primer sequences can be found in **Table 2.3**.

Primer sequences were experimentally checked for their specificity toward the corresponding plasmids by quantitative real time polymerase chain reaction (qPCR) and gel electrophoresis. Briefly, 100 ng of each plasmid was amplified against each of the five primer pairs to determine C_T values and generate the melt curve. 2 µL of pDNA, 2 µL of 3 µM forward primer, 2 µL of 3 µM reverse primer, and 14 µL of PowerUp SYBR Green Master Mix solutions were mixed for qPCR amplification. PCR reaction consisted of initial polymerase activation stage at 95 °C for 2 min, followed by 40 cycles of denaturation at 95 °C for 15 sec, annealing at 55 °C for 15 sec, and elongation at 72 °C for 1 min. After PCR amplification, the 25 qPCR products along with DNA ladder were also run through gel electrophoresis in 1% agarose gel.

Validation of qPCR protocol using fresh tissue lysates spiked with pDNA

A 5–7-week-old female BALB/c mouse was euthanized and major organs – liver, kidneys, spleen, lungs, and heart – were harvested. Organs were washed with 1X PBS three times, cut into small pieces with a razor blade, and minced between the frosted ends of two microscope slides. Then, 10 mg of liver sample and 5 mg of samples from all other organs were separately placed into 1.5mL tubes. Tissues were digested using digestion solution provided in the Purelink Genomic DNA Extraction kit. Following the digestion, 10 ng to 10 pg of each pDNA were spiked into digested tissue. Subsequent steps of DNA extraction were followed as instructed and the final purified DNA was then diluted with water ten-fold for liver samples and two-fold for all other organ samples. The same qPCR reaction protocol was followed as described above.

Nanoparticle formulation and characterization

NPs were formed by bulk mixing of PBAE polymer and pDNA in aqueous conditions to allow electrostatic interaction and particle self-assembly. PBAE polymer in DMSO at 100

mg/mL and pDNA in water at 1 mg/mL were diluted to 12.5 mg/mL and 0.5 mg/mL, respectively, using 25 mM sodium acetate (NaAc) buffer at pH 5.0. Equal volume of polymer and DNA solutions were mixed and incubated for 10 min to form NPs. This ensures the mass ratio of polymer to DNA to be consistent at 25 w/w across the different NPs evaluated.

Hydrodynamic diameter was measured by dynamic light scattering, and zeta potential was measured by electrophoretic mobility using the Zetasizer Pro (Malvern Instruments, Malvern, UK). Immediately before these measurements, NPs were diluted 1:10 in a 1:1 ratio of 25 mM sodium acetate and 1X PBS to a final volume of 1 mL. Encapsulation efficiency of pDNA in NPs was assessed by gel electrophoresis. NP prepared at 25 w/w with 0.03 mg/mL pDNA was combined with 6X Gel Loading Dye with no SDS. Samples were loaded into a 0.8% agarose gel containing 1 μg/mL ethidium bromide. Free unencapsulated pDNA at the same dose was used as a positive control. The gel was run with 90 V applied for 30 min and visualized by UV exposure.

Förster resonance energy transfer (FRET) between Cy3- and Cy5-labeled NPs

FRET analysis was conducted to investigate any intermixing between different NPs co-dispersed in a single solution, as would occur during a co-injection. pEGFP DNA was labeled with Cy3 and Cy5 fluorophores following a protocol by Wilson et al[35]. Labeling density was measured using a determined using a NanoDrop spectrophotometer (ThermoFisher Scientific, Waltham, MA). Three different pairs of NPs were tested: PBAE 447 with Cy3-labeled pEGFP DNA and PBAE 457 with Cy5-labeled pEGFP DNA, PBAE 457 with Cy3-labeled pEGFP DNA and PBAE 536 with Cy5-labeled pEGFP DNA, and PBAE 536 with Cy3-labeled pEGFP DNA and PBAE 447 with Cy5-labeled pEGFP DNA. NPs were prepared separately and incubated together at 1:1 v/v ratio with gentle pipette mixing, and peak emission intensities of Cy3 (565-

570 nm) and Cy5 (665-675 nm) was read following Cy3 excitation at 540 nm using spectrofluorophotometry (Shimadzu RF-5301). A positive control NP batch was formulated by complexing either PBAE polymer 447, 536 or 457 with 1:1 mixture of Cy3-labeled and Cy5-labeled DNAs.

2.8 In vitro transfection with mixture of PBAE NPs

HepG2 cells were purchased from ATCC (Manassas, VA), cultured in Minimum Essential Media (MEM) supplemented with 10% FBS, 100 U/mL Penicillin, 100 μg/mL Streptomycin, 100 μM of MEM non-essential amino acids solution, and 1 mM of sodium pyruvate, and maintained in a humidified incubator at 37°C with 5% CO_2. Cells were seeded in a 96-well plate at 10,000 cells / well and allowed to adhere for 24 hr. For *in vitro* screening (Fig S6), PBAE NPs were freshly prepared with equal amounts of each DNA barcode plasmid (A-E) at 25 w/w for a final DNA concentration of 0.3 μg/μL. For Fig S7, PBAE NPs were synthesized with pDNA A or a mixture of three NPs with pDNA A, D, or E at the same total pDNA dose each for a final DNA concentration of 0.3 or 0.1 μg/μL. 20 μL NPs were added to cells and allowed to incubate for 2 hours at 37ºC. RNA was isolated and reverse transcribed using a Cells-to-CT kit from ThermoFisher Scientific (Waltham, MA) according to the manufacturer's instructions. For qPCR analysis, 6 μL of sample DNA, 2 μL of 3 μM forward primer, 2 μL of 3 μM reverse primer, and 10 μL of PowerUp SYBR Green Master Mix (Applied Biosystems, Foster City, CA) solutions were mixed for qPCR amplification. qPCR was performed using a StepOnePlus™ Real-Time PCR System (Applied Biosystems, Foster City, CA) with the cycling parameters described above. Threshold and baseline values were standardized across all samples and all runs to ensure accurate comparison. The comparative CT method was used to quantify relative expression levels[36]. Barcode amplification was normalized to the housekeeping gene

GAPDH to quantify NP accumulation of each PBAE with each barcode relative to the genomic DNA content. Then, this value was normalized to non-specific background amplification in untreated cells, by subtracting the ΔC_T of amplification in untreated animals from animals which received barcoded NPs, thereby obtaining $\Delta\Delta C_T$.

$$\Delta\Delta C_T = (C_{T\text{barcode x}} - C_{T\text{GAPDH}})_{\text{treated}} - (C_{T\text{barcode x}} - C_{T\text{GAPDH}})_{\text{untreated}}$$

High throughput biodistribution analysis

All *in vivo* procedures were approved and overseen by the Johns Hopkins Institutional Animal Care and Use Committee (IACUC). Biodistribution of 8 different PBAE polymers was tested in 5–7-week-old female BALB/c mice (The Jackson Laboratory, Bar Harbor, ME). For each mouse, a single 200 μL cocktail solution containing five different PBAE NPs was prepared for tail-vein injection. Each of the five NPs was formulated by pairing one of 8 PBAE polymers with one of the five pDNAs to serve as the identifier barcode (**Figure 2.3**). Each NP formulation contained 10 μg of pDNA for a total of 50 μg pDNA in the cocktail solution. Biodistribution of PBAE 447 NPs from the high-throughput samples was compared against that from additional mice injected only with NPs prepared from PBAE polymer 447 and 50 μg pEGFP DNA to validate accuracy of the high-throughput method. Mice were sacrificed 30 min post injection for DNA extraction. Major organs – liver, kidneys, spleen, lungs, and heart – were harvested, washed with PBS three times, cut into small pieces with a razor blade, and minced between the frosted ends of two microscope slides. Then, approximately 10 mg of liver sample and 5 mg of samples from all other organs were separately placed into 1.5 mL tubes, and pDNA was extracted from minced tissues following the manufacturer's instruction from the Purelink Genomic DNA Extraction kit (Invitrogen, Waltham, MA). Once DNA was purified through the extraction column, it was diluted with water ten-fold for liver samples and three-fold for all other

organ samples. The differences in the amount of minced tissues used to extract pDNA between organs was normalized by the total amount of genomic DNA content during qPCR analysis using the comparative CT method and GAPDH as a housekeeping gene.

High-throughput in vivo transfection analysis

5–7-week-old female BALB/c mice (The Jackson Laboratory) were injected via tail-vein with the same cocktail solutions as the biodistribution study (**Figure 2.3**). Mice were sacrificed 6 hours post injection for RNA extraction. Organs were harvested and washed in 1X PBS, then cut into small pieces using a razor and minced between frosted microscope slides. 50 mg of each sample was suspended in Trizol and homogenized. A 20% volume of chloroform was added, and tubes were vortexed briefly to emulsify. Samples were incubated at room temperature for 5 minutes, then centrifuged at 12,000 g for 15 minutes at 4 °C. The aqueous phase was transferred to a new tube, then isopropanol was added at 50 % of the original Trizol volume. Samples were inverted to mix, then incubated for 10 minutes at room temperature to allow for RNA precipitation. Samples were centrifuged at 12,000 g for 30 minutes at 4 °C. Isopropanol was decanted, and pelleted RNA was washed with 75% ethanol. After vortexing, samples were centrifuged at 7,500g for 5 minutes at 4 °C. Ethanol was carefully decanted, and the RNA pellet was air dried for 5-10 minutes. The dried pellet was resuspended in 30 µL water, and RNA concentration was determined using a NanoDrop spectrophotometer (ThermoFisher Scientific, Waltham, MA). RNA was purified of DNA using the TURBO DNA-free kit (Invitrogen, Carlsbad, CA) according to manufacturer's instructions. Using the High-Capacity RNA-to-cDNA^{TM} kit (Invitrogen, Carlsbad, CA), 20 µg of RNA was reverse transcribed according to the manufacturer's instructions. Reverse transcription was performed at 37 °C for 1 hour, followed by 5 minutes at 95 °C to stop the reaction. PCR reactions were comprised of 10 µL PowerUp

SYBR Green Master Mix (Applied Biosystems, Foster City, CA), 2 μL forward primer (3 μM), 2 μL reverse primer (3 μM), and 1 μL cDNA. Baseline and thresholds were standardized across all samples. $\Delta\Delta C_T$ values were calculated as previously described. If there was no amplification for a given sample primer combination, the sample was assigned a C_T of 40, corresponding to the maximum amplification cycle, in order to compute $\Delta\Delta C_T$ value.

In vivo transfection using pfLuc

To form luciferase NPs for *in vivo* use, pfLuc DNA was complexed with PBAE 456, 536, and 546 at a 25 w/w ratio in 25 mM sodium acetate (pH = 5.0) for a final DNA concentration of 0.25 μg/μL. 200 μL of NPs (50 μg DNA) was injected via the tail vein in 5–7-week-old BALB/c mice. After 30 minutes, 1 hour, 3 hours, or 6 hours, animals were injected intraperitoneally with 150 mg/kg D-luciferin (Gold Biotechnology, St. Louis, MO). After 10 minutes, the animals were anesthetized using isoflurane and bioluminescence was imaged using the IVIS Spectrum (Xenogen, Alameda, CA). Images were analyzed using Living Image® 4.7.3 software (PerkinElmer, Waltham, MA).

Statistical analysis

All statistical analysis was performed with GraphPad Prism 8 software package. For *in vivo* experiments, statistically significant barcode amplification was calculated by one-tailed Student's t-test between the experimental $-\Delta\Delta C_T$ values and zero. Statistical significance was defined as $p < 0.05$ after correcting for multiple comparisons using the Holm-Sidak method.

2.3 Results

Primers' specificity to DNA barcodes

Primers were selected via BLAST with the most conservative conditions to ensure highly selective binding to barcoded plasmid used in the study. Three of the five plasmids used in the

study each contained an insert serving as the barcode, which can be detected directly as protein or in its transcribed mRNA form (**Figure 2.3**).

The forward and reverse primer pairs for each barcode gene were designed to produce an approximately 100-basepair long amplicon. Every possible combination of the primer pairs and the plasmids were mixed for qPCR reaction to confirm the primers' specificity to the corresponding plasmids. As shown in **Figure 2.4A**, only conditions with correctly matched primers and plasmid resulted in amplification. Also, each set of primers run either alone or mixed with other primer sets did not yield any false positive PCR results from self- or hetero dimerization. The melt curves also showed a clean single peak only for correctly matched conditions, which indicates that there is no off-target amplification occurring in the PCR reaction (**Figure 2.5**). qPCR of fresh tissue lysates from all major organs of a BALB/c mouse showed no amplification from the primers, indicating no off-target amplification of genomic DNA. PCR-amplified products were run on gel electrophoresis to confirm that the amplicons had the expected length, based on our primer design. The gel image shows bands appearing for primer-plasmid matching conditions only at the height level of approximately 100-basepair mark on the DNA ladder (**Figure 2.4B**). These observations validate the specificity of each primer set to its corresponding plasmid.

We also evaluated whether the C_T value from qPCR varies linearly with pDNA mass. A range of pDNA mass from 10 pg to 10 ng was spiked into fresh tissue lysates and subjected to DNA extraction for qPCR. As shown in **Figure 2.4C**, each of the 5 barcode plasmids has a linear correlation with $R^2 > 0.96$ between its mass and C_T values in the 5 major organs tested. All C_T values collected in the experiments and used in the analysis were within the linear region of these curves. Amplification of each barcode plasmids was not affected by the type of tissue lysates, as

demonstrated by the overlapping standard curves in each panel of Figure 2C. Interestingly, however, amplification of 5 barcode plasmids showed varying degree of sensitivity in each type of tissue lysates, as demonstrated by the non-overlapping standard curves in each panel of **Figure 2.6**. This requires each unique barcode plasmid to be tested for linearity between C_T value and a range of plasmid mass. In this study, each PBAE NP formulation is tested with 5 different barcode plasmids, and the biodistribution and *in vivo* transfection data are averaged to mitigate the small difference in sensitivity across barcode plasmids.

Nanoparticle characterization

PBAE NPs formulated with 8 different PBAE polymers were characterized based on hydrodynamic diameter and surface charge. As shown in **Figure 2.7A**, PBAE NP hydrodynamic diameter measured by dynamic light scattering ranged from 100 – 200 nm for all NP formulations. All NPs showed positive zeta potential between 15 – 22 mV, due to the exposure of positively charged polymer on the surface. While positive charge of NPs could cause toxicity, previous literatures on PBAE NPs with similar positive surface charge report minimal toxicity both *in vitro* and *in vivo*[20,35]. Also, all NPs showed 100% encapsulation of pDNA, with no evidence that barcode sequence or polymer structure significantly affects encapsulation efficiency (**Figure 2.8**).

FRET analysis showing the absence of nanoparticle intermixing

The high-throughput *in vivo* screening method is based on different PBAE NPs being injected as a cocktail solution into a single animal and subsequently individually identified in tissue lysates. While inorganic nanoparticles (such as gold NPs) and lipid-based NPs (such as liposomes) form discrete NPs, it is conceivable that polyplex NPs, which are formed from molecular interactions between polyelectrolytes of opposing charge, could intermix components

together. Such potential intermixing of PBAE polyplexes has not been previously investigated and could conceivably prevent the barcodes from staying matched to a specific NP. Each PBAE NP formulation is formulated with one barcode pDNA, which serves for NP identification. Thus, the capability of PBAE polyplex NPs to resist exchange of
DNA cargo in a cocktail solution to ensure that mixed NPs encapsulate only their original defining barcode plasmids. To evaluate this, we formulated two separate batches of NPs encapsulating pDNAs labeled with either Cy3 or Cy5 fluorophores, then mixed the two batches into a single solution. Exchange of Cy3-labeled DNA from a NP with Cy5-labeled DNA from another NP in the mixture brings the fluorophores in close proximity to each other within a NP and causes emission of a FRET signal. Negative control NPs were separately prepared with each of Cy3- or Cy5-labeled DNA alone and positive control NPs were prepared with a 1:1 mixture Cy3- and Cy5-labeled DNA within the same NPs.

Each NP sample was excited at the excitation wavelength for Cy3 (540 nm), and emission was measured at the emission wavelength for Cy3 (565-575 nm) and Cy5 (665-675 nm), shown in **Figures 2.7B/C and 2.9.** Cy3 NPs alone showed emission at 565-575 nm, and Cy5 NPs alone showed no emission, because there is minimal excitation of this fluorophore at 540 nm. The positive control NPs showed FRET activity, with 35% decreased signal at 565-575 nm (Cy3 emission) in comparison to Cy3 NP alone, and an increase in signal of >3 RFU at 665-675 nm (Cy5 emission) in comparison to Cy5 NP alone (~1 RFU). This suggests that part of Cy3 emission was able to excite neighboring Cy5-pDNA encapsulated in the same nanoparticle. In the test case, where NPs were formulated separately then combined, minimal FRET activity was observed as indicated by the similar signal intensity at 565-575 nm compared to Cy3 NPs alone. The signal intensity at 665-675 nm for the test case was similar to the negative control at ~1

RFU. Given the high labeling density of Cy3 and Cy5 DNAs (1 fluorophore per 63.4 base pairs and 54.9 base pairs respectively) and high density of plasmid DNA in PBAE NPs reported in previous work[37], we determined that there was not substantial intermixing of plasmid DNAs between PBAE NPs. While these results do not exclude the possibility of small amounts of exchange, the lack of FRET signal in a cocktail solution indicates that the Cy3 and Cy5 fluorophores mostly maintain separation in distinct NPs. Therefore, we can correlate accumulation of unique barcode DNA with its corresponding unique NP.

In vitro transfection of PBAE NPs with mixed barcoded pDNAs

HepG2 cells were transfected *in vitro* with 8 PBAE NPs with 120 ng each of barcoded pDNAs A, B, C, D, and E. After 48 hours, qRT-PCR results show significant differences in transfection between NP formulations, with PBAE 447 as the most effective formulation for transfection and PBAE 546 as the least effective (**Figure 2.10**). To evaluate differential expression between the barcodes, the percentage of variation from the mean was calculated for each barcode (**Figure 2.11**). Barcode A and B had significantly increased expression over C, D, and E within the same NP formulations. This indicates a difference in expression which is sequence dependent. To control for any bias from these differences, we formulated each PBAE NP with each barcode in subsequent studies. This redundancy ensured that variation in biodistribution, transfection efficiency, PCR amplification efficiency, transcript half-life, or plasmid immunogenicity due to the difference in barcode sequences would not bias the results.

To verify that screening results from mixed barcode formulations are representative of transfection results from a single pDNA, NPs were formulated at either a full dose of pDNA A or a mixture of 1/3 dose each of pDNA A, D, or E. RT-qPCR results showed a decrease in -ΔΔCT of Barcode A mRNA from 9.1 for the single, full dose NP to 7.4 for the mix, 1/3 dose NPs,

corresponding to a 1/3 decrease in mRNA concentration (**Figure 2.12**). This indicates that RT-qPCR results from mixed barcode NPs are predictive of transfection with a full dose NP. Interestingly, decreasing the total DNA concentration by 1/3 from 0.03 μg/μL to 0.01 μg/μL does not result in a similar decrease in transfection measured by RT-qPCR, suggesting that changing the overall DNA concentration may affect transfection levels.

High-throughput screening of tissue targeting

Utilizing five barcoded pDNAs and their specific primers, we developed a scheme to test biodistribution of five PBAE NP formulations per animal. In each animal, all PBAEs were paired with a different barcode to distinguish the polymers from one another. Further, each PBAE NP was tested separately in 5 animals, and it was paired with a different barcode in each replicate, as shown in **Table 2.4**. NPs were freshly prepared by separately combining barcode DNA and PBAE for each formulation, then mixing the five formulations for each animal immediately prior to injection, to minimize exchange of pDNA between NP formulations. The NPs were administered intravenously via the tail vein in BALB/c mice.

30 minutes after NP injection, the animals were sacrificed and the heart, lungs, spleen, liver, and kidneys were collected. DNA was isolated and purified from the organs, then qPCR was performed for each sample using primer sets for each barcode. By matching each barcode to its corresponding PBAE NP in a particular animal, we calculated the average relative accumulation of each formulation in the major organs **(Figure 2.13)**. The plots show accumulation of any given PBAE NP across organs to screen for PBAEs that direct NPs to specific organs over others. Statistically significant barcode accumulation over untreated samples was observed in organs involved in clearance, including the spleen (PBAE 546), liver (PBAE 456, 534, 546), and kidneys (PBAE 534). Although not statistically significant, higher barcode

accumulation was also observed in the lung, which presents the first capillary bed that the NPs are exposed to once injected intravenously. Accumulation in the heart was negligible for all formulations. The mean highest levels of barcode DNA were detected in the liver and spleen for 7 out of 8 formulations. This is consistent with rapid MPS clearance of NPs in the range of 100-200 nm.

High-throughput screening of tissue-specific gene expression

While NP accumulation in the target tissue is necessary for gene delivery, cellular uptake, endosomal escape, and nuclear localization are critical steps for transfection that are not captured by biodistribution studies alone. To this end, we further explored the use of barcoded pDNA to directly quantify PBAE NP transfection in the major organs. Transfection was quantified by performing RT-qPCR on transcribed barcode mRNA isolated from treated animals. Animals were treated with the same NP mixtures as described in **Table 2.4**, and organs were harvested after 6 hours, a timepoint that shows a notable increase in *in vivo* expression signal and therefore captures transfection efficacy (**Figure 2.14**). The isolated RNA was purified of any contaminating DNA and reverse transcribed into cDNA. RT-qPCR was performed using each set of primers for each sample, and $\Delta\Delta C_T$ values were calculated as previously described.

Barcode transfection of each PBAE across organs is shown in **Figure 2.15**. Transfection was predominantly observed in the kidney, spleen, and liver. For the heart and lungs, there was no detectable transfection as PCR amplification was equivalent to amplification in untreated samples for all NP formulations. Transfection was primarily localized to the liver and spleen, with statistically significant spleen transfection detected for 447, 457, and 536 PBAEs, and liver transfection detected for 546 PBAE. Transfection in the kidneys was relatively low / not significant, despite similar levels of barcode DNA accumulation to the liver and spleen. This

may be because small, fragmented particles or free pDNA ineffective for transfection may preferentially be cleared by the renal system. Interestingly, PBAEs showing similar level of accumulation in an organ did not necessarily resulted in similar level of transfection. For example, comparable amounts of pDNA were delivered to the liver by both 456 and 546 PBAEs, however 546 PBAE NP showed a significant level of transfection in the liver while 456 did not. This difference in transfection efficiency could be explained by the differential effect of each PBAE polymer structure following tissue accumulation in the downstream intracellular delivery steps, including interaction with cell surface, internalization, endosomal escape, and pDNA release. These differences are particularly striking as the chemical structures of 456 and 546 are so similar. In the repeating unit of the polymer, 456 contains 4 carbons between acrylate groups and 5 carbons between the amine group and the alcohol group in the side chain, whereas 546 contains 5 carbons between acrylate groups and 4 carbons between the amine group and the alcohol group in the side chain. Yet, this small molecular difference generates a dramatic biological difference in the ability of the polymer to facilitate gene delivery in a tissue-specific way, in this case transfection of liver. This result highlights the utility of a high-throughput *in vivo* assay to evaluate differential activity of gene delivery effectiveness between closely related materials from a nanoparticle library. While it is difficult to identify a single parameter from the properties of a given PBAE polymer that directs specific accumulation or transfection in an organ (**Table 2.1**), a thorough statistical correlation analysis can elucidate the structure-function relationship of gene delivery polymers(26).

It is also important to note that PBAE NP that showed significant transfection in the liver *in vivo* was not the optimal candidate from *in vitro* transfection screening (**Figure 2.10**). While there were significant differences in *in vitro* transfection efficacy with all 8 PBAE NP

formulations in HepG2 liver cancer cells, these differences were not predictive of *in vivo* performance. For example, PBAE 546 showed the lowest *in vitro* expression in these cells but showed a high degree of liver targeting *in vivo* as shown by barcode screening and luciferase imaging. This further highlights the significance of the *in vivo* high-throughput screening method.

Validation of liver- and spleen-specific gene delivery by 536 PBAE NPs

To verify that this system accurately predicted transfection patterns for a particular NP formulation, we delivered a reporter plasmid, firefly luciferase (fLuc) intravenously using 456, 536, and 546 PBAE and imaged bioluminescence after 6 hours. Luciferase expression was localized primarily to the spleen for 456, liver and spleen for 536, and liver for 546 PBAE NP **(Figure 2.16)**. Bioluminescence in heart, lung, and kidney were negligible in all three formulations. These gene expression results from singular injection agree with high-throughput transfection screening results for each of the respective PBAE NPs. The agreement between high-throughput screening and singular injection results suggests that the barcode method is predictive of NPs functional outcome based on specific polymer composition regardless of the nucleic acid sequence of pDNA. In addition, 456 and 536 PBAE NPs exhibited conflicting patterns between the biodistribution and gene expression results, where 456 PBAE NP showed highest accumulation in the liver but highest expression in spleen, and 536 PBAE NP showed similar levels of accumulation across organs but significant expression only in the spleen and liver. This again highlights the importance of directly quantifying transfection at the level of mRNA or protein, rather than biodistribution of NPs and DNA, to evaluate gene delivery *in vivo*.

2.4 Discussion

Many different polymers and lipids libraries have been synthesized to formulate NPs by combinatorial methods. These NPs have extensively been characterized to elucidate structure-function relationships[15,19,38]. This often requires high-throughput methods for standardized and efficient screening for optimization. Multi-well plates and automated pipetting robots have enabled fast and efficient *in vitro* analysis of cytotoxicity, cellular uptake, and transfection[39]. Because these *in vitro* cell culture studies are rapid and reproducible, they are often used to identify optimal formulations from the library for further *in vivo* testing. However, many studies have found that *in vitro* transfection efficacy is a poor predictor of *in vivo* efficacy because cell culture conditions do not recapitulate the many barriers to systemic gene delivery[40,41]. Cost, time, and loss of animal life are bottlenecks preventing *in vivo* screening of large numbers of NP formulations. A high-throughput strategy for *in vivo* gene therapy experiments with novel methods to investigate multiple NPs in a single animal reduces the labor, cost, and use of animals. The study showed how only 8 mice could be used to perform a biodistribution experiment of 8 NP formulations with n=5, which would otherwise have required 40 mice without high-throughput methods. The barcode strategy also mitigates variability between individual animals unduly influencing observed differences in NP behavior. While each PBAE NP formulation is still evaluated in five separate mice, variability between animals across the five different PBAE NP formulations is reduced, as a complete set of five NP formulations is evaluated in a single mouse and thus different NPs are being evaluated in the same animals instead of in unique animals. Furthermore, just as automation adds efficiency to high throughput, this *in vivo* screening approach could be adapted for additional NP types per animal and further efficiency on the analysis side obtained by using automated pipettors and high-throughput 384-well qPCR.

Several methods for high-throughput *in vivo* screening using nucleic acid barcodes have been recently reported. Dahlman *et al.* used deep sequencing methods to simultaneously characterize biodistribution of dozens of lipid NPs harboring barcoded oligonucleotides[32,33]. This innovative approach highlights the power of barcoding methods to impact the field of drug and gene delivery. While oligonucleotide barcodes offer flexibility and versatility due to their small size, they are used as a passive tag to measure biodistribution rather than functional delivery. We chose to incorporate DNA barcodes in plasmid vectors to assess biodistribution (extracellular barriers) and transfection (intracellular barriers) in target tissues using the same barcodes. Because properties of NPs may be affected by the properties of their cargo depending on the NP system, including potentially by adding a noncoding nucleic acid barcode tag or conjugating labeling molecules to the nucleic acid cargo, the presented strategy also allows us to evaluate NPs specifically formulated for delivery of their standard pDNA cargo without an additional labeled component. We show that directly measuring transfection is critical, as biodistribution results did not accurately predict *in vivo* transfection. Particles that accumulate in tissues may become entrapped in mucosal or extracellular matrix barriers[42], sequestered in vesicles[43], or exocytosed into the interstitial space[44]. Successful gene therapy is dependent on overcoming all extracellular and intracellular barriers, ultimately resulting in the transcription and translation of a therapeutic protein.

The type of genetic cargo, including DNA, mRNA, siRNA, and short oligonucleotide, can interact with the vectors differently and affect the NP's physicochemical properties as well as biodistribution profile. For example, Guimaraes *et al.* showed that NPs with the same lipid but either mRNA or DNA oligonucleotide exhibited different levels of accumulation in liver and spleen[34]. We simplified NP's nucleic acid cargo to a single plasmid vector harboring both the

barcode and a functional gene, eliminating the need for a secondary barcode oligonucleotide and the possibility of its differential molecular interaction with various vectors. This strategy also allows broad utilization of the technology with other NP formulations. Moreover, our study shows that randomly generated nucleotide sequences can function well as barcodes, which indicates that many NPs with similar random barcodes can be evaluated simultaneously as a larger NP cocktail within a single animal. Increased number of barcodes would increase the utility of the high-throughput screening strategy. In contrast to prior work, our system uses qPCR for barcode quantification, which is routinely used with well-established analysis methods. Therefore, this strategy is easily adaptable to different NP systems and laboratories to characterize gene delivery.

Quantifying transfection at the cellular level would add further value to this approach for gene therapy development. To achieve this degree of granularity, cell types of interest could be sorted using immunocytochemistry and flow cytometry or other single cell methodologies, then barcode accumulation and transfection could be quantified in the population of interest. This would enable identification of NPs that target individual cancer cells within a heterogeneous population, specific immune cells, and other phenotypes affected by genetic disease.

Our reported biodistribution results from high-throughput barcode NP screening agree with the current understanding of NP pharmacokinetics, which has been extensively reported in the literature[45,46]. Particles with diameter < ~10 nm are rapidly cleared by the renal system and accumulate in the kidneys, bladder, and urine[47]. NPs larger than ~20 nm are cleared by the MPS in the liver and spleen[48]. Our characterization of PBAE NPs by DLS sizing confirms that all PBAE NPs tested are between 100 and 200 nm, suggesting that MPS clearance would dominate their pharmacokinetics. In agreement with these principles, we found by high throughput barcode

screening that PBAE NPs accumulate in the liver and spleen at 30 min post administration. Biodistribution was evaluated at 30 min post administration due to short half-life (10 min) of PBAE NPs in the blood[49] and potential DNA degradation, while *in vivo* transfection was quantified at 6 hours based on similar methods reported by previous literature on luciferase gene expression using PBAE NPs[24,50]. Interestingly, we also observed barcode accumulation in the kidneys, despite the average NP size being far above the maximum for renal clearance. Because transfection in the kidney was negligible, we hypothesize that barcode DNA accumulating in the kidney was unencapsulated DNA or very small, degraded NP fragments. We also observed consistent NP accumulation in the lung. NP entrapment in the lung capillaries has been observed and well-characterized in the literature[1]. Aside from NP size, aggregation with serum proteins may also play a role in lung accumulation, so the effects of PBAE NP physicochemical properties on protein adsorption should be further studied in future work[51]. Across the PBAE NPs evaluated in this study, while we found lung accumulation, we found that these entrapped NPs were not successful for gene delivery, potentially due to cell-specific transfection efficacy often demonstrated with PBAE polymers[20,23,24]. Success for gene delivery depended on polymer structure, with small, seemingly insignificant changes to structure of one or two carbons, making a significant difference to gene therapy performance, from tissue-specific accumulation to cell-specific transfection. This proof-of-concept study demonstrates that there is much to be learned by extending higher throughput nanobiotechnology studies from *in vitro* to *in vivo*, to better understand differential nanomaterial function in biological systems.

2.5 Conclusion

With gene therapy emerging as a viable and versatile approach to treat or potentially cure various diseases, optimizing non-viral delivery vectors has become an active area of research. In

this study, we explored the role of a polymer's chemical structure to direct tissue-specific nanoparticle targeting and gene transfection. To this end, we also successfully developed an innovative high-throughput method using pDNA itself as a barcode that consequently reduces the number of animals used and mitigates variability between animals. Using the method, we demonstrated certain PBAE polymeric nanoparticles are capable of delivering and transfecting pDNA in the liver and/or spleen. We also showed that tissue accumulation of PBAE NPs does not necessarily correlate with *in vivo* gene expression, emphasizing the importance of *in vivo* transfection screening to predict the therapeutic efficacy of gene therapy. Both polymer structure and tissue type were important to determine transfection efficiency. Finally, we validated the high-throughput screening method by showing correlation between its mRNA result and *in vivo* protein expression of the firefly luciferase reporter gene using the same PBAE NPs.

2.6 References

1. Blanco, E, Shen, H and Ferrari, M (2015). Principles of nanoparticle design for overcoming biological barriers to drug delivery. *Nat. Biotechnol.* **33**: 941.

2. Jones, CH, Chen, C-K, Ravikrishnan, A, Rane, S and Pfeifer, BA (2013). Overcoming nonviral gene delivery barriers: perspective and future. *Mol. Pharm.* **10**: 4082–4098.

3. Wiethoff, CM and Middaugh, CR (2003). Barriers to nonviral gene delivery. *J. Pharm. Sci.* **92**: 203–217.

4. Karlsson, J, Rhodes, KR, Green, JJ and Tzeng, SY (2020). Poly (beta-amino ester) s as gene delivery vehicles: challenges and opportunities. *Expert Opin. Drug Deliv.* **17**: 1395–1410.

5. Yin, H, Kanasty, RL, Eltoukhy, AA, Vegas, AJ, Dorkin, JR and Anderson, DG (2014). Non-viral vectors for gene-based therapy. *Nat. Rev. Genet.* **15**: 541–555.

6. Thomas, CE, Ehrhardt, A and Kay, MA (2003). Progress and problems with the use of viral vectors for gene therapy. *Nat. Rev. Genet.* **4**: 346–358.

7. Sharon, D and Kamen, A (2018). Advancements in the design and scalable production of viral gene transfer vectors. *Biotechnol. Bioeng.* **115**: 25–40.

8. Kim, J, Sunshine, JC and Green, JJ (2014). Differential polymer structure tunes mechanism of cellular uptake and transfection routes of poly (β-amino ester) polyplexes in human breast cancer cells. *Bioconjug. Chem.* **25**: 43–51.

9. Routkevitch, D, Sudhakar, D, Conge, M, Varanasi, M, Tzeng, SY, Wilson, DR, *et al.* (2020). Efficiency of Cytosolic Delivery with Poly(β-amino ester) Nanoparticles is

Dependent on the Effective pKa of the Polymer. *ACS Biomater. Sci. Eng.* **6**: 3411–3421.

10. Sunshine, JC, Peng, DY and Green, JJ (2012). Uptake and transfection with polymeric nanoparticles are dependent on polymer end-group structure, but largely independent of nanoparticle physical and chemical properties. *Mol. Pharm.* **9**: 3375–3383.

11. Muhammad, K, Zhao, J, Ullah, I, Guo, J, Ren, X and Feng, Y (2020). Ligand targeting and peptide functionalized polymers as non-viral carriers for gene therapy. *Biomater. Sci.* **8**: 64–83.

12. Hatakeyama, H, Akita, H and Harashima, H (2013). The polyethyleneglycol dilemma: advantage and disadvantage of PEGylation of liposomes for systemic genes and nucleic acids delivery to tumors. *Biol. Pharm. Bull.* **36**: 892–899.

13. Khalil, IA, Sato, Y and Harashima, H (2019). Recent advances in the targeting of systemically administered non-viral gene delivery systems. *Expert Opin. Drug Deliv.* **16**: 1037–1050.

14. Zhu, D, Yan, H, Zhou, Z, Tang, J, Liu, X, Hartmann, R, *et al.* (2018). Detailed investigation on how the protein corona modulates the physicochemical properties and gene delivery of polyethylenimine (PEI) polyplexes. *Biomater. Sci.* **6**: 1800–1817.

15. Akinc, A, Zumbuehl, A, Goldberg, M, Leshchiner, ES, Busini, V, Hossain, N, *et al.* (2008). A combinatorial library of lipid-like materials for delivery of RNAi therapeutics. *Nat. Biotechnol.* **26**: 561–569.

16. Chen, DJ, Majors, BS, Zelikin, A and Putnam, D (2005). Structure–function relationships of gene delivery vectors in a limited polycation library. *J. Control. release* **103**: 273–283.

17. Hao, J, Kos, P, Zhou, K, Miller, JB, Xue, L, Yan, Y, *et al.* (2015). Rapid synthesis of a lipocationic polyester library via ring-opening polymerization of functional valerolactones for efficacious siRNA delivery. *J. Am. Chem. Soc.* **137**: 9206–9209.

18. Sun, S, Wang, M, Knupp, SA, Soto-Feliciano, Y, Hu, X, Kaplan, DL, *et al.* (2012). Combinatorial library of lipidoids for in vitro DNA delivery. *Bioconjug. Chem.* **23**: 135–140.

19. Green, JJ, Langer, R and Anderson, DG (2008). A combinatorial polymer library approach yields insight into nonviral gene delivery. *Acc. Chem. Res.* **41**: 749–759.

20. Guerrero-Cázares, H, Tzeng, SY, Young, NP, Abutaleb, AO, Quiñones-Hinojosa, A and Green, JJ (2014). Biodegradable Polymeric Nanoparticles Show High Efficacy and Specificity at DNA Delivery to Human Glioblastoma in Vitro and in Vivo. *ACS Nano* **8**: 5141–5153.

21. Kim, J, Kang, Y, Tzeng, SY and Green, JJ (2016). Synthesis and application of poly(ethylene glycol)-co-poly(β-amino ester) copolymers for small cell lung cancer gene therapy. *Acta Biomater.* **41**: 293–301.

22. Mangraviti, A, Tzeng, SY, Gullotti, D, Kozielski, KL, Kim, JE, Seng, M, *et al.* (2016). Non-virally engineered human adipose mesenchymal stem cells produce BMP4, target brain tumors, and extend survival. *Biomaterials* **100**: 53–66.

23. Shmueli, RB, Sunshine, JC, Xu, Z, Duh, EJ and Green, JJ (2012). Gene delivery nanoparticles specific for human microvasculature and macrovasculature. *Nanomedicine Nanotechnology, Biol. Med.* **8**: 1200–1207.

24. Zamboni, CG, Kozielski, KL, Vaughan, HJ, Nakata, MM, Kim, J, Higgins, LJ, *et al.* (2017). Polymeric nanoparticles as cancer-specific DNA delivery vectors to human hepatocellular carcinoma. *J. Control. Release* **263**: 18–28.

25. Shen, J, Kim, J, Tzeng, SY, Ding, K, Hafiz, Z, Long, D, *et al.* (2020). Suprachoroidal gene transfer with nonviral nanoparticles. *Sci. Adv.* **6**: eaba1606.

26. Bishop, CJ, Abubaker-Sharif, B, Guiriba, T, Tzeng, SY and Green, JJ (2015). Gene delivery polymer structure-function relationships elucidated via principal component analysis. *Chem. Commun. (Camb).* **51**: 12134–12137.

27. Bishop, CJ, Ketola, T-M, Tzeng, SY, Sunshine, JC, Urtti, A, Lemmetyinen, H, *et al.* (2013). The Effect and Role of Carbon Atoms in Poly(β-amino ester)s for DNA Binding and Gene Delivery. *J. Am. Chem. Soc.* **135**: 6951–6957.

28. Fields, RJ, Cheng, CJ, Quijano, E, Weller, C, Kristofik, N, Duong, N, *et al.* (2012). Surface modified poly (β amino ester)-containing nanoparticles for plasmid DNA delivery. *J. Control. release* **164**: 41–48.

29. Jones, CH, Chen, M, Ravikrishnan, A, Reddinger, R, Zhang, G, Hakansson, AP, *et al.* (2015). Mannosylated poly (beta-amino esters) for targeted antigen presenting cell immune modulation. *Biomaterials* **37**: 333–344.

30. Liu, S, Gao, Y, Zhou, D, Greiser, U, Guo, T, Guo, R, *et al.* (2017). Biodegradable highly branched poly (β-amino ester) s for targeted cancer cell gene transfection. *ACS Biomater. Sci. Eng.* **3**: 1283–1286.

31. Kim, J, Mondal, SK, Tzeng, SY, Rui, Y, Alkharboosh, R, Kozielski, KK, *et al.* (2020).

Poly (ethylene glycol)-poly (beta-amino ester)-based nanoparticles for suicide gene therapy enhance brain penetration and extend survival in a preclinical human glioblastoma orthotopic xenograft model. *ACS Biomater. Sci. Eng.*

32. Dahlman, JE, Kauffman, KJ, Xing, Y, Shaw, TE, Mir, FF, Dlott, CC, *et al.* (2017). Barcoded nanoparticles for high throughput in vivo discovery of targeted therapeutics. *Proc. Natl. Acad. Sci.* **114**: 2060–2065.

33. Sago, CD, Lokugamage, MP, Paunovska, K, Vanover, DA, Monaco, CM, Shah, NN, *et al.* (2018). High-throughput in vivo screen of functional mRNA delivery identifies nanoparticles for endothelial cell gene editing. *Proc. Natl. Acad. Sci.* **115**: E9944–E9952.

34. Guimaraes, PPG, Zhang, R, Spektor, R, Tan, M, Chung, A, Billingsley, MM, *et al.* (2019). Ionizable lipid nanoparticles encapsulating barcoded mRNA for accelerated in vivo delivery screening. *J. Control. Release* **316**: 404–417.

35. Wilson, DR, Mosenia, A, Suprenant, MP, Upadhya, R, Routkevitch, D, Meyer, RA, *et al.* (2017). Continuous microfluidic assembly of biodegradable poly (beta-amino ester)/DNA nanoparticles for enhanced gene delivery. *J. Biomed. Mater. Res. Part A* **105**: 1813–1825.

36. Schmittgen, TD and Livak, KJ (2008). Analyzing real-time PCR data by the comparative C T method. *Nat. Protoc.* **3**: 1101.

37. Bhise, NS, Shmueli, RB, Gonzalez, J and Green, JJ (2012). A novel assay for quantifying the number of plasmids encapsulated by polymer nanoparticles. *Small* **8**: 367–373.

38. Li, L, Zahner, D, Su, Y, Gruen, C, Davidson, G and Levkin, PA (2012). A biomimetic lipid library for gene delivery through thiol-yne click chemistry. *Biomaterials* **33**: 8160–

8166.

39. Rui, Y, Wilson, DR, Sanders, K and Green, JJ (2019). Reducible branched ester-amine quadpolymers (rBEAQs) codelivering plasmid DNA and RNA oligonucleotides enable CRISPR/Cas9 genome editing. *ACS Appl. Mater. Interfaces* **11**: 10472–10480.

40. Burke, RS and Pun, SH (2008). Extracellular barriers to in vivo PEI and PEGylated PEI polyplex-mediated gene delivery to the liver. *Bioconjug. Chem.* **19**: 693–704.

41. Whitehead, KA, Matthews, J, Chang, PH, Niroui, F, Dorkin, JR, Severgnini, M, *et al.* (2012). In Vitro–In Vivo Translation of Lipid Nanoparticles for Hepatocellular siRNA Delivery. *ACS Nano* **6**: 6922–6929.

42. Ruponen, M, Honkakoski, P, Rönkkö, S, Pelkonen, J, Tammi, M and Urtti, A (2003). Extracellular and intracellular barriers in non-viral gene delivery. *J. Control. release* **93**: 213–217.

43. Douglas, KL, Piccirillo, CA and Tabrizian, M (2008). Cell line-dependent internalization pathways and intracellular trafficking determine transfection efficiency of nanoparticle vectors. *Eur. J. Pharm. Biopharm.* **68**: 676–687.

44. Jiang, X, Rocker, C, Hafner, M, Brandholt, S, Dorlich, RM and Nienhaus, GU (2010). Endo-and exocytosis of zwitterionic quantum dot nanoparticles by live HeLa cells. *ACS Nano* **4**: 6787–6797.

45. Alexis, F, Pridgen, E, Molnar, LK and Farokhzad, OC (2008). Factors affecting the clearance and biodistribution of polymeric nanoparticles. *Mol. Pharm.* **5**: 505–515.

46. Moghimi, SM, Hunter, AC and Murray, JC (2001). Long-Circulating and Target-Specific

Nanoparticles: Theory to Practice. *Pharmacol. Rev.* **53**: 283 LP – 318.

47. Soo Choi, H, Liu, W, Misra, P, Tanaka, E, Zimmer, JP, Itty Ipe, B, *et al.* (2007). Renal clearance of quantum dots. *Nat. Biotechnol.* **25**: 1165–1170.

48. Gustafson, HH, Holt-Casper, D, Grainger, DW and Ghandehari, H (2015). Nanoparticle uptake: The phagocyte problem. *Nano Today* **10**: 487–510.

49. Karlsson, J, Rui, Y, Kozielski, KL, Placone, AL, Choi, O, Tzeng, SY, *et al.* (2019). Engineered nanoparticles for systemic siRNA delivery to malignant brain tumours. *Nanoscale* **11**: 20045–20057.

50. Kaczmarek, JC, Patel, AK, Kauffman, KJ, Fenton, OS, Webber, MJ, Heartlein, MW, *et al.* (2016). Polymer–lipid nanoparticles for systemic delivery of mRNA to the lungs. *Angew. Chemie* **128**: 14012–14016.

51. Shenoy, D, Little, S, Langer, R and Amiji, M (2005). Poly (ethylene oxide)-modified poly (β-amino ester) nanoparticles as a pH-sensitive system for tumor-targeted delivery of hydrophobic drugs: part 2. In vivo distribution and tumor localization studies. *Pharm. Res.* **22**: 2107–2114.

2.7 Figures and Tables

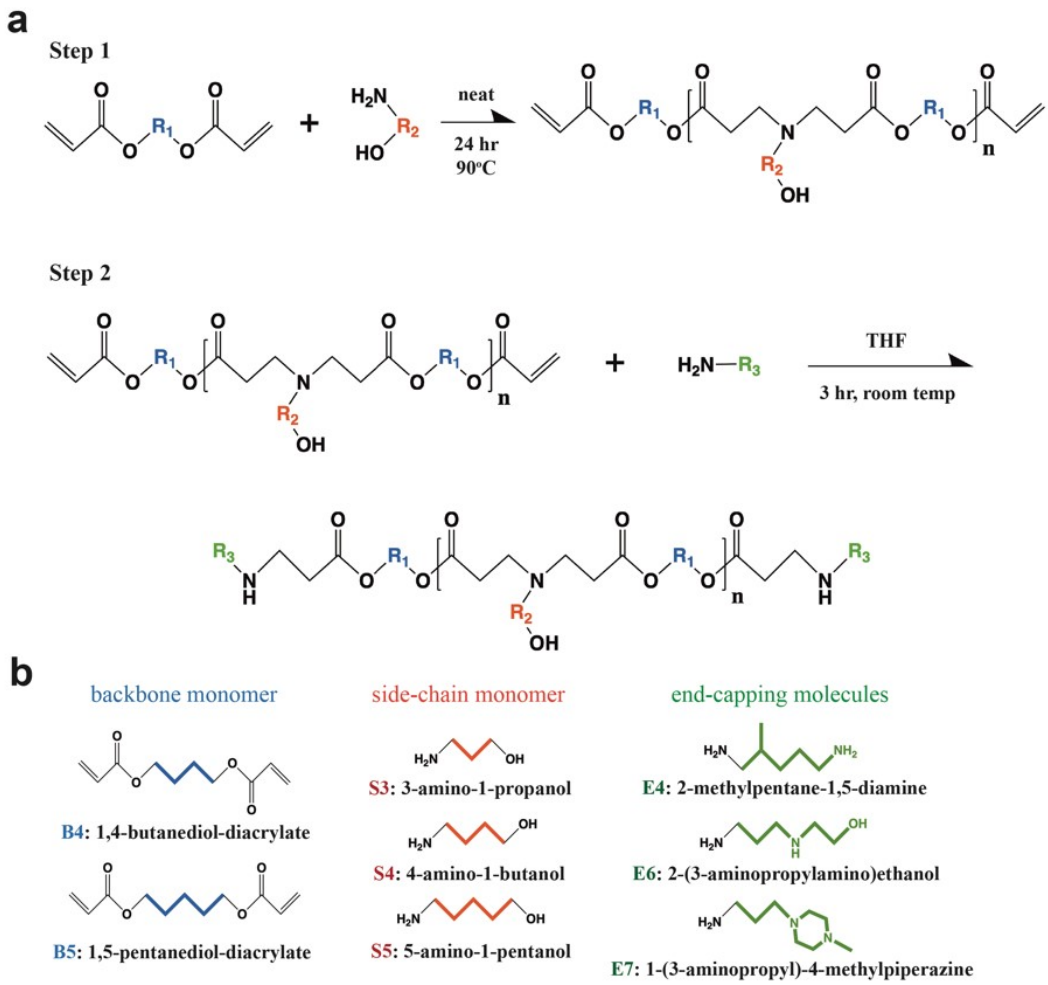

Figure 2.1 PBAE polymer synthesis. (a) PBAE polymer was synthesized using a two-step Michael addition reaction. Acrylate-terminated PBAE base polymer, synthesized by reacting a diacrylate monomer with a primary amine-containing alkanolamine monomer in the first step, is end-capped during the second step with a primary amine-containing molecule. (b) Monomers used in the synthesis of 8 different PBAE polymers.

a

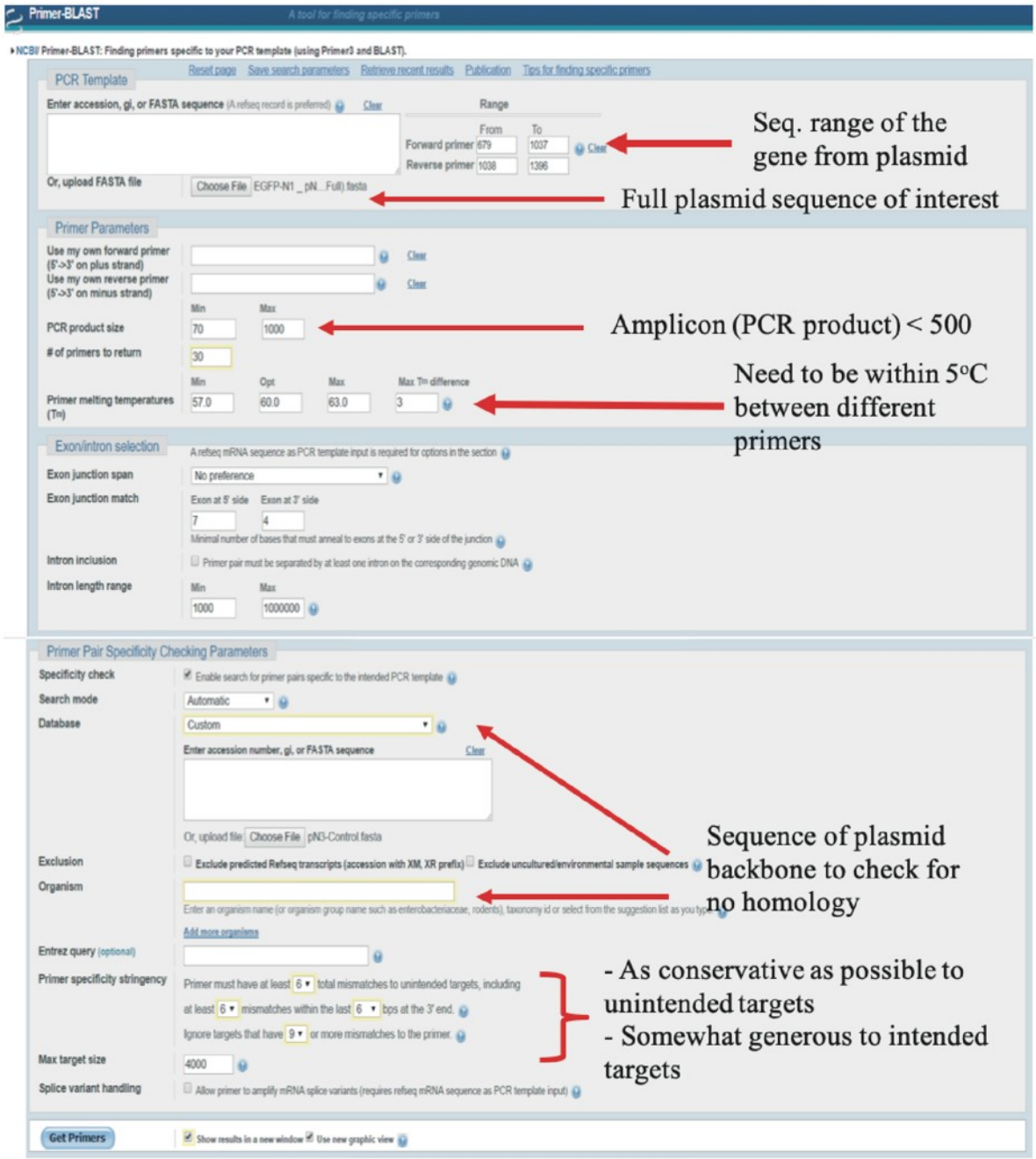
Primer-BLAST
A tool for finding specific primers
NCBI Primer-BLAST: Finding primers specific to your PCR template (using Primer3 and BLAST).
Reset page
Save search parameters
Retrieve recent results
Publication
Tips for finding specific primers
PCR Template
Enter accession, gi, or FASTA sequence (A refseq record is preferred)
Clear
Range
From
To
Forward primer 679 1037
Reverse primer 1038 1396
Seq. range of the gene from plasmid
Or, upload FASTA file
Choose File EGFP-N1 _ pN...Full).fasta
Full plasmid sequence of interest
Primer Parameters
Use my own forward primer (5'->3' on plus strand)
Use my own reverse primer (5'->3' on minus strand)
PCR product size 70 1000
Amplicon (PCR product) < 500
# of primers to return 30
Min Opt Max Max Tm difference
Primer melting temperatures (Tm) 57.0 60.0 63.0 3
Need to be within 5°C between different primers
Exon/intron selection
A refseq mRNA sequence as PCR template input is required for options in the section
Exon junction span No preference
Exon junction match Exon at 5' side 7 Exon at 3' side 4
Minimal number of bases that must anneal to exons at the 5' or 3' side of the junction
Intron inclusion
Primer pair must be separated by at least one intron on the corresponding genomic DNA
Intron length range Min 1000 Max 1000000
Primer Pair Specificity Checking Parameters
Specificity check
Enable search for primer pairs specific to the intended PCR template
Search mode Automatic
Database Custom
Enter accession number, gi, or FASTA sequence
Clear
Or, upload file Choose File pN3-Control.fasta
Sequence of plasmid backbone to check for no homology
Exclusion
Exclude predicted Refseq transcripts (accession with XM, XR prefix)
Exclude uncultured/environmental sample sequences
Organism
Enter an organism name (or organism group name such as enterobacteriaceae, rodents), taxonomy id or select from the suggestion list as you type
Add more organisms
Entrez query (optional)
Primer specificity stringency
Primer must have at least 6 total mismatches to unintended targets, including
at least 6 mismatches within the last 6 bps at the 3' end.
Ignore targets that have 9 or more mismatches to the primer.
- As conservative as possible to unintended targets
- Somewhat generous to intended targets
Max target size 4000
Splice variant handling
Allow primer to amplify mRNA splice variants (requires refseq mRNA sequence as PCR template input)
Get Primers
Show results in a new window
Use new graphic view

b

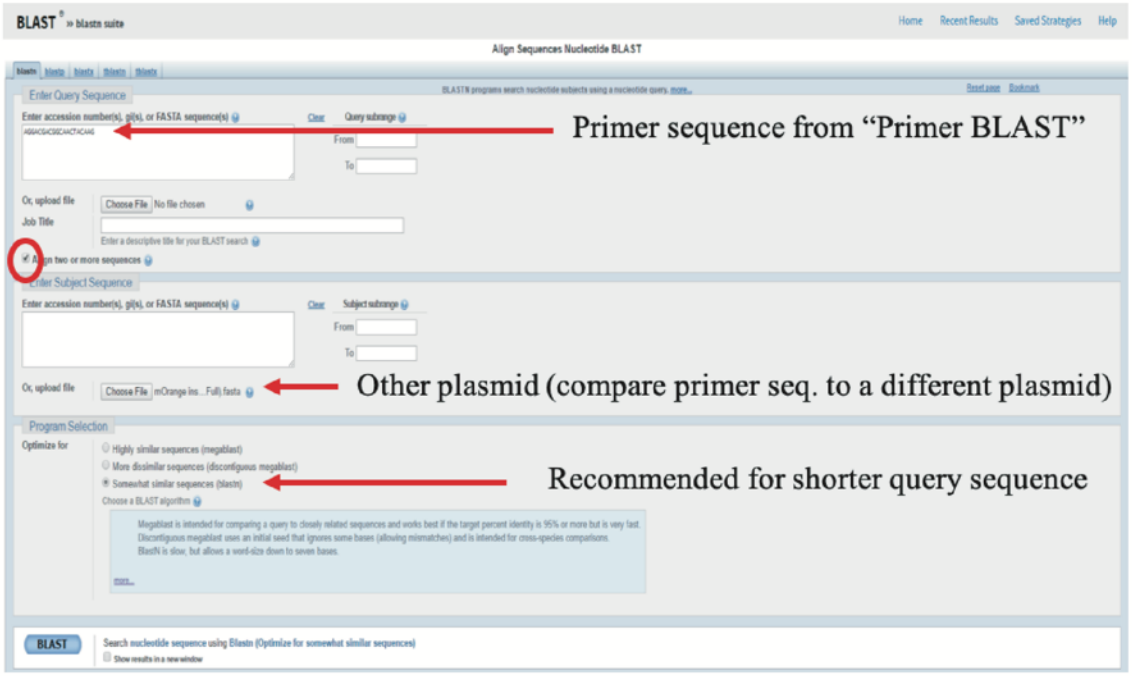
BLAST » blastn suite
Home
Recent Results
Saved Strategies
Help
Align Sequences Nucleotide BLAST
Enter Query Sequence
Primer sequence from "Primer BLAST"
Enter Subject Sequence
Other plasmid (compare primer seq. to a different plasmid)
Program Selection
Recommended for shorter query sequence
BLAST

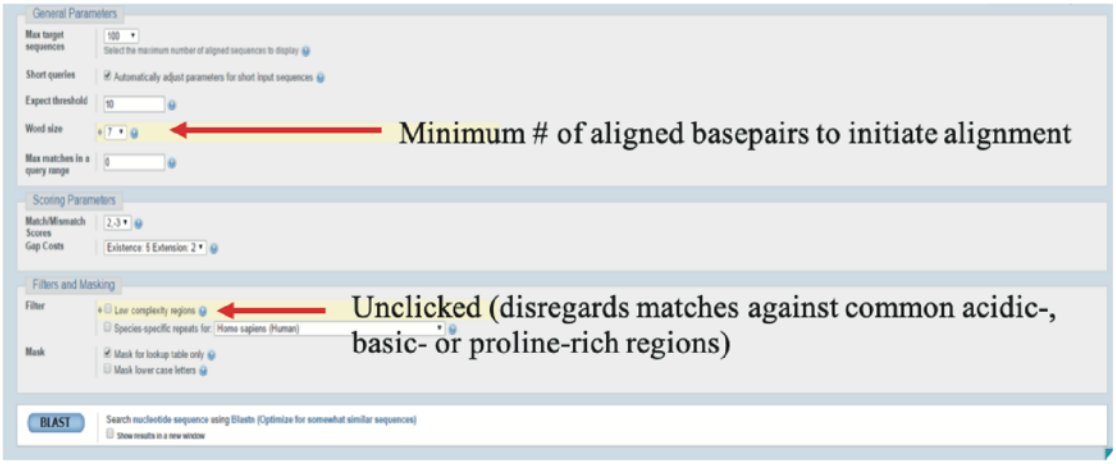
General Parameters
Minimum # of aligned basepairs to initiate alignment
Scoring Parameters
Filters and Masking
Unclicked (disregards matches against common acidic-, basic- or proline-rich regions)
BLAST

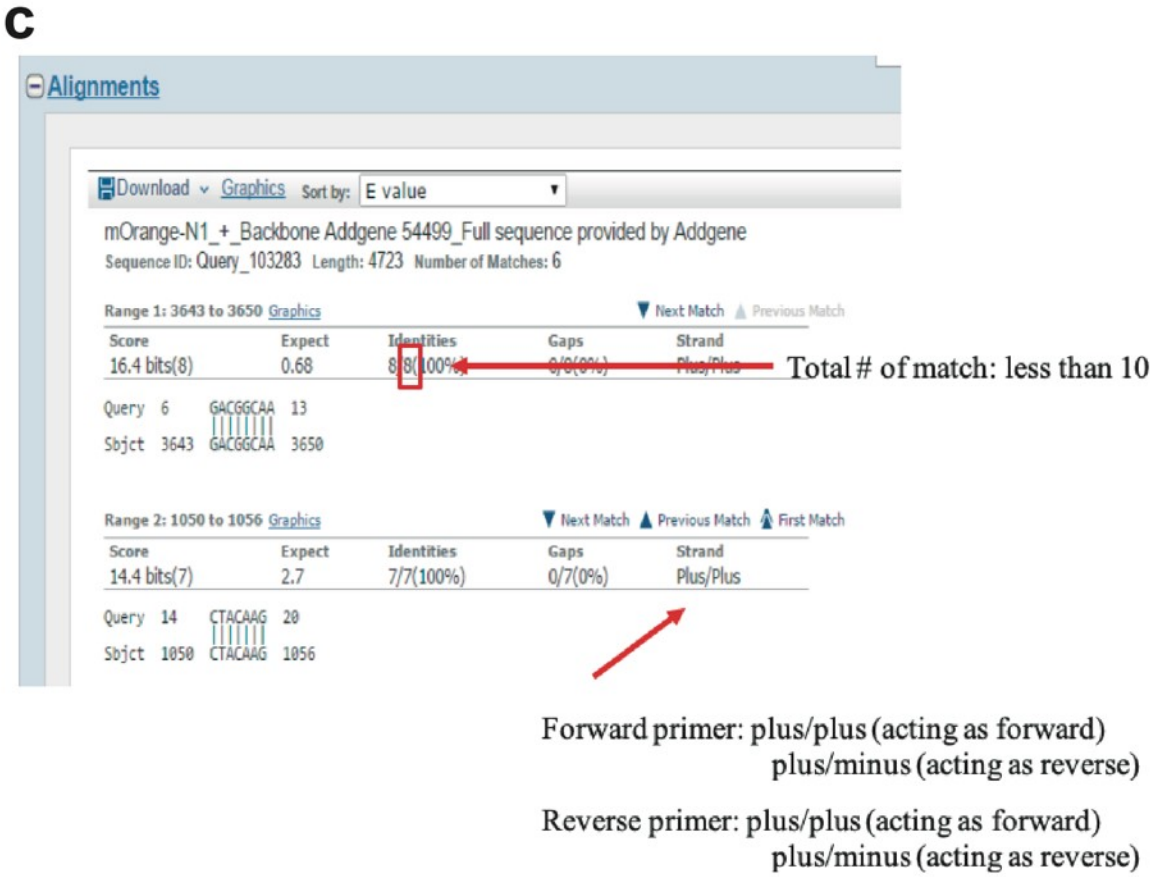

Figure 2.2 Primer design with BLAST (A) Generating forward and reverse primer candidates through Primer-BLAST based on minimizing homology against the plasmid backbone, restricting the amplicon size, and ensuring a window of melting temperature. (B) Checking specificity of primer candidate for a plasmid through BLASTn by comparing its homology against sequences of other barcoded plasmids. (C) Criteria for selecting the optimal primers from BLAST results.

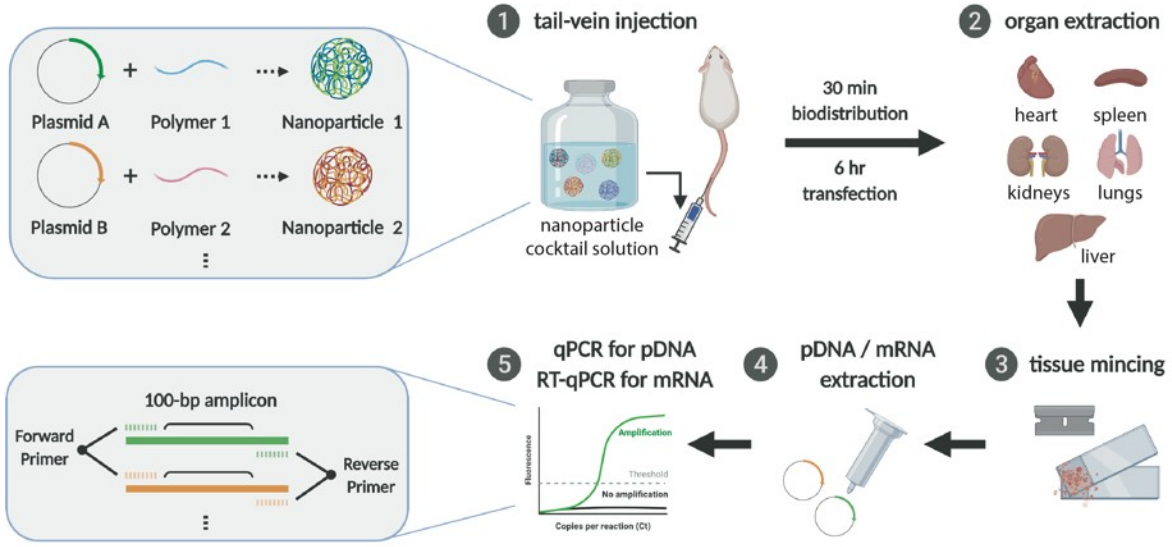

Figure 2.3 High-throughput screening of PBAE NP biodistribution and transfection via qPCR and RT-qPCR.

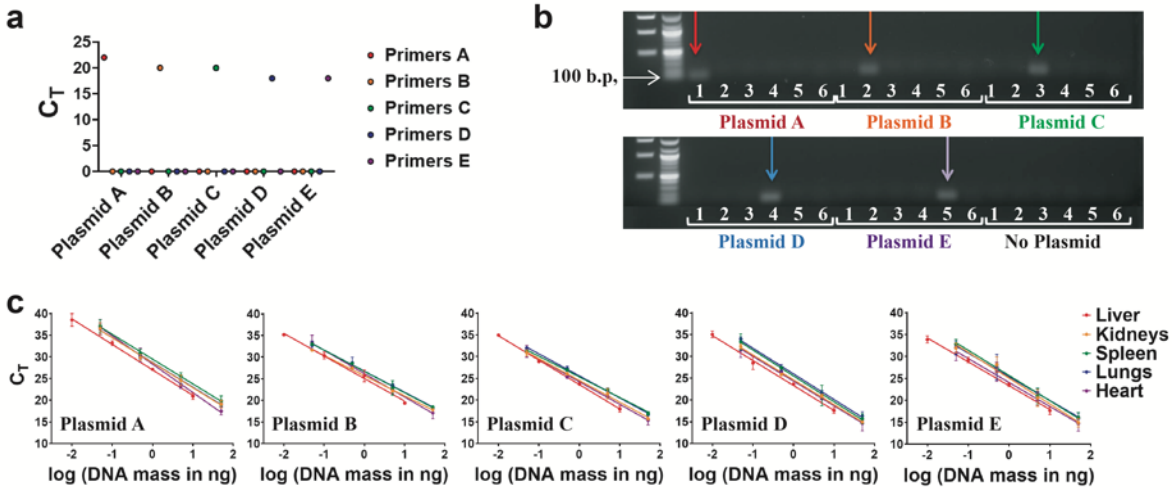

Figure 2.4 Primer optimization. (a) CT values from qPCR reaction of all possible combinations of 5 plasmids and 5 corresponding primers (n=3, mean ± SEM). (b) Gel electrophoresis of PCR-amplified product, showing specific amplicons' size of approximately 100 base-pairs. For each plasmid, there are 6 conditions with specific primers for pDNA A, B, C, D, E, or no primers going from left to right, as indicated by the index numbers 1-6, respectively. DNA ladder: 1 kbp left and 100 bp right. (c) CT values from qPCR reaction of tissue lysates from major organs spiked with known concentrations of 5 barcoded plasmid DNAs (n = 4, mean ± SEM)

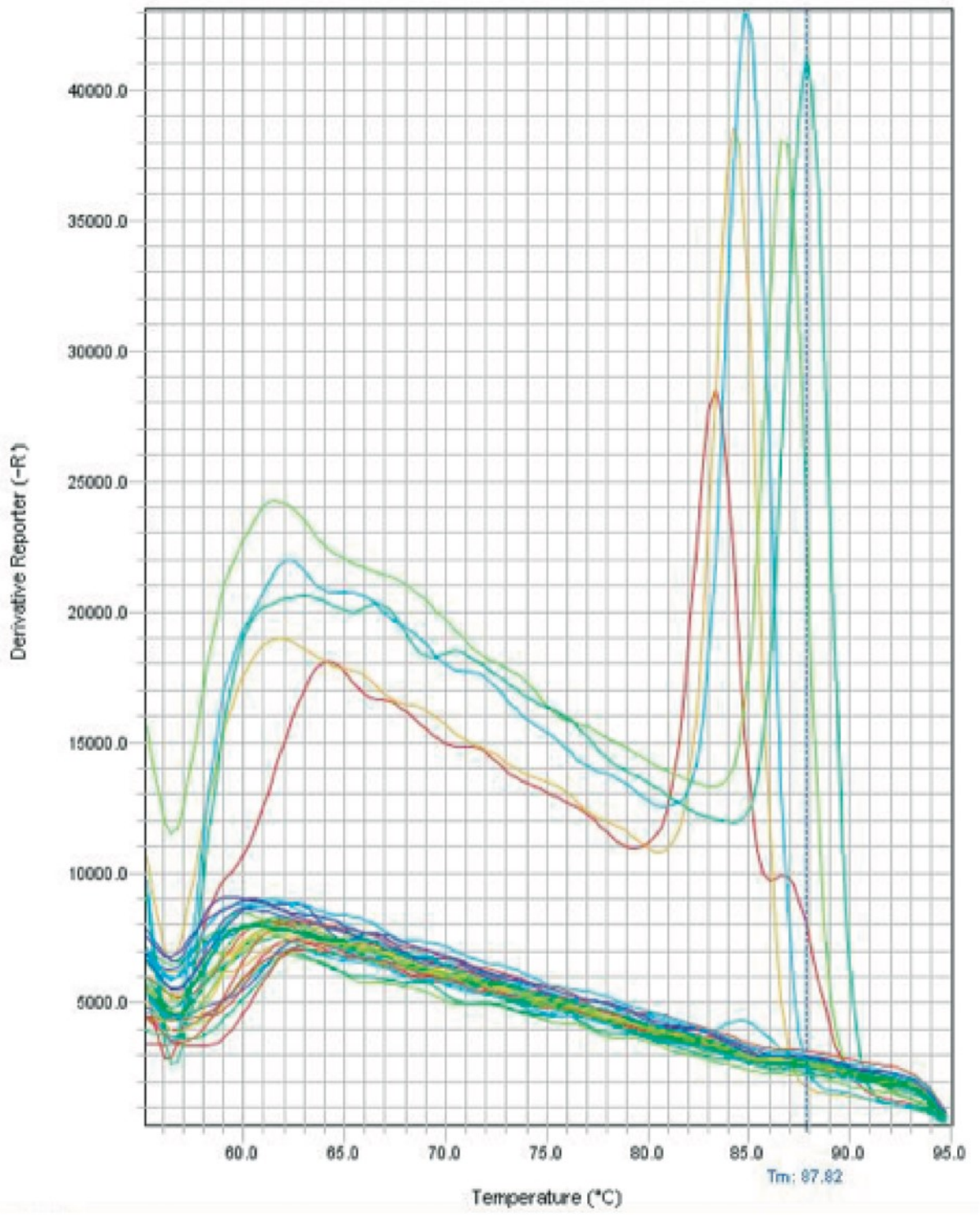

Figure 2.5 Melt curve from qPCR of barcode plasmids and primers. Single-peak melt curve for the qPCR conditions with matching barcode plasmid and primers (red: plasmid A, yellow:

plasmid B, cyan: plasmid C, dark green: plasmid D, light green: plasmid E) confirms specificity of the primers.

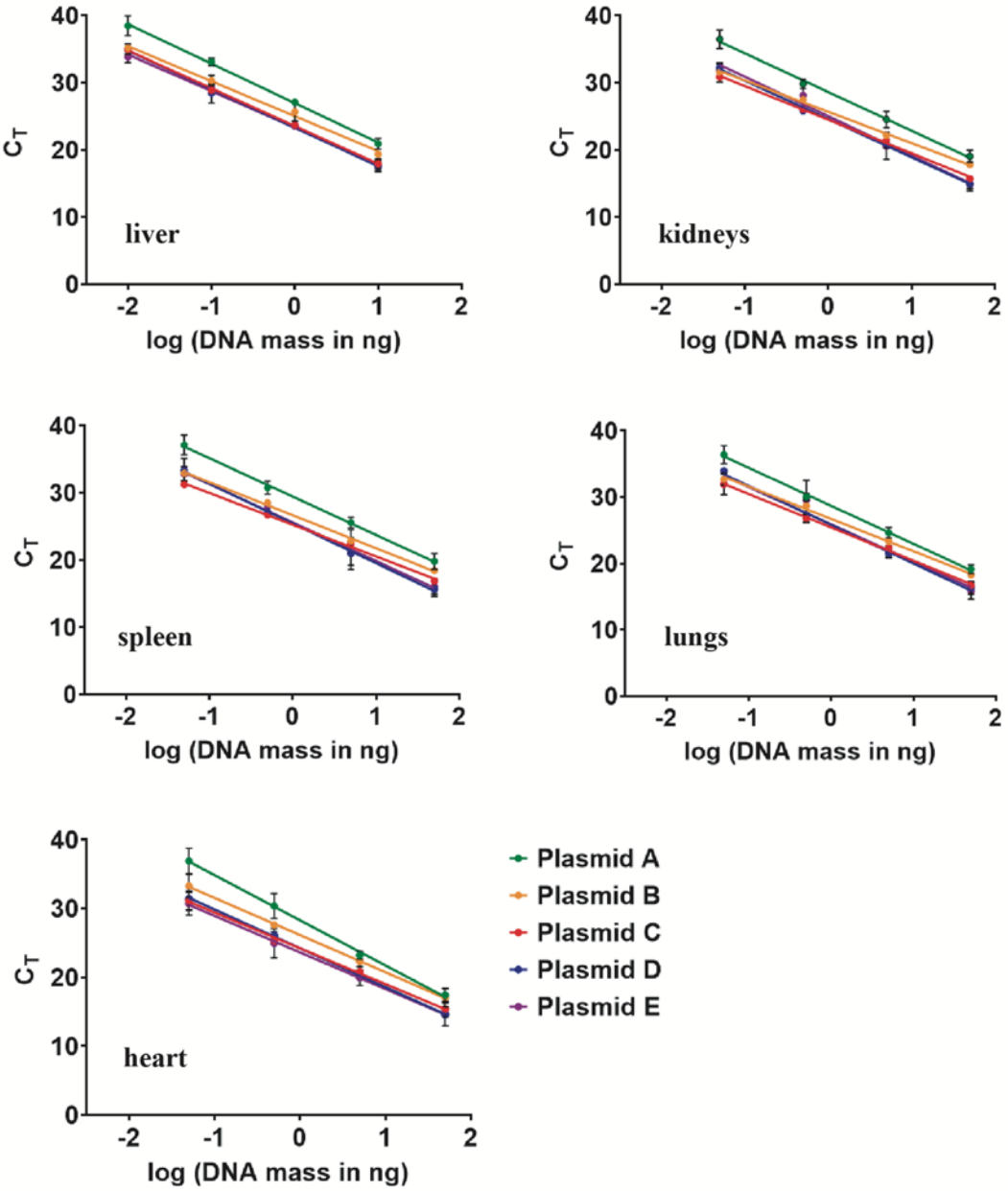

Figure 2.6 Primer Standard Curves C_T values from qPCR reaction of tissue lysates from major organs spiked with known concentrations of 5 barcoded plasmid DNAs (n = 4, mean ± SD).

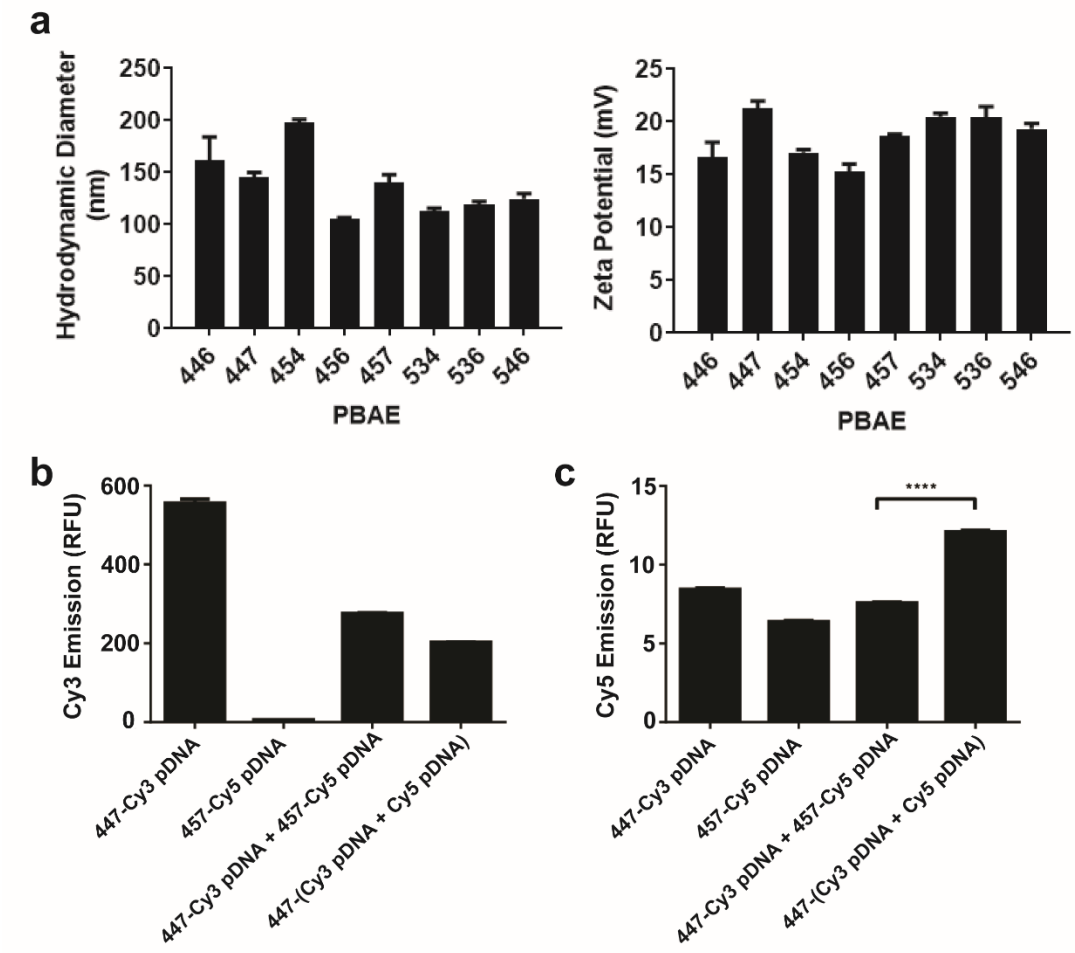

Figure 2.7. PBAE NP properties. (a) Hydrodynamic diameter and zeta potential of 8 PBAE NPs, measured by dynamic light scattering (n = 3, mean ± SEM). (b) Cy3 and (c) Cy5 emission following Cy3 excitation of a solution consisting of either 447 PBAE NP with Cy3-labeled pDNA, 457 PBAE NP with Cy5-labeled pDNA, 447 PBAE NP with a mixture of Cy3- and Cy5-labeled pDNAs, or a mixture of 447 PBAE NP with Cy3-labeled pDNA and 457 PBAE NP with Cy5-labeled pDNA (left to right).

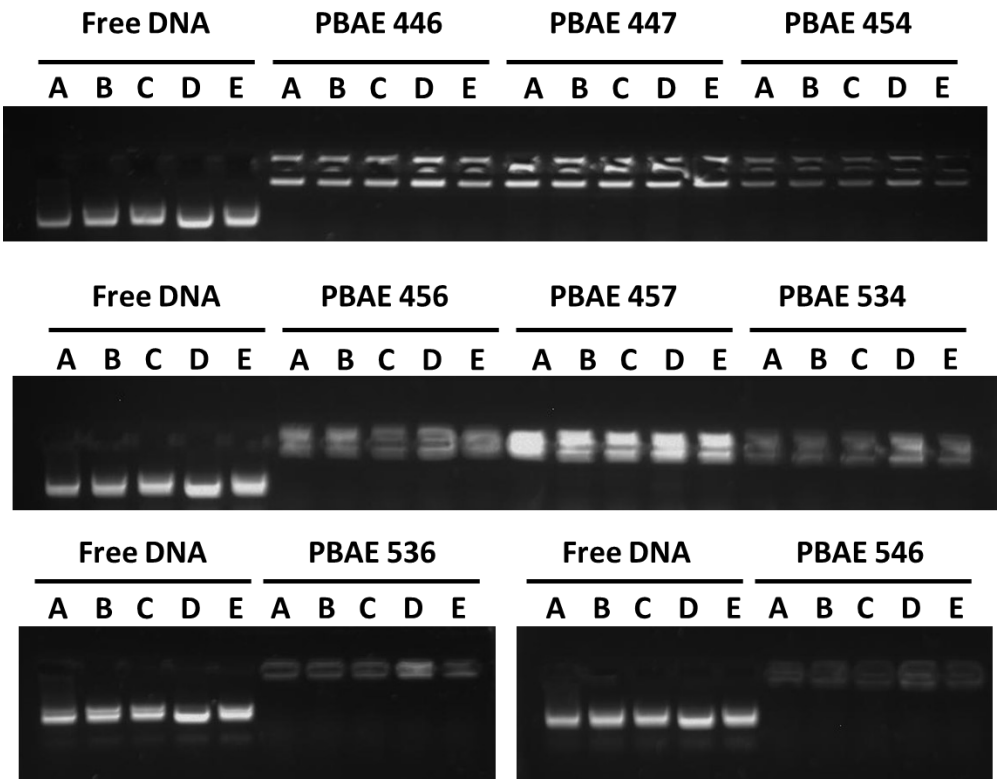

Figure 2.8. Gel electrophoresis of 8 PBAE NPs. Gel electrophoresis of NPs formulated with barcoded plasmids A-E with a final concentration of 0.03 mg/mL pDNA and 25 w/w ratio of PBAE polymer. Free unencapsulated plasmid DNA at the same dose was used as a positive control. All NP formulations showed 100% encapsulation for all barcode pDNA sequences.

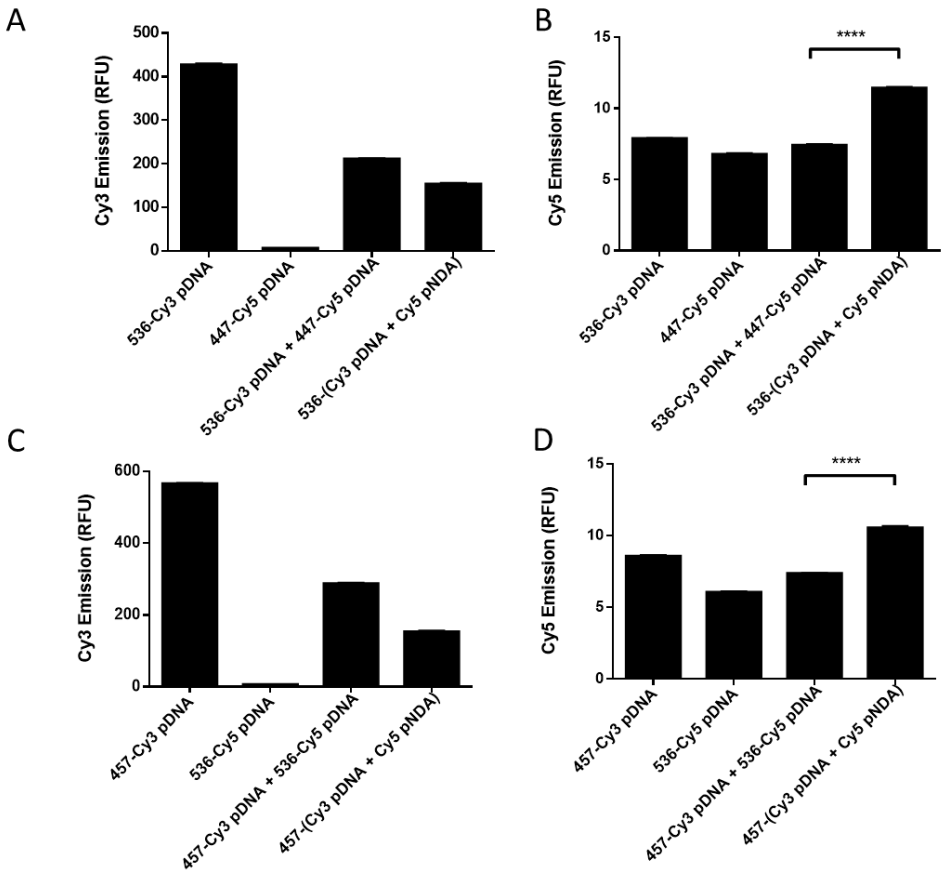

Figure 2.9. FRET analysis of a mixture of barcoded NPs. Cy3 (A) and Cy5 (B) emission of PBAE 536 NPs with Cy3 pDNA, PBAE 447 NPs with Cy5 pDNA alone, the mixture of these two NPs, and a positive control PBAE 536 NP formulated with equivalent concentrations of Cy3 and Cy5 pDNA. Emissions from PBAE 457 and PBAE 536 NPs are also shown (C, D). Data is shown as mean ± SEM from 3 replicates. Significant differences in Cy5 emission between mixed NPs and NPs formulated with both pDNAs were determined by one-way ANOVA and Sidak's multiple comparisons test. ****$P < 0.0001$

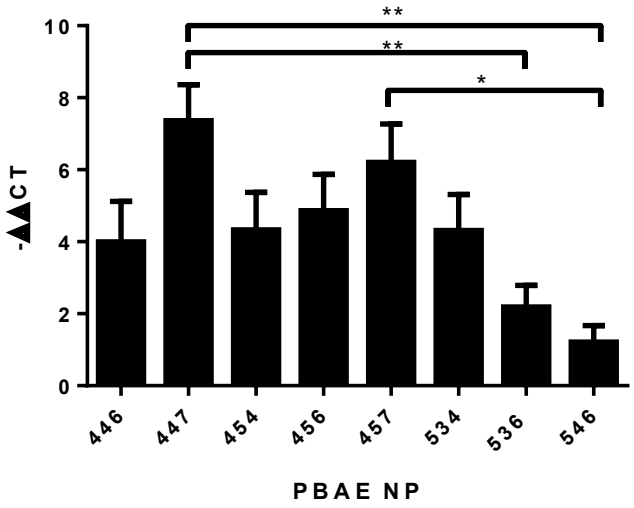

Figure 2.10. *In vitro* barcode screen of 8 PBAE NPs in HepG2 cells. Cells were transfected in 96-well plates at a dose of 600 ng DNA per well, and RT-qPCR was performed 48 hours later. Data represent mean ± SEM of n = 3. Statistical differences between NP formulations were calculated by one-way ANOVA with Holm Sidak's multiple comparison test. *: $p < 0.05$, **: $p < 0.01$

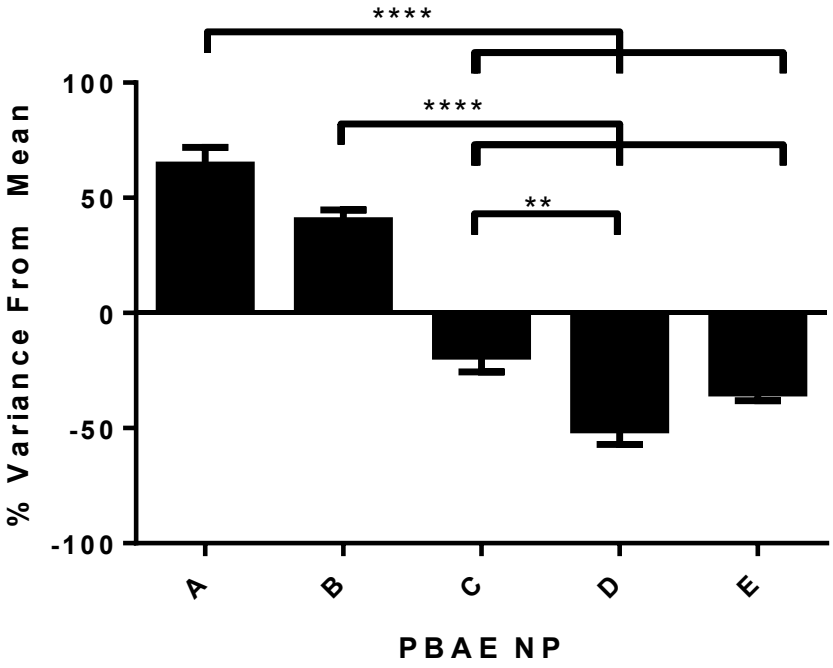

Figure 2.11. Variance in barcode amplification. Variance in barcode amplification from *in vitro* transfection of Hep3b cells with all PBAE NP formulations. Variance from mean indicates the percent deviation of the -ΔΔCT values from each barcode by the average -ΔΔCT value from all barcodes for the particular PBAE NP. (n = 8, mean ± SEM)

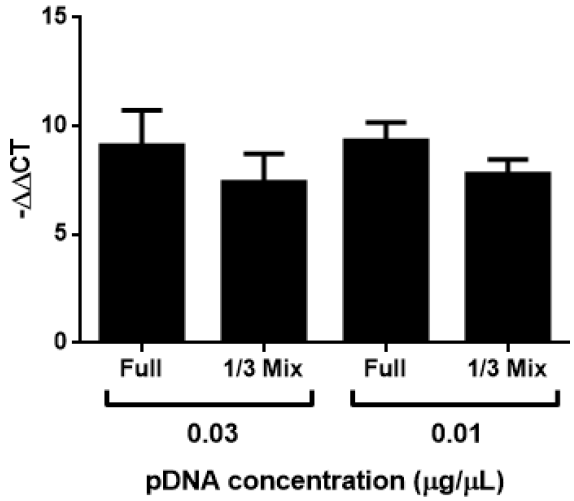

Figure 2.12. In vitro transfection of Hep3b cells with barcoded NPs. Hep3b cells were transfected with 0.03 or 0.01 μg/μg barcode pDNA A or a mixture of barcode pDNAs A, D, and E. Expression of barcode A mRNA was determined using RT-qPCR (-ΔΔCT of barcoded pDNA in each PBAE NP normalized to GAPDH). Data is shown as mean ± SEM of 3 biological replicates.

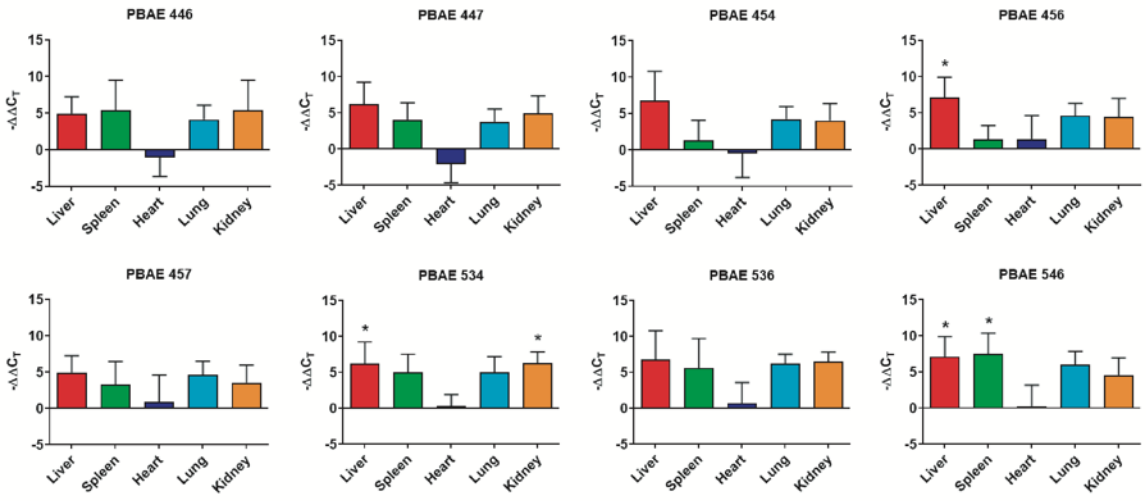

Figure 2.13. High-throughput screening of NP biodistribution. Pooled biodistribution data in major organs (liver, spleen, heart, lungs, kidneys) of each PBAE NP formulation with 5 distinct DNA barcodes from 5 different mice. 30 min post administration of barcoded PBAE NPs, the amount of DNA accumulated was quantified by the amplification of DNA barcodes in qPCR (-ΔΔCT of barcoded plasmid DNA in each PBAE NP normalized to GAPDH). Data represent mean ± SEM of n = 5 for each PBAE NP from a total of 8 mice (one-tailed Student's t-test between the experimental -ΔΔCT values and zero with Sidak's multiple comparisons, * = $p < 0.05$).

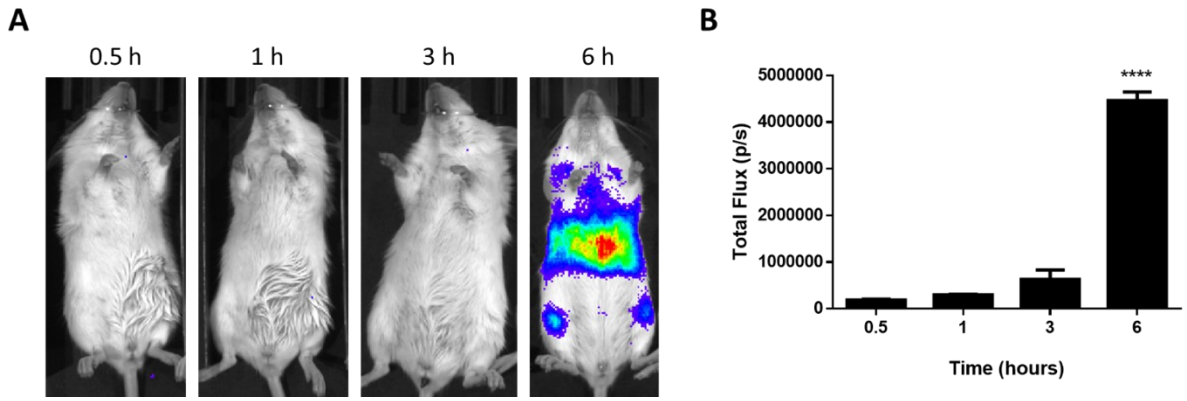

Figure 2.14. Time-course *in vivo* gene expression. *In vivo* bioluminescence after intravenous administration of PBAE 536 NPs (25 w/w) harboring 50 μg fLuc pDNA and subsequent IP injection of 150 mg/kg D-luciferin. Data represent mean ± SEM of n = 3. Statistical differences between time points were calculated by one-way ANOVA with Holm Sidak's multiple comparison test. ****: $p < 0.0001$

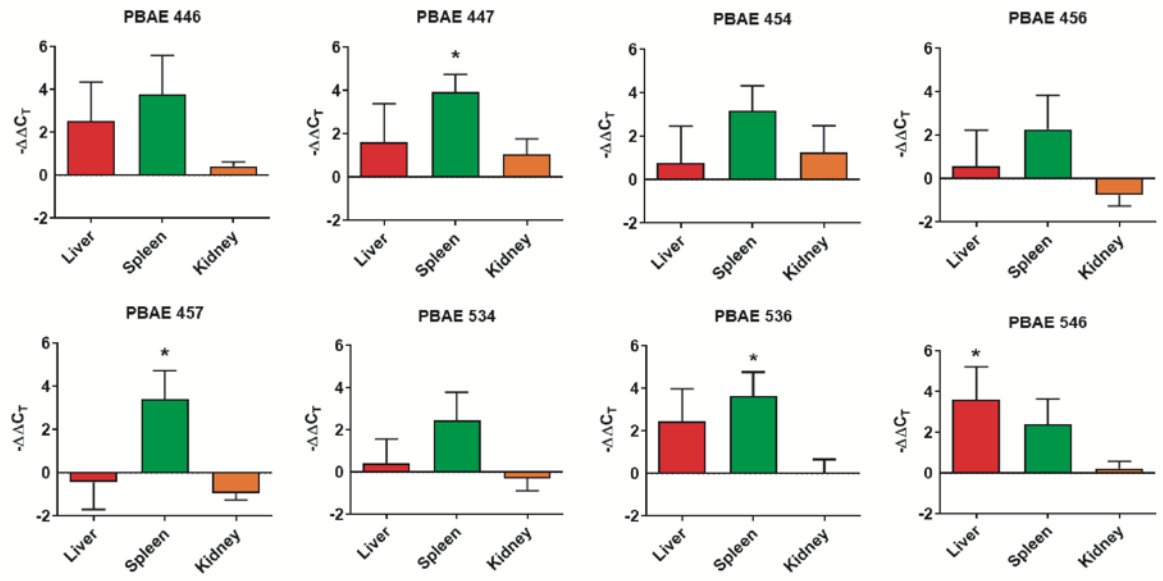

Figure 2.15. High-throughput screening of in vivo transfection. Pooled transfection data in organs with detectable transfection signal (liver, spleen, and kidneys) of each PBAE NP formulation with 5 distinct DNA barcodes from 5 different mice. 6 hours post administration of PBAE NPs, mRNA was extracted from organs and relative expression was quantified by RT-qPCR (-ΔΔCT of mRNA transcription of barcoded plasmid DNA in each PBAE NP normalized to GAPDH). Data represent mean ± SEM of n = 5 for each PBAE NP from a total of 8 mice (one-tailed Student's t-test between the experimental -ΔΔCT values and zero with Sidak's multiple comparisons, * = $P < 0.05$).

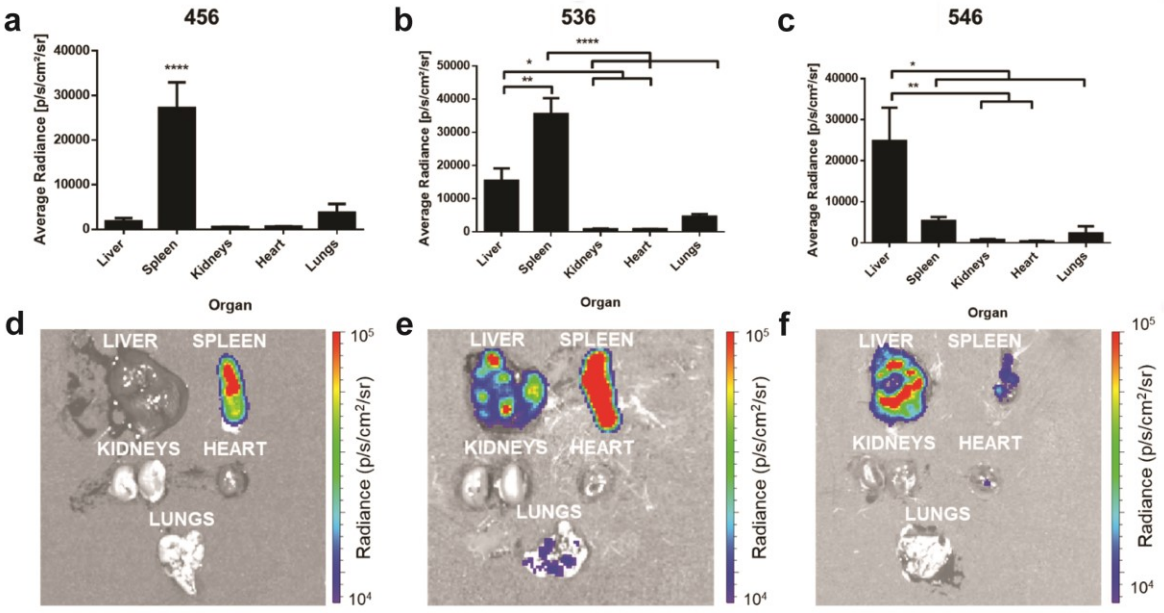

Figure 2.16. Luciferase expression after intravenous administration of PBAE NPs harboring fLuc plasmid DNA. Quantification and representative images of organ bioluminescence 6 hours after intravenous administration of PBAE 456 (A,D), PBAE 536 (B,E), and PBAE 546 (C,F) NPs. Data represent mean ± SEM of n = 3. Statistical differences between organ luminescence were calculated by one-way ANOVA with Holm Sidak's multiple comparison test. *: $P < 0.05$, **: $P < 0.01$, ****: $P < 0.0001$

PBAE polymer	446	447	454	456	457	534	536	546
Molecular weight: Mn (kDa)	4.38	14.8	3.85	3.05	5.99	7.37	4.73	6.02
Molecular weight: Mw (kDa)	9.40	103	9.50	10.6	20.5	14.7	10.8	11.9
PDI	2.15	6.96	2.47	3.48	3.42	2.00	2.27	1.97
# of carbons between diacrylates in diacrylate monomer group	4	4	4	4	4	5	5	5
# of carbons in side chain between amine and hydroxyl group	4	4	5	5	5	3	3	4
Total # of carbons	210	734	197	150	306	365	237	299
# of primary amines	0	0	2	0	0	2	0	0
# of secondary amines	4	2	2	4	2	2	4	4
# of tertiary amines	14	55	12	9	23	25	16	19

Table 2.1 Properties of PBAE polymers. Total numbers of carbons and tertiary amines are estimated from the molecular weight of each polymer.

Barcode A (eGFP)	ATGGTGAGCAAGGGCGAGGAGCTGTTCACCGGGGTGGTGCCCAT CCTGGTCGAGCTGGACGGCGACGTAAACGGCCACAAGTTCAGCG TGTCCGGCGAGGGCGAGGGCGATGCCACCTACGGCAAGCTGAC CCTGAAGTTCATCTGCACCACCGGCAAGCTGCCCGTGCCCTGGC CCACCCTCGTGACCACCCTGACCTACGGCGTGCAGTGCTTCAGC CGCTACCCCGACCACATGAAGCAGCACGACTTCTTCAAGTCCGCC ATGCCCGAAGGCTACGTCCAGGAGCGCACCATCTTCTTCAAGGAC GACGGCAACTACAAGACCCGCGCCGAGGTGAAGTTCGAGGGCGA CACCCTGGTGAACCGCATCGAGCTGAAGGGCATCGACTTCAAGG AGGACGGCAACATCCTGGGGCACAAGCTGGAGTACAACTACAAC AGCCACAACGTCTATATCATGGCCGACAAGCAGAAGAACGGCATC AAGGTGAACTTCAAGATCCGCCACAACATCGAGGACGGCAGCGT GCAGCTCGCCGACCACTACCAGCAGAACACCCCCATCGGCGACG GCCCCGTGCTGCTGCCCGACAACCACTACCTGAGCACCCAGTCC GCCCTGAGCAAAGACCCCAACGAGAAGCGCGATCACATGGTCCT GCTGGAGTTCGTGACCGCCGCCGGGATCACTCTCGGCATGGACG AGCTGTACAAGTAA
Barcode B (mOrange)	ATGGTGAGCAAGGGCGAGGAGAATAACATGGCCATCATCAAGGA GTTCATGCGCTTCAAGGTGCGCATGGAGGGCTCCGTGAACGGCC ACGAGTTCGAGATCGAGGGCGAGGGCGAGGGCCGCCCCTACGA GGGCTTTCAGACCGCTAAGCTGAAGGTGACCAAGGGTGGCCCCC TGCCCTTCGCCTGGGACATCCTGTCCCCTCAGTTCACCTACGGCT CCAAGGCCTACGTGAAGCACCCCGCCGACATCCCCGACTACTTCA AGCTGTCCTTCCCCGAGGGCTTCAAGTGGGAGCGCGTGATGAAC TTCGAGGACGGCGGCGTGGTGACCGTGACCCAGGACTCCTCCCT GCAGGACGGCGAGTTCATCTACAAGGTGAAGCTGCGCGGCACCA ACTTCCCCTCCGACGGCCCCGTAATGCAGAAGAAGACCATGGGC TGGGAGGCCTCCTCCGAGCGGATGTACCCCGAGGACGGCGCCCT GAAGGGCGAGATCAAGATGAGGCTGAAGCTGAAGGACGGCGGCC ACTACACCTCCGAGGTCAAGACCACCTACAAGGCCAAGAAGCCC GTGCAGCTGCCCGGCGCCTACATCGTCGGCATCAAGTTGGACAT CACCTCCCACAACGAGGACTACACCATCGTGGAACAGTACGAACG CGCCGAGGGCCGCCACTCCACCGGCGGCATGGACGAGCTGTAC AAGTAA
Barcode C (iRFP)	ATGGCGGAAGGATCTGTCGCCAGGCAGCCTGACCTCTTGACCTG CGACGATGAGCCGATCCATATCCCCGGTGCCATCCAACCGCATG GACTGCTGCTCGCCCTCGCCGCCGACATGACGATCGTTGCCGGC AGCGACAACCTTCCCGAACTCACCGGACTGGCGATCGGCGCCCT GATCGGCCGCTCTGCGGCCGATGTCTTCGACTCGGAGACGCACA ACCGTCTGACGATCGCCTTGGCCGAGCCTGGCGCGGCCGTCGGA GCACCGATCACTGTCGGCTTCACGATGCGAAAGGACGCAGGCTT CATCGGCTCCTGGCATCGCCATGATCAGCTCATCTTCCTGGAATT GGAGCCTCCCCAGCGGGACGTCGCCGAGCCGCAGGCGTTCTTCC GCCGCACCAACAGCGCCATCCGCCGCCTGCAGGCCGCCGAAACC

Barcode D (Non-coding)	GCTAGCCACCGGTCGCCACCATGCATTGATGCCACGGCGATTGT CGGGGAGCCAGCAGCGGCTGCAGACGTCAGACCGGAGCAACAC TAGCGAGCGATAAGTCCCTAACTGGCTGCGGCCTCCTGTAGAGC GAACTTCACCACATACGCTGTCTCTGGCACGTGGATGGTTTGGAG GAATCAGATCCAAGTCTGGCCAACCTCCAAGCAGGTCTAGAGTCT AAAACAGTGGTCCCCTGCGTGCGGGATGGGGGTACTAGGTGACT GCAGGGACTGCGACGTCTTGAACGTTGGCCCGTCAGAGGCGCCG TTCAGGATCACGTTACCCCGAAAAGAAGGCACCAGGAGCTCTTCT CCCCTGCGGCCAGGCCTGTAGAGACTACACCATTGACCCTCCTGA GAGCCGGGAGGCGGGAATCCGCCACGTATGAGAAGGTATTTGCC CGACAATCAATACCCCGGGCTCCTAACCTTTTCCACTCGCTTGGG CCGGCTTGGCCTCCCTGCCCGGAGATTCGCCGGACTGGTGCCGA CGCGCGGGCATAGTCCCAGGGGGGTTATCCGGGGGCAGCGGCA GCCAACATCTCGGGTCCTGCCCGGCCGGTCTACGCGCTGATACA GCGAATCGCCGAGGACCCGGCGCCGCGCAATGGAACGTCCTTAG CTCCGGCAGGCAATTAAGGGGAACGCATGCATGGCGCAAAAAAA CTGGGAAACCGGCGAGTAAAGCAAGCTT
Barcode E (Non-coding)	GCTAGCCACCGGTCGCCACCATGTATGCGCCGGTGTTGAGCCGC GCTTATGCCCAGCACCGTTACAACCAGACCGACACCAGATGTGTA ACGTCCGCCACGCAGACGAGACCGGTCGGAGACCACCGAGCGTT CTACCACGTCGGCGACCACCAGTGAGCTACTGGGGCCGAGGGGT AACGACGGTGCCCCTAAGAGCCCCTCGGTCGACGCAGGCGACTG CACTCCTGCCACATCATGATCGTTCGCTATTCAGGGGTTGACCGA CACCGGATGGCTTCTCACTTGAAGTGCTGTGCGCGACAGGGTGC GTGCACCAACCAAACCTGCTTTGACTTACCTCAGACCAGTTGGAA GTGCGGCCAGATCTCAGCTTTCGTCACCAGAGGGCCCACGCCCA GCCTCCATGATCCACTGACCTCCCAGACGCTGCAAGACTTGCAAC CAGGCAGACTCGGCGGTAGGTCCTAGTGCAGCGGGGCTTTTTTT CCGTGGTCGTCGAGAGGAGGGGTCGCCGGACCAGACACCTCTGA TGTCCTGATTGGGAGGACCGTTGGCCCCCGGCCCTTAGGCGGTG CACTCAGTTCCATAAACGGGCTGTTAGATATGGGGTCCGTGGATT GAAAAGGGTGACGGAACTCGCCCGGACGCGAGAGACGGGCAGC TAGGCACCCTGAGCACGGTTGCGCGTCCGAATCAAGCTCCTCCCT ACAGGCCCCGGTCTTAAAGCAAGCTT

Table 2.2. Sequence of 5 inserts to N1-backbone plasmid.

	Forward Primer (5' -> 3')	Reverse Primer (5' -> 3')
Primer for Plasmid A	CTACCCCGACCACATGAAGC	TGCTCAGGTAGTGGTTGTCG
Primer for Plasmid B	GGACATCCTGTCCCCTCAGT	TTGATGCCGACGATGTAGGC
Primer for Plasmid C	TCTTGACCTGCGACGATGAG	CCGGGTTGATGGTATAGAGCC
Primer for Plasmid D	CCAGGAGCTCTTCTCCCCT	TGCGTTCCCCTTAATTGCCT
Primer for Plasmid E	ACCGGATGGCTTCTCACTTG	GCGAGTTCCGTCACCCTTTT

Table 2.3 Primer sequences.

ANIMAL	PBAE NP							
	446	447	454	456	457	534	536	537
1	A	B	C	D	E			
2		A	B	C	D	E		
3			A	B	C	D	E	
4				A	B	C	D	E
5	E				A	B	C	D
6	D	E				A	B	C
7	C	D	E				A	B
8	B	C	D	E				A

Table 2.4 Barcode NP administration scheme. Each animal (1-8) listed in the row title was injected with a mixture of 5 NPs, where each NP is comprised one of 5 barcode pDNAs represented by a letter A, B, C, D, or E and a PBAE polymer listed in the column title.

Chapter 3: Non-Viral Gene Delivery to Hepatocellular Carcinoma Tumors via Intra-Arterial Injection

3.1 Introduction

Liver cancer is the fifth most prevalent type of cancer globally, and the third most common cause of cancer death[1]. Hepatocellular carcinoma (HCC) is the most common type of primary liver tumor, accounting for >80% of cases[2]. Patients with early-stage disease are eligible for tumor resection or liver transplantation, which can be curative. However, many HCC patients are diagnosed at a later stage when treatment options are generally limited to palliative care[3]. Treatment regimens for these patients are complicated due to the high prevalence of underlying liver disease. Globally, approximately 80% of HCC cases can be attributed to chronic hepatitis infection, and in the United States, non-alcoholic fatty liver disease underlies 10-20% of HCC cases[4]. These comorbidities cause inflammation and cirrhosis, significantly damaging the normal function of the liver. Therefore, systemic or non-targeted treatments such as general chemotherapy have a high risk of liver failure for these patients[5].

Locoregional approaches are preferable to target tumor tissue while avoiding off-target toxicity to the liver[6]. Ultrasonography or computed tomography are used to directly access HCC tumors and deliver a cytotoxic agent. Radiofrequency and microwave ablation use high energy waves directed at the tumor to cause tissue damage and cell death[7,8]. Percutaneous ethanol or acetic acid injection similarly induce ablation of smaller lesions[9]. These treatments are most successful in small tumors, but the rate of recurrence remains high.

Another locoregional approach for intermediate stage HCC is trans arterial chemoembolization (TACE)[10]. This is an interventional radiology procedure which involves

accessing the hepatic artery non-invasively, then delivering chemotherapy followed by an embolic agent. Because the hepatic artery preferentially supplies blood to HCC tumor while the rest of the liver is fed by the portal vein, embolizing the hepatic artery cuts off blood supply to the tumor. Local chemotherapy is a standard component of TACE, but clinical trials have shown no benefit to adding chemotherapeutic agents over the embolic agent alone[11]. This may be due to the poor pharmacokinetics of small molecule drugs. Another solution is drug eluting bead TACE (DEB-TACE), in which microspheres are used to embolize the artery and release drug over an extended period, resulting in sustained chemotherapy in the tumor. This procedure carries a higher risk of hepatic artery and biliary injuries, but reduced incidence of other complications, including abdominal pain, due to the controlled chemotherapy release[12]. However, in terms of effectiveness, DEB-TACE has not shown proven benefit over conventional TACE.

There is great interest in improving the therapeutic benefit of TACE by incorporating newer generations of therapeutics. Nanoparticles have different pharmacokinetics from small molecule drugs and benefit from the enhanced permeation and retention (EPR) effect[13]. Further, nanoparticle may be modified for enhanced targeting by optimizing the material of the delivery vehicle or adding targeting ligands to the surface[14]. Additionally, nanoparticle delivery vehicles have been developed for targeted delivery of nucleic acids, which can specifically target genetic abnormalities of HCC tumors. Poly(beta-amino ester) PBAE nanoparticles have been optimized for targeted DNA delivery to HCC cell lines *in vitro* and *in vivo*[15]. Therefore, we sought to develop a protocol for intra-arterial injection of PBAE nanoparticles in a rat xenograft liver tumor model and investigate this route for targeted DNA delivery to HCC.

3.2 Methods

Animal Experiments

All *in vivo* procedures were approved and overseen by the Johns Hopkins Institutional Animal Care and Use Committee (IACUC). RNU athymic rats were purchased from Charles River Laboratories (Wilmington, MA) or bred at Johns Hopkins from two homozygous RNU athymic rats. For all surgical procedures, animals were be anesthetized with 3% isoflurane in 100% oxygen until a sufficient plane of anesthesia was reached as gauged by rapidity and thoracic nature of breathing. Anesthesia was confirmed by monitoring response to stimuli (toe pinch). Ophthalmic ointment was applied while animals were under anesthesia. During surgical procedures, rats were placed onto a 37°C heated surface to ensure optimum thermoregulation and minimize post-op recovery time. The hair was removed from the surgical site (abdomen) using clippers or depilatory cream and prepared using a wash of povidone-iodine soap then rinsed with 70% ethanol. After surgery, the peritoneum was closed using simple continuous suturing of the muscle layer with absorbable sutures and skin layer was closed using wound clips or simple interrupted suturing with non-absorbable sutures. Finally, Vetbond tissue adhesive was applied topically to prevent dehiscence and to improve post-procedure healing. Warm, sterile isotonic fluids at 3-5% of the body weight was injected subcutaneously prior to and at the end of surgery. Analgesia was administered as meloxicam (2 mg/kg) delivered subcutaneously prior to surgery and again at 24 and 48 hours after surgery.

Liver tumor implantation surgery

To access the liver, a laparotomy was performed extending caudally from the xiphoid process. Under direct visualization, 1×10^6 N1-S1 cancer cells in a 1:1 solution of HBSS and High Concentration Matrigel (Corning, Corning, NY) were injected under the liver capsule. Successful inoculation with cancer cells was verified by pale, white protrusion at the point of

injection. Gentle compression was applied for at least 15 seconds using a sterile cotton tipped applicator to prevent cancer cell leakage or bleeding.

Nanoparticle Preparation

Firefly luciferase (fLuc) DNA was amplified by Aldevron (Fargo, ND) and used for *in vivo* transfection studies. For biodistribution studies, fLuc DNA was functionalized using Label IT Nucleic Acid Modifying Reagent (Mirus Bio Madison, WI) and labeled with IRDye 800RS NHS Ester Infrared Fluorescent Dye (LI-COR, Lincoln, NE). 10% labeled DNA was used for biodistribution studies. PBAE 536 was synthesized by Michael addition as previously described[15].

PBAE 536 was diluted in sodium acetate (40.4 mM, pH 5), the added to 1 mg/mL plasmid DNA in water for a final DNA concentration of 0.25 mg/mL and polymer: DNA weight ratio of 25 w/w. DNA and polymer were allowed to complex for 10 minutes, then sucrose was added for a final concentration of 90 mg/mL to make the solution isotonic. Nanoparticles were frozen at -80°C and thawed immediately prior to injection.

Jugular Injection

Under careful dissection, the right or left jugular was visualized. A 27G insulin needle was inserted into the overlying muscle and then directed towards the rat's head into the jugular vein lumen as it is visualized in vessel anterior to the trapezius muscle. Prior to injection, the plunger was pulled back, and proper placement was confirmed by visualizing blood in the syringe. Nanoparticles were injected slowly at 100 µL per minute in a total volume of 500 microliters and were visualized intravenously in the jugular vein during delivery.

Hepatic Artery Injection

After orthotopic liver tumor implantation described above, tumor-bearing animals were subjected to the following hepatic artery injection surgical procedure. Hepatic artery injection surgery was not performed sooner than two weeks after the orthotopic tumor implantation surgery, to minimize main and distress on the animals. The procedure was performed under a dissecting microscope to improve visualization of small delicate structures. Animals were prepared for surgery as described above, then an incision was made with a scalpel extending caudally from the xyphoid process ~3 cm. The peritoneum was cut with scissors along the linea alba. The lateral left lobe of the liver was externalized on a sterile piece of gauze soaked with saline and retracted. Similarly, the duodenum was externalized on gauze and retracted. The mesenteric connective tissues were dissected, and common bile duct was retracted using silk suture to allow visualization of the common hepatic artery, proper hepatic artery and gastroduodenal artery (GDA). The right GDA artery was freed from surrounding tissue and ligated at the distal end. A few drops of 2% lidocaine were applied to the GDA to promote vasodilation. The common hepatic artery was clamped using a bulldog clamp, occluding blood flow. A 27-gauge needle was inserted into the gastroduodenal artery, and 500 μL of experimental solution was slowly hand injected at a rate of ~100 μL per minute. Successful injection was confirmed by visualizing the displacement of blood in the proper hepatic artery. Following experimental injection, the needle was slowly withdrawn from the vessel. A suture was used to ligate the GDA proximal to the needle insertion site, and the clamp was removed from the common hepatic artery to restore blood flow through the proper hepatic artery. The duodenum and liver were replaced in the abdominal cavity, and the incision was closed as described above.

In Vivo *Imaging*

Biodistribution and transection were monitored by IVIS (IVIS Spectrum imaging system, Perkin Elmer, Waltham, MA). 150 mg/kg D-luciferin (Gold Biotechnology, St. Louis, MO) was administered intraperitoneally to mice, then 8 minutes later animals were sacrificed, and livers were harvested. Bioluminescence and fluorescence images were acquired. Images were analyzed across regions of interest (ROI) using Living Image software (Perkin Elmer, Waltham, MA).

3.3 Results

PBAE 536 NPs were specifically optimized to transfect HCC cell lines in previous work be Zamboni et al[15]. To evaluate biodistribution and transfection, firefly luciferase (fLuc) plasmid DNA was labeled with a near-infrared fluorophore. NPs were formulated with 10% labeled DNA and 90% unlabeled fLuc plasmid. DNA at 0.25 mg/mL was combined with PABE 536 polymer in sodium acetate (pH 5, 25 mM) and allowed to self-assemble. The tonicity of the solution was balanced using sucrose, for a final concentration of 90 mg/mL.

A microsurgical procedure was developed to administer NPs via the hepatic artery. A laparotomy was performed, and the liver and duodenum were retracted on sterile gauze. The gastroduodenal artery (GDA) was located near the caudate lobe, anterior to the portal vein and posterior to the common bile duct (**Figure 3.1**). To prevent bleeding, the GDA was selected as the injection site, as the vessel may be ligated without complications (cite). The GDA was isolated and ligated at the distal end. Next, a few drops of 2% lidocaine were applied directly to the GDA to induce vasodilation. The common hepatic artery was clamped temporarily using a micro bulldog clamp. A 27G insulin needle was used to inject 500 μL of NPs into the GDA, and flow was directed to the common hepatic artery. Successful injection was confirmed by visualizing the displacement of blood in the proper hepatic artery. Injections were performed at a rate of 100 μL per minute to minimize risk of embolism. After injection, the needle was carefully

removed, and the proximal end of the GDA was ligated before removing the clamp on the common hepatic artery. A latex solution was injected using this procedure to visualize the injection route and anatomy (**Figure 3.2**). Injected solution was directed into the proper hepatic artery and into the left and right branches and into the liver.

To assess biodistribution and transfection, nanoparticles were synthesized with fLuc DNA labeled (10%) with near-IR fluorescent dye (NIR-fLuc NPs). NIR-fLuc NPs were administered intravenously or via hepatic artery, and biodistribution (fluorescence) and transfection (luminescence) were assessed 6 hours later. In healthy RNU rats, NPs administered by either route accumulated in the liver (**Figure 3.3**). No transfection was observed in the liver. To evaluate intratumoral delivery, rats were implanted with N1-S1 tumors in the liver. Two weeks later, NIR-fLuc NPs were injected. Intravenously injected NPs accumulated in the liver, excluding the tumor tissue (**Figure 3.4**). NPs administered via the hepatic artery accumulated in the liver but also in the tumor. In the intra-arterial injection case only, transfection was detected in the primary tumor. Interestingly, there was also measurable transfection outside the tumor area, suggesting that micrometasteses may be transfected throughout the liver.

3.4 Discussion

Local delivery is an attractive option for targeting therapeutics directly to the tumor microenvironment. However, small molecule chemotherapies have poor pharmacokinetics and can still cause systemic toxicity with local administration. Nanoparticle formulations have superior retention in tumor tissue, which has been exploited in the development of many systemically administered therapeutic nanoformulations[16]. While passive targeting by the EPR effect has shown promise in preclinical studies, this effect has not translated to clinical trials in human patients with solid tumors[17]. In an orthotopic rat model of HCC, we showed that

intravenously administered PBAE nanoparticles do not accumulate in tumor tissue. With local delivery via the proper hepatic artery, intratumoral accumulation is increased. By taking advantage of the differential blood supply to tumor and liver tissue, nanoparticle biodistribution was improved.

Nucleic acid therapeutics may be used to target dysregulated oncogenes or tumor suppressor genes in cancer cells. Further, plasmid DNA may be targeted for cancer cell expression by employing a cancer-specific promoter for therapeutic gene expression[18,19]. Delivery efficiency is still a major barrier to DNA therapy for cancer, and local administration should lead to an increased concentration of nanoparticles at the target site[20]. Further, local administration routes lead to decreased exposure to systematic circulation, slowing clearance and reducing the risk of systemic toxicity[21]. We showed successful delivery of fLuc reporter DNA to HCC liver tumors with intra-arterial injection of PBAE NPs. Intravenous administration of NPs was not successful in transfecting tumor or liver tissue. Further investigation is necessary to characterize the cell populations targeted.

Local delivery is not a feasible option for many types of solid tumors. HCC tumors are uniquely accessible by the proper hepatic artery, and this has been harnessed in a clinical setting with the TACE procedure[10]. This procedure is minimally invasive, and specific branches of the artery can be accessed to target a patient's tumor more specifically. By developing a preclinical surgical procedure to access this artery for nanoparticle delivery, this route may be explored for the delivery of alternative agents, such as mRNA and siRNA. Additionally, active targeting agents which specifically bind to tumor cells may be developed and tested for additional targeting[22]. This rat model recapitulates many of the barriers of delivery to HCC tumors. Further development should be focused on toxin-induced or genetic HCC models which may model the

vasculature of these tumors more accurately. Additionally, a syngeneic HCC model is needed to investigate the immunological response to therapeutic agents, particularly in the development of cancer immunotherapies.

In conclusion, we describe a method for accessing the proper hepatic artery in rats. We show that this route of administration provides a significant advantage over intravenous administration for the delivery of PBAE NPs, improving both accumulation of NPs in the tumor and successful delivery of a reporter gene. Future work should incorporate anti-cancer nucleic acid to assess the therapeutic benefits of this approach.

3.5 References

1. Shaw, JJ and Shah, SA (2011). Rising incidence and demographics of hepatocellular carcinoma in the USA: what does it mean? *Expert Rev. Gastroenterol. Hepatol.* **5**: 365–370.
2. Ayuso, C, Rimola, J, Vilana, R, Burrel, M, Darnell, A, García-Criado, Á, *et al.* (2018). Diagnosis and staging of hepatocellular carcinoma (HCC): current guidelines. *Eur. J. Radiol.* **101**: 72–81.
3. Golabi, P, Fazel, S, Otgonsuren, M, Sayiner, M, Locklear, CT and Younossi, ZM (2017). Mortality assessment of patients with hepatocellular carcinoma according to underlying disease and treatment modalities. *Medicine (Baltimore).* **96**.
4. Yang, JD, Hainaut, P, Gores, GJ, Amadou, A, Plymoth, A and Roberts, LR (2019). A global view of hepatocellular carcinoma: trends, risk, prevention and management. *Nat. Rev. Gastroenterol. Hepatol.* **16**: 589–604.
5. El–Serag, HB and Rudolph, KL (2007). Hepatocellular Carcinoma: Epidemiology and Molecular Carcinogenesis. *Gastroenterology* **132**: 2557–2576.

6. Forner, A, Reig, M, Varela, M, Burrel, M, Feliu, J, Briceño, J, *et al.* (2016). [Diagnosis and treatment of hepatocellular carcinoma. Update consensus document from the AEEH, SEOM, SERAM, SERVEI and SETH]. *Med. Clin. (Barc).* **146**: 511.e1-511.e22.

7. Ido, K, Isoda, N, Kawamoto, C, Hozumi, M, Suzuki, T, Nagamine, N, *et al.* (1997). Laparoscopic microwave coagulation therapy for solitary hepatocellular carcinoma performed under laparoscopic ultrasonography. *Gastrointest. Endosc.* **45**: 415–420.

8. Liu, F-Y, Yu, X-L, Liang, P, Cheng, Z-G, Han, Z-Y, Dong, B-W, *et al.* (2012). Microwave ablation assisted by a real-time virtual navigation system for hepatocellular carcinoma undetectable by conventional ultrasonography. *Eur. J. Radiol.* **81**: 1455–1459.

9. Nakaji, S, Hirata, N, Kobayashi, M, Shiratori, T and Sanagawa, M (2015). Endoscopic ultrasonography-guided ethanol injection as a treatment for ruptured hepatocellular carcinoma in the left hepatic lobe. *Endoscopy* **47**: E558–E560.

10. Tsurusaki, M and Murakami, T (2015). Surgical and locoregional therapy of HCC: TACE. *Liver Cancer* **4**: 165–175.

11. Brown, KT, Do, RK, Gonen, M, Covey, AM, Getrajdman, GI, Sofocleous, CT, *et al.* (2016). Randomized trial of hepatic artery embolization for hepatocellular carcinoma using doxorubicin-eluting microspheres compared with embolization with microspheres alone. *J. Clin. Oncol.* **34**: 2046.

12. Zou, JH, Zhang, L, Ren, ZG and Ye, SL (2016). Efficacy and safety of cTACE versus DEB-TACE in patients with hepatocellular carcinoma: a meta-analysis.

13. Maeda, H, Wu, J, Sawa, T, Matsumura, Y and Hori, K (2000). Tumor vascular permeability and the EPR effect in macromolecular therapeutics: a review. *J. Control. Release* **65**: 271–284.

14. Zhong, Y, Meng, F, Deng, C and Zhong, Z (2014). Ligand-directed active tumor-targeting polymeric nanoparticles for cancer chemotherapy. *Biomacromolecules* **15**: 1955–1969.

15. Zamboni, CG, Kozielski, KL, Vaughan, HJ, Nakata, MM, Kim, J, Higgins, LJ, *et al.* (2017). Polymeric nanoparticles as cancer-specific DNA delivery vectors to human hepatocellular carcinoma. *J. Control. Release* **263**: 18–28.

16. Kang, H, Rho, S, Stiles, WR, Hu, S, Baek, Y, Hwang, DW, *et al.* (2020). Size-Dependent EPR Effect of Polymeric Nanoparticles on Tumor Targeting. *Adv. Healthc. Mater.* **9**: 1901223.

17. Maeda, H (2015). Toward a full understanding of the EPR effect in primary and metastatic tumors as well as issues related to its heterogeneity. *Adv. Drug Deliv. Rev.* **91**: 3–6.

18. Qiao, J, Doubrovin, M, Sauter, B V, Huang, Y, Guo, ZS, Balatoni, J, *et al.* (2002). Tumor-specific transcriptional targeting of suicide gene therapy. *Gene Ther.* **9**: 168–175.

19. Robson, T and Hirst, DG (2003). Transcriptional targeting in cancer gene therapy. *Biomed Res. Int.* **2003**: 110–137.

20. Wolinsky, JB, Colson, YL and Grinstaff, MW (2012). Local drug delivery strategies for cancer treatment: Gels, nanoparticles, polymeric films, rods, and wafers. *J. Control. Release* **159**: 14–26.

21. Hu, J, Dong, Y, Ding, L, Dong, Y, Wu, Z, Wang, W, *et al.* (2019). Local delivery of arsenic trioxide nanoparticles for hepatocellular carcinoma treatment. *Signal Transduct. Target. Ther.* **4**: 1–7.

22. Choi, CHJ, Alabi, CA, Webster, P and Davis, ME (2010). Mechanism of active targeting in solid tumors with transferrin-containing gold nanoparticles. *Proc. Natl. Acad. Sci.* **107**: 1235 LP – 1240.

3.6 Figures

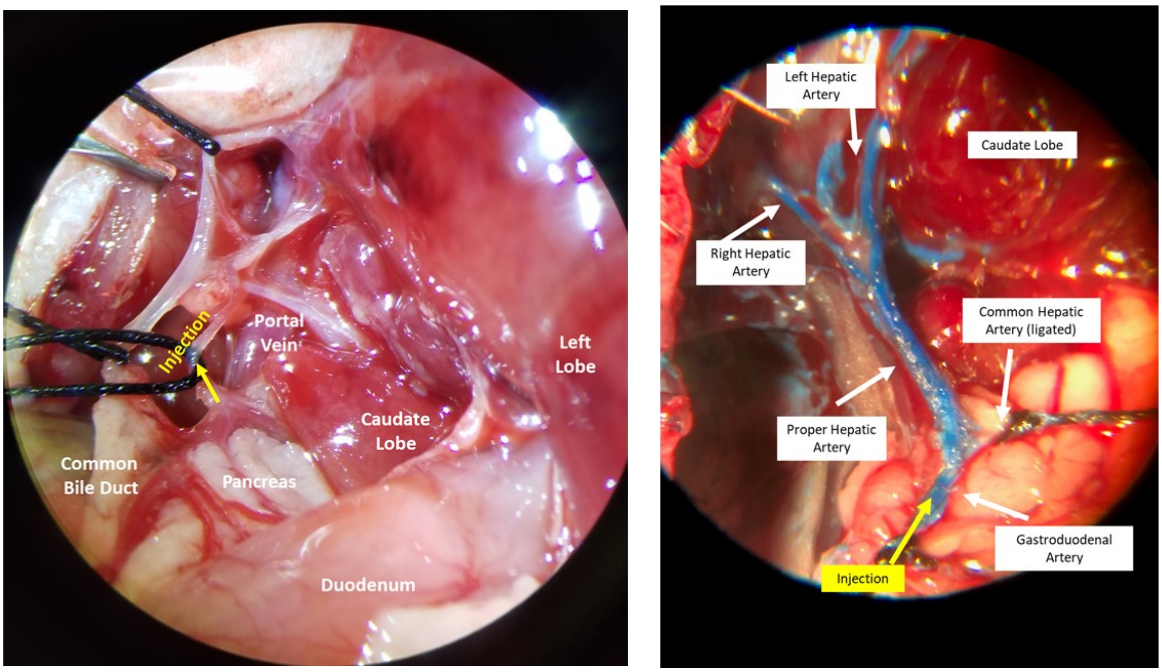

Figure 3.1 Intra-arterial Injection Procedure. A. Portal triad anatomy. The common biliary duct is retracted to visualize the hepatic artery. Arrow (yellow) indicates the injection site in the gastroduodenal artery. B. Intra-arterial injection to the hepatic artery visualized using a latex solution injection. Blue latex was injected into the gastroduodenal artery, then progresses into the common hepatic artery and into the liver. Images were acquired under magnification with a dissecting microscope.

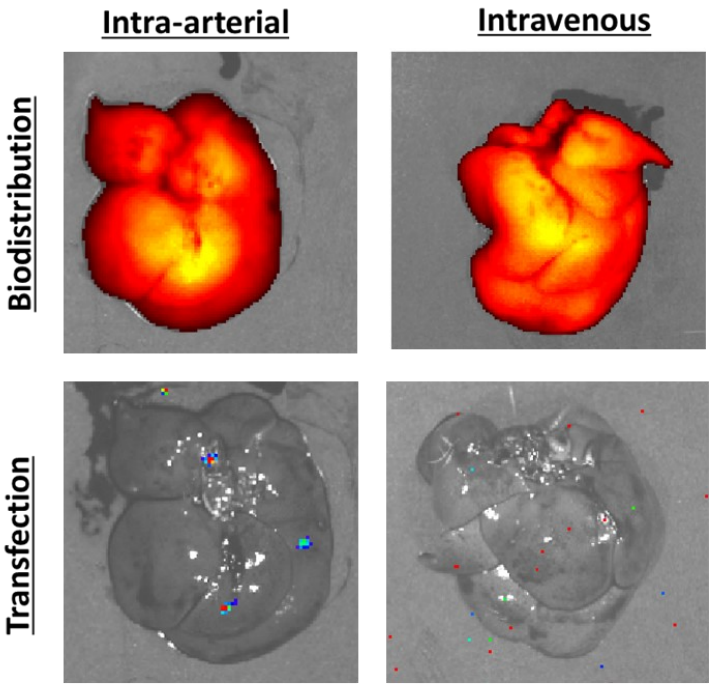

Figure 3.2 NIR-fLuc NP biodistribution and transfection following intra-arterial or intravenous injection in animals without liver tumors. Healthy rats were injected with 500 µL PBAE NPs harboring 125 µL of fLuc DNA, with 10% of DNA mass covalently labeled with near infra-red fluorophore. With both intravenous and trans arterial administration, NPs were localized to liver tissue, but no transfection was detected by bioluminescence imaging.

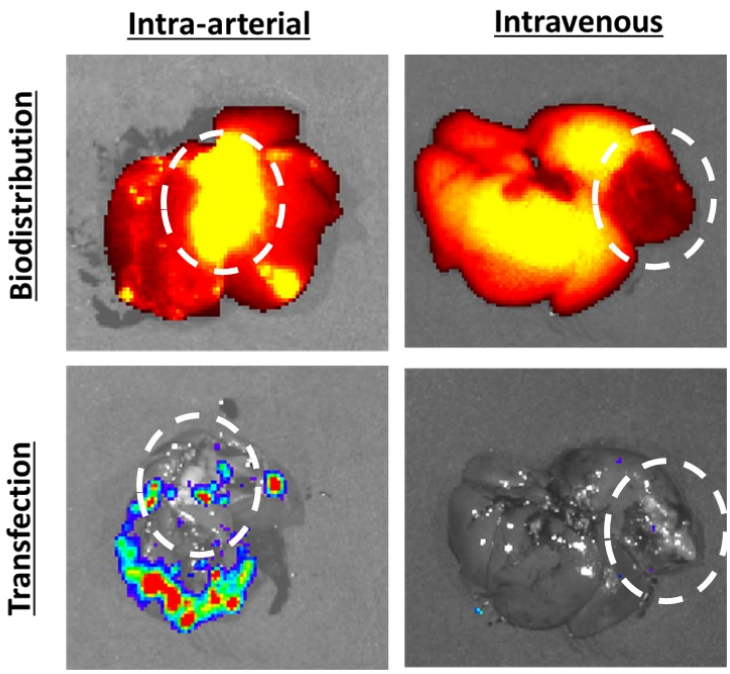

Figure 3.3 NIR-fLuc NP biodistribution and transfection following intra-arterial or intravenous injection in animals with N1-S1 xenograft tumors (circled). 2 weeks after N1-S1 tumor implantation, rats were injected with 500 µL PBAE NPs harboring 125 µL of fLuc DNA, with 10% of DNA mass covalently labeled with near infra-red fluorophore. NPs administered by intravenous injection accumulate in the liver but exclude the tumor. NPs administered via the hepatic artery accumulate in the liver and tumor, with gene expression shown by bioluminescence imaging.

Chapter 4: Poly(beta-amino ester) Nanoparticles Enable Tumor-Specific TRAIL Secretion and a Bystander Effect to Treat Liver Cancer

4.1 Introduction

Tumor necrosis factor-related apoptosis-inducing ligand (TRAIL) is a protein ligand that has been studied for over two decades as an anti-cancer agent.[1,2] Upon TRAIL binding to death receptors DR4 and DR5, intracellular death domains cluster and initiate apoptotic signaling via assembly of the death-inducing signaling complex (DISC).[3] DR4 and DR5 are overexpressed in many cancers, while healthy cells overexpress decoy receptors DcR1 and DcR2, which bind TRAIL protein but do not contain fully functional intracellular death domains required for apoptosis.[4,5] These differences in death receptor expression, as well as abnormal regulation of apoptotic signaling, result in TRAIL initiating apoptosis selectively in cancer cells with limited toxicity to healthy cells and tissues.[6]

Though TRAIL has shown promising therapeutic effects *in vitro* and in animal cancer models, it has failed to show significant anti-tumor efficacy in clinical trials.[7,8] Recombinant TRAIL protein is rapidly cleared, with a serum half-life of approximately 30 minutes.[9] This results in low TRAIL accumulation in the tumor, likely underpinning the lack of robust anti-tumor response. Additionally, there is evidence of acquired and innate TRAIL resistance in many tumor types, which has inspired investigation into combination therapies and sensitizing agents.[10]

This chapter contains material modified from the following article in press

Vaughan, H. J., Zamboni, C. G., Radant, N. P., Bhardwaj, P., Lechtich, E. R., Hassan, L., ... & Green, J. J. (2021). Poly (beta-amino ester) Nanoparticles Enable Tumor-Specific TRAIL Secretion and a Bystander Effect to Treat Liver Cancer. *Molecular Therapy-Oncolytics*. *In press.*

Lackluster clinical efficacy has motivated gene therapy approaches to improve TRAIL-based cancer treatment.[11] TRAIL gene therapy directly delivers TRAIL-encoding cDNA to cancer cells, enabling cytokine production locally in the tumor. This approach maximizes the local concentration of TRAIL protein, while minimizing systemic exposure and toxicity. Several groups have employed viral vectors for TRAIL gene therapy and achieved efficient suppression of xenograft tumor growth in various cancer types.[12–14] However, there are safety concerns inherent to viral gene therapy, including risk of immunogenicity,[15] tumorigenicity.[16] and cytotoxicity,[17] as well as the practical limitations of limited cargo carrying capacity and manufacturing challenges.

Non-viral gene delivery systems are generally safe and non-immunogenic but often have lower delivery efficacy than their viral counterparts.[18] To address this limitation, we have developed cDNA encoding a secreatable form of TRAIL which we deliver to hepatocellular carcinoma (HCC) using poly(beta-amino ester) PBAE nanoparticles (NPs). We explored combining this TRAIL NP therapy with histone deacetylase (HDAC) inhibitors, which have shown promise in sensitizing resistant cells to TRAIL[19–23]. We hypothesized that the bystander effect of secreted TRAIL to non-transfected cells combined with HDAC inhibitor sensitization could result in a potent yet cancer-specific non-viral TRAIL gene therapy **(Figure 4.1**).

4.2 Methods

Polymer Synthesis

1,5-pentanediol diacrylate (B5) (Monomer-Polymer and Dajac Labs, Trevose, PA), and 3-amino-1-propanol (S3) (Alfa Aesar, Ward Hill, MA) were combined in a 1:1.1 molar ratio of backbone to sidechain monomer and polymerized at 90°C under stirring for 24 hours. The resulting acrylate-terminated polymer (B5S3) was dissolved in THF, and 2-(3-aminopropylamino)ethanol

(E6) (Sigma-Aldrich, St. Louis, MO) was added at a 10-fold molar excess. The end capping reaction was allowed to proceed for 1 hour at RT under stirring. Endcapped PBAE polymer 536 was purified twice in diethyl ether to remove unreacted monomer and short oligomers, then dried under desiccant for approximately 48 hours to remove traces of ether. PBAE 536 was dissolved in anhydrous DMSO and stored at -20°C with desiccant. Molecular weight was characterized by Gel Permeation Chromatography (GPC, Waters 2414 Refractive Index Detector, Milford, MA).

Plasmid DNAs

pEGFP-N1 (eGFP) DNA was purchased from Clontech Laboratories Inc. (Mountain View, CA) and amplified by Aldevron (Fargo, ND). pEGFP-TRAIL (mTRAIL) was a gift from Bingliang Fang (Addgene Plasmid #10953) (Cambridge, MA). Luciferase-pcDNA3 was a gift from William Kaelin (Addgene plasmid # 18964) and amplified by Aldevron (Fargo, ND).

A non-viral plasmid encoding sTRAIL was designed and synthesized based on published work.[24] Coding sequences from the extracellular domain of Flt3L (a.a. 1– 81), an isoleucine zipper sequence from the pFETZ vector, and the apoptosis-inducing sequence derived from the N-terminus of the human TRAIL sequence (a.a. 114 –281) were combined in-frame. sTRAIL cDNA was synthesized using custom gene synthesis from Integrated DNA Technologies, Inc. (IDT) (Coralville, IA). The empty pN3-Control backbone was a gift from Guntram Suske (Addgene plasmid # 24544). sTRAIL cDNA was cloned into pN3-control backbone by restriction enzyme digest and amplified using ZymoPURE Plasmid Gigaprep kit (Zymo Research, Irvine, CA).

Nanoparticle Synthesis and Characterization

Plasmid DNA and PBAE 536 polymer were separately dissolved in pH 5 25 mM sodium acetate and combined at equal volumes, with a 1:25 mass ratio of polymer to DNA. NPs were

allowed to assemble for 10 minutes, then diluted 5x or 10x in pH 7.4 PBS. Size was measured by dynamic light scattering (DLS) and zeta potential was measured by electrophoretic light scattering by a Malvern Zetasizer Nano ZS (Malvern Instruments, Malvern, UK). To measure encapsulation efficiency PBAE NPs were combined with 6X loading dye without SDS. The samples were run through 0.8% agarose gel and using ethidium bromide staining and UV exposure to visualize the DNA bands.

Cell Culture

HepG2 and THLE3 cells were purchased from ATCC (Manassas, VA) and cultured according to the vendor's specifications. HepG2 cells were cultured in MEM media supplemented with 10% FBS, 1% Pen/Strep, 100 μM MEM Non-Essential Amino Acids, and 1 mM sodium pyruvate. THLE3 were cultured in Bronchial Epithelial Cell Growth Medium (BEBM) supplemented with 10% FBS, 1% Pen/Strep, 5 ng/mL human epithelial growth factor (EGF), 70 ng/mL O-phosphorylethanolamine, and the BEGM bullet kit (Lonza/Clonetics Corporation, Walkersville, MD) except Gentamycin-Amphotericin and Epinephrine. THLE3 cells were grown on plates and flasks coated with 0.01 mg/mL fibronectin, 0.03 mg/mL bovine collagen type I, and 0.01 mg/mL bovine serum albumin dissolved in culture media. Coating was performed overnight at 37°C.

In vitro *transfection*

Cells were plated in tissue culture treated 96-well plates at 10,000 cells per well and allowed to attach overnight. PBAE 536 NPs were freshly prepared and added to wells at a final DNA dose of 0.6 μg per well. Cells were incubated with the NPs for 2 hours at 37°C, then replenished with cell culture media. In HDAC inhibitor experiments, vorinostat (Adipogen, San Diego, CA), sodium butyrate (Sigma-Aldrich, St. Louis, MO), and MS-275 (Sigma-Aldrich, St. Louis, MO)

were diluted from stock solutions in cell culture media and added to cells after NP incubation. For media transfer studies in Supplemental Figure 4B, transfected cells were cultured for 48 hours, then conditioned media was spun down at 300 rcf for 5 minutes to remove dead cells and debris. HDAC inhibitors were added to conditioned media and transferred to non-transfected HepG2 or THLE3 cells, seeded 24 hours prior.

Viability and transfection analysis

Brightfield images were acquired 48 hours after transfection using a Zeiss (Oberkochen, Germany) Axio Observer fluorescence microscope at 10X magnification. Flow cytometry was performed 48 hours after transfection using a BD Accuri™ C6 Flow Cytometer (BD Biosciences, San Jose, CA) outfitted with a HyperCyt™ autosampler (IntelliCyt Corporation, Albuquerque, NM) to enable high throughput analysis. Cells were prepared for flow by detaching in 0.25% trypsin-EDTA (HepG2) or 0.05% trypsin-EDTA (THLE3), then resuspending in 30 µL of 2% FBS solution in 1X PBS. To assess viability, cells were also stained with a 1:200 dilution of propidium iodide (PI). Data was analyzed using FlowJo v10 (Ashland, OR). Events were gated on FSC-H and SSC-H to identify the cell population, then on FSC-H and FSC-A to exclude doublets. For transfection toxicity analysis, % cells were calculated by determining the percentage of cells stained positive for PI. For GFP transfection analysis, dead cells which stained PI+ (FL3-A) cells were also excluded. % GFP positive cells and normalized geometric mean fluorescence (FL1-A) were calculated. For TRAIL efficacy studies, viability was measured 24 hours after transfection using an MTT cell proliferation assay (Promega, Madison, WI).

Western Blot

Total protein was extracted from tumor cells 24 hours following treatment with DMSO (Sigma Aldrich, USA), 0.1 μM and 0.5 μM of Vorinostat (Thermo Fisher Scientific, USA), and quantified using Bradford protein assay (Bio-Rad, USA). 10 μg of the protein lysates from these samples were loaded onto 10% Mini-PROTEAN® TGX™ Precast Protein Gels (Bio-Rad, USA) and conducted at 110 V for 90 minutes. Following the separation step, proteins were transferred to a PVDF membrane at 100 V for 1 h. Membranes were blocked with 5% dry milk or 5% bovine serum albumin (BSA) and 0.1% Tween-20 in TBS for 1 h at room temperature (RT), and incubated with primary antibodies in TBS-T overnight at 4 °C. After treatment with HRP-conjugated secondary antibodies in TBS-T for 1 h at RT, membranes were developed with Super Signal West Pico system (Thermo Fisher Scientific, USA) then, signals were visualized using autoradiographic films. Antibodies used: DR4 (ProSci 1139), DR5 (ProSci 2019), Vinculin (Sigma V4505), anti-rabbit IgG HRP-linked (Cell Signaling Technologies 7074), and goat anti-mouse IgG H&L (HRP) (Abcam ab97023). Vinculin was used as a loading and internal control.

Flow Cytometry Analysis of Cell Surface Receptors

Cells were harvested with trypsin, washed, and resuspended in PBS, then stained with Zombie UV™ Fixable Viability Kit (Biolegend 423107) for 30 minutes at RT, followed by a wash and then incubated with primary antibody for 60 minutes at 4 ºC in the dark; then samples were washed and incubated with secondary conjugated antibody for 60 minutes at 4 ºC in the dark. Samples were then resuspended in PBS with 1% FBS (Gibco, USA). Flow cytometry was performed using FACS Fortessa (BD) cell sorter and data was analyzed using FlowJo (BD). All washes were performed with PBS. Antibodies used: APC anti-human CD262 (DR5, TRAIL-R2) (Biolegend 307407), DR4 (Santa Cruz Biotechnology, sc-32255), and IgG1 cross-adsorbed goat anti-mouse, Alexa Fluor® 488, (Invitrogen A21121).

Annexin V Stain

Annexin V, FITC conjugate was purchased from BioLegend (San Diego, CA). 48 hours after transfection and/or sensitizer treatment, cells were resuspended in 100 µL staining buffer with 1:200 dilution of PI. 5 µL of Annexin V stain was added per well, and cells were incubated at RT for 15 minutes. Cells were spun down, washed once in 1X PBS, then resuspended in 2% FBS for flow cytometry, as described above. Geometric mean fluorescence (FL1-A) was calculated and reported. Histograms from representative wells were created using FlowJo v10 (Ashland, OR).

TRAIL ELISA

To collect lysates, cells were washed 3X with ice-cold PBS, then treated with cell extraction buffer (Invitrogen, Carlsbad, CA) supplemented with 5% protease inhibitor (Sigma Aldrich, St. Louis, MO) for 30 minutes in ice. Lysates were thoroughly mixed by pipetting, then centrifuged for 10 minutes at 13,000 rpm at 4°C. Supernatants were transferred and stored at -80°C until used. Conditioned cell culture media was collected and centrifuged for 10 minutes at 1,500 rpm at 4°C. Supernatants were also stored at -80°C. Human TRAIL ELISA was purchased from Invitrogen (Carlsbad, CA), and the assay was run according to manufacturer's instructions. Human TRAIL protein dilutions were used as standards and run in duplicate. Absorbance was measured at 450 nm using a Biotek Synergy 2 plate reader (Winooski, VT). Results from the standards were plotted and fit to a 5-parameter fit curve in GraphPad Prism 6 (San Diego, CA). Sample concentrations were calculated by interpolating the fit curve.

Total protein contents of cell lysates were measured using a Pierce™ BCA Protein Assay Kit (Waltham, MA). Bovine serum albumin (BSA) standards were prepared and run in duplicate to create a standard curve. The kit was used following manufacturer's instructions, and absorbance was measured at 562 nm on a Biotek Synergy 2 plate reader (Winooski, VT). Absorbance

measurements from the BSA standards were plotted and fit to a 5-parameter fit curve in Graphpad Prism 6 (San Diego, CA). Protein concentrations of samples were determined by interpolating the fit curve. TRAIL concentration in each sample was normalized to total protein content by BCA and was reported as pg of TRAIL per ug total protein.

Animal Models

All *in vivo* procedures were approved and overseen by the Johns Hopkins Institutional Animal Care and Use Committee (IACUC). To establish xenograft tumors, 1 million HepG2 cells were resuspended in 100 μL of 50% Matrigel matrix HC (Corning, Corning, NY) and 50% HBSS. Cells were injected subcutaneously in the hind flank of female 6-8 week-old athymic nude mice (The Jackson Laboratory, Bar Harbor, ME). During implantation, animals were anesthetized with 2.5% isoflurane in oxygen. Tumors developed in ~80% of mice after 14 days.

In vivo *gene delivery to SC tumors*

To make NPs for *in vivo* gene delivery, PBAE 536 was diluted in pH 7.4 sodium acetate, then fLuc plasmid was added for a final DNA concentration of 0.1 μg/μL. The polymer to DNA weight ratio was maintained at 25 w/w, and final sodium acetate concentration was 25 mM. NPs were stored at -80°C and thawed immediately prior to injection. Animals were anesthetized under isoflurane, and 50 μL of NPs were injected into the tumor using an insulin syringe, for a final 10 μg DNA dose. After 24, 48, 72, and 96 hours, live *in vivo* imaging was performed using an IVIS Spectrum imaging system (Perkin Elmer, Waltham, MA). 150 mg/kg D-luciferin (Gold Biotechnology, St. Louis, MO) was administered intraperitoneally to mice, then imaging was performed 10 minutes later. Images were analyzed across regions of interest (ROI) using Living Image software (Perkin Elmer, Waltham, MA).

Anti-tumor Efficacy and Survival Study

Mice were implanted with HepG2 tumors as previously described. PBAE NPs were synthesized with fLuc or sTRAIL plasmid in pH 7.4 sodium acetate at a DNA dose of 0.2 μg/μL and stored at -80°C. 14 days after tumor implantation, mice were randomized to three groups: (1) fLuc (control) NP + vehicle (N=7), (2) vorinostat only (N=3), (3) sTRAIL NP + vorinostat (N=8). Every four days, beginning on Day 14, mice received intratumoral injections of NPs and retroorbital injections of 100 μL vehicle or 150 μM vorinostat. Tumor dimensions were measured every other day using calipers, and area was calculated by multiplying the longest dimension (length) by its perpendicular width. An animal was sacrificed when its tumor area grew larger than 200 mm^2.

Statistical Analysis

All data is presented as a mean ± standard error of replicate tests. Comparisons between two groups were performed using a student's t test. Comparisons between multiple (>2) groups were performed using one-way ANOVA and Tukey or Dunnett post-hoc test for multiple comparisons. Tests between groups with multiple factors were performed using two-way ANOVA and Sidak's multiple comparison test. All statistical analyses were performed using GraphPad Prism 6 (San Diego, CA).

4.3 Results

PBAE NPs Enable DNA Delivery to HepG2 In Vitro and In Vivo

PBAEs are a class of biodegradable polyesters that have been employed for nucleic acid delivery to a wide range of cell types.[25] To form DNA NPs, PBAE cationic polymer is combined with anionic plasmid DNA at varying weight/weight (w/w) ratios, and the polyelectrolytes self-assemble electrostatically into polyplexes. These NPs facilitate efficient cellular uptake, endosomal escape, and expression of the encapsulated gene cargo. Our lab has shown that by

varying the composition of PBAE polyplexes, we can tune transfection efficacy in a wide range of cell types, while minimizing NP cytotoxicity.[26,27] Notably, we recently used high-throughput screening to optimize DNA delivery to an array of nine HCC cells lines and identified a polymer termed PBAE 536 **(Figure 4.2A)** as the superior candidate for gene delivery across these cell lines.[28] Therefore, we selected PBAE 536 NPs as a non-viral DNA delivery vehicle for HCC cells in this study.

PBAE NPs were characterized and evaluated for DNA delivery in both HCC cells and healthy human hepatocytes. PBAE 536 was synthesized via Michael addition in a two-step reaction **(Figure 4.3)**. To form NPs, PBAE 536 was combined with eGFP-N1 plasmid DNA at 25 w/w and allowed to self-assemble in sodium acetate (pH=5). Electrostatic interactions between the cationic polymer and anionic nucleic acid facilitated the formation of NPs with a hydrodynamic diameter of ~200 nm and a zeta potential of +16 mV. Gel electrophoresis was performed to quantify DNA encapsulation efficiency as a function of w/w ratio. Encapsulation efficiency was ~100% for all formulations tested **(Figure 4.4)**. Dynamic light scattering (DLS) measurements were performed on NPs formulated with various plasmid DNAs as well as PBAE polymer alone. We determined that NP size is independent of the plasmid sequence, and there is a significant decrease in particle size in the absence of plasmid DNA, demonstrating that electrostatic complexation drives the formation of the NPs **(Figure 4.5)**. To evaluate these NPs for gene delivery, *in vitro* cultures of HepG2 human HCC cells and THLE-3 healthy human hepatocytes were incubated with varying doses of eGFP-N1 PBAE 536 NPs. Increasing doses of NPs caused increased toxicity in both HepG2 and THLE-3 cells **(Figure 4.2B)**. Transfection efficacy was also dose-dependent, with increasing transfection with higher DNA doses in both cell types **(Figure 4.2C)**. An intermediate dose of 600 ng DNA per well was selected for further

studies because this was the lowest dose tested with significantly increased transfection in HepG2 HCC cells over THLE-3 hepatocytes. At this dose, toxicity was maintained below 15% for both cell types, and transfection rates were 41±3% and 27±1% in HepG2 and THLE-3 cells, respectively. Therefore, PBAE 536 NPs enable specific transfection of HepG2 cells over healthy hepatocytes, without toxicity to either cell line. HepG2 cells transfected with empty pN3 backbone plasmid showed similar toxicity profile to eGFP transfected cells and no significant fluorescence, indicating that transgene expression does not cause significant toxicity or background fluorescence in transfected cells **(Figure 4.6)**. These results confirm a biomaterial-mediated cancer-specificity of PBAE 536 NPs that has been previously reported.[29]

PBAE NP Transfection with sTRAIL Plasmid Results in TRAIL Protein Secretion

With the aim of developing a TRAIL gene therapy with a potent bystander effect, we engineered a secretable TRAIL (sTRAIL) plasmid **(Figure 4.7A)**. The non-viral sTRAIL construct, based on a viral construct developed by Shah et al., is comprised of three components: 1) A secretion signal derived from the extracellular domain of Flt3L, a ligand for the Flt tyrosine kinase receptor involved in protein secretion, 2) An isoleucine zipper trimerization domain to facilitate the assembly of a biologically active TRAIL homotrimer, and 3) The apoptosis-inducing sequence derived from the N-terminus of the human TRAIL sequence.[24] The coding sequences of these three domains were combined and inserted into the multiple cloning site of the pN3 backbone downstream of the CMV promoter-enhancer sequence.[30] The full cDNA sequence can be found in **Figure 4.8** (Addgene #154246). As a positive control, we utilized a plasmid encoding for the endogenous transmembrane human TRAIL protein in a pEGFP-C3 backbone, which we refer to as mTRAIL (membrane TRAIL) to differentiate it from secretable TRAIL (sTRAIL).[31,32]

Next, we evaluated TRAIL protein expression and secretion in cells transfected with sTRAIL and mTRAIL plasmids. PBAE 536 NPs were fabricated with mTRAIL or sTRAIL DNA, and these NPs were used to transfect HepG2 cells. After 48 hours, lysates and media samples were collected from transfected cells, and an ELISA for human TRAIL was performed on these samples. These results showed that cells treated with sTRAIL-NPs had intracellular TRAIL expression of 530 pg per μg of total protein, an expression level similar to cells treated with the mTRAIL positive control plasmid **(Figure 4.7B)**. However, there were striking differences in the conditioned cell culture media from mTRAIL and sTRAIL transfected cells. sTRAIL-treated cells secreted TRAIL protein extracellularly, with a concentration of 850 pg/mL after 48 hours **(Figure 4.7C)**. However, cells transfected with mTRAIL showed no detectable protein secretion. Taken together, these results confirm that the sTRAIL sequence developed for these studies encodes for human TRAIL protein, as detected by ELISA. Additionally, the modifications made in the engineered sTRAIL cDNA enable secretion of this TRAIL protein.

We next measured cellular viability to confirm that the protein secreted by sTRAIL transfected cells maintained the pro-apoptotic function of TRAIL. After 24 hours, HepG2 cells treated with sTRAIL NPs are sparser, rounded, and form smaller clumps than cells transfected with control eGFP-N1 NPs (**Figure 4.7D).** By MTT assay, the viability of sTRAIL transfected cells was reduced by 37% over untreated cells, while the loss in viability from control GFP NPs was only 1% **(Figure 4.7E).** Transfection with mTRAIL showed only 21% decrease in viability, although there is not a statistically significant difference in comparison to sTRAIL transfected cells. These results suggest that the modifications to the sTRAIL sequence did not mitigate the anticancer effect of TRAIL protein.

HDAC Inhibitors Sensitize HepG2 cells to TRAIL-Induced Apoptosis

HDAC inhibitors have been explored as a cancer treatment as a monotherapy and in combination with chemotherapy or radiation.[33] This class of drugs acts by inhibiting histone deacetylases, effectively opening chromatin and affecting gene expression at the epigenetic level, including key tumor suppressors and resistance genes.[34] Some studies have also shown a synergistic anti-cancer effects between TRAIL and HDAC inhibitors.[35–37] Western blot analysis shows that the HDAC inhibitor vorinostat alters death receptor expression in HepG2 cells **(Figure 4.9A)**. After 24-hour treatment with vorinostat, DR4 and DR5 expression are increased. Flow cytometry confirms that surface expression of DR5 increases with vorinostat exposure in a dose-dependent manner **(Figure 4.9B)**. However, surface DR4 is unchanged by vorinostat exposure, suggesting that trafficking of death receptors to the cell membrane remains a barrier. Receptor mutation studies have shown that DR5 has a greater contribution to TRAIL mediated apoptosis than DR4, so we hypothesized that increased DR5 expression alone could mediate a significant sensitizing effect.[38–40]

We combined PBAE 536 sTRAIL NP treatment with low doses of three HDAC inhibitors as sensitizing agents: vorinostat, sodium butyrate, and MS-275. HepG2 cells were incubated with NPs for 2 hours, then sensitizers were added. While HDAC inhibitors have shown promise as anti-cancer agents, we used low doses with limited toxicity to cancer cells when used alone **(Figure 4.10)**. After 48 hours, viability was measured by MTT assay, and treatment wells were normalized to wells treated with control GFP NPs and the same sensitizer dose to isolate TRAIL-mediated apoptosis.

HepG2 cells treated with HDAC inhibitors showed higher TRAIL-mediated cell death, compared with TRAIL NP treatment alone **(Figure 4.9C-E)**. This sensitizing effect was dose-dependent, with higher HDAC inhibitor concentration resulting in >70% loss in viability. This

suggests that the increased surface DR5 expression from HDAC inhibitor treatment effectively sensitize HepG2 cells to TRAIL-mediated cell death. Further, combination treatment with sTRAIL NPs was more potent than with mTRAIL NPs at most of the HDAC inhibitor doses tested. This demonstrates that the bystander effect enabled by TRAIL secretion increases the potency of TRAIL gene therapy.

Combination Treatment of sTRAIL PBAE NPs and HDAC Inhibitors shows Cancer-Specific Apoptosis In Vitro

We evaluated apoptotic cell death by quantifying phosphatidyl serine expression on the outer cell membrane using Annexin V staining. Apoptosis in HepG2 cells increases with sTRAIL transfection, as indicated by a shift in the Annexin V histogram curve **(Figure 4.11A).** Annexin V staining further increases with higher HDAC inhibitor doses, confirming that TRAIL-mediated apoptosis is dose dependent with HDAC inhibitor concentration. This increased Annexin V staining is not observed in GFP-transfected HepG2 cells treated with HDAC inhibitors **(Figure 4.11B)**. This confirms that treatment-mediated apoptosis is due to a synergistic effect from secreted TRAIL and HDAC inhibitors, not from the inhibitors alone or NP cytotoxicity.

Next, we evaluated the cancer-specificity and off-target toxicity of our combination approach by comparing treatment effect in HepG2 HCC cells to THLE3 hepatocytes. While TRAIL-induced apoptosis is generally considered cancer-specific, there is evidence that modified versions of TRAIL protein may cause hepatotoxicity in healthy human cells.[41] Further, certain sensitizing drugs, including HDAC inhibitors, have shown hepatotoxicity when combined with TRAIL therapy.[42] We treated both HepG2 HCC and THLE3 hepatocyte cell lines with sTRAIL NPs and HDAC inhibitors, then compared the treatment-mediated cell death in the healthy and cancer cell types **(Figure 4.11C)**. sTRAIL NPs alone caused very low toxicity in hepatocytes,

with 5% cell death in THLE3 cells compared with 27% in HepG2 cells. When HDAC inhibitors were used to sensitize the cells, treatment-mediated cell death was increased to 80-90%. The combination treatment was significantly more toxic to HepG2 cells over THLE3 at all HDAC inhibitor doses, with up to 40-fold higher cell death in the cancer cells. At higher HDAC inhibitor concentrations, cell death was increased in both HepG2 and THLE3 cells, indicating that the sensitizer dose must be carefully balanced to achieve a potent anticancer effect but not cause hepatotoxicity.

To deduce a mechanism of cancer-specificity, we used an ELISA to quantify TRAIL secretion from each cell type. HepG2 cells transfected with sTRAIL NPs secreted over 9-times more TRAIL protein than THLE3 cells **(Figure 4.11D).** To account for this difference in TRAIL secretion, THLE3 and HepG2 cells were treated with sTRAIL-conditioned media from transfected HepG2 cells. Without HDAC inhibitors, there was an 18% increase in HepG2 cell death with sTRAIL-conditioned media, indicating that the secreted TRAIL can potentiate a bystander effect to non-transfected cancer cells **(Figure 4.12)**. This effect was dose-dependent with HDAC inhibitor concentration, with the greatest effect of 37% TRAIL-mediated cell death at 2 μM vorinostat. The cancer-specificity of the sTRAIL NP treatment is predominantly due to higher and preferential transfection of HCC cells by PBAE 536 NPs leading to cancer-specific apoptosis.

Locally Administered PBAE NPs Enable DNA Delivery to HepG2 Xenograft Tumors and Slow Tumor Growth

To evaluate the translational potential of this approach *in vivo,* we assessed delivery of a reporter gene to HCC xenograft tumors. HepG2 tumors were established in the hind flank of athymic nude mice. PBAE NPs carrying a plasmid encoding firefly luciferase (fLuc)[43] were

injected directly into the tumors at a 5 μg DNA dose. 24, 48, 72, and 96 hours later, D- luciferin was administered, and *in vivo* bioluminescence imaging was performed. Strong luciferase expression was detected as early as 24 hours after treatment **(Figure 4.13A).** The average total flux across the tumor area was significantly higher than background, with an average total flux of $1.1 \pm 0.3 \times 10^6$ p/s **(Figure 4.13B)**. Radiance was greatest at 24 hours, then decreased over the course of four days, with the average total flux still 5-fold higher than background 96 hours after injection. All *in vivo* imaging can be found in **Figure 4.14.** This study confirmed that PBAE 536 NPs enable efficient gene delivery to HepG2 tumors *in vivo.*

Finally, to evaluate the *in vivo* efficacy of this system, subcutaneous xenograft HepG2 tumors were randomly assigned to one of three treatment arms: control fLuc NPs, IV vorinostat, or sTRAIL NPs with IV vorinostat. Nanoparticles harboring fLuc plasmid were selected to control for potential immunogenicity or toxicity from expression of a foreign protein and isolate the TRAIL-mediated anti-tumor effect.[44] Vorinostat was selected for *in vivo* testing because it showed promising *in vitro* anti-cancer activity in combination with sTRAIL NPs, and this drug is already clinically approved for human use to treat cutaneous T-cell lymphoma.[45] Starting 14 days after tumor implantation, every four days animals received intratumoral injection of PBAE NPs at a 10 μg DNA dose and/or intravenous administration of vorinostat at an estimated blood concentration of 10 μM. Tumor measurements over the first four days of treatment indicated that sTRAIL NP with vorinostat showed significantly slowed growth compared with animals receiving control NPs, from **(Figure 4.15A)**. No antitumor effect was observed from vorinostat alone. Median survival with sTRAIL NP and vorinostat treatment was 39 days, compared to a median of 26 days in the control NP alone and vorinostat alone groups **(Figure 4.15B)**, an increase of 50%.

4.4 Discussion

Here we describe a novel non-viral TRAIL gene therapy that induces potent and cancer-specific cell death in HCC. We utilize PBAE 536 NPs, a gene delivery vehicle which facilitates cancer-specific transfection in a wide range of HCC cell lines[28]. Structurally similar polymers have been optimized to specifically transfect brain, lung, and breast cancers, showing the versatility of this strategy in heterogeneous tumors and diverse cancer types.[29,46–48] While the mechanism of cancer-specific uptake and transfection is not fully understood, work by Zamboni et al. indicates that it is not driven by differences in cell division rate or NP uptake alone[28]. Our group found that changes in PBAE endcap structure bias the route of endocytosis, thereby influencing NP uptake and transfection.[26,49,50] Kim et al. showed that endocytosis route is predictive of transfection efficacy, with clathrin-mediated endocytosis of PBAE NPs disproportionately responsible for transfection over caveolae-mediated endocytosis and macropinocytosis.[48] Because endocytosis is one of many pathways frequently dysregulated in cancer, a link between material properties and biological mechanism may provide a means for rational design of cancer-targeting biomaterials.[51]

A non-viral plasmid was constructed to enable exogenous expression of a secretable trimeric TRAIL protein. We show that the HCC-targeted PBAE 536 NPs enabled therapeutic delivery of the new plasmid encoding for secretable TRAIL. Transfection of HepG2 HCC cells with sTRAIL plasmid results in high levels of TRAIL protein secretion, enabling cell killing of both transfected cells and non-transfected bystander cancer cells. Because non-viral delivery vehicles tend to have lower transfection efficacy than viral methods, and penetration of tumors can be difficult, this bystander effect is critical to achieve potent tumor killing. In this case, PBAE NPs enable 53% transfection, but >80% cell death by sTRAIL gene therapy.

Corroborative results by Shah et al. demonstrated that a cDNA encoding secretable TRAIL protein delivered virally to glioma cells also induced apoptosis in non-infected bystander cells.[24] Due to this bystander effect, transfection with sTRAIL cDNA produces a significantly enhanced therapeutic effect over non-secreted TRAIL. In contrast to previous work, the current research demonstrates that secretable TRAIL can be delivered efficaciously through non-viral NPs.

One major barrier to TRAIL therapy for cancer is the well-documented innate and acquired TRAIL resistance in certain tumors.[52] We used HDAC inhibitors vorinostat, sodium butyrate, and MS-275 to sensitize HepG2 cells to TRAIL gene therapy. With increasing concentrations of these small molecule drugs, there is a synergistic and dose-dependent increase in TRAIL-mediated cell death and upregulation of phosphatidyl serine on the outer cell membrane. Studies have shown that HDAC inhibitors caused upregulation of death receptors and Bcl-2 family proapoptotic factors while simultaneously downregulating inhibitors of apoptosis.[53] We found that vorinostat treatment induced upregulation of death receptor expression in HepG2 cells, suggesting a mechanism for the observed increase in TRAIL sensitivity. While it remains to be seen whether this sensitizing mechanism is conserved between cancer types, these results are further evidence that clinically approved HDAC inhibitors may improve clinical efficacy of TRAIL therapies, including gene therapy. Future studies of sTRAIL combination therapy in cells derived from primary human tumors would be valuable to better understand the heterogeneity of TRAIL resistance in a clinical setting. These studies may also reveal biomarkers that can be used to select for patients who are more likely to respond to TRAIL treatment in a personalized medicine approach.[46]

TRAIL is known to selectively initiate apoptosis in cancer cells while sparing normal cells, which has underpinned its investigation as a targeted cancer therapy. Interestingly, we find

that TRAIL-conditioned media combined with HDAC inhibitors may have equivalent or greater toxicity to healthy hepatocytes than to HCC cells. This contrasts with historical studies showing that TRAIL has minimal off-target toxicity to normal cells.[6,54] However, there have been published reports of elevated TRAIL toxicity in human hepatocytes relative to rodent or primate cells, which suggests that TRAIL sensitivity in normal cells is species-specific.[55] Additionally, combination treatment with sensitizing drugs has been reported to also sensitize healthy cells to TRAIL.[56] Therefore, the hepatotoxicity observed in these studies is consistent with the established literature. Death receptors have also been implicated in liver injury, including steatohepatitis and hepatitis.[57] Elevated DR4 and DR5 expression in these conditions result in increased TRAIL-mediated hepatocyte apoptosis. Because liver tumors often develop in patients with underlying liver disease, this highlights the importance of employing cancer-targeted delivery vehicles for TRAIL therapy to minimize off-target hepatotoxicity.[58] In further development of sTRAIL NPs in orthotopic tumor models, it will be essential to evaluate the bystander effect to healthy hepatocytes and closely monitor toxicity to the surrounding liver tissue.

The *in vivo* results demonstrate that PBAE NPs are effective for gene delivery to solid HCC tumors. A secretable TRAIL plasmid was constructed and validated to release sTRAIL to the supernatant, cause apoptosis of liver cancer cells, and synergize with small molecule drugs. PBAE NPs were validated to selectively transfect liver cancer cells over healthy hepatocytes, and via delivery of sTRAIL, enable liver cancer cell-specific killing. PBAE NPs shuttling a cDNA encoding for sTRAIL slow HepG2 tumor growth when combined with systemically administered vorinostat. To our knowledge, this is the first demonstrated application of PBAE NPs for the treatment of liver cancer. Successful development of a potent non-viral TRAIL gene therapy has

broad implications for cancer treatment. While subcutaneous tumors were used for these studies to allow direct access for intratumoral injection and measurement, they fail to accurately recapitulate the tumor microenvironment and interactions between cancer and stromal cells.[59] Further, intratumoral injection of therapeutic agents is not feasible in a clinical setting, and systemic delivery introduces additional delivery barriers, including serum aggregation or degradation, macrophage uptake, and intratumoral pressure.[60] Therefore, future work should employ orthotopic HCC tumor models to study biodistribution, off-target transfection, and systemic toxicity of PBAE NPs.

Because death receptors are upregulated on many cancer types, sTRAIL gene therapy is not limited to HCC. Tzeng et al. showed that PBAE NPs encoding for membrane-expressed TRAIL selectively induced > 60% cell death in lung and pancreatic cancers, suggesting that these cancer types may be suitable future targets for sTRAIL NPs.[31] These NPs also have a promising safety profile, due to their rapid degradation in physiological conditions. Here we show that PBAE 536 NPs are non-toxic to hepatocytes, and PBAE NPs also have been proven safe in brain and retinal tissues *in vivo*.[61,62] Further, PBAE 536 NPs are within the size range to potentially passively target tumors by the EPR effect. In addition, recent work shows that PEG-conjugated PBAE NPs have enhanced stability and tumor penetrating properties.[63] Thus, non-viral PBAE sTRAIL NPs, with favorable pharmacokinetics and enabling sustained *in vivo* gene expression, may have therapeutic promise for various solid tumors.

4.5 Conclusion

Non-viral delivery of cDNA encoding for secreatable TRAIL in combination with HDAC inhibitors results in *in vitro* and *in vivo* anti-tumor efficacy in hepatocellular carcinoma with

minimal toxicity to human hepatocytes. Considering the safety benefits of utilizing a non-viral gene therapy vector, this approach should be investigated further for clinical use.

4.6 References

1. Wiley, SR, Schooley, K, Smolak, PJ, Din, WS, Huang, C-P, Nicholl, JK, *et al.* (1995). Identification and characterization of a new member of the TNF family that induces apoptosis. *Immunity* **3**: 673–682.

2. Pitti, RM, Marsters, SA, Ruppert, S, Donahue, CJ, Moore, A and Ashkenazi, A (1996). Induction of apoptosis by Apo-2 ligand, a new member of the tumor necrosis factor cytokine family. *J. Biol. Chem.* **271**: 12687–12690.

3. Hymowitz, SG, Christinger, HW, Fuh, G, Ultsch, M, O'Connell, M, Kelley, RF, *et al.* (1999). Triggering cell death: the crystal structure of Apo2L/TRAIL in a complex with death receptor 5. *Mol. Cell* **4**: 563–571.

4. LeBlanc, HN and Ashkenazi, A (2003). Apo2L/TRAIL and its death and decoy receptors. *Cell Death Differ.* **10**: 66–75.

5. Mérino, D, Lalaoui, N, Morizot, A, Schneider, P, Solary, E and Micheau, O (2006). Differential inhibition of TRAIL-mediated DR5-DISC formation by decoy receptors 1 and 2. *Mol. Cell. Biol.* **26**: 7046–7055.

6. Ashkenazi, A, Pai, RC, Fong, S, Leung, S, Lawrence, DA, Marsters, SA, *et al.* (1999). Safety and antitumor activity of recombinant soluble Apo2 ligand. *J. Clin. Invest.* **104**: 155–162.

7. Soria, J-C, Márk, Z, Zatloukal, P, Szima, B, Albert, I, Juhász, E, *et al.* (2011). Randomized phase II study of dulanermin in combination with paclitaxel, carboplatin, and

bevacizumab in advanced non-small-cell lung cancer. *J Clin Oncol* **29**: 4442–4451.

8. Belada, D, Mayer, J, Czuczman, MS, Flinn, IW, Durbin-Johnson, B and Bray, GL (2010). Phase II study of dulanermin plus rituximab in patients with relapsed follicular non-Hodgkin's lymphoma (NHL). *J. Clin. Oncol.* **28**: 8104.

9. Kelley, SK, Harris, LA, Xie, D, DeForge, L, Totpal, K, Bussiere, J, *et al.* (2001). Preclinical studies to predict the disposition of Apo2L/tumor necrosis factor-related apoptosis-inducing ligand in humans: characterization of in vivo efficacy, pharmacokinetics, and safety. *J. Pharmacol. Exp. Ther.* **299**: 31–38.

10. Dimberg, LY, Anderson, CK, Camidge, R, Behbakht, K, Thorburn, A and Ford, HL (2013). On the TRAIL to successful cancer therapy? Predicting and counteracting resistance against TRAIL-based therapeutics. *Oncogene* **32**: 1341–1350.

11. Griffith, TS, Stokes, B, Kucaba, TA, Earel, J, James, K, VanOosten, RL, *et al.* (2009). TRAIL gene therapy: from preclinical development to clinical application. *Curr. Gene Ther.* **9**: 9–19.

12. Zheng, L, Weilun, Z, Minghong, J, Yaxi, Z, Shilian, L, Yanxin, L, *et al.* (2012). Adeno-associated virus-mediated doxycycline-regulatable TRAIL expression suppresses growth of human breast carcinoma in nude mice. *BMC Cancer* **12**: 153.

13. Kock, N, Kasmieh, R, Weissleder, R and Shah, K (2007). Tumor therapy mediated by lentiviral expression of shBcl-2 and S-TRAIL. *Neoplasia (New York, NY)* **9**: 435.

14. Jiang, M, Liu, Z, Xiang, Y, Ma, H, Liu, S, Liu, Y, *et al.* (2011). Synergistic antitumor effect of AAV-mediated TRAIL expression combined with cisplatin on head and neck

squamous cell carcinoma. *BMC Cancer* **11**: 54.

15. Verdera, HC, Kuranda, K and Mingozzi, F (2020). AAV vector immunogenicity in humans, a long journey to successful gene transfer. *Mol. Ther.*

16. Chandler, RJ, Sands, MS and Venditti, CP (2017). Recombinant adeno-associated viral integration and genotoxicity: insights from animal models. *Hum. Gene Ther.* **28**: 314–322.

17. Hinderer, C, Katz, N, Buza, EL, Dyer, C, Goode, T, Bell, P, *et al.* (2018). Severe toxicity in nonhuman primates and piglets following high-dose intravenous administration of an adeno-associated virus vector expressing human SMN. *Hum. Gene Ther.* **29**: 285–298.

18. Yin, H, Kanasty, RL, Eltoukhy, AA, Vegas, AJ, Dorkin, JR and Anderson, DG (2014). Non-viral vectors for gene-based therapy. *Nat. Rev. Genet.* **15**: 541–555.

19. Zhang, B, Liu, B, Chen, D, Setroikromo, R, Haisma, HJ and Quax, WJ (2019). Histone deacetylase inhibitors sensitize TRAIL-induced apoptosis in colon cancer cells. *Cancers (Basel).* **11**: 645.

20. Choi, SA, Lee, C, Kwak, PA, Park, C-K, Wang, K-C, Phi, JH, *et al.* (2019). Histone deacetylase inhibitor panobinostat potentiates the anti-cancer effects of mesenchymal stem cell-based sTRAIL gene therapy against malignant glioma. *Cancer Lett.* **442**: 161–169.

21. Bruix, J, Boix, L, Sala, M and Llovet, JM (2004). Focus on hepatocellular carcinoma. *Cancer Cell* **5**: 215–219.

22. Arhoma, A, Chantry, AD, Haywood-Small, SL and Cross, NA (2017). SAHA-induced TRAIL-sensitisation of Multiple Myeloma cells is enhanced in 3D cell culture. *Exp. Cell Res.* **360**: 226–235.

23. Elmallah, MIY and Micheau, O (2019). Epigenetic regulation of TRAIL signaling: implication for cancer therapy. *Cancers (Basel).* **11**: 850.

24. Shah, K, Tung, C-H, Yang, K, Weissleder, R and Breakefield, XO (2004). Inducible Release of TRAIL Fusion Proteins from a Proapoptotic Form for Tumor Therapy. *Cancer Res.* **64**: 3236 LP – 3242.

25. Green, JJ, Langer, R and Anderson, DG (2008). A combinatorial polymer library approach yields insight into nonviral gene delivery. *Acc. Chem. Res.* **41**: 749–759.

26. Sunshine, JC, Peng, DY and Green, JJ (2012). Uptake and transfection with polymeric nanoparticles are dependent on polymer end-group structure, but largely independent of nanoparticle physical and chemical properties. *Mol. Pharm.* **9**: 3375–3383.

27. Bishop, CJ, Kozielski, KL and Green, JJ (2015). Exploring the role of polymer structure on intracellular nucleic acid delivery via polymeric nanoparticles. *J. Control. Release* **219**: 488–499.

28. Zamboni, CG, Kozielski, KL, Vaughan, HJ, Nakata, MM, Kim, J, Higgins, LJ, *et al.* (2017). Polymeric nanoparticles as cancer-specific DNA delivery vectors to human hepatocellular carcinoma. *J. Control. Release* **263**: 18–28.

29. Kozielski, KL, Ruiz-Valls, A, Tzeng, SY, Guerrero-Cázares, H, Rui, Y, Li, Y, *et al.* (2019). Cancer-selective nanoparticles for combinatorial siRNA delivery to primary human GBM in vitro and in vivo. *Biomaterials* **209**: 79–87.

30. Sapetschnig, A, Koch, F, Rischitor, G, Mennenga, T and Suske, G (2004). Complexity of translationally controlled transcription factor Sp3 isoform expression. *J. Biol. Chem.* **279**:

42095–42105.

31. Tzeng, SY, Wilson, DR, Hansen, SK, Quiñones-Hinojosa, A and Green, JJ (2016). Polymeric nanoparticle-based delivery of TRAIL DNA for cancer-specific killing. *Bioeng. Transl. Med.* **1**: 149–159.

32. Kagawa, S, He, C, Gu, J, Koch, P, Rha, S-J, Roth, JA, *et al.* (2001). Antitumor activity and bystander effects of the tumor necrosis factor-related apoptosis-inducing ligand (TRAIL) gene. *Cancer Res.* **61**: 3330–3338.

33. New, M, Olzscha, H and La Thangue, NB (2012). HDAC inhibitor-based therapies: can we interpret the code? *Mol. Oncol.* **6**: 637–656.

34. Lane, AA and Chabner, BA (2009). Histone deacetylase inhibitors in cancer therapy. *J. Clin. Oncol.* **27**: 5459–5468.

35. Srivastava, RK, Kurzrock, R and Shankar, S (2010). MS-275 sensitizes TRAIL-resistant breast cancer cells, inhibits angiogenesis and metastasis, and reverses epithelial-mesenchymal transition in vivo. *Mol. Cancer Ther.* **9**: 3254–3266.

36. Dzieran, J, Beck, JF and Sonnemann, J (2008). Differential responsiveness of human hepatoma cells versus normal hepatocytes to TRAIL in combination with either histone deacetylase inhibitors or conventional cytostatics. *Cancer Sci.* **99**: 1685–1692.

37. Pathil, A, Armeanu, S, Venturelli, S, Mascagni, P, Weiss, TS, Gregor, M, *et al.* (2006). HDAC inhibitor treatment of hepatoma cells induces both TRAIL-independent apoptosis and restoration of sensitivity to TRAIL. *Hepatology* **43**: 425–434.

38. Kelley, RF, Totpal, K, Lindstrom, SH, Mathieu, M, Billeci, K, DeForge, L, *et al.* (2005).

Receptor-selective mutants of apoptosis-inducing ligand 2/tumor necrosis factor-related apoptosis-inducing ligand reveal a greater contribution of death receptor (DR) 5 than DR4 to apoptosis signaling. *J. Biol. Chem.* **280**: 2205–2212.

39. Bagci-Onder, T, Agarwal, A, Flusberg, D, Wanningen, S, Sorger, P and Shah, K (2013). Real-time imaging of the dynamics of death receptors and therapeutics that overcome TRAIL resistance in tumors. *Oncogene* **32**: 2818–2827.

40. Bhere, D, Tamura, K, Wakimoto, H, Choi, SH, Purow, B, Debatisse, J, *et al.* (2018). microRNA-7 upregulates death receptor 5 and primes resistant brain tumors to caspase-mediated apoptosis. *Neuro. Oncol.* **20**: 215–224.

41. Lawrence, D, Shahrokh, Z, Marsters, S, Achilles, K, Shih, D, Mounho, B, *et al.* (2001). Differential hepatocyte toxicity of recombinant Apo2L/TRAIL versions. *Nat. Med.* **7**: 383–385.

42. Koschny, R, Walczak, H and Ganten, TM (2007). The promise of TRAIL—potential and risks of a novel anticancer therapy. *J. Mol. Med.* **85**: 923–935.

43. Safran, M, Kim, WY, O'Connell, F, Flippin, L, Günzler, V, Horner, JW, *et al.* (2006). Mouse model for noninvasive imaging of HIF prolyl hydroxylase activity: assessment of an oral agent that stimulates erythropoietin production. *Proc. Natl. Acad. Sci.* **103**: 105–110.

44. Ansari, AM, Ahmed, AK, Matsangos, AE, Lay, F, Born, LJ, Marti, G, *et al.* (2016). Cellular GFP toxicity and immunogenicity: potential confounders in in vivo cell tracking experiments. *Stem cell Rev. reports* **12**: 553–559.

45. Duvic, M, Talpur, R, Ni, X, Zhang, C, Hazarika, P, Kelly, C, *et al.* (2007). Phase 2 trial of oral vorinostat (suberoylanilide hydroxamic acid, SAHA) for refractory cutaneous T-cell lymphoma (CTCL). *Blood* **109**: 31–39.

46. Kim, J, Wilson, DR, Zamboni, CG and Green, JJ (2015). Targeted polymeric nanoparticles for cancer gene therapy. *J. Drug Target.* **23**: 627–641.

47. Mangraviti, A, Tzeng, SY, Kozielski, KL, Wang, Y, Jin, Y, Gullotti, D, *et al.* (2015). Polymeric Nanoparticles for Nonviral Gene Therapy Extend Brain Tumor Survival in Vivo. *ACS Nano* **9**: 1236–1249.

48. Kim, J, Kang, Y, Tzeng, SY and Green, JJ (2016). Synthesis and application of poly(ethylene glycol)-co-poly(β-amino ester) copolymers for small cell lung cancer gene therapy. *Acta Biomater.* **41**: 293–301.

49. Bhise, NS, Gray, RS, Sunshine, JC, Htet, S, Ewald, AJ and Green, JJ (2010). The relationship between terminal functionalization and molecular weight of a gene delivery polymer and transfection efficacy in mammary epithelial 2-D cultures and 3-D organotypic cultures. *Biomaterials* **31**: 8088–8096.

50. Kim, J, Sunshine, JC and Green, JJ (2014). Differential polymer structure tunes mechanism of cellular uptake and transfection routes of poly (β-amino ester) polyplexes in human breast cancer cells. *Bioconjug. Chem.* **25**: 43–51.

51. Floyd, S and De Camilli, P (1998). Endocytosis proteins and cancer: a potential link? *Trends Cell Biol.* **8**: 299–301.

52. Zhang, L and Fang, B (2005). Mechanisms of resistance to TRAIL-induced apoptosis in

cancer. *Cancer Gene Ther.* **12**: 228–237.

53. Singh, TR, Shankar, S and Srivastava, RK (2005). HDAC inhibitors enhance the apoptosis-inducing potential of TRAIL in breast carcinoma. *Oncogene* **24**: 4609–4623.

54. Walczak, H, Miller, RE, Ariail, K, Gliniak, B, Griffith, TS, Kubin, M, *et al.* (1999). Tumoricidal activity of tumor necrosis factor–related apoptosis–inducing ligand in vivo. *Nat. Med.* **5**: 157–163.

55. Jo, M, Kim, T-H, Seol, D-W, Esplen, JE, Dorko, K, Billiar, TR, *et al.* (2000). Apoptosis induced in normal human hepatocytes by tumor necrosis factor-related apoptosis-inducing ligand. *Nat. Med.* **6**: 564–567.

56. Ganten, TM, Koschny, R, Sykora, J, Schulze-Bergkamen, H, Büchler, P, Haas, TL, *et al.* (2006). Preclinical differentiation between apparently safe and potentially hepatotoxic applications of TRAIL either alone or in combination with chemotherapeutic drugs. *Clin. cancer Res.* **12**: 2640–2646.

57. Akazawa, Y and Gores, GJ (2007). Death receptor-mediated liver injury. *Semin. Liver Dis.* **27**, GEORG THIEME VERLAG: p 327.

58. Tsukuma, H, Hiyama, T, Tanaka, S, Nakao, M, Yabuuchi, T, Kitamura, T, *et al.* (1993). Risk factors for hepatocellular carcinoma among patients with chronic liver disease. *N. Engl. J. Med.* **328**: 1797–1801.

59. Newell, P, Villanueva, A, Friedman, SL, Koike, K and Llovet, JM (2008). Experimental models of hepatocellular carcinoma. *J. Hepatol.* **48**: 858–879.

60. Blanco, E, Shen, H and Ferrari, M (2015). Principles of nanoparticle design for

overcoming biological barriers to drug delivery. *Nat. Biotechnol.* **33**: 941.

61. Sunshine, JC, Sunshine, SB, Bhutto, I, Handa, JT and Green, JJ (2012). Poly (β-amino ester)-nanoparticle mediated transfection of retinal pigment epithelial cells in vitro and in vivo. *PLoS One* **7**.

62. Guerrero-Cázares, H, Tzeng, SY, Young, NP, Abutaleb, AO, Quiñones-Hinojosa, A and Green, JJ (2014). Biodegradable Polymeric Nanoparticles Show High Efficacy and Specificity at DNA Delivery to Human Glioblastoma in Vitro and in Vivo. *ACS Nano* **8**: 5141–5153.

63. Kim, J, Mondal, SK, Tzeng, SY, Rui, Y, Alkharboosh, R, Kozielski, KK, *et al.* (2020). Poly (ethylene glycol)-poly (beta-amino ester)-based nanoparticles for suicide gene therapy enhance brain penetration and extend survival in a preclinical human glioblastoma orthotopic xenograft model. *ACS Biomater. Sci. Eng.*

4.7 Figures and Tables

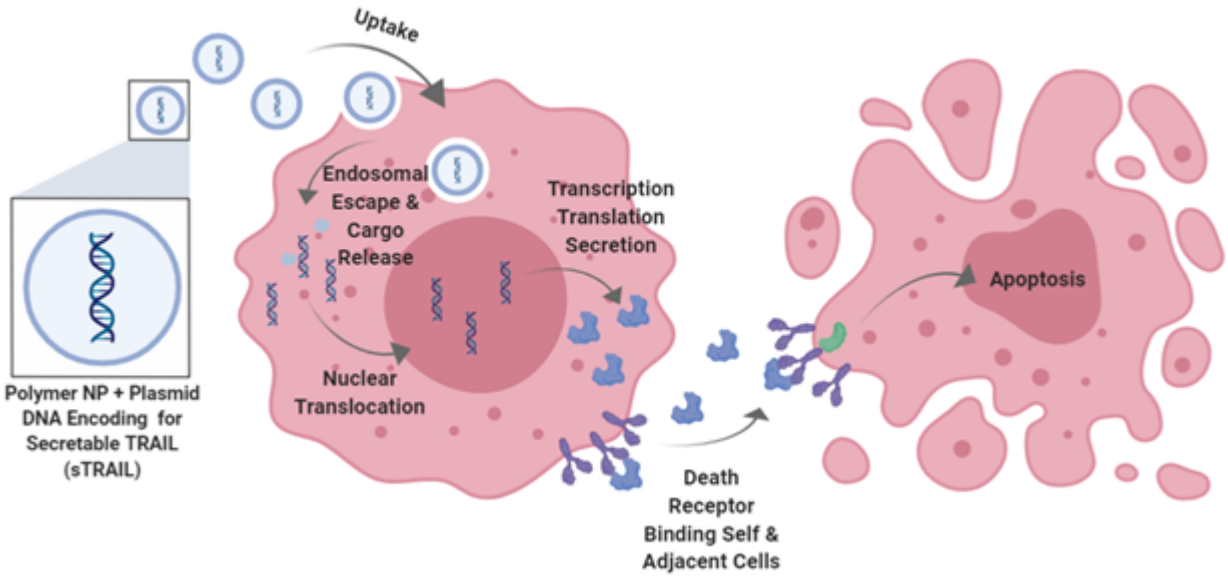

Figure 4.1 PBAE NPs for HCC-Specific TRAIL Secretion

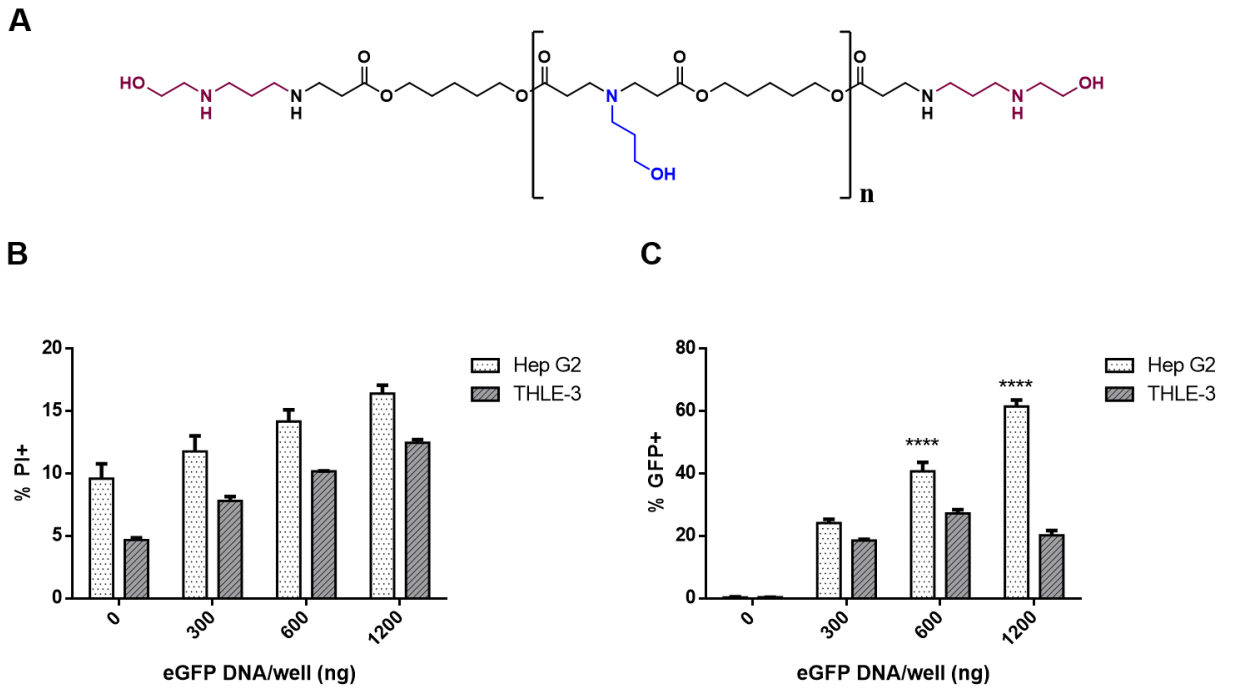

Figure 4.2 PBAE 536 NPs Enable Selective Intracellular Delivery of a Reporter Gene to HepG2 Cells *In Vitro*. A. Chemical structure of polymer 2-((3-aminopropyl)amino)ethanol end-modified poly(1,5-pentanediol diacrylate-co-3-amino-1-propanol) (PBAE 536). **B.** Viability of HepG2 and THLE3 cells after treatment with PBAE 536 NPs at a range of eGFP DNA doses. Toxicity was determined by staining samples 1:200 with propidium iodide (PI) and measuring the percentage of PI+ cells by flow cytometry. **C.** *In vitro* eGFP transfection of HepG2 HCC cells and THLE3 hepatocytes by PBAE 536 NPs measuring the percentage of GFP+ cells by flow cytometry. Data represent mean ± SEM of three replicate wells. Statistically significant differences in transfection between HepG2 and THLE3 determined using two-way ANOVA and Sidak's multiple comparisons test **** $P < 0.0001$

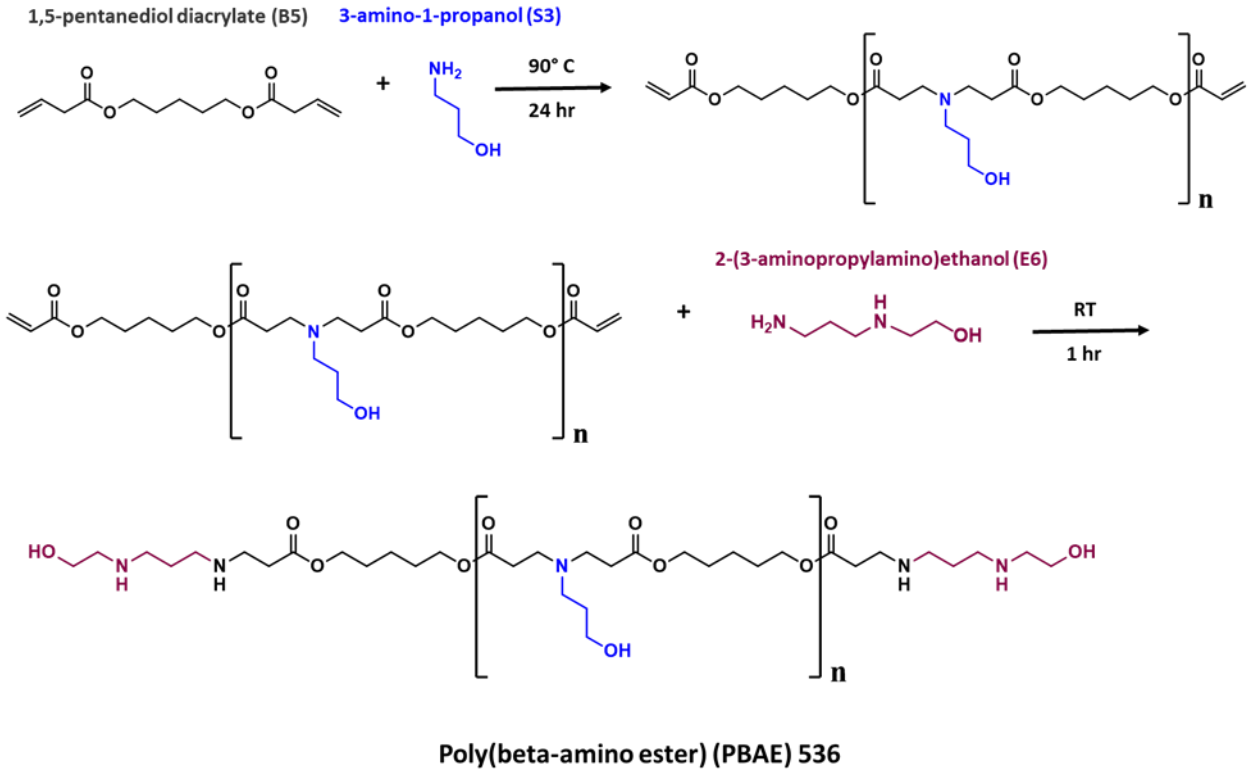

Figure 4.3 Synthesis of polymer 2-((3-aminopropyl)amino)ethanol end-modified poly(1,5-pentanediol diacrylate-co-3-amino-1-propanol) (PBAE 536). 1,5-pentanediol diacrylate (B5) is combined with 3-amino-1-propanol (S3) at a 1:1.1 ratio of B5 to S3 and reacted neat under stirring at 90° C for 24 hours. The resulting acrylate-terminated polymer is dissolved in THF and reacted with 2-(3-aminopropylamino)ethanol (E6) in 10-fold excess for 1 hour at room temperature. Endcapped polymer is ether purified and dried under vacuum. Resulting polymer had a weight average of 5638 Da and polydispersity of 1.29 by GPC.

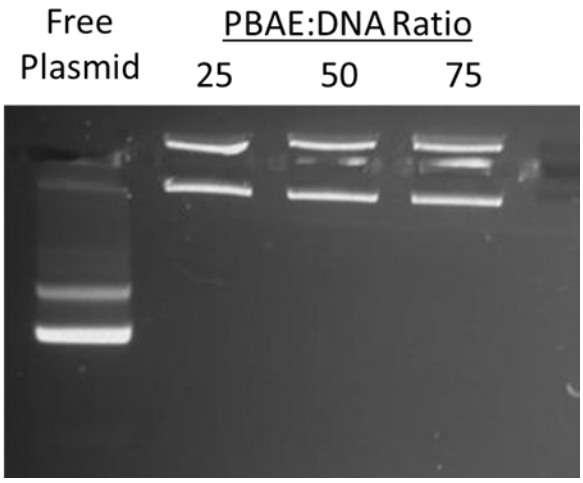

Figure 4.4 Encapsulation efficiency of PBAE 536 NPs. Gel electrophoresis of 0.03 µg/µL eGFP plasmid and PBAE NPs formulated with eGFP plasmid and a 25, 50, and 75 w/w ratio of PBAE 536 polymer.

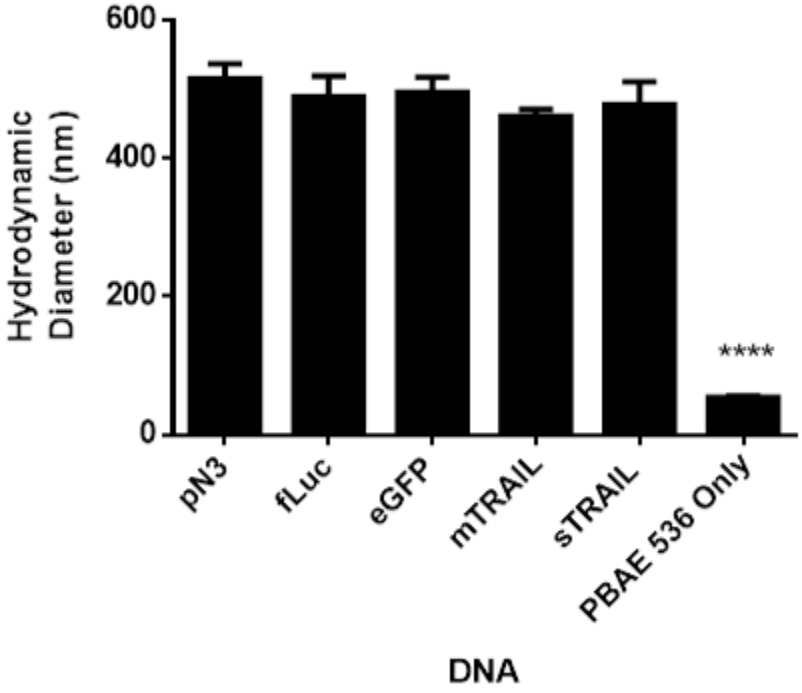

Figure 4.5 Hydrodynamic diameter of PBAE 536 NPs. Diameter of electrostatically complexed NPs comprised of PBAE 536 and plasmid DNA at a 25 weight ratio (w/w). Nanoparticles were synthesized in NaAc pH 7.4 and diluted in PBS pH 7.4 for DLS analysis

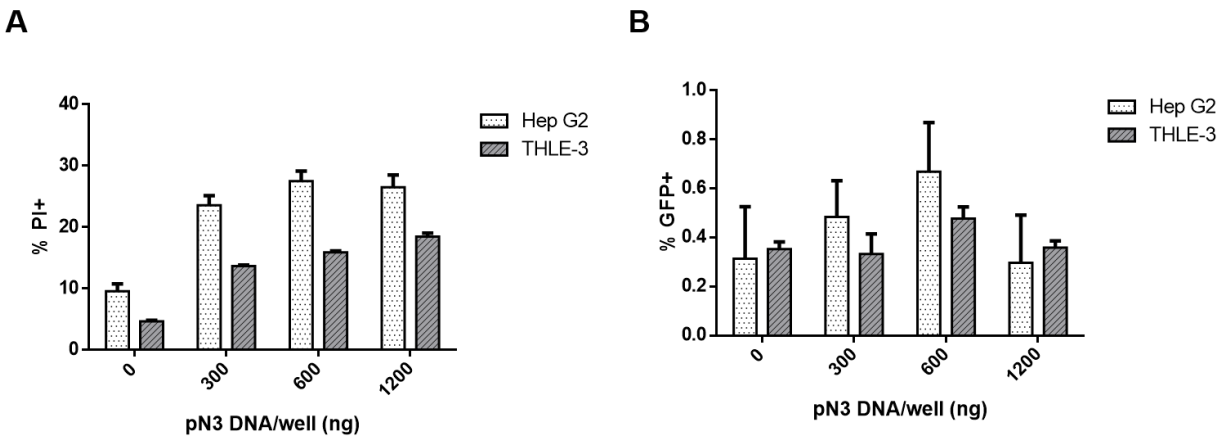

Figure 4.6 Viability and cellular fluorescence after transfection with empty pN3 backbone **A.** Viability of HepG2 and THLE3 cells after treatment with PBAE 536 NPs at a range of pN3 DNA doses. Toxicity was determined by staining samples 1:200 with propidium iodide (PI) and measuring the percentage of PI+ cells by flow cytometry. **B.** *In vitro* pN3 transfection of GFP+ HepG2 HCC cells and THLE3 hepatocytes transfected by PBAE 536 / pN3 NPs as measured by flow cytometry.

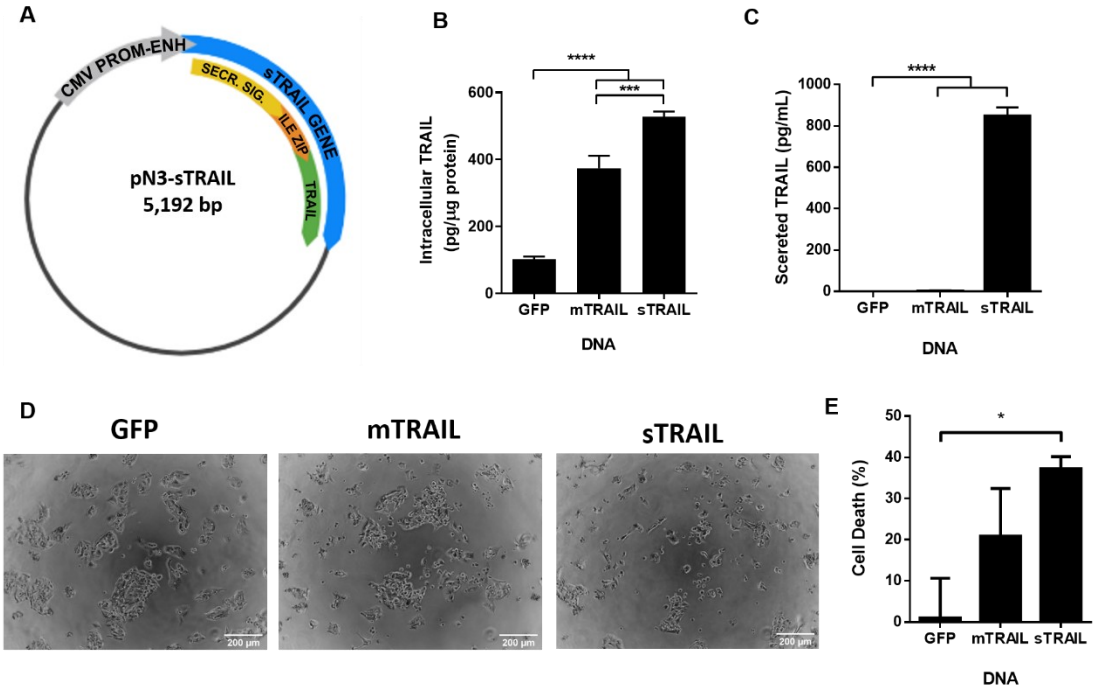

Figure 4.7 Transfection with PBAE 536 NPs Carrying the sTRAIL Plasmid Results in Production and Secretion of Human TRAIL Protein A. Map of the engineered sTRAIL plasmid. **B.** Intracellular and **C.** Secreted human TRAIL protein in HepG2 cells measured by ELISA after PBAE 536 NP treatment. **D.** Representative phase contrast images of HepG2 cells after transfection with PBAE 536 NPs containing eGFP, mTRAIL, or sTRAIL plasmid DNA. Scale bar = 200 µm. **E.** Treatment-mediated cell death in HepG2 cells measured by MTT, expressed as a percentage of metabolic activity normalized to untreated HepG2 cells. All data represented as mean ± SEM of n = 3 replicate wells. Significant differences between groups determined by one-way ANOVA and Tukey post-hoc test. *****P < 0.0001, ***P < 0.001 *P < 0.05*

sTRAIL Sequence:

ATGACAGTGCTGGCGCCAGCCTGGAGCCCAACAACCTATCTCCTCCTGCTGCTGCT
GCTGAGCTCGGGACTCAGTGGGACCCAGGACTGCTCCTTCCAACACAGCCCCATC
TCCTCCGACTTCGCTGTCAAAATCCGTGAGCTGTCTGACTACCTGCTTCAAGATTAC
CCAGTCACCGTGGCCTCCAACCTGCAGGACGAGGAGCTCTGCGGGGGCCTCTGG
CGGCTGGTCCTGGCACAGCGCTGGATGGAGCGGCTCAAGACTGTCGCTGGGTCCA
AGATGCAAGGCTTGCTGGAGCGCGTGAACACGGAGATACACTTTGTCACCAAATGT
GCCTTTCAGCCCCCCCCTAGCTGTCTTCGCTTCGTCCAGACCAACATCTCCCGCCT
CCTGCAGGAGACCTCCGAGCAGCTGGTGGCGCTGAAGCCCTGGATCACTCGCCA
GAACTTCTCCCGGTGCCTGGAGCTGCAGTGTCAGCCCGACTCCTCAACCCTGCCA
CCCCCATGGAGTCCCCGGCCCCTGGAGGCCACAGCCCCGACAGCCCCGATGAAG
CAGATCGAGGACAAAATTGAGGAAATCCTGTCCAAGATTTACCACATCGAGAACGA
GATCGCCCGGATTAAGAAACTCATTGGCGAGAGGGAATTCACCTCTGAGGAAACCA
TTTCTACAGTTCAAGAAAAGCAACAAAATATTTCTCCCCTAGTGAGAGAAAGAGGTCC
TCAGAGAGTAGCAGCTCACATAACTGGGACCAGAGGAAGAAGCAACACATTGTCC
TCTCCAAACTCCAAGAATGAAAAGGCTCTGGGCCGCAAAATAAACTCCTGGGAATC
ATCAAGGAGTGGGCATTCATTCCTGAGCAACTTGCACTTGAGGAATGGTGAACTGG
TCATCCATGAAAAAGGGTTTTACTACATCTATTCCCAAACATACTTTCGATTTCAGGA
GGAAATAAAAGAAAACACAAAGAACGACAAACAAATGGTCCAATATATTTACAAATA
CACAAGTTATCCTGACCCTATATTGTTGATGAAAAGTGCTAGAAATAGTTGTTGGTCT
AAAGATGCAGAATATGGACTCTATTCCATCTATCAAGGGGGAATATTTGAGCTTAAG
GAAAATGACAGAATTTTTGTTTCTGTAACAAATGAGCACTTGATAGACATGGACCATG
AAGCCAGTTTTTTCGGGGCCTTTTTAGTTGGCTAA

MTVLAPAWSPTTYLLLLLLLSSGLSGTQDCSFQHSPISSDFAVKIRELSDYLLQDYPVTV
ASNLQDEELCGGLWRLVLAQRWMERLKTVAGSKMQGLLERVNTEIHFVTKCAFQPPP
SCLRFVQTNISRLLQETSEQLVALKPWITRQNFSRCLELQCQPDSSTLPPPWSPRPLEA
TAPTAPMKQIEDKIEEILSKIYHIENEIARIKKLIGEREFTSEETISTVQEKQQNISPLVRER
GPQRVAAHITGTRGRSNTLSSPNSKNEKALGRKINSWESSRSGHSFLSNLHLRNGELVI
HEKGFYYIYSQTYFRFQEEIKENTKNDKQMVQYIYKYTSYPDPILLMKSARNSCWSKDA
EYGLYSIYQGGIFELKENDRIFVSVTNEHLIDMDHEASFFGAFLVG*

Flt3L (a.a. 1– 81)

Isoleucine Zipper

Human TRAIL N Terminus (a.a. 114 –281)

Figure 4.8: sTRAIL sequence A. DNA sequence for sTRAIL gene B. Protein translation of sTRAIL DNA

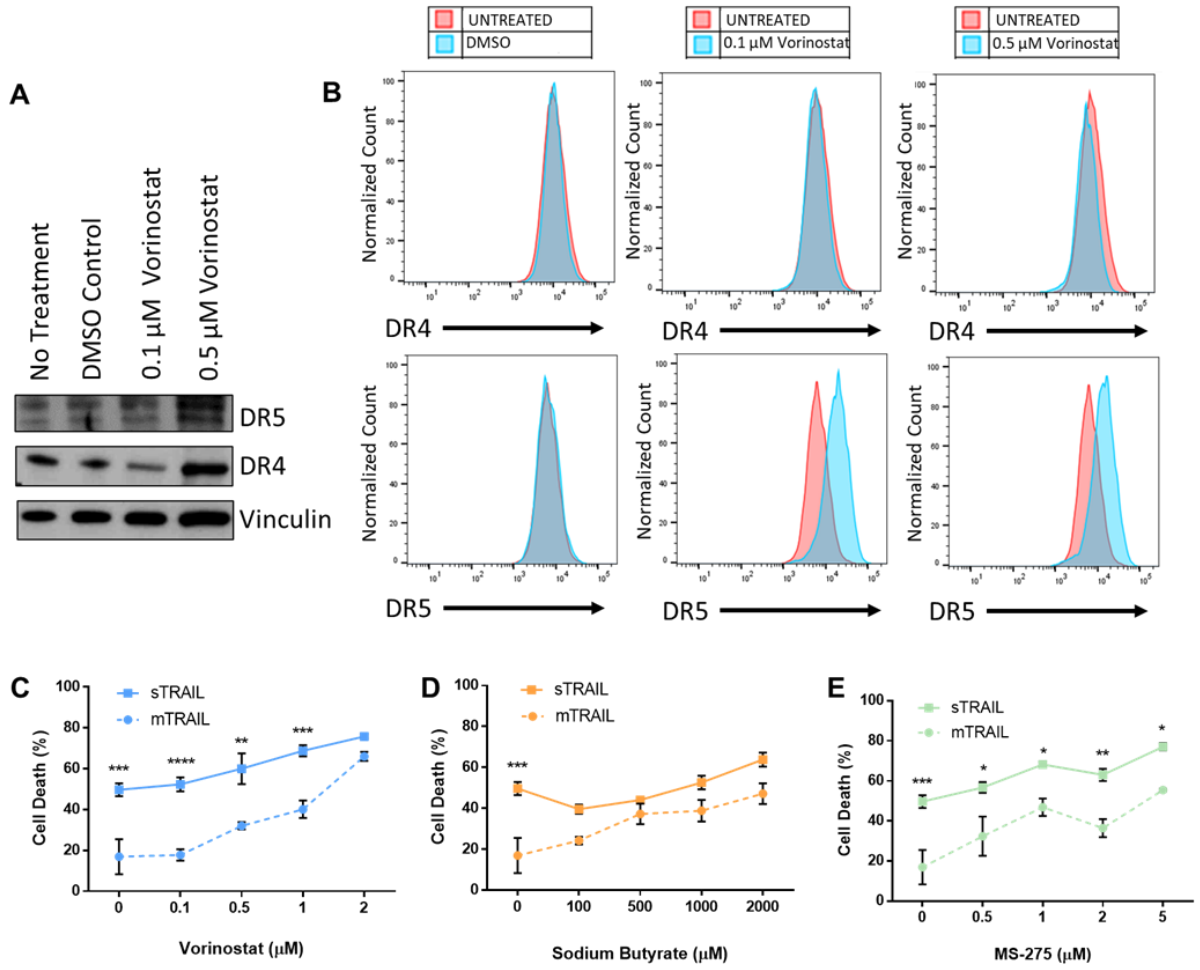

Figure 4.9 HDAC Inhibitors cause upregulation of death receptor expression and sensitize HepG2 cells to TRAIL NPs. HepG2 death receptor (DR4 and DR5) expression by **A.** Western blot and **B.** flow cytometry after 24-hour vorinostat treatment. HepG2 cell viability 48 hours after transfection with either mTRAIL or sTRAIL NPs and treated with varying doses of **C.** vorinostat, **D.** sodium butyrate, and **E.** MS-275. Data represented as mean ± SEM of n = 3 replicate wells. Significant differences between sTRAIL and mTRAIL-treated cells are determined by two-way ANOVA and Sidak's multiple comparison test. *$P < 0.05$, **$P < 0.01$, ***$P < 0.001$, ***$P < 0.0001$

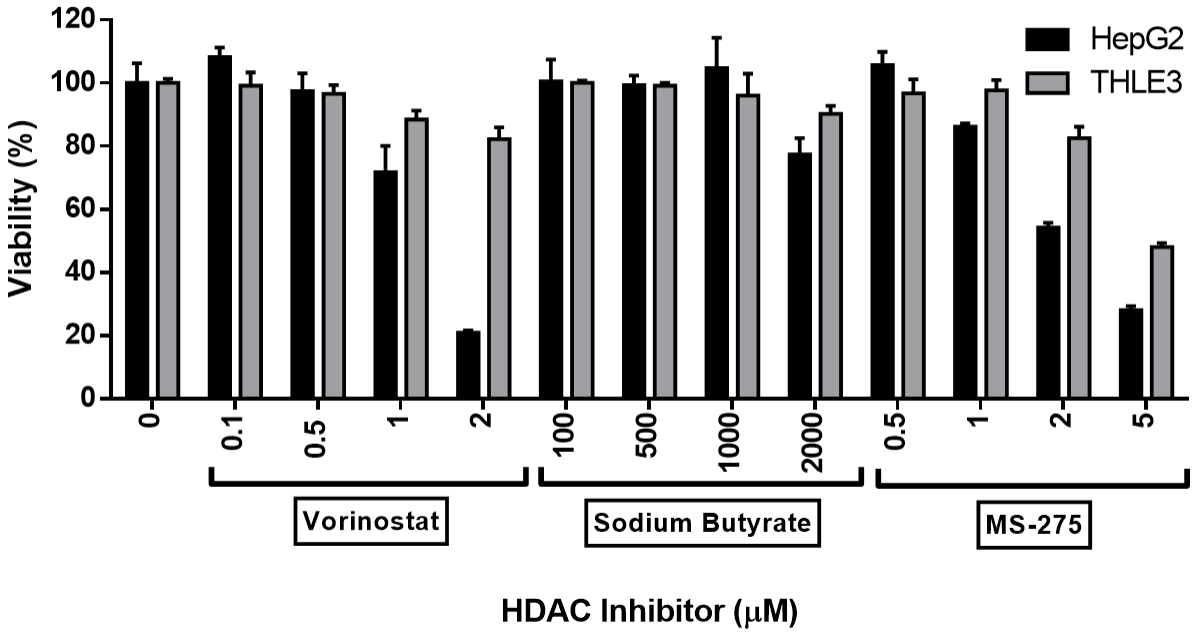

Figure 4.10 HDAC inhibitor cytotoxicity. Viability of HepG2 and THLE3 cells treated with HDAC inhibitors for 48 hours, measured by MTT

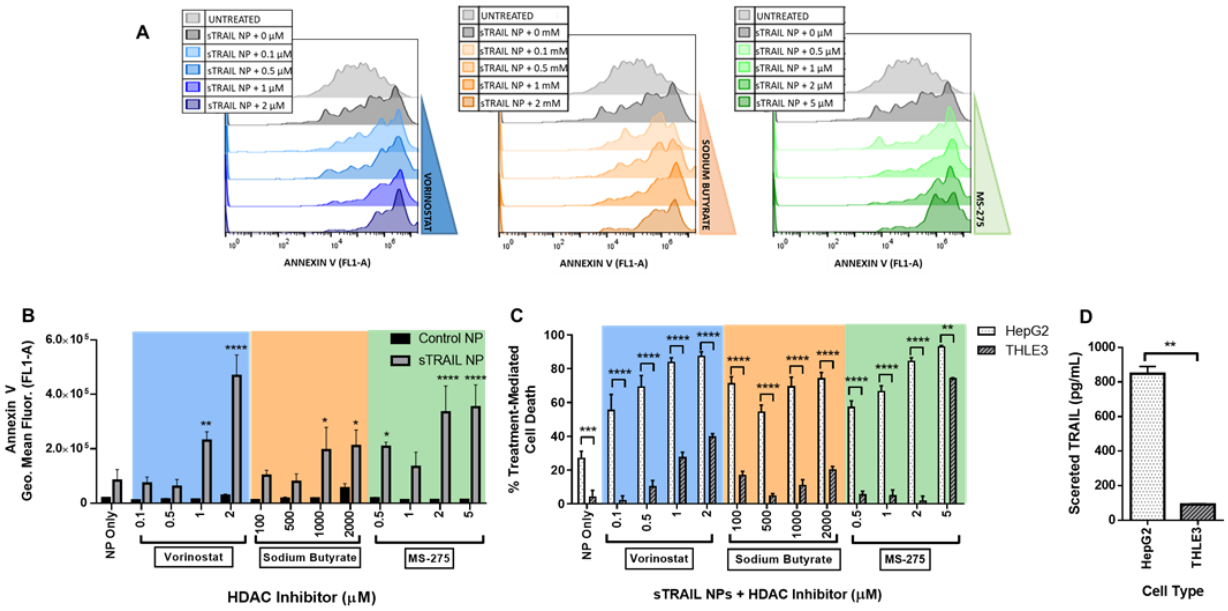

Figure 4.11 Combination Treatment with sTRAIL NPs and HDAC Inhibitors Causes a Dose-Dependent and Cancer-Specific Apoptosis. A. Histograms of Annexin V staining (FL1-A) in HepG2 cells transfected with sTRAIL NPs and treated with various doses of the HDAC inhibitors vorinostat, sodium butyrate, and MS-275. **B.** Quantification of Annexin V staining results by flow cytometry, showing HepG2 cells treated with HDAC inhibitors and with PBAE 536 NPs containing GFP or sTRAIL. Comparisons between sTRAIL and control NP treatments were made by two-way ANOVA and Sidak's multiple comparison test. **C.** Cell death 48 hours after transfection, normalized to negative controls treated with GFP NPs and corresponding HDAC inhibitor dose to calculate treatment-mediated cell death. Comparisons between HepG2 and THLE3 were made by two-way ANOVA and Sidak's multiple comparison test. **D.** Secreted human TRAIL protein in sTRAIL-transfected HepG2 HCC cells and THLE3 healthy hepatocytes, measured by ELISA 48 hours after transfection. Comparison of TRAIL secretion between HepG2 and THLE3 was made by unpaired t test with Welch's correction. Data represented as mean ± SEM of n = 3 replicate wells. *$P < 0.05$, **$P < 0.01$, ****$P < 0.0001$.

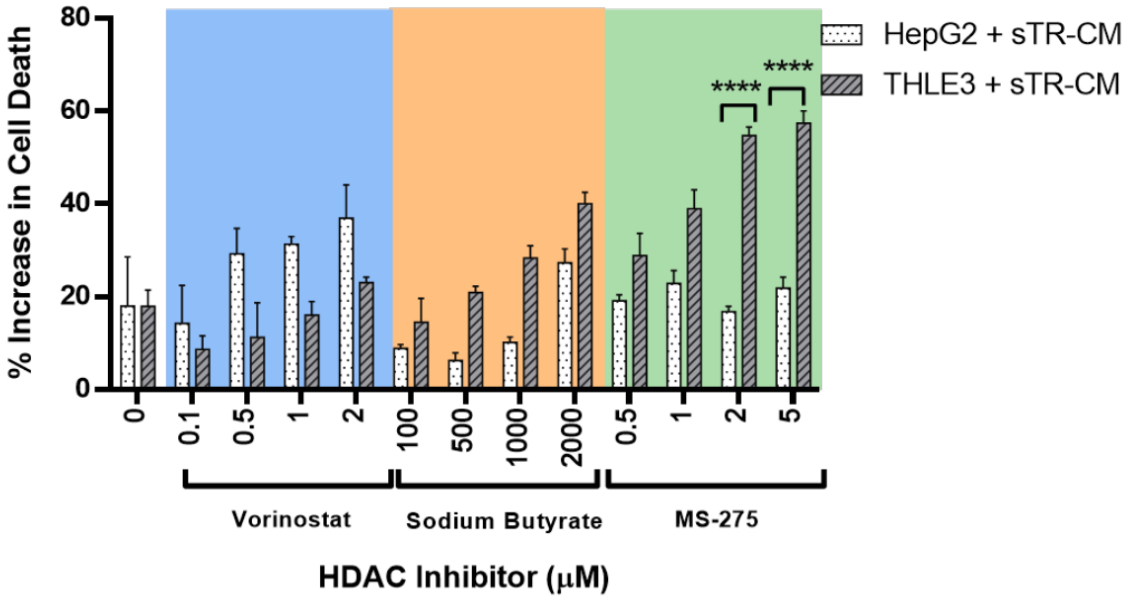

Figure 4.12 Effects of sTRAIL Conditioned Media Non-transfected HepG2 and THLE3 cells were treated with conditioned media from sTRAIL-transfected HepG2 cells (sTR-CM). After 48 hours, a viability assay was performed, and data was normalized to control wells with matched HDAC inhibitor exposure. All data is represented as mean ± SEM of n = 3 replicate wells. ***P* < *0.01,* ****P* < *0.0001.*

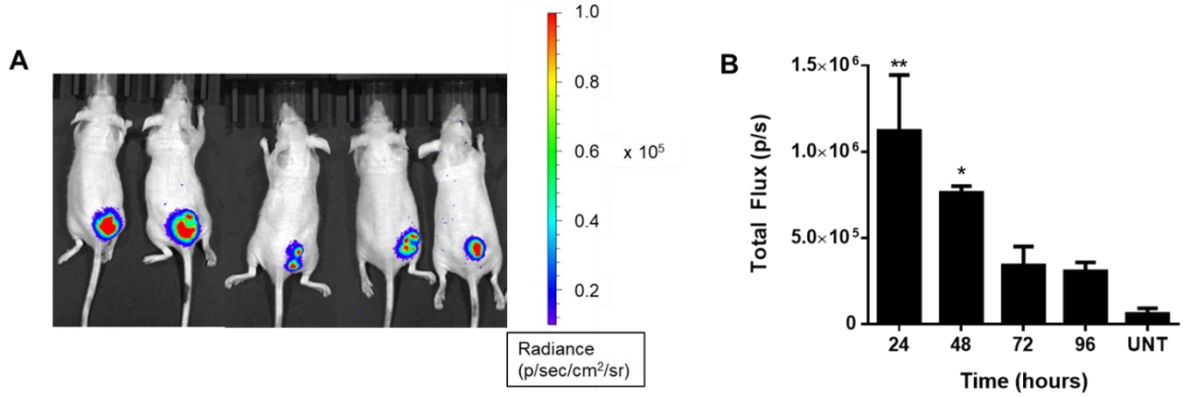

Figure 4.13 Intratumoral Administration of PBAE 536 NPs Results in Strong Gene Expression in Subcutaneous Xenograft Tumors. A. Bioluminescence images of subcutaneous HepG2 tumors 24 hours after treatment with fLuc-PBAE 536 NPs. **B.** Average bioluminescence over time in tumors injected with PBAE 536 NPs containing firefly luciferase plasmid DNA. Data represent mean ± SEM of 4-5 animals. Statistically significant differences between tumors treated and untreated tumors were calculated using one-way ANOVA with Dunnett's post-hoc test. **P* < *0.05,* ***P* < *0.01*

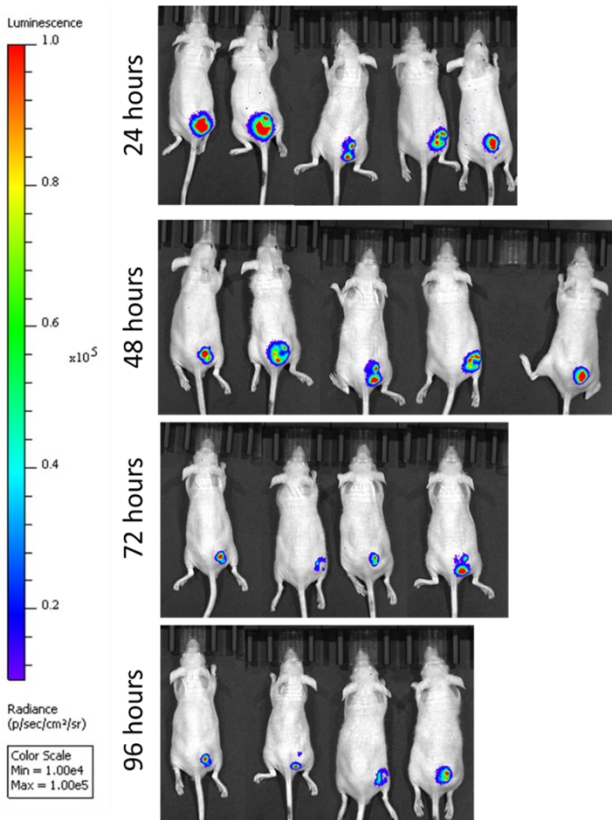

Figure 4.14 Intratumoral transfection time course. Bioluminescence images of subcutaneous xenograft HepG2 tumors treated with intratumoral injections of PBAE 536 NPs containing firefly luciferase plasmid DNA. Images were captured 24, 48, 72, and 96 hours after NP treatment.

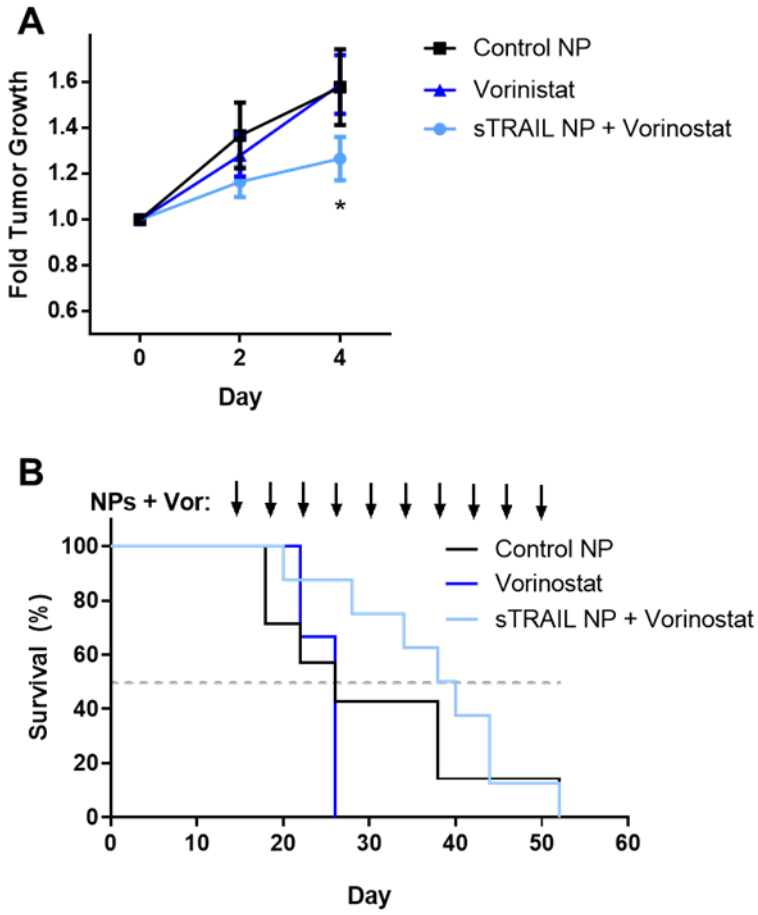

Figure 4.15 sTRAIL NPs Administered Intratumorally with Systemic Vorinostat Slow the Growth of HepG2 Subcutaneous Xenografts A. Normalized subcutaneous HepG2 tumor size over 4 days in animals treated with control NPs only (N=7), vorinostat only (N=3), and sTRAIL NPs with vorinostat (N=8). Data is represented as mean ± SEM. Significant differences in average tumor size between groups determined by two-way ANOVA with Sidak correction for multiple comparisons. *$P < 0.05$ **B.** Kaplan-Meyer survival curves of tumor-bearing mice. Dotted line drawn to indicate 50% survival.

Chapter 5: Poly(beta-amino ester) Nanoparticles for Transcriptionally Targeted Theranostic Gene Delivery to Hepatocellular Carcinoma

5.1 Introduction

Hepatocellular carcinoma (HCC) accounts for 90% of liver cancer and has an estimated overall 5-year survival rate of only 10%[1,2]. In the United States, incidence of HCC is increasing, and the mortality rate is rising faster than any other leading cancer[3]. While surgery or liver transplantation can be curative, most patients present with invasive HCC and are only eligible for palliative and locoregional treatments[4,5]. Broadly cytotoxic treatments, including chemotherapy and radiation, have off-target toxicities to healthy hepatocytes, which is particularly dangerous due to the high incidence of underlying liver disease[6,7]. Accordingly, there is a critical need for an effective, targeted treatment option for HCC.

In contrast to chemotherapy, gene therapies can target tumors by multiple mechanisms, including targeting of the delivery vehicle, transcriptional targeting, and molecular targeting[8]. This has led to interest in developing nucleic acid therapies. For example, oncolytic viruses have reached late stage clinical trials for treatment of bladder cancer, glioblastoma, head and neck cancer[9]. However, viral gene delivery methods have elicited concern due to risk of insertional mutagenesis and acute immunogenicity, which can be life-threatening. Viruses also have limitations of cargo capacity and manufacturing challenges, which limits scale-up[10].

In contrast, nanoparticle (NP) delivery vehicles are typically safer but historically suffered from low transfection efficiency[11]. Poly(beta-amino-ester) (PBAE) is a synthetic polymer that was developed to overcome barriers to intracellular gene delivery[12]. PBAEs contain hydrolysable ester bonds in the backbone which degrade on the order of hours and reduce the

toxicity of the polymer[13]. They also contain titratable amines that buffer the endosomal pH and facilitate endosomal escape and intracellular cargo release[14,15]. Cationic PBAE polymer complexes with anionic nucleic acids can be formulated as ~100 nm particles, which is a desirable size range for intracellular delivery and for accumulation in solid tumors through leaky vasculature[16,17].

Transcriptional targeting employs promoters with specific activity in target cells to restrict therapeutic gene expression[18,19]. There has been great interest in investigating regulatory elements that may target gene expression selectively in cancer cells. While truly cancer-specific promoters are relatively rare, notable examples include the promoter of telomerase[20], progression-elevated gene-3 (PEG-3)[21] and prostate-specific antigen (PSA)[22]. Alpha fetoprotein (AFP) is the main biomarker of liver cancer, as expression is undetectable in healthy adults, yet high levels are detected in ~80% of HCC cases[23]. AFP promoter and enhancer sequences have shown efficient and selective expression in AFP-producing HCC cells[24].

One hurdle to gene therapy is reducing the host immune system response to therapeutic nucleic acids. One such response is the recognition of unmethylated CpG sequences, which are found in bacterial DNA, by toll-like receptor 9 expressed in plasmacytoid dendritic cells[25,26]. When activated, the dendritic cells release cytokines to recruit and activate natural killer cells and T cells, and this has been shown to induce inflammation and shorten the duration of gene expression[27,28]. Therefore, there has been interest in developing CpG-free plasmids for gene therapy, including CpG free backbones, genes, and promoters[29–31].

Another hurdle is safe and selective delivery of nucleic acids to target cancer cells. We recently reported that select PBAE formulations enable robust and cancer-specific plasmid DNA delivery to HCC cells[32]. However, that initial finding has not yet been extended to tumor-

targeted therapy. Here we develop a completely CpG free transcriptionally targeted plasmid encoding for mutant herpes simplex virus type1 sr39 thymidine kinase (sr39) under the control of the AFP promoter and enhancer. Sr39 is a theranostic enzyme that 1) converts the prodrug ganciclovir (GCV) into a cancer-killing compound and 2) phosphorylates radiolabeled nucleoside analogs to enable PET imaging of gene expression (**Fig 1**). Combining two layers of selectivity, we show that an HCC-specific nontoxic, biodegradable nanocarrier (PBAE 536) with a transcriptionally targeted theranostic suicide gene therapy enables sr39 delivery to HCC tumors for safe and effective tumor control and molecular genetic imaging.

5.2 Methods

PBAE Synthesis

1,5-Pentanediol diacrylate (B5) (Monomer-Polymer and Dajac Labs, Trevose, PA), and 3-amino-1-propanol (S3) (Alfa Aesar, Ward Hill, MA) were combined neat at a 1:1.1 ratio for a 1.5 g total mass and allowed to polymerize under stirring for 24 hours at 90°C. This polymer was then dissolved in anhydrous THF. 2-(3-aminopropylamino)ethanol (E6) (Sigma-Aldrich, St. Louis, MO) was added in 10-fold molar excess and stirred at room temperature (RT) for 1 hour. The resulting polymer was washed 2X in diethyl ether and dried under vacuum for several days. Polymer was dissolved in anhydrous DMSO and stored with desiccant at -20°C at 100 mg/mL. Molecular weight was measured by gel permeation chromatography (GPC) relative to polystyrene standards (Waters 2414 Refractive Index Detector, Milford, MA).

NP Formation and Characterization

Plasmid DNA and PBAE 536 polymer were diluted separately in sodium acetate (25 mM, pH=5), then combined at equal volumes for a final DNA concentration of 0.03 mg/mL and polymer:DNA weight ratio (w/w) of 25. For transmission electron microscopy (TEM), NPs were

added to a plasma-treated, carbon-coated copper grid, stained with 0.5% uranyl acetate, then dried for one hour at RT. Images were acquired using a Philips/FEI BioTwin CM120 Transmission Electron Microscope. For aqueous analysis, NPs were diluted 5X in sodium acetate, then 1:1 in PBS. A Malvern Zetasizer Nano ZS (Malvern Instruments, Malvern, UK) was used to measure hydrodynamic radius and zeta potential.

Cell Culture

Hep 3b (ATCC® HB-8064™), SK-HEP-1 (ATCC® HTB-52™), PC-3 (ATCC® CRL-1435™), and THLE-3 (ATCC® CRL-11233™) cells were purchased from ATCC (Manassas, VA). Huh-7 was kindly provided by Dr. Phuoc Tran's laboratory from the Johns Hopkins University School of Medicine. Hep3b, SK-HEP-1 cells were cultured in Minimal Essential Medium (MEM) supplemented with 10% fetal bovine serum, 1% penicillin-streptomycin, 100 μM of MEM non-essential amino acids solution, and 1 mM of sodium pyruvate. Huh7 and PC-3 cells were cultured in high glucose Dulbecco's Modified Eagle Medium (DMEM) supplemented with 10% fetal bovine serum, 1% penicillin-streptomycin. THLE-3 cells were cultured in bronchial epithelial cell growth Medium (BEBM) with the additives from the kit (BEGM Bullet Kit [CC3170]; Lonza/Clonetics Corporation, Walkersville, MD), except gentamycin-amphotericin and epinephrine, 10% FBS and 1% penicillin-streptomycin. For THLE-3 culture, flasks and plates were coated with 0.01 mg/mL of human fibronectin, 0.03 mg/mL of bovine collagen type I, and 0.01 mg/mL of bovine serum albumin dissolved in BEBM basal medium and incubated overnight at 37°C. Coating solution was aspirated prior to seeding. THLE-3 cells were not used beyond passage 5. Cell cultures were maintained in a humidified incubator, at 37 °C, with 5% CO_2.

In Vitro Transfection

Cells were seeded in 96-well plates one day prior to transfection. Media was changed immediately prior to transfection. NPs were formulated as described above at 25 w/w and a final DNA concentration of 0.03 mg/mL (600 ng/well) or alternate dosing as specified. After waiting 10 minutes for assembly, 20 μL of NPs were added per well (100 μL of media). Cells were incubated with NPs for 2 hours, then media was changed. Viability was measured 24 hours after transfection using the MTS assay CellTiter 96 AQueous Nonradioactive Cell Proliferation Assay (Promega, Madison, WI). Transfection efficacy was determined 48 hours after using flow cytometry for GFP expression measurement. Cells were resuspended in 1X PBS with 2% FBS with a 1:200 dilution of propidium iodide, and a Attune NxT Flow Cytometer was used to measure GFP expression. Data was analyzed using FlowJo v10 (Ashland, OR). Events were gated on FSC-H and SSC-H to identify the cell population, then on BL1-A and YL1-A to gate for GFP expression in live cells.

CMV-sr39 and AFP-sr39

Geneious 8.0.4 (Biomatters, Auckland, New Zealand) was employed throughout the plasmid design process. The 1131 base pair sequence of the wild type herpes simplex virus (type 1 /strain RH2) thymidine kinase (HSV-TK) gene, obtained from the European Nucleotide Archive, was modified to produce the sr39 mutant[33], in which Leu, Ile, Phe, Ala, and Leu residues are replaced with Ile, Phe, Leu, Phe, and Met in the amino acid positions 159, 160, 161, 168 and 169, respectively. The 2144 base pair composite AFP enhancer and promoter sequence was obtained from the pDRVE-AFP-hAFP plasmid (Invivogen, San Diego, CA catatog # pdrive-afphafp). The sr39 gene was added to the 3' AFP enhancer and promoter sequence, separated by a the KpnI (5'-GGTACC-3') restriction endonuclease cutting site. A SbfI (5'-CCTGCAGG-3') restriction endonuclease cutting site was placed on the 5' end, and the NheI (5'-GCTAGC-3')

restriction endonuclease cutting site was added to the 3' end of the construct. This entire construct was then sent for custom synthesis by Genscript (Piscataway, NJ).

To synthesize the AFP-sr39 plasmid, 10 µg each of the gene synthesis product from Genscript and pCpGRich-mcs backbone from Invivogen (catalog # pcpgr-mcs) were separately digested with SbfI-HF and NheI-HF (New England Biolabs, Ipswich, MA) according to the manufacturer's instructions for 10 hours at 37°C. Digestion products were run on a 0.8% agarose gel and visualized under UV light. The bands of interest were excised from the gel, and DNA was recovered using the QIAquick Gel Extraction Kit (Qiagen catalog # 28704). DNA concentration from extraction products was assessed with a NanoDrop 2000 Spectrophotometer (Thermo Scientific), and ligation was carried out at a 1 to 7 vector to insert volume ratio. T4 DNA Ligase and buffer (NEB catalog # M0202S) were mixed with DNA at 4°C, and the ligation reaction was incubated at 16°C overnight. ChemiComp GT115 E. coli, acquired frozen from Invivogen (catalog # gt115-11), were transformed via heat shock using 5µL of the ligation product. Bacteria was cultured in 450 µL of SOC outgrowth medium (NEB catalog # B9020S) for 1 hour at 37°C. The full 500 µL of the bacteria suspension was streaked in an LB agar plate with Zeocin at 100 µg/mL. The plate was placed in a 37°C dark incubator for 16 hours. A single colony was then harvested, and bacteria allowed to grow for additional 8 hours in LB Broth (Quality Biological catalog # 340-004-101). QIAprep Spin Miniprep Kit (Qiaqen catalog # 27104) was used to isolate plasmid DNA, which was then sent for DNA sequencing (Sanger Method). This cloning process was repeated using KpnI-HF and NheI-HF to synthesize CMV-sr39.

CpGf-CMV-sr39

To eliminate all CpG dinucleotides within the sr39 gene, CpG-creating codons, i.e., containing a CpG or forming a CpG with the preceding or succeeding codons, were replaced with non-CpG-creating synonyms by following the degenerate human genetic code. The selection of the synonymous triplet substituting a CpG-creating codon was based on the Codon Usage Tabulated from GenBank (CUTG) and always prioritized synonyms with higher frequency of occurrence in humans. A 10 nucleotide construct containing the ScaI (5'-AGTACT-3') restriction endonuclease cutting site, and a 10 nucleotide sequence containing the NheI (5'-GCTAGC-3') restriction site were designed to flank the 5' and 3' ends of the gene, respectively. This construct was synthesized by Integrated DNA Technologies (IDT), and a 10 nucleotide overhang containing the ApaLI (5'-GTGCAC-3') restriction site was subsequently incorporated into the 5' end by PCR using FP: AATTCTGTGCACAGCTTAGACCAGTACTAT and RP: TGCTTATGCTTATATGGCTAATGCTAGCTC as primers. This CpG free sr39 insert was cloned into the pCpGfree-vitroNmcs backbone from Invivogen (catalog # pcpgvtn-mcsg) with the restriction enzymes ApaLI (NEB catalog # R0507S) and NheI-HF (NEB catalog # R3131S) as described above.

CpGf-AFP-sr39

To remove CpG dinucleotides from the AFP enhancer and promoter, the sequence evaluated for putative transcription factor binding sites using the TRANSFAC database (version 8.3) through the PROMO website[34,35]. A 95% similarity between predicted regulatory site and transcription factor matrix was the established threshold for a hit to be reported. CpG sequences within the AFP enhancer and promoter sequences were identified (total of 6) and modified according to the following strategies: 1) Only one nucleotide was replaced within each CpG

dinucleotide, and their purine or pyrimidine identity was maintained, i.e., cytosines were replaced by thymidines and guanines by adenines; and 2) The selection of cytosine or guanine for substitution was based on the distribution of regulatory sites. In the AFP promoter and enhancer, there were no cases in which both nucleotides were identified as being a part of predicted transcription factor binding sites. Next, a designed construct consisting of the CpG free sr39 gene was added to the 3' end of the CpG free AFP sequence. Also, a 1520 base pair sequence, corresponding to base pairs 4403 to 435 of the pCpGfree-vitroNmcs vector and containing the EcoRI restriction site, was added to the 5' end of the CpG free AFP sequence. This entire construct was then sent for custom synthesis by Genscript (Piscataway, NJ). This CpG free AFP-sr39 insert was cloned into the pCpGfree-vitroNmcs backbone from Invivogen (catalog # pcpgvtn-mcsg) with the restriction enzymes EcoRI-HF (NEB catalog # R3101S) and NheI-HF (NEB catalog # R3131S). Cloning was performed as described above.

TLR9 Activation Assay

HEK-Blue^{TM} hTLR9 cells were purchased from Invivogen (catalog # hkb-htlr9) and cultured according to manufacturer's instructions. Plasmid DNA or CpG ODN (positive control) was added at a volume of 20 µL per well. Cells were prepared in HEK-Blue^{TM} Detection medium, and ~80,000 cells were added to each well (180 µL volume). Cells were incubated overnight 37 °C, with 5% CO_2. Absorbance was measured at 620 nm using a Biotek Synergy 2 plate reader (Winooski, VT).

In vitro sr39 expression PCR

Transfection of Hep3b cells with sr39 plasmids was performed as described above. The mRNA was harvested 48 hours later, reverse transcribed, and prepared for PCR using a Cells-to-CT 1-step Power SYBR Green kit from Invitrogen (catalog # A25600) according to the

manufacturer's instructions. The optional DNase step was performed to remove plasmid DNA from the samples. The following primers were designed and used for sr39 detection: FP: GCCCTTCCTGAGGACAGACAC, RP: GGAGGCTGGGAGCTCACATG. qRT-PCR was performed using a StepOnePlus™ Real-Time PCR System (Applied Biosystems, Foster City, CA) with the cycling parameters specified for the Cells-to-CT kit. Threshold and baseline values were standardized across all samples and all runs to ensure accurate comparison. The comparative CT method was used to quantify relative expression levels[36]. Barcode amplification was normalized to the housekeeping gene GAPDH to quantify NP accumulation of each PBAE with each barcode relative to the genomic DNA content. Then, this value was normalized to non-specific background amplification in untreated cells, by subtracting the ΔC_T of amplification in untreated cells, thereby obtaining $\Delta\Delta C_T$.

$$\Delta\Delta C_T = (C_{T\ sr39} - C_{T\ GAPDH})_{treated} - (C_{T\ sr39} - C_{T\ GAPDH})_{untreated}$$

In vitro sr39 Cell Killing Assay

GCV was purchased from Invivogen (catalog # sud-gcv) and reconstituted according to the manufacturer's instructions. Transfection of Hep3b, Huh 7, SK-HEP-1, PC-3 and THLE-3 cells with sr39 plasmids was performed as described above. One day after transfection, media was prepared with GCV at the desired concentration, then added to the cells. For long-term studies, media with GCV was replenished every two days. To measure viability, the MTS assay CellTiter 96 AQueous Nonradioactive Cell Proliferation Assay (Promega, Madison, WI) was used according to the manufacturer's instructions.

Assessment of native AFP expression by cells lines

Huh-7, Hep 3b, SK-HEP-1, PC-3, and THLE3 cells were stained for native AFP expression using immunocytochemistry. Cells (~150,000) were fixed using BD Phosflow™ Fix

Buffer I (BD Biosciences catalog # 557870) at 37°C for 10 minutes. After washing with BD Pharmingen™ Stain Buffer (FBS) (BD Biosciences catalog # 554656), cells were permeabilized using cold BD Phosflow™ Perm Buffer III (BD Biosciences catalog # 558050) on ice for 30 minutes and washed twice with stain buffer. Cells were stained with PE Mouse Anti-Human Alpha-fetoprotein (BD Biosciences catalog # 563002) at a 1:20 dilution in stain buffer for 20 minutes. Cells were then washed twice with PBS then resuspended in a buffer solution (2% FBS in1xPBS). Stained cells were run through a HyperCyt™ autosampler (IntelliCyt Corporation, Albuquerque, NM) connected to a BD Accuri™ C6 Flow Cytometer (BD Biosciences, San Jose, CA). The collected data were analyzed using the FlowJo™ software v.10.1r7 (Ashland, OR) for percentage (AFP positive %) and intensity of AFP expression (geometric mean). Gating was performed using unstained samples and was adjusted to account for varying autofluorescence between cell types. Staining was performed in triplicate.

In vitro ^{18}F-FHBG Uptake Assay

PET radiotracer 9-(4-^{18}F-fluoro-3-hydroxymethylbutyl)guanine (^{18}F-FHBG) was radiolabeled immediately prior to the study[37,38]. Cells receiving no treatment were used as controls. At day 2 post-transfection, ^{18}F-FHBG uptake studies were performed. Huh-7, Hep3b, SK-HEP-1, and PC-3 cells were treated with serum-free media for 24 hours to sync cell cycles. THLE3 was not serum starved due to the sensitivity of this cell line. One hour prior to treatment, serum-free media was replaced with serum-containing media. Cells were incubated with 10 μCi/mL of freshly-prepared ^{18}F-FHBG for one hour at 37°C then washed 5x with RPMI media containing 10% serum to remove extracellular ^{18}F-FHBG. RIPA buffer (50 μL 1x) was added to the cells and incubated on ice for 5 minutes until cells were completely lysed. Radioactivity of the cell lysate samples was measured using an automated gamma counter (LKB Wallace 1282

Compugamma CS Universal Gamma Counter). Fifteen serial dilutions of ^{18}F-FHBG were used as standards to calculate radiotracer accumulation. Protein content for each sample was measured by Pierce™ BCA Protein Assay Kit (ThermoFisher catalog #23225) as directed by the manufacturer. Data were recorded as radioactivity (μCi) normalized to protein mass (μg). ^{18}F-FHBG uptake studies were performed in triplicate.

Orthotopic Tumor Model

All in vivo procedures were approved and overseen by the Johns Hopkins Institutional Animal Care and Use Committee (IACUC). Female athymic nude mice (NU/J) were purchased from Jackson Laboratory (Bar Harbor, ME) and were implanted with orthotopic liver tumors at 6-8 weeks of age. Hep3b cells with or without constitutive firefly luciferase expression (fLuc+) were resuspended in a 1:1 mixture of HBSS and Corning Matrigel Matrix High Concentration (Corning, catalog # 354248) at 50 million cells/mL. Prior to implantation, animals were anesthetized with 2.5% isoflurane in oxygen, and the skin was cleaned with povidone-iodide and ethanol. An incision was made with a scalpel extending caudally from the xiphoid process. The left lateral liver lobe was visualized, and 1 million (20 μL) cells were injected under the liver capsule. Successful inoculation with cancer cells was be verified by pale, white protrusion at the point of injection. fLuc+ Hep3b tumor growth was monitored by IVIS (IVIS Spectrum imaging system, Perkin Elmer, Waltham, MA). 150 mg/kg D-luciferin (Gold Biotechnology, St. Louis, MO) was administered intraperitoneally to mice, then imaging was performed 8 minutes later. Images were analyzed across regions of interest (ROI) using Living Image software (Perkin Elmer, Waltham, MA).

In vivo Gene Delivery to Orthotopic Tumors

NPs for intravenous delivery were formulated by combining DNA with PBAE 536 in sodium acetate (pH 5) for a final DNA concentration of 0.25 mg/mL and 25 w/w. NPs were allowed to assemble for 10 minutes before adding sucrose to a final concentration of 90 mg/mL, and a final solum acetate concentration of 25 mM. NPs were frozen at -80°C and thawed immediately prior to use. Four weeks after tumor implantation with non-fLuc expressing Hep3b cells, mice received a single retro-orbital injection of 100 μL NPs. For biodistribution, 10% of DNA was functionalized with amine groups using Label IT® Nucleic Acid Modifying Reagent (Mirus, Beltsville, MD, # MIR 3925), then labeled with IRDye® 800RS NHS Ester (Licor, Lincoln, NE). One hour after NP injection, fluorescence was measured in the organs of interest using IVIS imaging. For reporter gene transfection, fLuc expression was imaged using IVIS 24 hours after NP injection, as described above.

For qRT-PCR analysis, organs were harvested 24 hours after NP injection. Tissues were homogenized in Trizol reagent, then chloroform was added for phase separation. After precipitation with isopropanol and washing with 75% ethanol, the RNA was resuspended in water. Next, the samples were treated with RNase-Free DNase Set (Qiagen, Hilden, Germany) to remove plasmid DNA. Reverse transcription was performed using High-Capacity cDNA Reverse Transcription Kit (Thermo Fisher Scientific, Waltham, MA). cDNA was amplified using Power SYBR Green (Thermo Fisher Scientific, Waltham, MA) and a StepOnePlus Real-Time Polymerase Chain Reaction (RT-PCR) System (Applied Biosystems) with sr39 primers: FP: GCCCTTCCTGAGGACAGACAC, RP: GGAGGCTGGGAGCTCACATG. Expression was quantified using the comparative CT method normalized to GAPDH expression. Fold expression was calculated as follows:

$$Fold\ Expression = 2^{-\Delta\Delta CT}$$

sr39 Therapeutic Efficacy Study

Mice were implanted with fLuc+ Hep3b tumors, and tumor growth was monitored by IVIS beginning 2 weeks after implantation and every 4 days thereafter. NP treatment began when tumor luminescence (total flux) reached 10^9 p/s. Animals were randomly assigned to treatment groups to receive either fLuc NPs, CpGf-CMV NPs, or CpGf-AFP NPs. NPs were formulated for IV injection as described above and were administered every 4 days by retro-orbital injection. GCV was administered daily at 50 mg/kg via intraperitoneal injection. 16 days after the start of treatment, animals were anesthetized, and blood was collected by cardiac puncture for liver enzyme analysis. Blood was incubated at RT to clot, then spun down to isolate the serum. Liver enzyme levels were analyzed using an Alanine Aminotransferase Activity Assay Kit and an Aspartate Aminotransferase Activity Kit from Sigma Aldrich (St. Louis, MO). After euthanasia, tumor area was measured using calipers. Outliers were identified and removed using the ROUT method with the most stringent criteria (Q = 0.1%). Significant differences between groups were identified by ordinary one-way ANOVA and Tukey's multiple comparisons test.

For histopathology, tissues were fixed in 10% formalin for 2 days, dehydrated and cleared, then embedded in paraffin. Paraffin sections were stained using hematoxylin and eosin, then mounted and imaged using a Zeiss AxioObserver.Z2 (Oberkochen, Germany). Sections were analyzed by a trained veterinary pathologist (KLG). T2 weighted MRI scans were performed using a Bruker 9.4T horizontal bore spectrometer and analyzed using ImageJ.

sr39 PET Imaging Study

Mice were implanted with fLuc+ Hep3b tumors. Four weeks after implantation, animals were imaged using IVIS to determine relative tumor size, then randomly assigned to receive

either fLuc NPs, CpGf-CMV NPs, or CpGf-AFP NPs. NPs were formulated for IV injection as described above and were by retro-orbital injection. The next day, ^{18}F-FHBG was radiolabeled [37,38], and a 150 μCi dose in an isotonic 10% ethanol solution was administered to animals via tail vein injection. Two hours after injection, animals were imaged using a 7T PET-MR (Bruker, Billerica, MA). After imaging, animals were euthanized, and liver, tumor, spleen, kidneys, heart, and lungs were dissected, weighed, and measured using a Wizard 2 Automatic Gamma Counter (Perkin Elmer, Waltham, MA). Tissue radiopharmaceutical uptake values were calculated compared with 15 μCi ^{18}F-FHBG as a standard.

5.3 Results

PBAE 536 (**Figure 5.2A**) was selected for DNA delivery based on its ability to specifically transfect HCC cancer cells in previous studies[32]. The polymer was synthesized by Michael addition as previously described[32], with a final molecular weight of 5638 Da and a polydispersity index of 1.29 by GPC. PBAE 536 NPs harboring plasmid DNA had a hydrodynamic diameter of 137 ± 3 nm (PDI=0.064) and zeta potential of +18.5 ± 0.6 mV. TEM images showed that dried NPs have a spherical morphology and a diameter of ~50-100 nm (**Figure 5.2B**). Hep3b HCC cells were transfected in vitro with PBAE 536 NPs at doses of 300-1200 ng GFP DNA per well to assess transfection efficacy. GFP expression was dose dependent with a maximal transfection rate of 47 ± 3% (**Figure 5.2C and E**). Viability was maintained at > 80% for all formulations tested (**Figure 5.2D**).

The HSV-TK system is a promising approach for cancer suicide gene therapy[39]. This enzyme catalyzes the phosphorylation of GCV, converting it into a nucleotide analog which inhibits DNA polymerization in dividing cells[39]. sr39 is a mutant form of HSV-TK with significantly increased affinity for GCV[33]. ^{18}F-FHBG is a substrate of sr39 used for molecular

genetic imaging[40,41]. ^{18}F-FHBG accumulates in cells transfected with sr39, and this activity may be imaged using PET to monitor therapeutic gene expression. This theranostic functionality allows for optimization of the treatment protocol, enabling precision dosing.

The sequence of the wild type herpes simplex virus (type 1 /strain RH2) thymidine kinase gene was modified to produce the sr39 mutant[33]. The coding sequence for sr39 was placed under the control of a human elongation factor 1 (EF1) alpha core promoter with mouse CMV enhancer sequence (**Figure 5.3A**), enabling ubiquitous expression of the theranostic gene (CMV-sr39). For a transcriptionally targeted vector, the sr39 sequence was placed under the control of a human AFP promoter and enhancer (AFP-sr39) (**Figure 5.3B**).

CpG free versions of these plasmids were designed to reduce TLR9 activation and reduce the risk of inflammation[31,42]. In the sr39 coding sequence, codon redundancy was employed to eliminate CpG sequences while maintaining the amino acids translated. Codons were selected based on usage bias in the human genome to maximize translational efficiency. Regulatory elements were modified to maintain known transcriptional elements while removing CpG sequences. Known human transcription factor binding sites within the human AFP promoter and enhancer sequences were identified using PROMO[34,35]. Six CpG sequences were identified, with each sequence overlapping with a known transcriptional regulatory element by only one base pair. The non-overlapping base pair was changed to remove the CpG, with purines exchanged for purines (G to A) and pyrimidines for pyrimidines (C to T).

Final CpG free plasmids were constructed by cloning CpG free sr39, into a completely CpG free pCpGfree-mcs backbone with the included CpG free EF1-CMV promoter (CpGf CMV sr39) or replacing that promoter with the engineered CpG free AFP promoter and enhancer (CpGf AFP sr39). Control plasmids with CpG-containing sr39 sequence and regulatory

sequences were designed in a control CpG containing pCpGrich-mcs backbone. These control plasmids containing CpG are referred to as “unmodified” CMV-sr39 and AFP-sr39.

To assess the effect of removing CpG on plasmid immunogenicity, HEK Blue reporter cells for human TLR-9 activation were incubated with CpG-containing or CpG free sr39 plasmids. Both CMV-sr39 and AFP-sr39 DNA containing CpG caused dose-dependent elevated TLR9 activation (**Figure 5.3C**, **D**)**.** The CpG free versions of these plasmids did not cause any detectable TLR9 activation, demonstrating that removal of CpG sequences reduces the innate immune response to these therapeutic plasmids. To evaluate the effect of CpG on promoter strength, Hep3b cells were transfected with each sr39 plasmid using PBAE 536 NPs and qRT-PCR was performed on isolated mRNA. Both CMV-sr39 and CpGf-CMV-sr39 promoted robust sr39 expression, with no detrimental effect from removing the CpG sequences (**Figure 5.3E**). AFP-sr39 also showed significant expression but had a significant decrease in expression following removal of CpG sequences. This result highlights the importance of balancing the decrease on immunogenicity with possible decreased efficacy when utilizing CpG free vectors.

Despite differences in relative promoter strength, Hep3b cells transfected with each sr39 formulation with 4 days of GCV treatment showed a significant decrease in viability, with maximal effect at a DNA dose of 900 ng per well (**Figure 5.3F**). Under these conditions, cell viability was reduced to 25 ± 1% and 57 ± 1% with CpGf-CMV-sr39 and CpGf-AFP-sr39, respectively. Additionally, CpGf-CMV-sr39 maintained superior cell killing effect to wild-type HSV-TK, despite extensive modifications to the coding sequence (**Figure 5.4**). The optimal concentration of GCV for in vitro cell killing was determined to be 1.25 μg/mL due to the strong therapeutic effect in sr39-transfected cells with no toxicity to cells transfected with control GFP NPs (**Figure 5.5**).

To evaluate transcriptional targeting in heterogeneous populations, several cell lines were tested for sr39 cell killing in vitro. Huh7 and Hep-3b are AFP-producing HCC cells, SK-HEP-1 is a non-AFP-producing HCC cell line, PC3 is a non-AFP-producing prostate cancer cell line, and THLE-3 is a healthy human hepatocyte cell line[43]. AFP expression was confirmed by flow cytometry (**Figure 5.6A**). Each cell line was transfected with a GFP reporter gene using PBAE 536 NPs and screened for expression to determine transfection rates. All cancer cell lines showed significantly elevated transfection of 40-60%, compared with 12% in healthy hepatocytes (**Figure 5.6B**). This result was expected, as PBAE 536 NPs were optimized by screening for high transfection rates in HCC cell lines and low transfection in hepatocytes[32]. All transfected cell lines maintained > 80% viability (**Figure 5.6C**).

Next, each cell line was transfected with CpG free sr39 plasmids using PBAE 536 NPs, treated with GCV, and viability was measured over 9 days (**Figure 5.6D-H**). In all lines, cells transfected with CpGf-CMV-sr39 showed significant cell death, with 3-10% viability by day 9. With CpGf-AFP-sr39 transfection, there was also significant cell death in AFP-producing HCC cells, with 26 ± 1% and 15 ± 2% viability on Day 9 in Hep3b and Huh 7 cells, respectively. However, in all non-AFP-producing cells, viability remained high for the course of the study. PC3 and THLE-3 cells were >90% viable, while SK-HEP-1 cells viability dipped to 72 ± 9% by Day 9, indicating that there may be limited activity in SK-HEP-1 cells despite no detectable AFP production.

To evaluate the utility of this approach for molecular genetic imaging, transfected cells were incubated with 10 μCi/mL ^{18}F-FHBG, and in vitro tracer uptake was measured 1 hour later (**Figure 5.7A-E**). Significant radioactivity was measured in all cells transfected with CpGf-CMV-sr39, ranging from 1600-7200 pCi/μg protein in cancer cells and 220 pCi/μg protein in

THLE-3 hepatocytes. With CpGf-AFP-sr39 transfection, significant accumulation was only measured in AFP-producing HCC cells, with 800 ± 100 and 720 ± 50 pCi/μg protein in Hep3b and Huh7, respectively. While not statistically significant, SK-HEP-1 cells transfected with CpGf-AFP-sr39 had 220 ± 20 pCi/μg protein, again suggesting low levels of activity. Transfection with CpGf-AFP-sr39 resulted in 43 ± 3 and 50 ± 9 fold higher accumulation in Huh7 and Hep3b over THLE3, and this HCC-specificity was not observed with CpGf-CMV-sr39 (**Figure 5.7F, G**).

To recapitulate barriers to systemic gene delivery, we employed an orthotopic xenograft model of HCC, implanting Hep3b cells in the livers of athymic NU/J mice. When PBAE 536 NP harboring fluorescently labeled DNA were administered intravenously in tumor-bearing mice, NPs largely accumulated in the liver (**Figure 5.8A,B**). This is in agreement with biodistribution metanalyses of NPs of this size[44]. Of the major organs, ~7% of total fluorescence signal was localized to the tumor. To further probe gene delivery in this model, PBAE 536 NP were used to deliver firefly luciferase (fLuc) reporter DNA in tumor-bearing mice (**Figure 5.8C, D**). 24 hours later, transfection was localized to the tumor, with 8-fold higher radiance in the tumor than liver on average.

Next, CpGf-CMV-sr39 and CpGf-AFP-sr39 were administered to tumor-bearing mice to probe sr39 expression in vivo using these two vectors. Relative expression of sr39 was determined using qRT-PCR 24 hours after NP administration. CpGf-CMV-sr39 promoted sr39 expression in the tumor, but also off-target expression in the liver and lung (**Figure 5.8E**). With transcriptional targeting, CpGf-AFP-sr39 NPs resulted in highly targeted sr39 expression in the tumor alone (**Figure 5.8F**). On average, sr39 expression was higher in animals treated with

CpGf-CMV-sr39 than in those treated with CpGf-AFP-sr39, which is consistent with the in vitro analysis of relative promoter strengths.

To evaluate the therapeutic potential of this approach, tumor-bearing mice were divided into treatment groups receiving intravenous injections of fLuc NPs, CpGf-CMV-sr39 NPs, or CpGf-AFP-NPs. Each animal received 4 NP injections spaced 4 days apart, then were sacrificed 16 days after the start of treatment. All animals received 50 mg/kg GCV daily by intraperitoneal injection. When tumors were measured at the end of the study, animals treated with CpGf-AFP-sr39 NPs had an average tumor area of 27 ± 4 mm^2 compared with 71 ± 8 mm^2 and 79 ± 16 mm^2 for fLuc NP and CpGf-CMV-sr39 treated animals respectively (**Figure 5.9A, 7B**). This represents a significant decrease of 62% compared to fLuc NP treated tumors. Markedly smaller tumor size is also evident in representative MRI scans of mice treated with CpGf-AFP-sr39 (**Figure 5.10**). At the end of the study, serum liver enzymes ALT and AST were not elevated compared with untreated controls for any NP group (**Figure 5.11**). Additionally, there were no signs of abnormalities or toxicities in tissues harvested at the end of this study, as determined by histopathology of hematoxylin and eosin-stained paraffin tissue sections (**Figure 5.12**).

Next, this system was tested for in vivo PET imaging. Four weeks after tumor implantation, animals were divided into treatment groups to receive a single intravenous injection of fLuc NPs, CpGf-CMV-sr39 NPs, or CpGf-AFP-NPs. The following day, the mice received a 150 μCi injection of ^{18}F-FHBG and were imaged 2 hours later with PET and T2-weighted MRI (**Figure 5.9C**). Activity was observed in the tumor in animals treated with CpGf-AFP-sr39, but not in animals treated with fLuc or CpGf-CMV-sr39 NPs (**Figure 5.13**). Following imaging, organs were harvested, and ^{18}F activity was measured in major organs (**Figure 5.9D**) Animals treated with CpGf-AFP-NPs showed significant and specific activity in

tumor tissue. Interestingly, CpGf-CMV-sr39 showed lower activity in the tumor and no significant off-target transfection. This result is in agreement with the results of the therapeutic study, which surprisingly showed no therapeutic effect from CpGf-CMV-sr39 NPs, despite significantly stronger activity in vitro. This may be due to silencing mediated by the innate immune system, which has been shown to affect strong ubiquitous viral promoters such as CMV and EF1 more strongly than tissue-specific promoters, particularly in the liver[45–47].

5.4 Discussion

Suicide gene therapy has shown promise but ultimately has faced several hurdles in clinical translation for patients with HCC. In a 2010 phase I study, a thymidine kinase-based adenoviral gene therapy was well-tolerated, showing potential for safe use in humans[48]. However, transgene expression was not detectable with repeated administrations of viral particles, indicating rapid immune recognition and silencing, leading to a modest overall median survival time of 5 months[48]. This highlights the need for alternative delivery strategies with lower immunogenicity and improved targeting. Here we advanced such a strategy using: 1) a safe, non-viral delivery vehicle, 2) AFP promoter for transcriptional targeting, and 3) completely CpG free plasmids to reduce TLR9 activation.

PBAE NPs offer several advantages for DNA delivery to solid tumors. A large library of PBAE polymers may be synthesized rapidly using combinatorial chemistry to formulate a library of polymers with wide structural diversity[12]. Small changes in properties including hydrophobicity, molecular weight, and effective pK_a can dramatically affect cellular uptake and transfection efficacy of NPs [49–51]. Additionally, next generation PBAE polymers incorporating bioreducible, branched, and carboxylated structures have enabled delivery of siRNA, miRNA, and protein therapeutics[52–54]. PBAE NPs have low toxicity and no risk of insertional

mutagenesis, clear benefits over viral delivery strategies. This study is the first use of PNAE NPs for systemic DNA delivery, which enables the use of orthotopic tumor models and is a more clinically relevant intravenous route of administration, particularly for treating metastases, compared with intratumoral injection. Despite modest levels of NP accumulation within tumor tissue, PBAE 536 enabled expression of a reporter gene as well as theranostic sr39 genes in orthotopic HCC tumors with a high degree of specificity, which ultimately resulted in effective tumor cell killing and tumor imaging.

This specificity is further enhanced by incorporating the AFP promoter and enhancer for transcriptional targeting, safeguarding against systemic toxicity from systemic administration. In this study, the AFP promoter and enhancer restricted sr39 expression to AFP-producing HCC cell lines, with no off-target cell killing or radiotracer accumulation in non-HCC cells, including healthy human hepatocytes. This specificity also translated in vivo, where systemically administered CpGf-AFP-sr39 NPs transfected the tumor but not liver or other healthy mouse tissues. Overall, this clearly demonstrates the specificity of this platform for AFP-producing HCC cells. Interestingly, despite reduced promoter strength, CpGf-AFP-sr39 showed improved therapeutic activity over CpGf-CMV-sr39 in vivo. This may be due to transcriptional silencing of the strong ubiquitous CMV/EF1 promoter[45–47]. Alternatively, the non-targeted platform may result in off-target transfection and killing of Kupffer cells, significantly altering the liver and tumor microenvironments and potentially affecting tumor growth[55]. While CpGf-AFP-sr39 NPs showed high potency in vivo, improving the strength of this promoter should be investigated to maximize therapeutic potential. Employing a two-step transcriptional amplification (TSTA) strategy with the AFP promoter may significantly enhance expression while maintaining cancer specificity[19,56].

A novel CpG free version of the sr39 gene was developed and utilized in two theranostic plasmids: CpGf-CMV-sr39 and CpGf-AFP-sr39. Methylated CpG dinucleotides have been shown to stimulate cytokine production and reduce the duration of transgene expression[27]. This is the first reported use of a completely CpG free sr39 gene and AFP promoter, which we showed reduces TLR9 activation while maintaining cell killing and molecular genetic imaging functionality in vitro and in vivo, despite extensive sequence alterations. We noted that removing CpG dinucleotides from the AFP promoter and enhancer sequences resulted in reduction of sr39 expression and activity. This highlights the importance of balancing the safety concerns of CpG sequences and promoter strength for therapeutic gene expression. Nonetheless, CpGf-AFP-sr39 showed impressive therapeutic efficacy in vivo, with a 62% reduction in tumor size compared with controls. Studies have also shown significant T cell involvement in thymidine kinase gene therapy[57], raising the possibility for further enhanced therapeutic benefit in a syngeneic model.

Overall, this approach improves upon clinically tested adenoviral TK-gene therapy by: 1) employing a safe, biodegradable non-viral polymer DNA delivery system rather than immunogenic viral vectors, 2) removing CpG sequences to reduce TLR-9 activation, which has been linked to gene silencing and inflammation in vivo, 3) using sr39, a mutant form of HSV-TK with higher affinity for GCV and improved efficacy, and 4) employing AFP transcriptional targeting for highly specific expression in cancer cells. Altogether, these advancements improve the clinical compatibility of the system and improve its translational potential and have the potential to improve treatment options for patients suffering from HCC.

5.5 References

1. Golabi, P, Fazel, S, Otgonsuren, M, Sayiner, M, Locklear, CT and Younossi, ZM (2017). Mortality assessment of patients with hepatocellular carcinoma according to underlying disease and treatment modalities. *Medicine (Baltimore).* **96**.
2. El–Serag, HB and Rudolph, KL (2007). Hepatocellular Carcinoma: Epidemiology and Molecular Carcinogenesis. *Gastroenterology* **132**: 2557–2576.
3. Shaw, JJ and Shah, SA (2011). Rising incidence and demographics of hepatocellular carcinoma in the USA: what does it mean? *Expert Rev. Gastroenterol. Hepatol.* **5**: 365–370.
4. Bruix, J, Boix, L, Sala, M and Llovet, JM (2004). Focus on hepatocellular carcinoma. *Cancer Cell* **5**: 215–219.
5. Park, J, Chen, M, Colombo, M, Roberts, LR, Schwartz, M, Chen, P, *et al.* (2015). Global patterns of hepatocellular carcinoma management from diagnosis to death: the BRIDGE Study. *Liver Int.* **35**: 2155–2166.
6. Huang, Y-S, Chiang, J-H, Wu, J-C, Chang, F-Y and Lee, S-D (2002). Risk of hepatic failure after transcatheter arterial chemoembolization for hepatocellular carcinoma: predictive value of the monoethylglycinexylidide test. *Am. J. Gastroenterol.* **97**: 1223–1227.
7. Yang, JD, Hainaut, P, Gores, GJ, Amadou, A, Plymoth, A and Roberts, LR (2019). A global view of hepatocellular carcinoma: trends, risk, prevention and management. *Nat. Rev. Gastroenterol. Hepatol.* **16**: 589–604.
8. Karlsson, J, Vaughan, HJ and Green, JJ (2018). Biodegradable Polymeric Nanoparticles

for Therapeutic Cancer Treatments. *Annu. Rev. Chem. Biomol. Eng.* **9**: 105–127.

9. Lundstrom, K (2018). Viral Vectors in Gene Therapy. *Dis. (Basel, Switzerland)* **6**: 42.

10. Phillips, AJ (2001). The challenge of gene therapy and DNA delivery. *J. Pharm. Pharmacol.* **53**: 1169–1174.

11. Zhou, Z, Liu, X, Zhu, D, Wang, Y, Zhang, Z, Zhou, X, *et al.* (2017). Nonviral cancer gene therapy: Delivery cascade and vector nanoproperty integration. *Adv. Drug Deliv. Rev.* **115**: 115–154.

12. Green, JJ, Langer, R and Anderson, DG (2008). A combinatorial polymer library approach yields insight into nonviral gene delivery. *Acc. Chem. Res.* **41**: 749–759.

13. Guerrero-Cázares, H, Tzeng, SY, Young, NP, Abutaleb, AO, Quiñones-Hinojosa, A and Green, JJ (2014). Biodegradable Polymeric Nanoparticles Show High Efficacy and Specificity at DNA Delivery to Human Glioblastoma in Vitro and in Vivo. *ACS Nano* **8**: 5141–5153.

14. Wilson, DR, Rui, Y, Siddiq, K, Routkevitch, D and Green, JJ (2019). Differentially Branched Ester Amine Quadpolymers with Amphiphilic and pH-Sensitive Properties for Efficient Plasmid DNA Delivery. *Mol. Pharm.* **16**: 655–668.

15. Eltoukhy, AA, Siegwart, DJ, Alabi, CA, Rajan, JS, Langer, R and Anderson, DG (2012). Effect of molecular weight of amine end-modified poly (β-amino ester) s on gene delivery efficiency and toxicity. *Biomaterials* **33**: 3594–3603.

16. Maeda, H, Wu, J, Sawa, T, Matsumura, Y and Hori, K (2000). Tumor vascular permeability and the EPR effect in macromolecular therapeutics: a review. *J. Control. Release* **65**: 271–284.

17. Kang, H, Rho, S, Stiles, WR, Hu, S, Baek, Y, Hwang, DW, *et al.* (2020). Size-Dependent

EPR Effect of Polymeric Nanoparticles on Tumor Targeting. *Adv. Healthc. Mater.* **9**: 1901223.

18. Robson, T and Hirst, DG (2003). Transcriptional targeting in cancer gene therapy. *Biomed Res. Int.* **2003**: 110–137.

19. Qiao, J, Doubrovin, M, Sauter, B V, Huang, Y, Guo, ZS, Balatoni, J, *et al.* (2002). Tumor-specific transcriptional targeting of suicide gene therapy. *Gene Ther.* **9**: 168–175.

20. Abdul-Ghani, R, Ohana, P, Matouk, I, Ayesh, S, Ayesh, B, Laster, M, *et al.* (2000). Use of transcriptional regulatory sequences of telomerase (hTER and hTERT) for selective killing of cancer cells. *Mol. Ther.* **2**: 539–544.

21. Su, Z-Z, Sarkar, D, Emdad, L, Duigou, GJ, Young, CSH, Ware, J, *et al.* (2005). Targeting gene expression selectively in cancer cells by using the progression-elevated gene-3 promoter. *Proc. Natl. Acad. Sci.* **102**: 1059–1064.

22. Yu, D, Chen, D, Chiu, C, Razmazma, B, Chow, Y-H and Pang, S (2001). Prostate-specific targeting using PSA promoter-based lentiviral vectors. *Cancer Gene Ther.* **8**: 628–635.

23. Park, JH, Kim, K Il, Lee, YJ, Lee, TS, Kim, KM, Nahm, S-S, *et al.* (2011). Non-invasive monitoring of hepatocellular carcinoma in transgenic mouse with bioluminescent imaging. *Cancer Lett.* **310**: 53–60.

24. Ahn, B-C, Ryu, MJ, Ahn, SJ, Yoon, SM, Choi, SH, Yoo, J, *et al.* (2006). Construction of a highly hepatoma specific adenoviral vector system carrying NIS gene activated by AFP enhancer. *J. Nucl. Med.* **47**: 409P-409P.

25. Bauer, S, Kirschning, CJ, Häcker, H, Redecke, V, Hausmann, S, Akira, S, *et al.* (2001). Human TLR9 confers responsiveness to bacterial DNA via species-specific CpG motif recognition. *Proc. Natl. Acad. Sci.* **98**: 9237 LP – 9242.

26. Wagner, H (2004). The immunobiology of the TLR9 subfamily. *Trends Immunol.* **25**: 381–386.

27. Hodges, BL, Taylor, KM, Joseph, MF, Bourgeois, SA and Scheule, RK (2004). Long-term Transgene Expression from Plasmid DNA Gene Therapy Vectors Is Negatively Affected by CpG Dinucleotides. *Mol. Ther.* **10**: 269–278.

28. Scheule, RK (2000). The role of CpG motifs in immunostimulation and gene therapy. *Adv. Drug Deliv. Rev.* **44**: 119–134.

29. Davies, LA, Hyde, SC, Nunez-Alonso, G, Bazzani, RP, Harding-Smith, R, Pringle, IA, *et al.* (2012). The use of CpG-free plasmids to mediate persistent gene expression following repeated aerosol delivery of pDNA/PEI complexes. *Biomaterials* **33**: 5618–5627.

30. Takahashi, Y, Nishikawa, M and Takakura, Y (2012). Development of safe and effective nonviral gene therapy by eliminating CpG motifs from plasmid DNA vector. *Front. Biosci. S* **4**: 133–141.

31. Hyde, SC, Pringle, IA, Abdullah, S, Lawton, AE, Davies, LA, Varathalingam, A, *et al.* (2008). CpG-free plasmids confer reduced inflammation and sustained pulmonary gene expression. *Nat. Biotechnol.* **26**: 549–551.

32. Zamboni, CG, Kozielski, KL, Vaughan, HJ, Nakata, MM, Kim, J, Higgins, LJ, *et al.* (2017). Polymeric nanoparticles as cancer-specific DNA delivery vectors to human hepatocellular carcinoma. *J. Control. Release* **263**: 18–28.

33. Black, ME, Kokoris, MS and Sabo, P (2001). Herpes simplex virus-1 thymidine kinase mutants created by semi-random sequence mutagenesis improve prodrug-mediated tumor cell killing. *Cancer Res.* **61**: 3022–3026.

34. Farré, D, Roset, R, Huerta, M, Adsuara, JE, Roselló, L, Albà, MM, *et al.* (2003).

Identification of patterns in biological sequences at the ALGGEN server: PROMO and MALGEN. *Nucleic Acids Res.* **31**: 3651–3653.

35. Messeguer, X, Escudero, R, Farré, D, Nuñez, O, Martínez, J and Albà, MM (2002). PROMO: detection of known transcription regulatory elements using species-tailored searches. *Bioinformatics* **18**: 333–334.

36. Schmittgen, TD and Livak, KJ (2008). Analyzing real-time PCR data by the comparative C T method. *Nat. Protoc.* **3**: 1101.

37. Castanares, MA, Mukherjee, A, Chowdhury, WH, Liu, M, Chen, Y, Mease, RC, *et al.* (2014). Evaluation of Prostate-Specific Membrane Antigen as an Imaging Reporter. *J. Nucl. Med.* **55**: 805–811.

38. Ponde, DE, Dence, CS, Schuster, DP and Welch, MJ (2004). Rapid and reproducible radiosynthesis of [18F] FHBG. *Nucl. Med. Biol.* **31**: 133–138.

39. Fillat, C, Carrio, M, Cascante, A and Sangro, B (2003). Suicide gene therapy mediated by the Herpes Simplex virus thymidine kinase gene/Ganciclovir system: fifteen years of application. *Curr. Gene Ther.* **3**: 13–26.

40. Yaghoubi, SS and Gambhir, SS (2006). PET imaging of herpes simplex virus type 1 thymidine kinase (HSV1-tk) or mutant HSV1-sr39tk reporter gene expression in mice and humans using [18 F] FHBG. *Nat. Protoc.* **1**: 3069.

41. Tjuvajev, JG, Doubrovin, M, Akhurst, T, Cai, S, Balatoni, J, Alauddin, MM, *et al.* (2002). Comparison of radiolabeled nucleoside probes (FIAU, FHBG, and FHPG) for PET imaging of HSV1-tk gene expression. *J. Nucl. Med.* **43**: 1072–1083.

42. Surana, S, Shenoy, AR and Krishnan, Y (2015). Designing DNA nanodevices for compatibility with the immune system of higher organisms. *Nat. Nanotechnol.* **10**: 741–

747.

43. Kaneko, S, Hallenbeck, P, Kotani, T, Nakabayashi, H, McGarrity, G, Tamaoki, T, *et al.* (1995). Adenovirus-mediated gene therapy of hepatocellular carcinoma using cancer-specific gene expression. *Cancer Res.* **55**: 5283–5287.

44. Wilhelm, S, Tavares, AJ, Dai, Q, Ohta, S, Audet, J, Dvorak, HF, *et al.* (2016). Analysis of nanoparticle delivery to tumours. *Nat. Rev. Mater.* **1**: 16014.

45. Herweijer, H, Zhang, G, Subbotin, VM, Budker, V, Williams, P and Wolff, JA (2001). Time course of gene expression after plasmid DNA gene transfer to the liver. *J. Gene Med.* **3**: 280–291.

46. Harms, JS and Splitter, GA (1995). Interferon-γ Inhibits Transgene Expression Driven by SV40 or CMV Promoters but Augments Expression Driven by the Mammalian MHC I Promoter. *Hum. Gene Ther.* **6**: 1291–1297.

47. Löser, P, Jennings, GS, Strauss, M and Sandig, V (1998). Reactivation of the Previously Silenced Cytomegalovirus Major Immediate-Early Promoter in the Mouse Liver: Involvement of NFκB. *J. Virol.* **72**: 180 LP – 190.

48. Sangro, B, Mazzolini, G, Ruiz, M, Ruiz, J, Quiroga, J, Herrero, I, *et al.* (2010). A phase I clinical trial of thymidine kinase-based gene therapy in advanced hepatocellular carcinoma. *Cancer Gene Ther.* **17**: 837–843.

49. Bishop, CJ, Kozielski, KL and Green, JJ (2015). Exploring the role of polymer structure on intracellular nucleic acid delivery via polymeric nanoparticles. *J. Control. Release* **219**: 488–499.

50. Bishop, CJ, Ketola, T-M, Tzeng, SY, Sunshine, JC, Urtti, A, Lemmetyinen, H, *et al.* (2013). The Effect and Role of Carbon Atoms in Poly(β-amino ester)s for DNA Binding

and Gene Delivery. *J. Am. Chem. Soc.* **135**: 6951–6957.

51. Routkevitch, D, Sudhakar, D, Conge, M, Varanasi, M, Tzeng, SY, Wilson, DR, *et al.* (2020). Efficiency of Cytosolic Delivery with Poly(β-amino ester) Nanoparticles is Dependent on the Effective pKa of the Polymer. *ACS Biomater. Sci. Eng.* **6**: 3411–3421.

52. Kozielski, KL, Ruiz-Valls, A, Tzeng, SY, Guerrero-Cázares, H, Rui, Y, Li, Y, *et al.* (2019). Cancer-selective nanoparticles for combinatorial siRNA delivery to primary human GBM in vitro and in vivo. *Biomaterials* **209**: 79–87.

53. Lopez-Bertoni, H, Kozielski, KL, Rui, Y, Lal, B, Vaughan, H, Wilson, DR, *et al.* (2018). Bioreducible polymeric nanoparticles containing multiplexed cancer stem cell regulating miRNAs inhibit glioblastoma growth and prolong survival. *Nano Lett.* **18**: 4086–4094.

54. Rui, Y, Wilson, DR, Choi, J, Varanasi, M, Sanders, K, Karlsson, J, *et al.* (2019). Carboxylated branched poly(β-amino ester) nanoparticles enable robust cytosolic protein delivery and CRISPR-Cas9 gene editing. *Sci. Adv.* **5**: eaay3255.

55. Kelley, SK, Harris, LA, Xie, D, DeForge, L, Totpal, K, Bussiere, J, *et al.* (2001). Preclinical studies to predict the disposition of Apo2L/tumor necrosis factor-related apoptosis-inducing ligand in humans: characterization of in vivo efficacy, pharmacokinetics, and safety. *J. Pharmacol. Exp. Ther.* **299**: 31–38.

56. Iyer, M, Wu, L, Carey, M, Wang, Y, Smallwood, A and Gambhir, SS (2001). Two-step transcriptional amplification as a method for imaging reporter gene expression using weak promoters. *Proc. Natl. Acad. Sci.* **98**: 14595–14600.

57. Kuriyama, S, Kikukawa, M, Masui, K, Okuda, H, Nakatani, T, Akahane, T, *et al.* (1999). Cancer gene therapy with HSV-tk/GCV system depends on t-cell-mediated immune responses and causes apoptotic death of tumor cells In vivo. *Int. J. Cancer* **83**: 374–380.

5.6 Figures

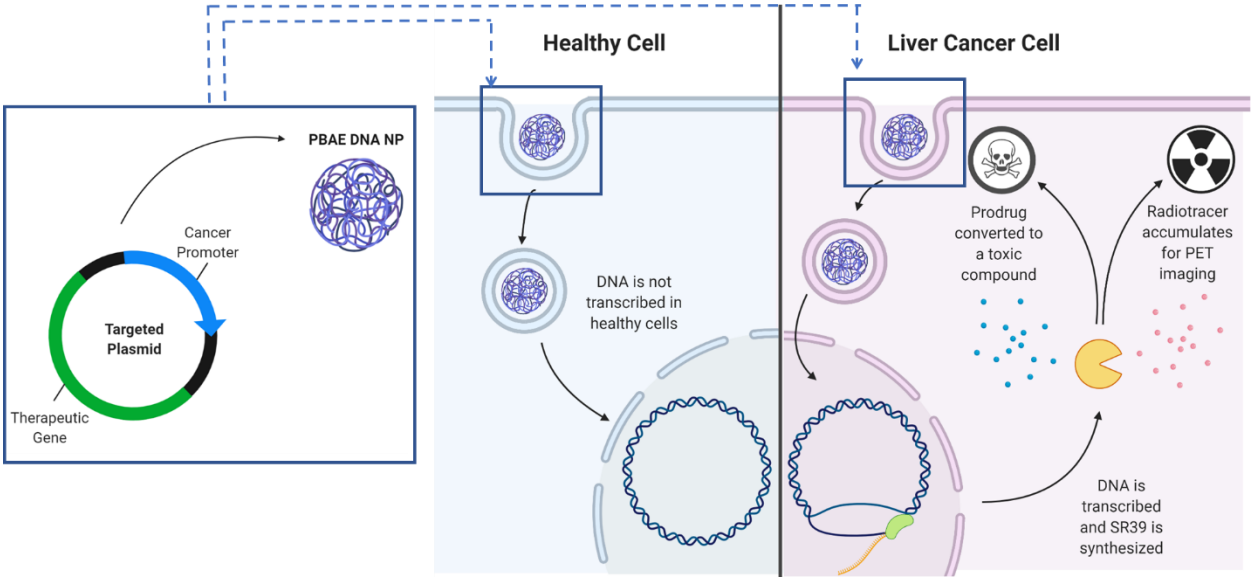

Figure 5.1 A schema describing a tumor-targeted theranostic approach for the treatment of HCC. PBAE NPs are synthesized with transcriptionally targeted plasmid encoding for sr39 gene. DNA delivery to healthy cells does not result in therapeutic gene expression.

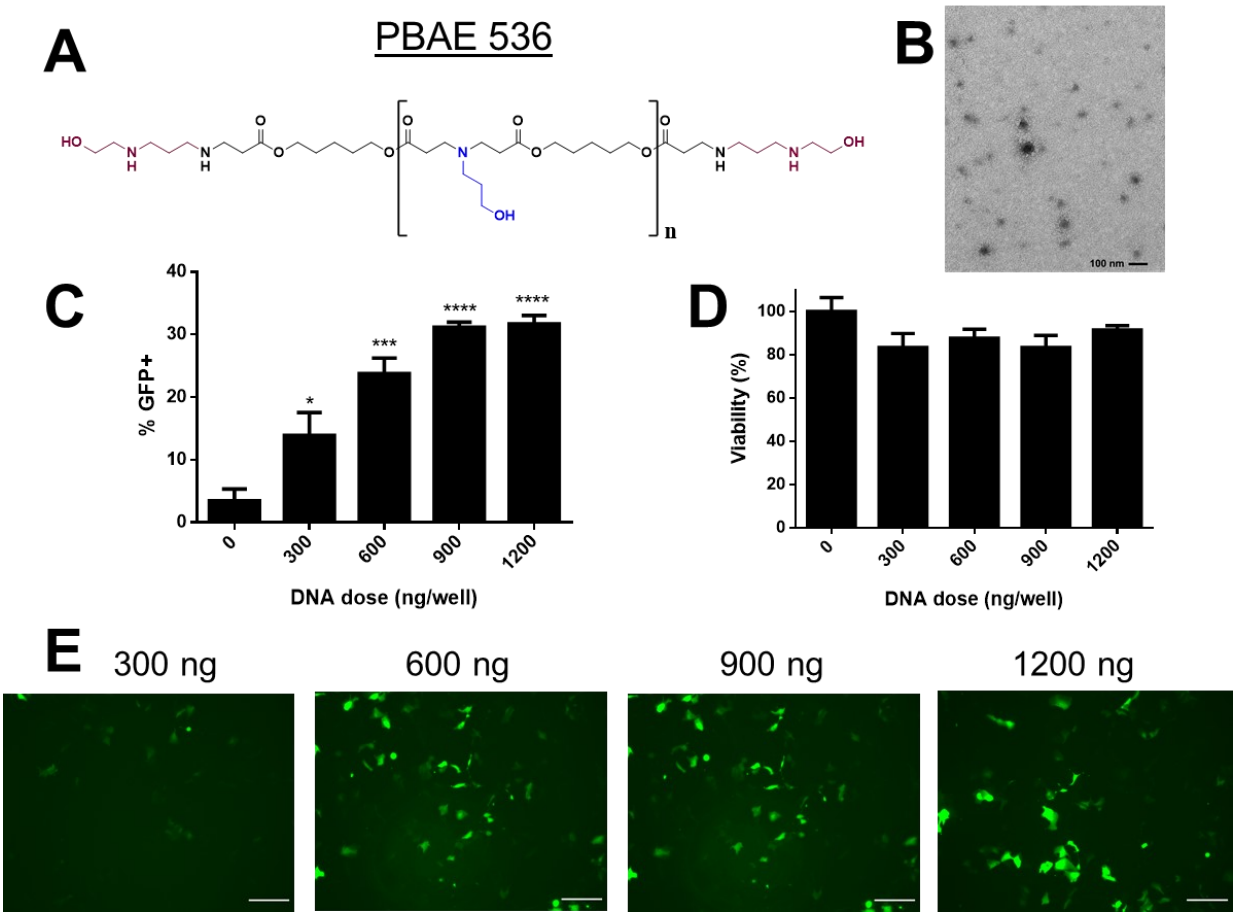

Figure 5.2. PBAE 536 NPs transfect liver cancer cells with a reporter gene *in vitro* A. Structure of polymer PBAE 536 **B.** TEM image of PBAE 536 NPs **C.** In vitro transfection efficacy and **D.** cell viability of Hep3b cells transfected with varying doses of GFP DNA. PBAE NPs were synthesized with PBAE 536 at a polymer:DNA mass ratio of 25 (w/w). Mean ± SE are shown (n=3). Statistically significant transfection was calculated by one-way ANOVA with Dunnett's multiple comparison test compared to the control. **E.** Fluorescence micrographs of GFP expression in transfected Hep3b cells. Scale bar = 500 μm. **P* < 0.05; ***P* < 0.01; ****P* < 0.001; *****P* < 0.0001

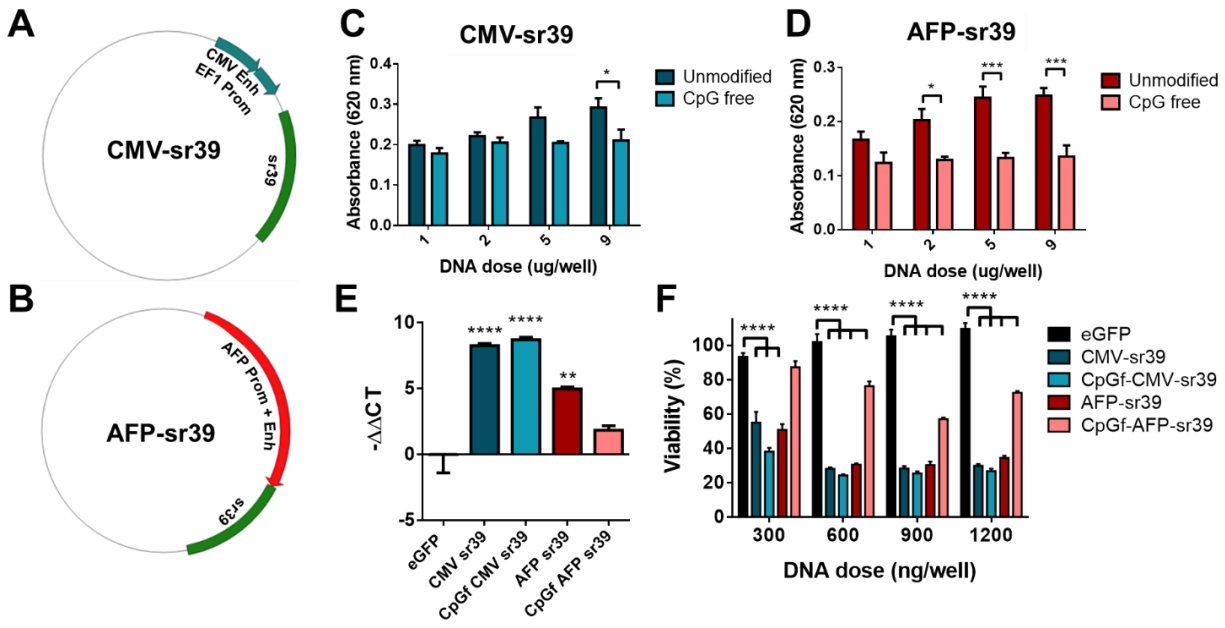

Figure 5.3. CpG free sr39 plasmids induce sr39tk expression *in vitro* without elevated TLR9 activation (A and B) Plasmid maps are shown for CMV-sr39 and AFP-sr39. (C) hTLR-9 activation in HEK-blue reporter cells after exposure to CpG-containing and CpG-free CMV-sr39 and (D) AFP-sr39 plasmid DNA. Statistically significant differences in TLR9 activation between unmodified and CpG free plasmids were determined by two-way ANOVA and Sidak's multiple comparison test. (D) qRT-PCR analysis of sr39 expression in transfected cells. F. Hep3b cellular viability 5 days after transfection with sr39 NPs and treatment with 1.25 µg/mL GCV. Statistically significant differences among DNAs were determined by two-way ANOVA and Sidak's multiple comparison test. Mean ± SE are shown for all graphs (n=3) *$P < 0.05$; **$P < 0.01$; ***$P < 0.001$; ****$P < 0.0001$.

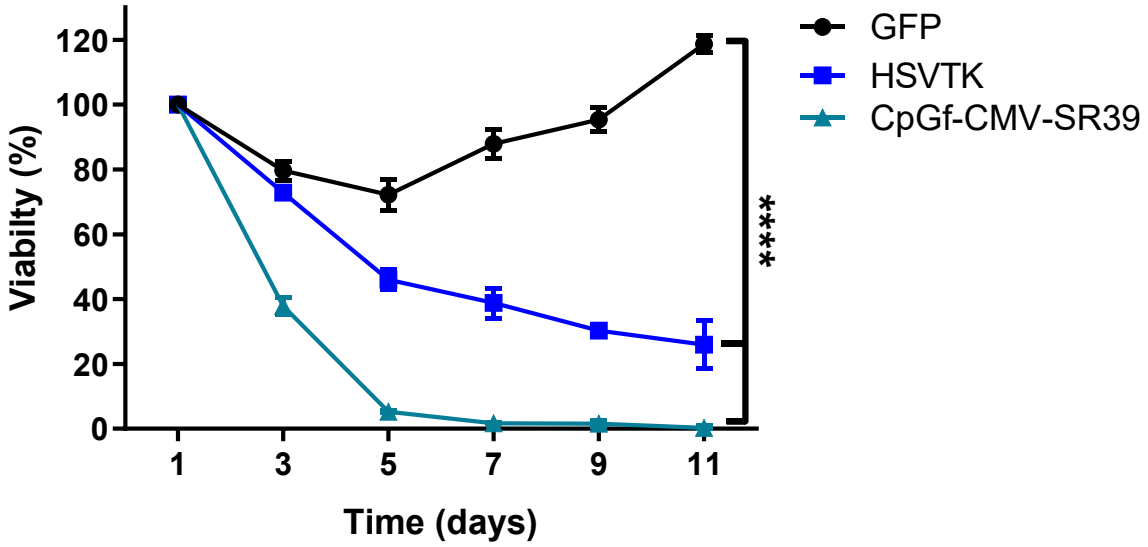

Figure 5.4 CpG-free SR39 has superior cell killing effect compared with wild-type HSV-TK. Hep3b cells were transfected with NPs harboring GFP, HSVTK, or CpGf-CMV-SR39 DNA and treated with 1.25 µg/mL GCV on days 1, 3, 5, 7, and 9. Significant differences between groups were calculated for each time point by two-way ANOVA with Dunnett's multiple comparisons. Mean ± SE are shown (n=3) ****$P < 0.0001$.

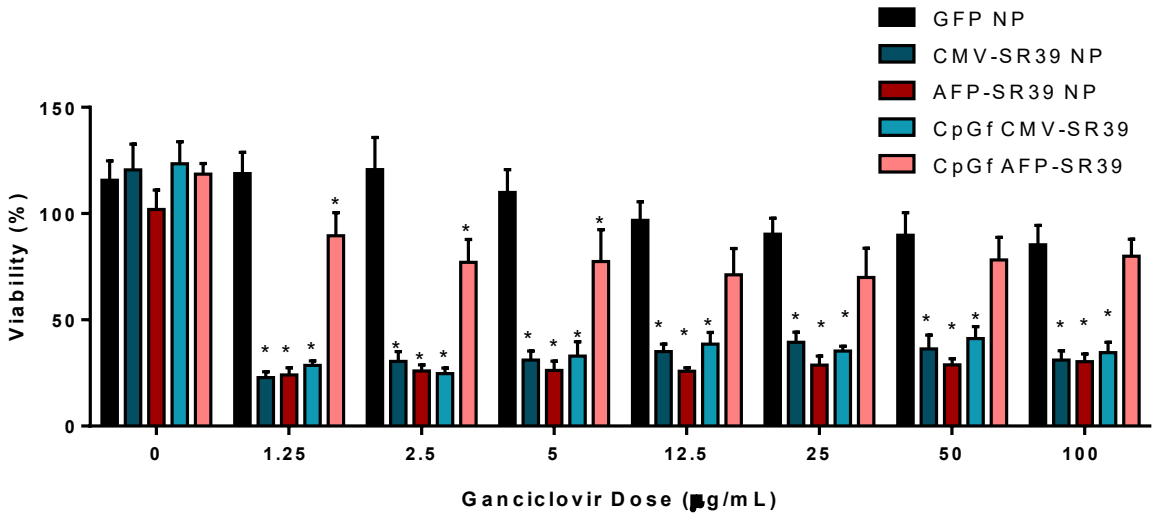

Figure 5.5 SR39-mediated cell death with varying GCV doses. Hep3b cells were transfected with NPs harboring GFP or SR39 plasmids, then treated with GCV 1 and 3 days after transfection. Viability was measured 5 days after transfection by MTS assay. Significant differences between groups were calculated for each time point by two-way ANOVA with Dunnett's multiple comparisons. Mean ± SE are shown (n=3) *$P < 0.05$.

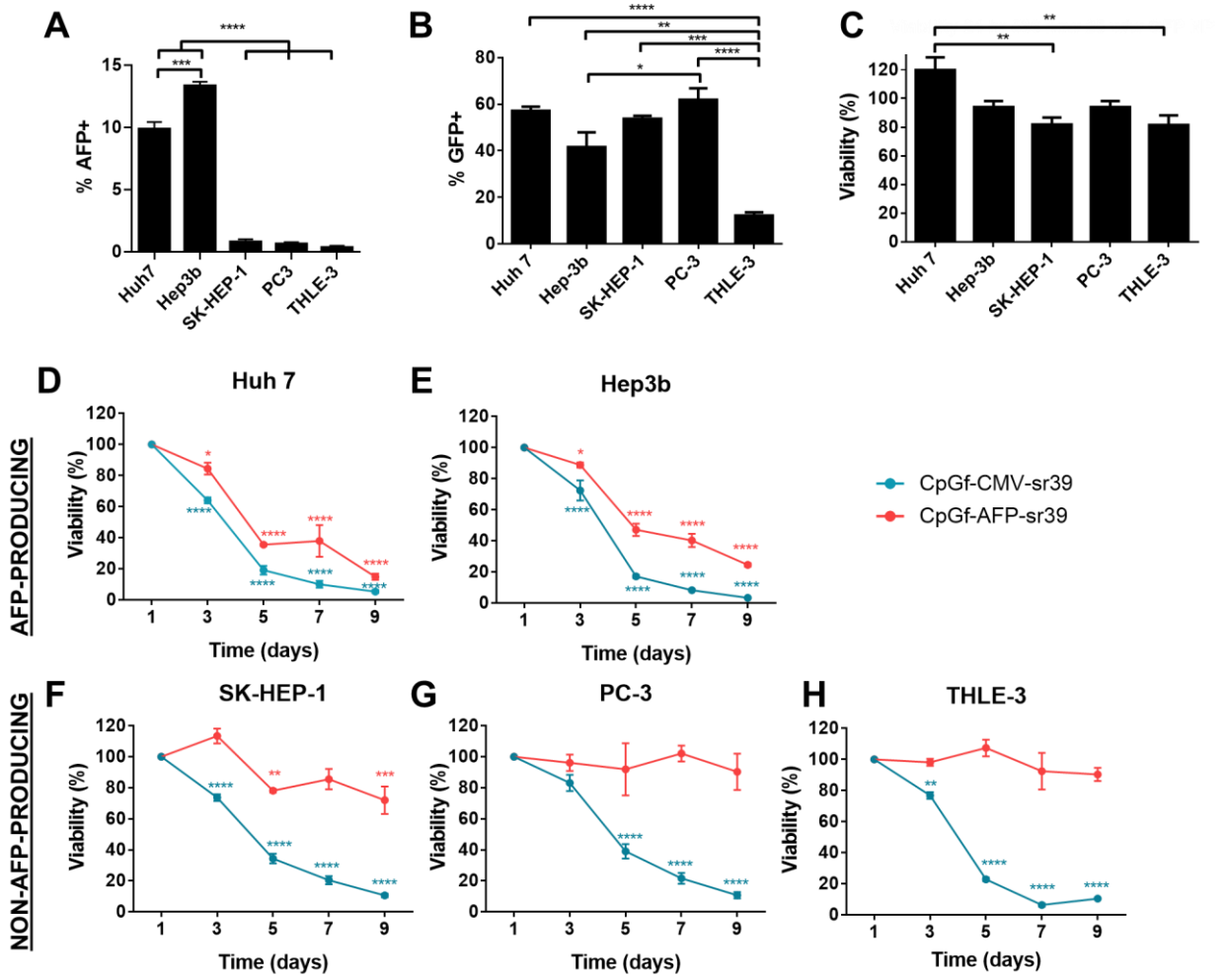

Figure 5.6 AFP transcriptional targeting restricts sr39-mediated cell death to AFP-producing HCC cells (A) AFP expression in fixed and permeabilized Huh7, Hep 3b, SK-HEP-1, PC-3, and THLE-3 cells measured by flow cytometry. (B and C) Transfection efficacy and viability of cell lines transfected with 600 ng/well GFP DNA using PBAE 536 NPs. Statistically significant differences between cell lines were determined using one-way ANOVA with Tukey's multiple comparison's test. (D-H) Viability time course of cells transfected with CpG free CMV-sr39 and AFP-sr39 DNA and treated with 1.25 ug/mL GCV. Statistically significant loss in viability for each DNA was calculated by two-way ANOVA with Dunnett's multiple comparisons between each timepoint and Day 1. Mean ± SE are shown for all graphs (n=3) *P < 0.05; **P < 0.01; ***P < 0.001; ****P < 0.0001.

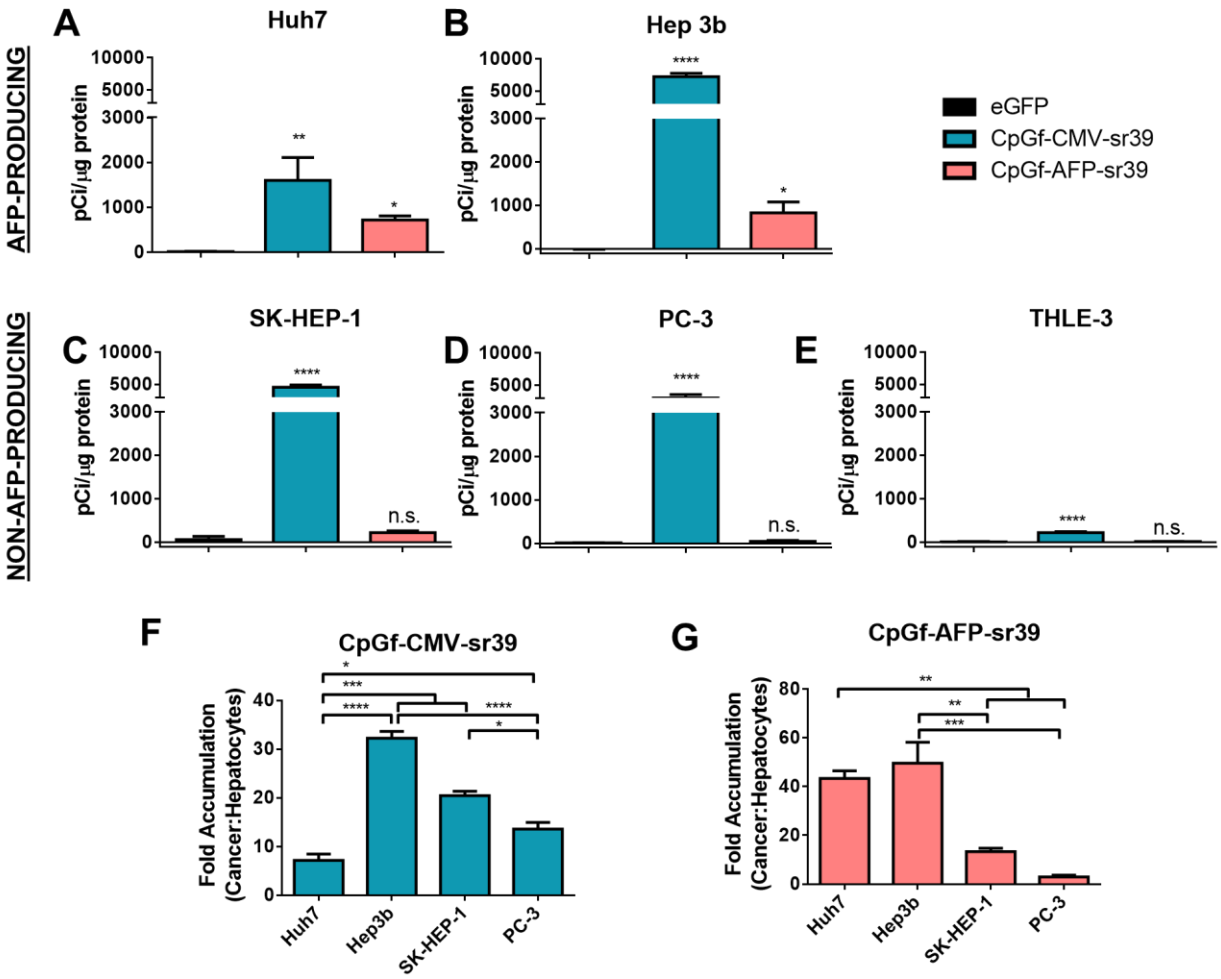

Figure 5.7 sr39 NPs enable specific accumulation of ^{18}F-FHBG in target HCC cells (*A-E*). Cellular radioactivity in transfected cells incubated with 10 μCi ^{18}F-FHBG for 1 hour, normalized to total protein content. Statistically significant differences were calculated by one-way ANOVA with Dunnett's multiple comparison test between treatment groups and controls. (*F,G*) Fold radioactivity accumulation in cancer cells normalized to THLE3 cells treated with the same NP. Mean ± SE are shown for all graphs (n=3) **P* < 0.05; ***P* < 0.01; ****P* < 0.001; *****P* < 0.0001.

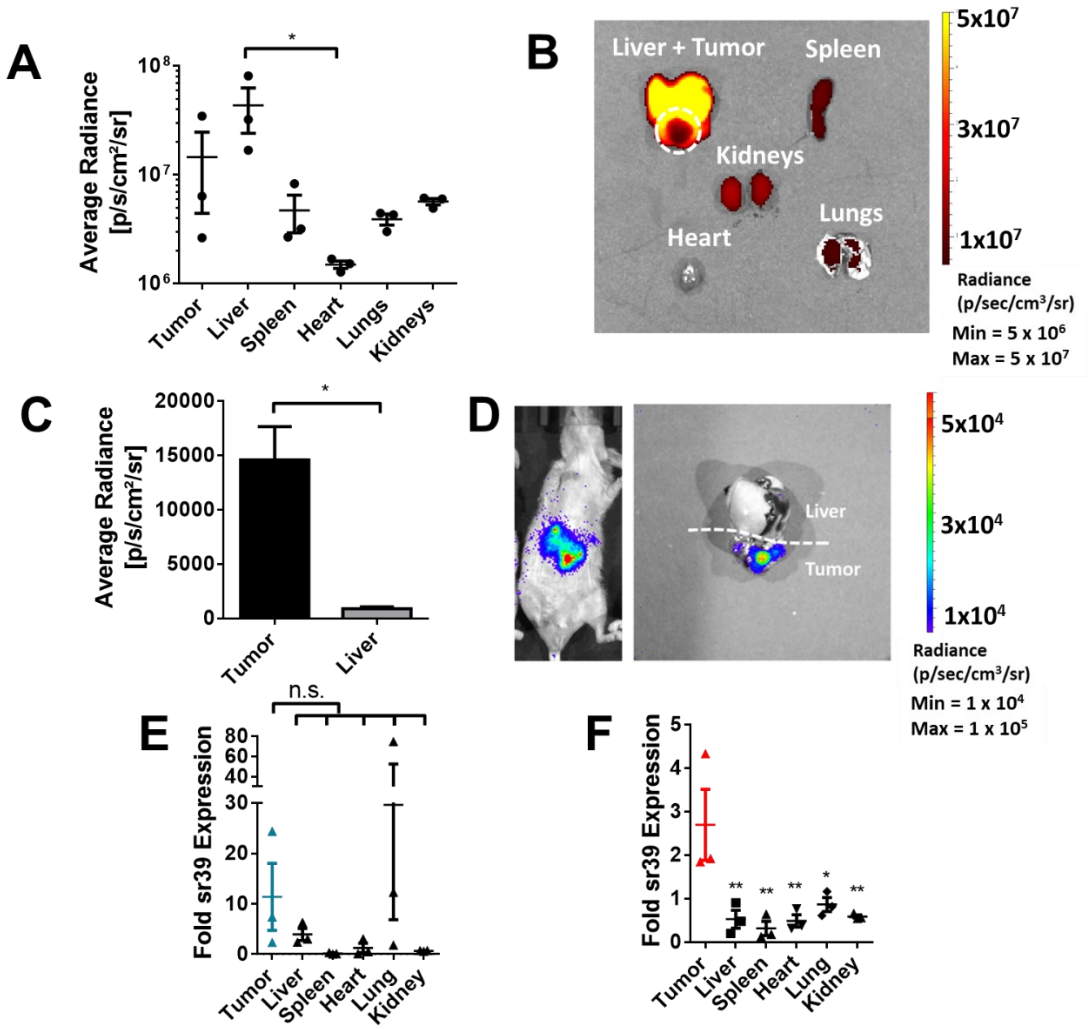

Figure 5.8 Intravenously Administered NPs Efficiently Transfect Orthotopic HCC Tumors
A. Average radiance (p/s/cm^2/sr) of major organs 1 hours after fluorescent NP administration and B. representative image of organs. Significant differences between organ radiance were calculated by Kruskal-Wallis nonparametric test and Dunn's test for multiple comparisons. *$P <$ 0.05 Data shown as mean ± SE (n=3). C. Average radiance and D. representative images of orthotopic tumor and liver transfected with fLuc-NPs administered by tail vein injection. Statistically significant differences in radiance between liver and tumor tissue were determined by a ratio-paired t test between average radiance over the region of interest. *$P < 0.05$ Data shown as mean ± SE (n=3). E. Fold sr39 expression in organs after IV administration of CMV-sr39 NPs or F. AFP-sr39 NPs by qRT-PCR. Significant differences between tumor and healthy tissue were calculated by Ordinary one-way ANOVA and Dunnett's test for multiple comparisons. *$P < 0.05$, **$P < 0.01$, corrected for multiple comparisons. Data shown as mean ± SE (n=3).

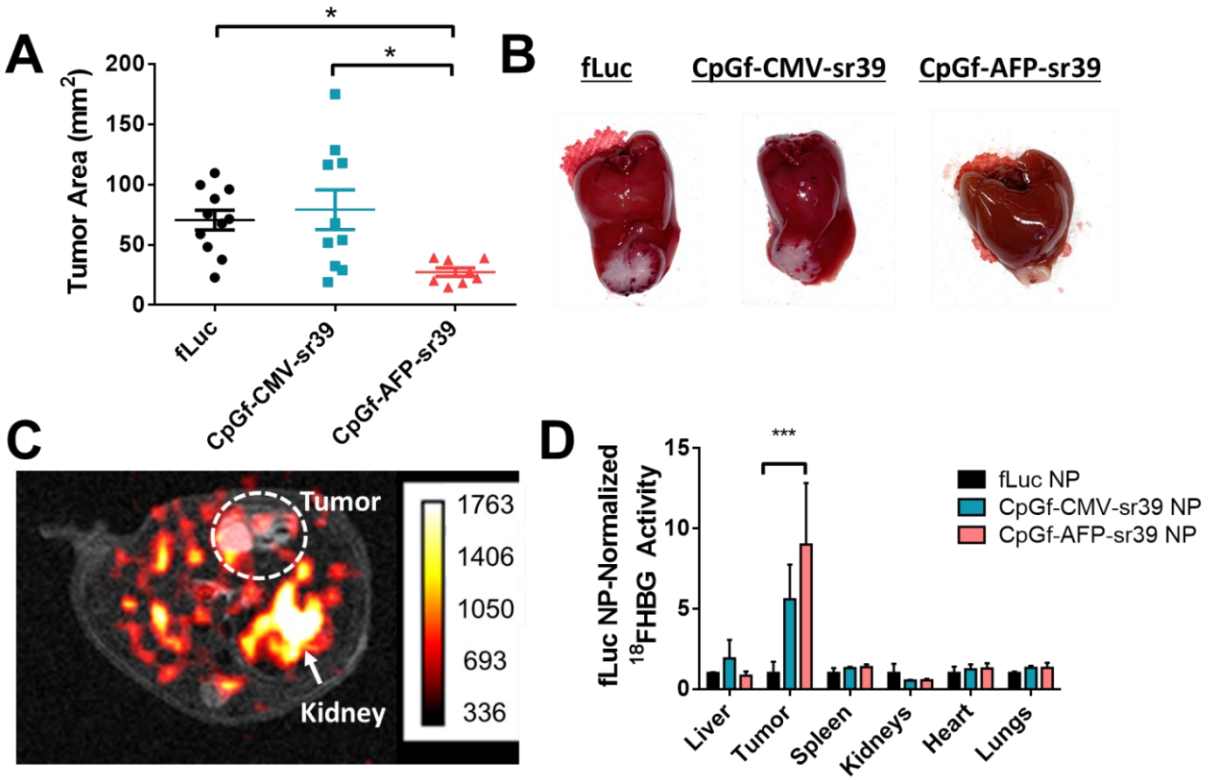

Figure 5.9 CpGf-sr39 NP treatment significantly inhibits tumor growth and enables monitoring by PET/CT. Mice with orthotopic xenograft Hep3b tumors were treated with IV administration of fLuc NPs (n = 11), CpGf-CMV-sr39 NPs (n = 10), or CpGf-AFP-sr39 NPs (n = 8) with systemic GCV. A. After 16 days, tumors treated with CpGf-AFP-sr39 had significantly smaller tumors than the other two groups. Mean ± SE are shown. Significant differences between treatment groups were determined by one-way ANOVA with Tukey posttests among the three groups. *$P < 0.05$ B. Representative images show differences in tumor size. C. Representative PET/MRI imaging shows intratumoral ^{18}F-FHBG activity in a tumor-bearing mouse treated with CpGf-AFP-sr39. D. Activity in major organs with fLuc (n=2), CpGf-CMV-sr39 (n=2), or CpGf-AFP-sr39 (n=3) NPs and subsequent ^{18}F-FHBG injection. Activity was calculated per mass of tissue, then normalized to activity in the control group (fLuc NP). Significant differences between treatment groups were determined by two-way ANOVA and Tukey posttest. ***$P < 0.001$. All data shown as mean ± SE.

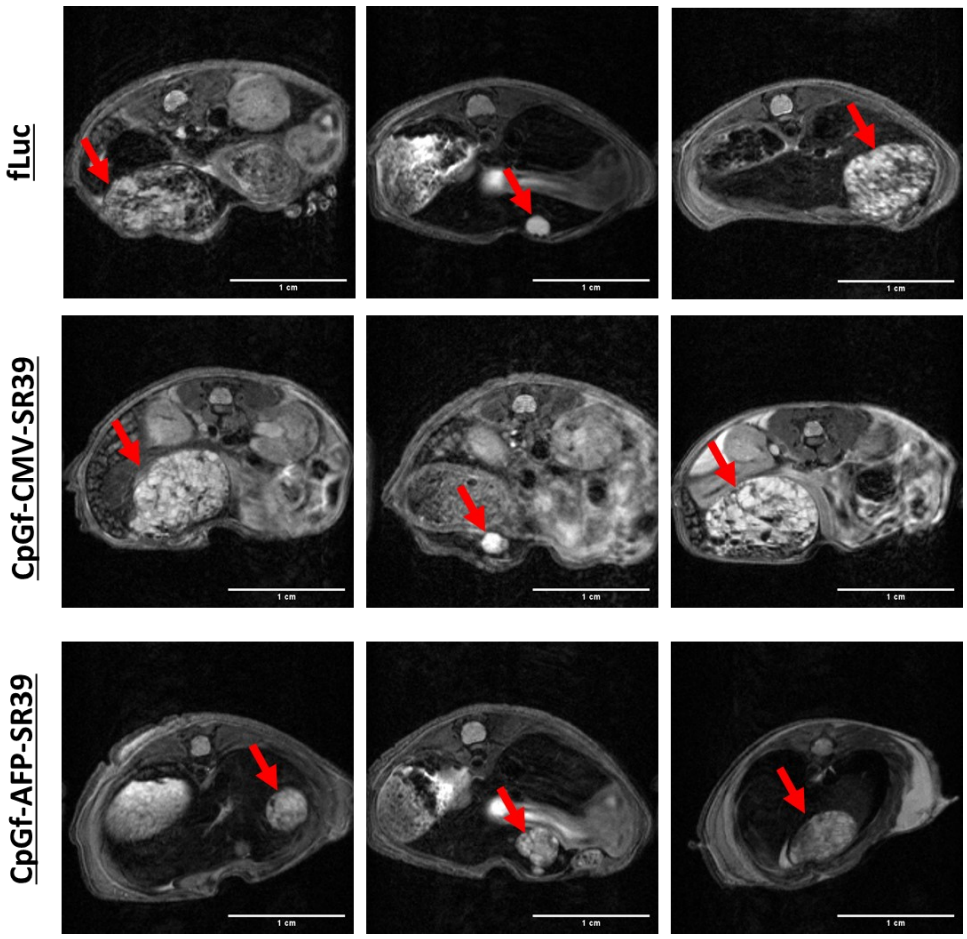

Figure 5.10 T2-weighted MRI scans of the liver and HCC tumors on Day 16. Arrows point to hyperintense tumors. Scale bar = 1 cm.

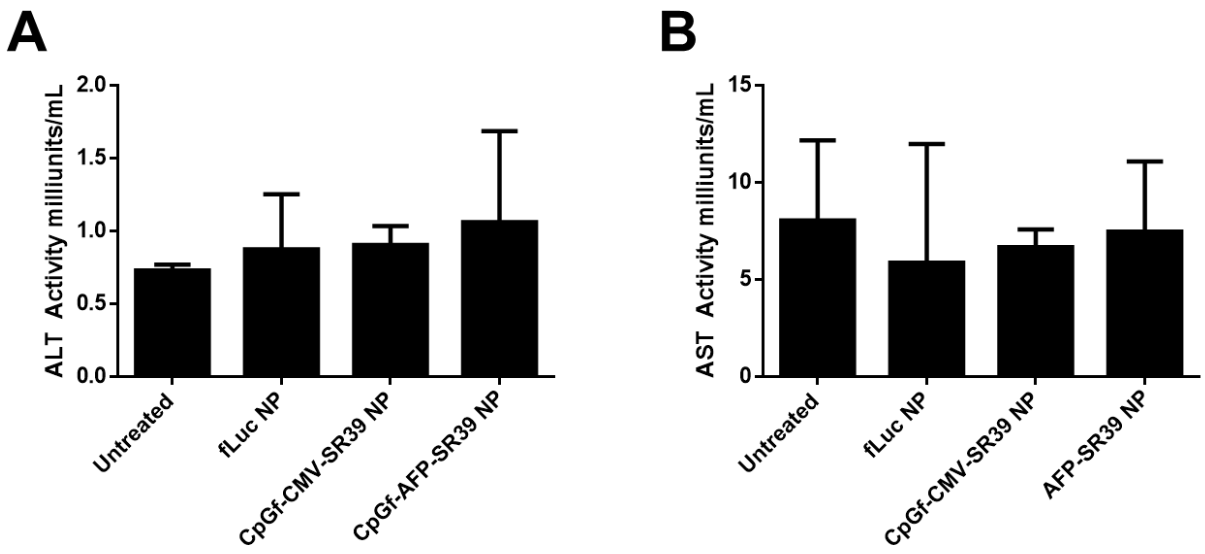

Figure 5.11 Liver enzyme levels in serum after 16 days of NP + GCV treatment A. ALT levels and B. AST levels for untreated animals (n = 3), and tumor-bearing mice treated with fLuc NPs (n = 6), CpGf-CMV-sr39 (n = 5), and CpGf-AFP-sr39 (n = 3). Mean ± SE are shown.

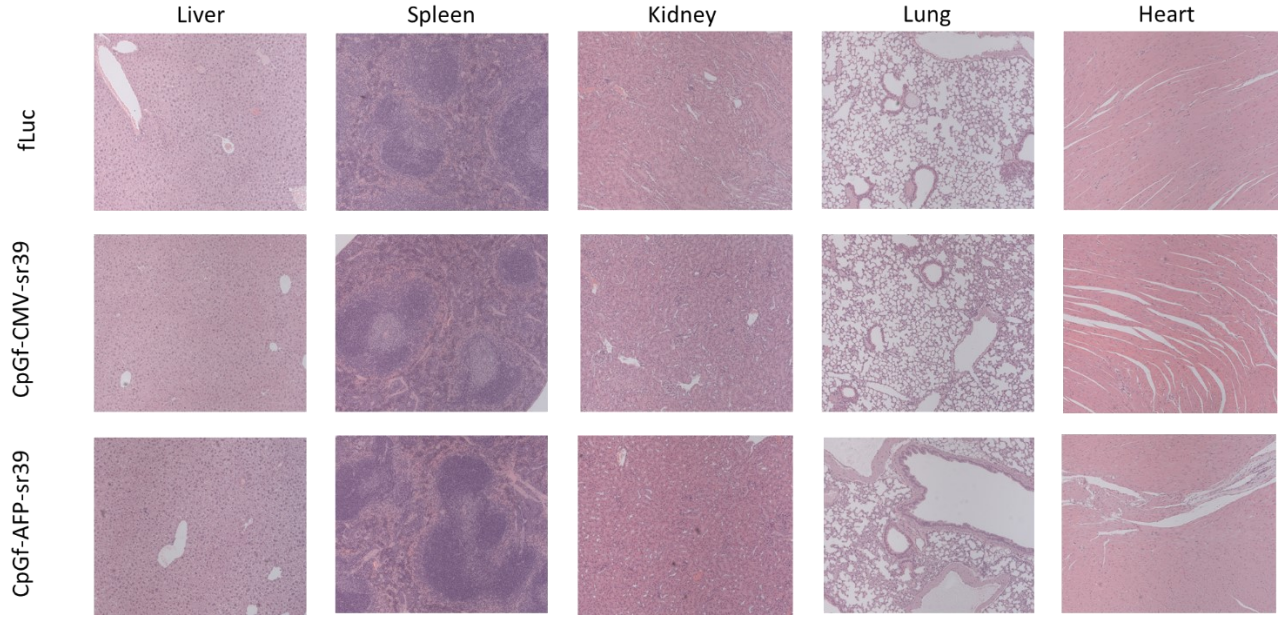

Figure 5.12 Representative histopathology after 16 days of NP + GCV treatment Formalin-fixed and paraffin-embedded tissue sections from the liver, tumor, spleen, kidney, heart, and lungs. Sections were stained with hematoxylin and eosin. All images are at 10X magnification.

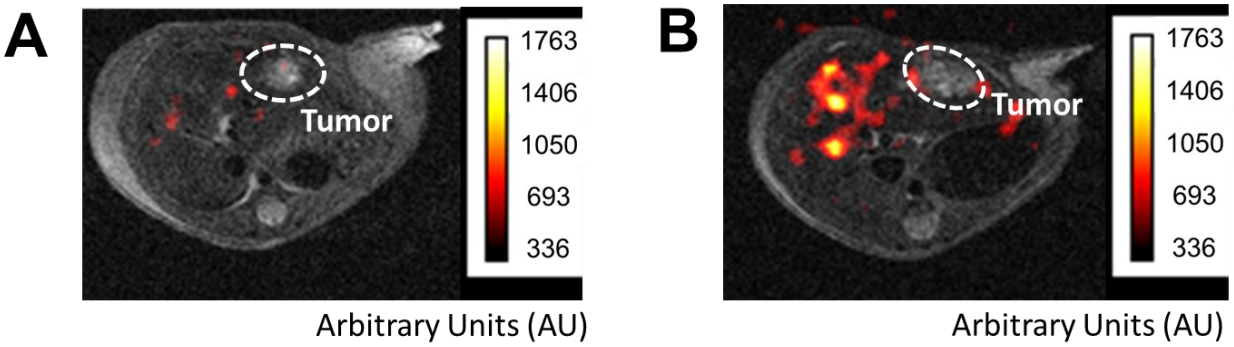

Figure 5.13 Representative PET/MRI imaging of Hep3b orthotopic tumor-bearing mice treated with A. fLuc NPs or B. CpGf-CMV-sr39 NPs and 150 mCi ^{18}F-FHBG.

Chapter 6: Recent Advances in Gene Therapy for Theranostic Cancer Medicine

6.1 Introduction

While there have been many advances in cancer treatment over the past decades, the efficacy of a novel therapy in a particular patient's tumor remains unpredictable[1,2]. With the advent of nanomedicines for cancer treatment, small differences in tumor biology, vascularity and immune microenvironment can have a large impact on the efficacy of a particular therapeutic[3,4]. Therefore, there is growing interest in developing approaches which incorporate agents with therapeutic efficacy as well as capabilities for monitoring the location and activity of the therapeutic agent. Gene delivery, in particular, can enable such promising theranostic approaches. There is great interest in developing gene therapies for many disease indications, including cancer. However, successful delivery of nucleic acids to tumor cells is a major challenge, and in vivo efficacy is difficult to predict. Cancer theranostics is an approach combining anti-tumor therapy with imaging or diagnostic capabilities, with the goal of monitoring successful delivery and efficacy of a therapeutic agent in a tumor. Successful theranostics must maintain a high degree of anticancer targeting and efficacy while incorporating high-contrast imaging agents that are nontoxic and compatible with clinical imaging modalities. This review highlights recent advancements in theranostic strategies, including imaging technologies and genetic engineering approaches (**Figure 6.1**).

6.2 Multifunctional Nanoparticles

This chapter contains material modified from the following article in press:
Vaughan, H.J., Green J.J.; Recent Advances in Gene Therapy for Theranostic Cancer Medicine. (2021). *Current Opinion in Biomedical Engineering. In Press.*

Multifunctional nanoparticles incorporate two or more biological or chemical modifications for enhanced functionality[5–7]. This may include targeting ligands, bioresponsive chemistries, and multiple encapsulated agents which serve therapeutic or diagnostic functions. By incorporating an imaging agent into a nanoparticle, it is possible to monitor tissue-level biodistribution and functional molecular interactions within the tumor. Imaging agents can be linked to nucleic acid cargo through direct covalent conjugation or incorporation into supramolecular NPs which also include biomaterials, such as lipids, polymers, and peptides to aid in nucleic acid encapsulation and release. Several types of imaging agents have been successfully incorporated in therapeutic nanoparticles, with varying sensitivity, resolution, and clinical compatibility.

6.2.1 MR and CT Imaging

Inorganic materials are popular choices for imaging nanoparticles, as they have desirable properties for detection under a range of clinical imaging modalities[8]. In particular, superparamagnetic iron oxide (SPIO) nanoparticles have magnetic properties well suited for MR imaging[9]. SPIO nanoparticles may be coated in polymer or lipid materials to allow nucleic acid encapsulation as well as surface functionalization and targeting[10]. For further spatial targeting, an external magnetic force may be used to localize nanoparticles in the tumor tissue and aid in gene delivery in a process called magnetofection[11]. Recent work by Cui and colleagues demonstrated that polymer nanoparticles loaded with SPIO showed successful localized transfection of primary hippocampal neurons *in vivo* under an external magnetic field, providing evidence for the safety and efficacy of this approach[12].

Gold nanoparticles have also been investigated for dual imaging and nucleic acid delivery. Gold nanoparticles have a high degree of X-ray attenuation, generating contrast on a

CT scan[13]. As a delivery material, gold is attractive because it can be functionalized with chemical and biological ligands through gold - sulfur (Au-S) bonding[14]. Thiolated oligonucleotides may be conjugated directly to the surface of gold nanoparticles, and work by Mirkin and coworkers shows that dense nucleic acid conjugation prevents nuclease degradation and improves cellular uptake[15]. Gold nanoparticles can also be encapsulated in ultrasound responsive microbubbles for spatially controlled disruption of cellular membranes, which has been shown to enhance intracellular delivery of nucleic acid cargo[16–18].

6.2.2 Optical Imaging and Sensing

Fluorescent dyes and quantum dots have also been used to enable *in vivo* tracking by optical imaging[19]. These optical imaging strategies are advantageous because they are sensitive, versatile, and enable multiplexing of different agents. The limitations of optical imaging strategies are significant background fluorescence and shallow penetration depth **(Table 6.1)**. Recently there has been much focus on the development of NIR-IIb (1500–1700 nm) fluorescent probes, which are compatible with *in vivo* imaging due to low tissue autofluorescence and photo-scattering. Inorganic agents, including quantum dots[20], rare-earth nanoprobes[21], and carbon nanotubes[22] have all shown promise in imaging at wavelengths > 1500 nm. A new technology termed aggregation-induced emission lumigens (AIEgens) has shown promise as an organic probe in the NIR II range[23].

To probe molecular interactions in target cells, biosensors may be incorporated into therapeutic nanoparticles by chemical conjugation[24,25] or encapsulation[26]. Sensors can be designed to emit a signal in response to the presence of nucleic acids, proteins, or other hallmarks of a particular disease[27]. Typically, these sensors undergo a conformational change in the presence of a target molecule or environmental change, and this conformational change

affects the spatial position of a fluorophore to change its proximity to a quencher or another fluorophore. Sensors have been designed to detect environmental changes such as pH change[28,29], reactive oxygen[30], and ion concentrations[31]. Sensors have also been developed to detect biological activity including enzyme activity[32–34] and expression of specific nucleic acid sequences[35,36].

6.3 Co-expression of Genetically Encoded Therapeutic and Diagnostic Agents

Nonviral nanoparticle delivery vehicles have the potential to deliver multiple nucleic acid sequences in a combinatorial manner through simple mixing during particle fabrication[37]. Theranostic functionality can be achieved by either delivering a plasmid that encodes an enzyme with both therapeutic and diagnostic function[38,39] or by co-delivering nucleic acids encoding for diagnostic and therapeutic agents. Therapeutic and diagnostic sequences may be placed in a single plasmid under the control of the same promoter in a bicistronic vector[40,41] or using a bidirectional promoter[42,43]. Alternatively, two or more different plasmids or RNA sequences may be co-encapsulated, allowing the ratio of each component to be controlled.

6.3.1 Genetically Encoded Diagnostic Agents

A. Optical Imaging

Encoded fluorescent proteins are powerful tools for monitoring the dynamics of gene expression. Protein engineering strategies have been employed to increase chromophore brightness, improve stability, and shift the excitation and emission wavelengths[44]. Specifically, longer wavelength fluorescent proteins have been developed which are less susceptible to absorption and scattering from tissue[45]. Additionally, there have been advancements in genetically encoded fluorescent biosensors, including optimized sensors for FRET, dimerization, translocation, complementation, and fluorescence-modulated single fluorescent protein sensors[44].

Optoacoustic imaging measures the conversion of optical photon energy to ultrasound waves by thermoelastic expansion of a material. This enables measurements to be obtained from deeper within the tissue than fluorescence-based methods. Endogenous chromophores include melanin and hemoglobin. Stritzker et al. used vaccinia virus to genetically manipulate tumor cells to overproduce the polymerized melanin, enabling optoacoustic imaging as well as photothermal therapy of tumors[46].

B. MRI

To create contrast in MRI imaging, the expressed protein or peptide must interfere with nuclear spins of surrounding tissue[47,48]. Much of this work has focused on the development of proteins that bind and sequester contrast agents that are endogenous to the target tissue or are systemically administered. Ferritin is an iron storage molecule that augments iron uptake in cells where it is overexpressed, and engineered ferritin proteins have been developed for enhanced imaging properties[49,50]. More recently, a family of prokaryotic nano compartments called encapsulins were expressed in human cells and showed high levels of nontoxic iron sequestration[51]. Encoded proteins have also been designed to sequester intravenously administered contrast, including Gd^{3+} agents[52].

Engineered proteins capable of proton exchange with surrounding molecules are detectable by chemical exchange saturation transfer (CEST) MRI[53]. Gilad et al developed a genetically encoded lysine-rich peptide (LRP) reporter with high amide proton exchange rate which enables frequency-selective contrast with CEST MRI[54]. 9L xenograft brain tumors expressing the LRP exhibited significant differences in signal-intensity change by CEST MRI compared with contralateral control tumors.

Finally, genetically encoded agents have been developed to alter cell and tissue water content for local MRI contrast. One elegant approach by Mukherjee et al. demonstrates that overexpression of the water channel protein aquaporin 1 enables tumor imaging by diffusion-weighted MRI by changing the cellular permeability to water[55]. Alternative proteins have also been explored in a similar approach, including a pH-sensitive bacterial channel[56] and a urea transporters[57]. Similarly, vasoactive peptides or proteins may be locally expressed to increase local blood flow and induce contrast changes detectable by MRI[58].

C. Ultrasound

Gas bubbles in the form of injected microbubbles are a well-established contrast agent for ultrasound[59]. In recent work by Farhadi et al, researchers engineered genes from waterborne microbes to express gas vesicles in mammalian cells **(Figure 6.2)** [60]. Expression of these mammalian acoustic reporter genes (mARGs) result in the intracellular production of gas-filled nanocompartments, allowing for genetic expression of ultrasound contrast *in vitro* and *in vivo*.

6.3.2 Therapeutic Nucleic Acids

Many different strategies have been employed to genetically induce cancer cell death[61]. One strategy is to overexpress pro-apoptotic genes in tumor cells, including sequences that induce apoptosis[62–64], mediate cell cycle arrest[65,66], and regulate DNA damage response[67]. The most prominent of these genes in clinical trials is p53, a transcription factor that controls cellular stress response and is dysregulated in a majority of human tumors[68]. Adenovirus expressing p53 has been tested in many tumor types in clinical trials, including hepatocellular carcinoma, non-small cell lung cancer, and squamous cell carcinoma[69]. These trials show the feasibility, safety, and antitumor efficacy of this approach, which has led to the approval of the AAV product Gendicine in China[70]. However, no p53 gene therapy has been approved in the US[71].

Immunotherapy approaches have shown promise in reprograming the immune system to destroy tumor cells[72]. Genetic cancer vaccines deliver nucleic acids encoding for tumor antigen to antigen presenting cells for a systemic immune response[73–75]. Potent antitumor responses have also been achieved with the delivery of cytokines to tumors, recruiting pro-inflammatory immune cells to the immunosuppressive tumor microenvironment[76–78]. Cell therapies are a new promising category of cancer therapeutic, and much work has been focused on imaging technologies for tracking and monitoring adoptively transferred cells *in vivo.* Prior to adoptive transfer, therapeutic cells may be transduced or transfected with genetically encoded imaging agents, including fluorescent and luminescent proteins. These imaging strategies have been used to study migration, persistence, and proliferation of adoptively transferred cells[79]. Minn and colleagues recently developed chimeric antigen receptor (CAR) T cells expressing a reporter transgene with prostate-specific membrane antigen (PSMA), a cancer-specific biomarker targeted by a number of radiotracer ligands (**Figure 6.3**)[80]. Engineered anti-CD19 CAR T cells (CD19-tPSMA$^{(N9Del)}$) were tracked *in vivo* using [^{18}F]DCFPyL PET in a model of acute lymphoblastic leukemia, showing infiltration in bone marrow metastases as well as the primary tumor. Importantly, the PSMA-transduced CAR T cells maintained antitumor efficacy, indicating that incorporating this tracking strategy does not impair T cell function.

Advances in siRNA and miRNA delivery have enabled the targeting of alternative pathways involved in cancer progression. siRNAs serve to transiently silence oncogene expression in a sequence-dependent manner[81]. In cancer therapy, targets for siRNA therapy include genes involved in proliferation[82], survival[83,84], and migration[85]. miRNAs are multifunctional sequences which are important for gene expression and regulation and are often dysregulated in tumor cells. Recent work to target miRNAs to tumor cells has shown preclinical

efficacy, either through delivery of anti-tumor miRNAs[86] or anti-miR sequences which target destruction of pro-cancer miRNAs[87].

6.4 Expression of Dual-function Theranostic Protein

Gene-directed enzyme prodrug therapy (GDEPT) utilizes a single enzyme with dual substrates for combination therapeutic and diagnostic functions[88]. One enzyme of this type with therapeutic promise is Herpes Simplex Virus-1 Thymidine Kinase (HSV-TK), which converts the prodrug ganciclovir into a toxic nucleoside analog[89]. The same enzyme phosphorylates the radiotracer 2'-deoxy-2'-[18F]-fluoro-1-beta-D-arabinofuranosyl-5-iodouracil ([18F]-FIAU) and causes accumulation which is detectable by PET imaging. Thus, the expression in HSV-TK alone in tumor cells enables cancer killing and monitoring using imaging. A mutant form of HSV-TK termed SR39 was developed by Black et al for enhanced prodrug sensitivity[90]. Both the mutant and wild-type forms have been tested in humans for clinical efficacy[91–93] and PET imaging[94].

Similarly, nitroreductase enzyme converts the prodrug CB1954 into a bifunctional alkylating agent, which induces apoptosis in tumor cells by crosslinking DNA[95]. This system is advantageous over HSV-TK/GCV because it is cell cycle-independent. Substrates for nitroreductase include both PET[96] and optical[97] imaging agents. Additional enzyme/prodrug combinations include cytochrome P450/cyclophosphamide[98,99] and cytosine deaminase/5-Fluorocytosine (5-FC) [100–102], although radiotracer substrates for these enzymes have been limited[103]. While these enzymes are paired with a therapeutic prodrug and separate tracer molecule, sodium and iodide symporter gene therapy enables both imaging and radiotherapy with the administration of radioiodine alone[104]. This symporter actively transports iodine isotopes into the cell, effectively concentrating the radiotracer[105]. These dual function theranostic

strategies that utilize a single enzyme encoded by a delivered gene therapy plasmid are advantageous by simplifying manufacturing as well as enabling tight correlation between the activity of the therapeutic and the diagnostic imaging read out.

6.5 Clinical Translation

While most of the approaches described in this review are in early stages of development, there has been early-stage progress in translating theranostic technologies to patients (**Table 6.2**). Nanoparticle imaging agents, including radiolabeled colloids for PET and iron oxide nanoparticles for MRI, have been clinically approved to improve contrast in certain solid tumors or surrounding lymph nodes[106,107]. True theranostic strategies remain in early stage clinical development. HSV-TK therapy has been the most commonly explored genetically encoded theranostic approach, with several Phase I/II trials completed. The major hurdle in translation remains improving intratumoral transgene expression[108]. While viral vectors historically have shown improved delivery efficacy over non-viral methods, there are safety concerns and reduced efficacy with repeated administrations due to the vector immunogenicity. Additionally, achieving improved targeting would improve local concentrations of therapeutics while reducing off-target dose-limiting toxicities. Taken together, improving delivery technologies is critical to the clinical success of all gene therapies, including theranostic approaches.

6.6 Conclusions

Nucleic acid therapeutics have incredible potential for innovative molecular therapy, improved cancer specificity, and the ability to disrupt multiple cancer mechanisms simultaneously. This review highlights the recent progress that has been made in gene delivery systems to monitor biodistribution and activity. Relevant imaging modalities span from PET and MRI to optical and ultrasound. Delivery remains a major barrier to translation of cancer gene

therapy, with key improvements needed in tumor targeting and robust transfection throughout heterogeneous tumors[109,110]. Additionally, improved technology and analysis of data is needed to better correlate theranostic imaging to clinical prognosis in order to fully realize the potential of the theranostic approach. By monitoring therapeutic efficacy in a comprehensive way, it becomes possible to better understand the interactions of next-generation nucleic acid therapies with the heterogeneous and dynamic biology of human tumors and ultimately improve clinical practice.

6.7 References

1. Marusyk, A and Polyak, K (2010). Tumor heterogeneity: causes and consequences. *Biochim. Biophys. Acta (BBA)-Reviews Cancer* **1805**: 105–117.
2. Alizadeh, AA, Aranda, V, Bardelli, A, Blanpain, C, Bock, C, Borowski, C, *et al.* (2015). Toward understanding and exploiting tumor heterogeneity. *Nat. Med.* **21**: 846.
3. Longo, DL (2012). Tumor heterogeneity and personalized medicine. *N Engl J Med* **366**: 956–957.
4. Kleppe, M and Levine, RL (2014). Tumor heterogeneity confounds and illuminates: assessing the implications. *Nat. Med.* **20**: 342–344.
5. Bao, G, Mitragotri, S and Tong, S (2013). Multifunctional nanoparticles for drug delivery and molecular imaging. *Annu. Rev. Biomed. Eng.* **15**: 253–282.
6. Yu, MK, Park, J and Jon, S (2012). Targeting strategies for multifunctional nanoparticles in cancer imaging and therapy. *Theranostics* **2**: 3.
7. Lee, D-E, Koo, H, Sun, I-C, Ryu, JH, Kim, K and Kwon, IC (2012). Multifunctional nanoparticles for multimodal imaging and theragnosis. *Chem. Soc. Rev.* **41**: 2656–2672.

8. Kim, D, Kim, J, Park, Y Il, Lee, N and Hyeon, T (2018). Recent Development of Inorganic Nanoparticles for Biomedical Imaging. *ACS Cent. Sci.* **4**: 324–336.

9. Dadfar, SM, Roemhild, K, Drude, NI, von Stillfried, S, Knüchel, R, Kiessling, F, *et al.* (2019). Iron oxide nanoparticles: Diagnostic, therapeutic and theranostic applications. *Adv. Drug Deliv. Rev.* **138**: 302–325.

10. Jiang, S, Eltoukhy, AA, Love, KT, Langer, R and Anderson, DG (2013). Lipidoid-Coated Iron Oxide Nanoparticles for Efficient DNA and siRNA delivery. *Nano Lett.* **13**: 1059–1064.

11. Schillinger, U, Brill, T, Rudolph, C, Huth, S, Gersting, S, Krötz, F, *et al.* (2005). Advances in magnetofection—magnetically guided nucleic acid delivery. *J. Magn. Magn. Mater.* **293**: 501–508.

12. Cui, Y, Li, X, Zeljic, K, Shan, S, Qiu, Z and Wang, Z (2019). Effect of PEGylated Magnetic PLGA-PEI Nanoparticles on Primary Hippocampal Neurons: Reduced Nanoneurotoxicity and Enhanced Transfection Efficiency with Magnetofection. *ACS Appl. Mater. Interfaces* **11**: 38190–38204.

13. Dong, YC, Hajfathalian, M, Maidment, PSN, Hsu, JC, Naha, PC, Si-Mohamed, S, *et al.* (2019). Effect of Gold Nanoparticle Size on Their Properties as Contrast Agents for Computed Tomography. *Sci. Rep.* **9**: 14912.

14. Ding, Y, Jiang, Z, Saha, K, Kim, CS, Kim, ST, Landis, RF, *et al.* (2014). Gold Nanoparticles for Nucleic Acid Delivery. *Mol. Ther.* **22**: 1075–1083.

15. Seferos, DS, Prigodich, AE, Giljohann, DA, Patel, PC and Mirkin, CA (2009). Polyvalent DNA Nanoparticle Conjugates Stabilize Nucleic Acids. *Nano Lett.* **9**: 308–311.

16. Passineau, MJ, Zourelias, L, Machen, L, Edwards, PC and Benza, RL (2010). Ultrasound-

assisted non-viral gene transfer to the salivary glands. *Gene Ther.* **17**: 1318–1324.

17. Wang, L, Lu, H, Gao, Q, Yuan, C, Ding, F, Li, J, *et al.* (2019). A multifunctional theranostic contrast agent for ultrasound/near infrared fluorescence imaging-based tumor diagnosis and ultrasound-triggered combined photothermal and gene therapy. *Acta Biomater.* **99**: 373–386.
18. Kinoshita, M, McDannold, N, Jolesz, FA and Hynynen, K (2006). Noninvasive localized delivery of Herceptin to the mouse brain by MRI-guided focused ultrasound-induced blood–brain barrier disruption. *Proc. Natl. Acad. Sci.* **103**: 11719–11723.
19. Medarova, Z, Pham, W, Farrar, C, Petkova, V and Moore, A (2007). In vivo imaging of siRNA delivery and silencing in tumors. *Nat. Med.* **13**: 372–377.
20. Zhang, M, Yue, J, Cui, R, Ma, Z, Wan, H, Wang, F, *et al.* (2018). Bright quantum dots emitting at∼ 1,600 nm in the NIR-IIb window for deep tissue fluorescence imaging. *Proc. Natl. Acad. Sci.* **115**: 6590–6595.
21. Li, Y, Zeng, S and Hao, J (2019). Non-invasive optical guided tumor metastasis/vessel imaging by using lanthanide nanoprobe with enhanced down-shifting emission beyond 1500 nm. *ACS Nano* **13**: 248–259.
22. Diao, S, Blackburn, JL, Hong, G, Antaris, AL, Chang, J, Wu, JZ, *et al.* (2015). Fluorescence Imaging In Vivo at Wavelengths beyond 1500 nm. *Angew. Chemie Int. Ed.* **54**: 14758–14762.
23. Li, Y, Cai, Z, Liu, S, Zhang, H, Wong, STH, Lam, JWY, *et al.* (2020). Design of AIEgens for near-infrared IIb imaging through structural modulation at molecular and morphological levels. *Nat. Commun.* **11**: 1255.
24. Zhang, L, Mazouzi, Y, Salmain, M, Liedberg, B and Boujday, S (2020). Antibody-Gold

Nanoparticle Bioconjugates for Biosensors: Synthesis, Characterization and Selected Applications. *Biosens. Bioelectron.*: 112370.

25. Liu, Y, Wang, Y-M, Zhu, W-Y, Zhang, C-H, Tang, H and Jiang, J-H (2018). Conjugated polymer nanoparticles-based fluorescent biosensor for ultrasensitive detection of hydroquinone. *Anal. Chim. Acta* **1012**: 60–65.

26. Hu, J, Kwak, KJ, Shi, J, Yu, B, Sheng, Y and Lee, LJ (2018). Overhang molecular beacons encapsulated in tethered cationic lipoplex nanoparticles for detection of single-point mutation in extracellular vesicle-associated RNAs. *Biomaterials* **183**: 20–29.

27. Boehnke, N, Correa, S, Hao, L, Wang, W, Straehla, JP, Bhatia, SN, *et al.* (2020). Theranostic Layer-by-Layer Nanoparticles for Simultaneous Tumor Detection and Gene Silencing. *Angew. Chemie Int. Ed.* **59**: 2776–2783.

28. Dennis, AM, Rhee, WJ, Sotto, D, Dublin, SN and Bao, G (2012). Quantum Dot–Fluorescent Protein FRET Probes for Sensing Intracellular pH. *ACS Nano* **6**: 2917–2924.

29. Huang, J, Ying, L, Yang, X, Yang, Y, Quan, K, Wang, H, *et al.* (2015). Ratiometric fluorescent sensing of pH values in living cells by dual-fluorophore-labeled i-motif nanoprobes. *Anal. Chem.* **87**: 8724–8731.

30. Rivero, PJ, Ibañez, E, Goicoechea, J, Urrutia, A, Matias, IR and Arregui, FJ (2017). A self-referenced optical colorimetric sensor based on silver and gold nanoparticles for quantitative determination of hydrogen peroxide. *Sensors Actuators B Chem.* **251**: 624–631.

31. Yang, Y, Huang, J, Yang, X, Quan, K, Xie, N, Ou, M, *et al.* (2016). Aptamer-based FRET nanoflares for imaging potassium ions in living cells. *Chem. Commun.* **52**: 11386–11389.

32. Ma, Y, Mao, G, Wu, G, Fan, J, He, Z and Huang, W (2020). A novel nano-beacon based

on DNA functionalized QDs for intracellular telomerase activity monitoring. *Sensors Actuators B Chem.* **304**: 127385.

33. Gu, P, Liu, X, Tian, Y, Zhang, L, Huang, Y, Su, S, *et al.* (2017). A novel visible detection strategy for lysozyme based on gold nanoparticles and conjugated polymer brush. *Sensors Actuators B Chem.* **246**: 78–84.

34. Zhang, J, He, L, Zhang, X, Wang, J, Yang, L, Liu, B, *et al.* (2017). Colorimetric and SERS dual-readout for assaying alkaline phosphatase activity by ascorbic acid induced aggregation of Ag coated Au nanoparticles. *Sensors Actuators B Chem.* **253**: 839–845.

35. Conde, J, Edelman, ER and Artzi, N (2015). Target-responsive DNA/RNA nanomaterials for microRNA sensing and inhibition: The jack-of-all-trades in cancer nanotheranostics? *Adv. Drug Deliv. Rev.* **81**: 169–183.

36. Zhang, C-Y, Yeh, H-C, Kuroki, MT and Wang, T-H (2005). Single-quantum-dot-based DNA nanosensor. *Nat. Mater.* **4**: 826–831.

37. Vaughan, HJ, Green, JJ and Tzeng, SY (2020). Cancer-targeting nanoparticles for combinatorial nucleic acid delivery. *Adv. Mater.* **32**: 1901081.

38. Barton, KN, Siddiqui, F, Pompa, R, Freytag, SO, Khan, G, Dobrosotskaya, I, *et al.* (2021). Phase I trial of oncolytic adenovirus-mediated cytotoxic and interleukin-12 gene therapy for the treatment of metastatic pancreatic cancer. *Mol. Ther.* **20**: 94–104.

39. Dührsen, L, Hartfuß, S, Hirsch, D, Geiger, S, Maire, CL, Sedlacik, J, *et al.* (2019). Preclinical analysis of human mesenchymal stem cells: tumor tropism and therapeutic efficiency of local HSV-TK suicide gene therapy in glioblastoma. *Oncotarget* **10**: 6049.

40. Wong, ET, Ngoi, SM and Lee, CGL (2002). Improved co-expression of multiple genes in vectors containing internal ribosome entry sites (IRESes) from human genes. *Gene Ther.*

9: 337–344.

41. Kim, JH, Lee, S-R, Li, L-H, Park, H-J, Park, J-H, Lee, KY, *et al.* (2011). High cleavage efficiency of a 2A peptide derived from porcine teschovirus-1 in human cell lines, zebrafish and mice. *PLoS One* **6**: e18556.

42. Xu, Z, Wei, W, Gagneur, J, Perocchi, F, Clauder-Münster, S, Camblong, J, *et al.* (2009). Bidirectional promoters generate pervasive transcription in yeast. *Nature* **457**: 1033–1037.

43. Trinklein, ND, Aldred, SF, Hartman, SJ, Schroeder, DI, Otillar, RP and Myers, RM (2004). An abundance of bidirectional promoters in the human genome. *Genome Res.* **14**: 62–66.

44. Sanford, L and Palmer, A (2017). Recent advances in development of genetically encoded fluorescent sensors. *Methods Enzymol.* **589**: 1–49.

45. Ng, H-L and Lin, MZ (2016). Structure-guided wavelength tuning in far-red fluorescent proteins. *Curr. Opin. Struct. Biol.* **39**: 124–133.

46. Stritzker, J, Kirscher, L, Scadeng, M, Deliolanis, NC, Morscher, S, Symvoulidis, P, *et al.* (2013). Vaccinia virus-mediated melanin production allows MR and optoacoustic deep tissue imaging and laser-induced thermotherapy of cancer. *Proc. Natl. Acad. Sci.* **110**: 3316 LP – 3320.

47. Wei, L, Li, S, Yang, J, Ye, Y, Zou, J, Wang, L, *et al.* (2011). Protein-Based MRI Contrast Agents for Molecular Imaging of Prostate Cancer. *Mol. Imaging Biol.* **13**: 416–423.

48. Jasanoff, A (2007). MRI contrast agents for functional molecular imaging of brain activity. *Curr. Opin. Neurobiol.* **17**: 593–600.

49. Cohen, B, Dafni, H, Meir, G, Harmelin, A and Neeman, M (2005). Ferritin as an Endogenous MRI Reporter for Noninvasive Imaging of Gene Expression in C6 Glioma

Tumors. *Neoplasia* **7**: 109–117.

50. Cozzi, A, Corsi, B, Levi, S, Santambrogio, P, Albertini, A and Arosio, P (2000). Overexpression of Wild Type and Mutated Human Ferritin H-chain in HeLa Cells: IN VIVO ROLE OF FERRITIN FERROXIDASE ACTIVITY*. *J. Biol. Chem.* **275**: 25122–25129.

51. Sigmund, F, Massner, C, Erdmann, P, Stelzl, A, Rolbieski, H, Desai, M, *et al.* (2018). Bacterial encapsulins as orthogonal compartments for mammalian cell engineering. *Nat. Commun.* **9**: 1990.

52. Yang, JJ, Yang, J, Wei, L, Zurkiya, O, Yang, W, Li, S, *et al.* (2008). Rational Design of Protein-Based MRI Contrast Agents. *J. Am. Chem. Soc.* **130**: 9260–9267.

53. Wu, B, Warnock, G, Zaiss, M, Lin, C, Chen, M, Zhou, Z, *et al.* (2016). An overview of CEST MRI for non-MR physicists. *EJNMMI Phys.* **3**: 1–21.

54. Gilad, AA, McMahon, MT, Walczak, P, Winnard, PT, Raman, V, van Laarhoven, HWM, *et al.* (2007). Artificial reporter gene providing MRI contrast based on proton exchange. *Nat. Biotechnol.* **25**: 217–219.

55. Mukherjee, A, Wu, D, Davis, HC and Shapiro, MG (2016). Non-invasive imaging using reporter genes altering cellular water permeability. *Nat. Commun.* **7**: 1–9.

56. Yang, L, Zheng, H, Ratnakar, JS, Adebesin, BY, Do, QN, Kovacs, Z, *et al.* (2018). Engineering a pH-sensitive liposomal MRI agent by modification of a bacterial channel. *Small* **14**: 1704256.

57. Schilling, F, Ros, S, Hu, D-E, D'Santos, P, McGuire, S, Mair, R, *et al.* (2017). MRI measurements of reporter-mediated increases in transmembrane water exchange enable detection of a gene reporter. *Nat. Biotechnol.* **35**: 75.

58. Desai, M, Slusarczyk, AL, Chapin, A, Barch, M and Jasanoff, A (2016). Molecular imaging with engineered physiology. *Nat. Commun.* **7**: 13607.

59. Quaia, E (2007). Microbubble ultrasound contrast agents: an update. *Eur. Radiol.* **17**: 1995–2008.

60. Farhadi, A, Ho, GH, Sawyer, DP, Bourdeau, RW and Shapiro, MG (2019). Ultrasound imaging of gene expression in mammalian cells. *Science (80-.).* **365**: 1469 LP – 1475.

61. Amer, MH (2014). Gene therapy for cancer: present status and future perspective. *Mol. Cell. Ther.* **2**: 1–19.

62. Jia, L-T, Chen, S-Y and Yang, A-G (2012). Cancer gene therapy targeting cellular apoptosis machinery. *Cancer Treat. Rev.* **38**: 868–876.

63. Yamabe, K, Shimizu, S, Ito, T, Yoshioka, Y, Nomura, M, Narita, M, *et al.* (1999). Cancer gene therapy using a pro-apoptotic gene, caspase-3. *Gene Ther.* **6**: 1952–1959.

64. Griffith, TS, Stokes, B, Kucaba, TA, Earel, J, James, K, VanOosten, RL, *et al.* (2009). TRAIL gene therapy: from preclinical development to clinical application. *Curr. Gene Ther.* **9**: 9–19.

65. Kastan, MB and Bartek, J (2004). Cell-cycle checkpoints and cancer. *Nature* **432**: 316–323.

66. Tanaka, M and Grossman, HB (2003). In vivo gene therapy of human bladder cancer with PTEN suppresses tumor growth, downregulates phosphorylated Akt, and increases sensitivity to doxorubicin. *Gene Ther.* **10**: 1636–1642.

67. Lord, CJ and Ashworth, A (2012). The DNA damage response and cancer therapy. *Nature* **481**: 287–294.

68. Muller, PAJ and Vousden, KH (2013). p53 mutations in cancer. *Nat. Cell Biol.* **15**: 2–8.

69. Chen, G-X, Zhang, S, He, X-H, Liu, S-Y, Ma, C and Zou, X-P (2014). Clinical utility of recombinant adenoviral human p53 gene therapy: current perspectives. *Onco. Targets. Ther.* **7**: 1901–1909.

70. Zhang, W-W, Li, L, Li, D, Liu, J, Li, X, Li, W, *et al.* (2018). The first approved gene therapy product for cancer Ad-p53 (Gendicine): 12 years in the clinic. *Hum. Gene Ther.* **29**: 160–179.

71. Edelstein, ML, Abedi, MR, Wixon, J and Edelstein, RM (2004). Gene therapy clinical trials worldwide 1989–2004—an overview. *J. Gene Med. A cross-disciplinary J. Res. Sci. gene Transf. its Clin. Appl.* **6**: 597–602.

72. Mukalel, AJ, Riley, RS, Zhang, R and Mitchell, MJ (2019). Nanoparticles for nucleic acid delivery: Applications in cancer immunotherapy. *Cancer Lett.* **458**: 102–112.

73. Pan, R-Y, Chung, W-H, Chu, M-T, Chen, S-J, Chen, H-C, Zheng, L, *et al.* (2018). Recent development and clinical application of cancer vaccine: targeting neoantigens. *J. Immunol. Res.* **2018**.

74. Aurisicchio, L, Peruzzi, D, Koo, G, Wei, W-Z, La Monica, N and Ciliberto, G (2014). Immunogenicity and therapeutic efficacy of a dual-component genetic cancer vaccine cotargeting carcinoembryonic antigen and HER2/neu in preclinical models. *Hum. Gene Ther.* **25**: 121–131.

75. Roos, A, Pavlenko, M, Charo, J, Egevad, L and Pisa, P (2005). Induction of PSA-specific CTLs and anti-tumor immunity by a genetic prostate cancer vaccine. *Prostate* **62**: 217–223.

76. Kim, TH, Jin, H, Kim, HW, Cho, M-H and Cho, CS (2006). Mannosylated chitosan nanoparticle–based cytokine gene therapy suppressed cancer growth in BALB/c mice

bearing CT-26 carcinoma cells. *Mol. Cancer Ther.* **5**: 1723–1732.

77. Podhajcer, OL, Lopez, MV and Mazzolini, G (2007). Cytokine gene transfer for cancer therapy. *Cytokine Growth Factor Rev.* **18**: 183–194.

78. Tzeng, SY, Patel, KK, Wilson, DR, Meyer, RA, Rhodes, KR and Green, JJ (2020). In situ genetic engineering of tumors for long-lasting and systemic immunotherapy. *Proc. Natl. Acad. Sci.* **117**: 4043–4052.

79. Cazaux, M, Grandjean, CL, Lemaître, F, Garcia, Z, Beck, RJ, Milo, I, *et al.* (2019). Single-cell imaging of CAR T cell activity in vivo reveals extensive functional and anatomical heterogeneity. *J. Exp. Med.* **216**: 1038–1049.

80. Minn, I, Huss, DJ, Ahn, H-H, Chinn, TM, Park, A, Jones, J, *et al.* (2019). Imaging CAR T cell therapy with PSMA-targeted positron emission tomography. *Sci. Adv.* **5**: eaaw5096.

81. Devi, GR (2006). siRNA-based approaches in cancer therapy. *Cancer Gene Ther.* **13**: 819–829.

82. Xu, X, Wu, J, Liu, Y, Saw, PE, Tao, W, Yu, M, *et al.* (2017). Multifunctional Envelope-Type siRNA Delivery Nanoparticle Platform for Prostate Cancer Therapy. *ACS Nano* **11**: 2618–2627.

83. Salzano, G, Riehle, R, Navarro, G, Perche, F, De Rosa, G and Torchilin, VP (2014). Polymeric micelles containing reversibly phospholipid-modified anti-survivin siRNA: A promising strategy to overcome drug resistance in cancer. *Cancer Lett.* **343**: 224–231.

84. Kozielski, KL, Ruiz-Valls, A, Tzeng, SY, Guerrero-Cázares, H, Rui, Y, Li, Y, *et al.* (2019). Cancer-selective nanoparticles for combinatorial siRNA delivery to primary human GBM in vitro and in vivo. *Biomaterials* **209**: 79–87.

85. Davudian, S, Shajari, N, Kazemi, T, Mansoori, B, Salehi, S, Mohammadi, A, *et al.* (2016).

BACH1 silencing by siRNA inhibits migration of HT-29 colon cancer cells through reduction of metastasis-related genes. *Biomed. Pharmacother.* **84**: 191–198.

86. Lopez-Bertoni, H, Kozielski, KL, Rui, Y, Lal, B, Vaughan, H, Wilson, DR, *et al.* (2018). Bioreducible polymeric nanoparticles containing multiplexed cancer stem cell regulating miRNAs inhibit glioblastoma growth and prolong survival. *Nano Lett.* **18**: 4086–4094.

87. Cheng, CJ, Bahal, R, Babar, IA, Pincus, Z, Barrera, F, Liu, C, *et al.* (2015). MicroRNA silencing for cancer therapy targeted to the tumour microenvironment. *Nature* **518**: 107–110.

88. F Tietze, L and Schmuck, K (2011). Prodrugs for targeted tumor therapies: recent developments in ADEPT, GDEPT and PMT. *Curr. Pharm. Des.* **17**: 3527–3547.

89. Fillat, C, Carrio, M, Cascante, A and Sangro, B (2003). Suicide gene therapy mediated by the Herpes Simplex virus thymidine kinase gene/Ganciclovir system: fifteen years of application. *Curr. Gene Ther.* **3**: 13–26.

90. Black, ME, Kokoris, MS and Sabo, P (2001). Herpes simplex virus-1 thymidine kinase mutants created by semi-random sequence mutagenesis improve prodrug-mediated tumor cell killing. *Cancer Res.* **61**: 3022–3026.

91. Sangro, B, Mazzolini, G, Ruiz, M, Ruiz, J, Quiroga, J, Herrero, I, *et al.* (2010). A phase I clinical trial of thymidine kinase-based gene therapy in advanced hepatocellular carcinoma. *Cancer Gene Ther.* **17**: 837–843.

92. Rainov, NG (2000). A phase III clinical evaluation of herpes simplex virus type 1 thymidine kinase and ganciclovir gene therapy as an adjuvant to surgical resection and radiation in adults with previously untreated glioblastoma multiforme. *Hum. Gene Ther.* **11**: 2389–2401.

93. Klatzmann, D, Valery, CA, Bensimon, G, Marro, B, Boyer, O, Mokhtari, K, *et al.* (1998). A phase I/II study of herpes simplex virus type 1 thymidine kinase "suicide" gene therapy for recurrent glioblastoma. *Hum. Gene Ther.* **9**: 2595–2604.

94. Yaghoubi, SS and Gambhir, SS (2006). PET imaging of herpes simplex virus type 1 thymidine kinase (HSV1-tk) or mutant HSV1-sr39tk reporter gene expression in mice and humans using [18 F] FHBG. *Nat. Protoc.* **1**: 3069.

95. Nouri, FS, Wang, X and Hatefi, A (2015). Genetically engineered theranostic mesenchymal stem cells for the evaluation of the anticancer efficacy of enzyme/prodrug systems. *J. Control. Release* **200**: 179–187.

96. Mowday, AM, Copp, JN, Syddall, SP, Dubois, LJ, Wang, J, Lieuwes, NG, *et al.* (2020). E. coli nitroreductase NfsA is a reporter gene for non-invasive PET imaging in cancer gene therapy applications. *Theranostics* **10**: 10548.

97. Liu, Z, Song, F, Shi, W, Gurzadyan, G, Yin, H, Song, B, *et al.* (2019). Nitroreductase-Activatable Theranostic Molecules with High PDT Efficiency under Mild Hypoxia Based on a TADF Fluorescein Derivative. *ACS Appl. Mater. Interfaces* **11**: 15426–15435.

98. WAXMAN, DJ, CHEN, L, HECHT, JED and JOUNAIDI, Y (1999). Cytochrome P450-based cancer gene therapy: recent advances and future prospects. *Drug Metab. Rev.* **31**: 503–522.

99. Chen, L, Li, JY and Waxm, DJ (1997). Potentiation of cytochrome P450/cyclophosphamide-based cancer gene therapy by coexpression of the P450 reductase gene. *Cancer Res.* **57**: 4830–4837.

100. Kanai, F, Lan, K-H, Shiratori, Y, Tanaka, T, Ohashi, M, Okudaria, T, *et al.* (1997). In vivo gene therapy for α-fetoprotein-producing hepatocellular carcinoma by adenovirus-

mediated transfer of cytosine deaminase gene. *Cancer Res.* **57**: 461–465.

101. Austin, EA and Huber, BE (1993). A first step in the development of gene therapy for colorectal carcinoma: cloning, sequencing, and expression of Escherichia coli cytosine deaminase. *Mol. Pharmacol.* **43**: 380–387.

102. Akbulut, H, Coleri, A, Sahin, G, Tang, Y and Icli, F (2019). A Bicistronic Adenoviral Vector Carrying Cytosine Deaminase and Granulocyte-Macrophage Colony-Stimulating Factor Increases the Therapeutic Efficacy of Cancer Gene Therapy. *Hum. Gene Ther.* **30**: 999–1007.

103. Sharma, V, Luker, GD and Piwnica-Worms, D (2002). Molecular imaging of gene expression and protein function in vivo with PET and SPECT. *J. Magn. Reson. Imaging An Off. J. Int. Soc. Magn. Reson. Med.* **16**: 336–351.

104. Ahn, B-C (2012). Sodium iodide symporter for nuclear molecular imaging and gene therapy: from bedside to bench and back. *Theranostics* **2**: 392–402.

105. Mandell, RB, Mandell, LZ and Link, CJ (1999). Radioisotope concentrator gene therapy using the sodium/iodide symporter gene. *Cancer Res.* **59**: 661–668.

106. Cortajarena, AL, Ortega, D, Ocampo, SM, Gonzalez-García, A, Couleaud, P, Miranda, R, *et al.* (2014). Engineering iron oxide nanoparticles for clinical settings. *Nanobiomedicine* **1**: 1–2.

107. Thacker, C, Korn, R, Millstine, J, Harvin, H, Ribbink, JAVL and Gotway, MB (2010). Sclerosing angiomatoid nodular transformation of the spleen: CT, MR, PET, and 99m Tc-sulfur colloid SPECT CT findings with gross and histopathological correlation. *Abdom. Imaging* **35**: 683–689.

108. Shirakawa, T, Terao, S, Hinata, N, Tanaka, K, Takenaka, A, Hara, I, *et al.* (2007). Long-

term outcome of phase I/II clinical trial of Ad-OC-TK/VAL gene therapy for hormone-refractory metastatic prostate cancer. *Hum. Gene Ther.* **18**: 1225–1232.

109. Shim, G, Kim, D, Le, Q-V, Park, GT, Kwon, T and Oh, Y-K (2018). Nonviral delivery systems for cancer gene therapy: strategies and challenges. *Curr. Gene Ther.* **18**: 3–20.

110. El-Aneed, A (2004). An overview of current delivery systems in cancer gene therapy. *J. Control. Release* **94**: 1–14.

111. Karabulut, N and Elmas, N (2006). Contrast agents used in MR imaging of the liver. *Diagnostic Interv. Radiol.* **12**: 22.

112. Luo, G, Liu, Z, Guo, M, Jin, K, Xiao, Z, Liu, L, *et al.* (2014). 18F-FDG PET/CT can be used to detect non-functioning pancreatic neuroendocrine tumors. *Int J Oncol* **45**: 1531–1536.

113. Snipstad, S, Berg, S, Mørch, Ý, Bjørkøy, A, Sulheim, E, Hansen, R, *et al.* (2017). Ultrasound improves the delivery and therapeutic effect of nanoparticle-stabilized microbubbles in breast cancer xenografts. *Ultrasound Med. Biol.* **43**: 2651–2669.

114. Lee, JYK, Pierce, JT, Thawani, JP, Zeh, R, Nie, S, Martinez-Lage, M, *et al.* Near-infrared fluorescent image-guided surgery for intracranial meningioma. *J. Neurosurg. JNS* **128**: 380–390.

115. Sivasubramanian, M, Hsia, Y and Lo, L-W (2014). Nanoparticle-facilitated functional and molecular imaging for the early detection of cancer. *Front. Mol. Biosci.* **1**: 15.

116. Barsanti, C, Lenzarini, F and Kusmic, C (2015). Diagnostic and prognostic utility of non-invasive imaging in diabetes management. *World J. Diabetes* **6**: 792.

6.8 Figures and Tables

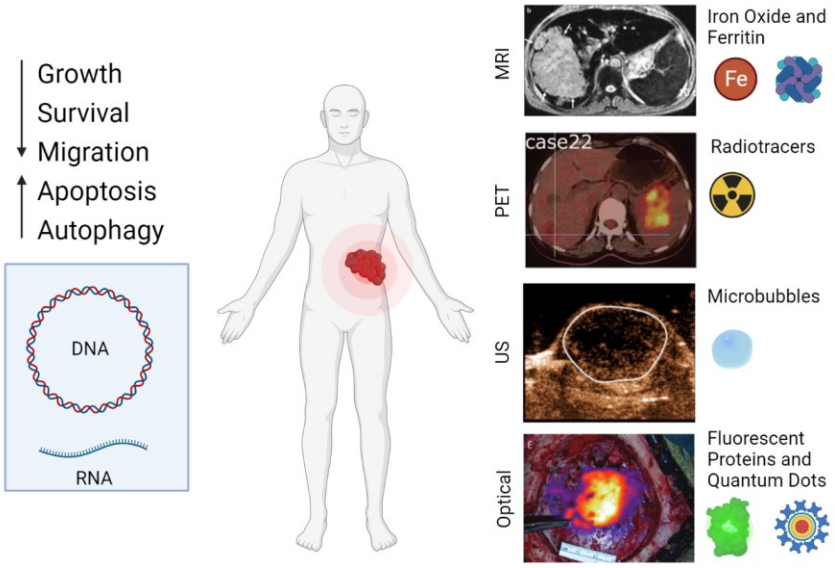

Figure 6.1 Theranostic strategies allow for simultaneous therapeutic nucleic acid delivery and imaging. MRI: Magnetic Resonance Imaging. PET: Positron Emission Tomography, US: Ultrasound. MRI image adapted from ref. [111] Figure 5 B with permission from the Turkish Society of Radiology. PET image adapted from ref. [112] Figure 1 with permission from the World Academy of Sciences. US image adapted from ref. [113] Figure 4 B with permission from the World Federation for Ultrasound in Medicine & Biology. Optical image adapted from ref. [114] 1 E with permission from the American Association of Neurological Surgeons.

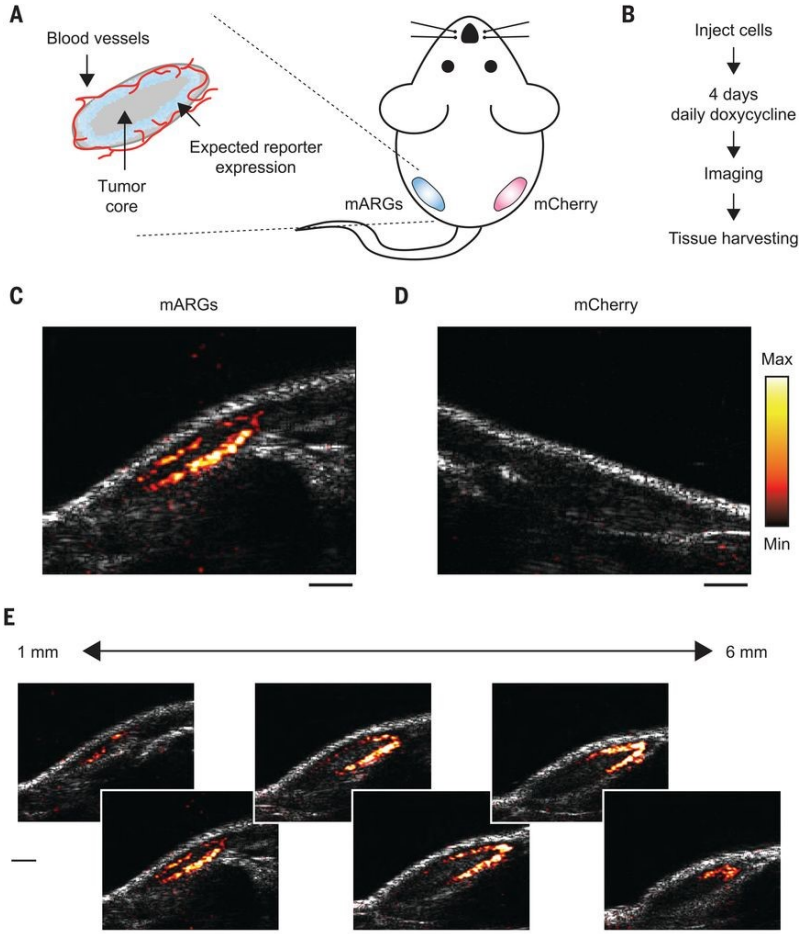

Figure 6.2. Genetically encoded gas vesicles (mARGs) enable ultrasound imaging of gene expression *in vivo* A. Schematic and B. timeline of subcutaneous tumor implantation and doxycycline included expression on mARGs and mCherry in contralateral tumors. C. Representative image of mARGs-related ultrasound contrast (heat map) overlayed on B-mode imaging showing tumor anatomy. D. Representative image of a control tumor expressing mCherry. E. Sequential slices spaced 1 mm apart showing mARG expression in the tumor. Adapted from ref. [60] Figure 4 A-E with permission from the American Association for the Advancement of Science.

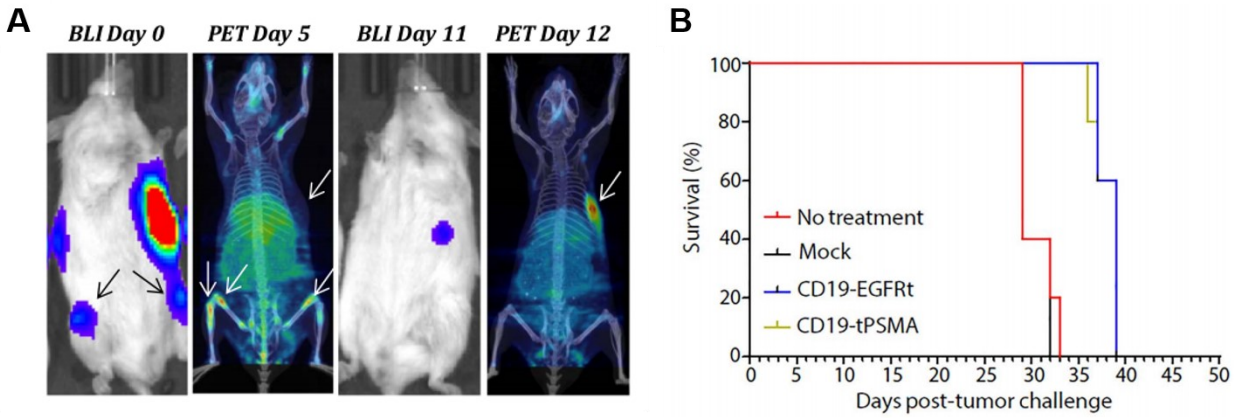

Figure 6.3. PSMA-transduced CAR T cells enable *in vivo* tracking and extend survival. A. Tumor burden on Day 0 and Day 11 of treatment is shown using bioluminescence imaging (BLI), and CD19-tPSMA$^{(N9Del)}$ cell tracking in bone marrow metastases (Day 5) and primary tumor (Day 12) by PET imaging. B. PSMA-transduced CD19-tPSMA$^{(N9Del)}$ cells extend survival compared with negative controls, with efficacy similar to CD19-EGFRt positive control cells. Adapted from ref. [80] Figure 4 B and 2 D with permission from the American Association for the Advancement of Science.

Modality	Resolution	Imaging Depth	Advantages	Drawbacks
MR	50-500 μm	Full Body	Excellent resolution, high contrast soft tissue imaging	Expensive, long acquisition time
CT	0.5-1 mm	Full Body	Whole body anatomical imaging, low acquisition time	Radiation exposure
Ultrasound	~200 μm	1-10 cm	Real-time imaging, low acquisition time	Modest penetration depth, restricted imaging area
PET	0.3-3 mm	Full Body	Functional imaging	Radiation exposure
Optical	0.1-10 mm	1-10 mm	Multiplexing, real-time imaging	Poor Penetration Depth

Table 6.1 Common imaging modalities and properties[115,116]. MR: Magnetic resonance, CT: Computed tomography, PET: Positron emission tomography

Modality	Select Product(s)	Trial Phase	Trial Identifier(s)
Radiolabeled Colloids	99mTc-labeled sulfur colloid	Approved	NCT01668914
Dextran-coated Iron Oxide Imaging Agents	Ferumoxide, ferumoxtran, ferucarbotran	Approved	NCT00307866 NCT00622973
Targeted Radionuclide Therapy	Cu-SARTATE™ 111In-CP04	Phase I/IIa Phase I	NCT03936426 NCT03246659
Focused Ultrasound-Triggered Delivery	ThermoDox® (LTLD)	Phase III	NCT00617981
Gene-directed enzyme prodrug therapy (GDEPT)	TK Suicide Gene Therapy	Phase I/II	NCT00002824 NCT00844623 NCT00751270
Genetically encoded fluorescent protein	GL-ONC1	Phase I	NCT00794131

Table 6.2 Select theranostic agents in clinical development.

Vita

Hannah Vaughan

Biomedical Engineering Ph.D. candidate

hvaughan@jhmi.edu

Education

Johns Hopkins University School of Medicine (JHUSOM): 2016-2021

- Ph.D. in Biomedical Engineering, expected graduation 2021

- Ruth L. Kirchstein F31 NIH National Research Service Award Fellowship, National Cancer Institute (2020-present)

- NIH Cancer Nanobiotechnology Training Center Fellowship (2016 - 2019)

Duke University (2012 - 2016)

- B.S. in Biomedical Engineering, Concentration in Cell and Tissue Engineering

- Graduation with Departmental Distinction

- Cum Laude

Peer-reviewed Publications

1. ***Vaughan, H.J.,*** Zamboni, C.G.; Radant, N.P.; Bhardwaj P.; Mease, R.C.; Pomper, M.G.; Green, J.J.; Polymeric Nanoparticles for Transcriptionally Targeted Theranostic Gene Delivery to Hepatocellular Carcinoma. (2021). *Manuscript In Preparation*
2. ***Vaughan, H.J.,*** Green J.J.; Recent Advances in Gene Therapy for Theranostic Cancer Medicine. (2021). *Current Opinion in Biomedical Engineering. In Press.*
3. Kim, J.*, ***Vaughan, H.J.*,*** Zamboni, C.G., Sunshine, J.C., Green, J.J., High-throughput Screening of Polymer Structure on Tissue-targeted Gene Expression In Vivo Using Barcoded Plasmid DNA. (2021) *Journal of Controlled Release. In Press.*
4. ***Vaughan, H.J.,*** Zamboni, C.G., Radant, N.P., Bhardwaj, P. Hassan, L., Green, J.J., 2021. Poly(beta-amino ester) nanoparticles enable tumor-specific TRAIL secretion and a bystander effect to treat liver cancer. *Molecular Therapy: Oncolytics.*
5. ***Vaughan, H. J.,*** Green, J. J., & Tzeng, S. Y. (2020). Cancer-Targeting Nanoparticles for Combinatorial Nucleic Acid Delivery. *Advanced Materials*, *32*(13), 1901081.
6. Karlsson, J.*, ***Vaughan, H.J.*** ,and Green, J.J., 2018. Biodegradable polymeric nanoparticles for therapeutic cancer treatments. *Annual review of chemical and biomolecular engineering*, *9*, pp.105-127.
7. Zamboni, C.G., Kozielski, K.L., ***Vaughan, H.J.***, Nakata, M.M., Kim, J., Higgins, L.J., Pomper, M.G. and Green, J.J., 2017. Polymeric nanoparticles as cancer-specific DNA delivery vectors to human hepatocellular carcinoma. *Journal of Controlled Release*, *263*, pp.18-28.

8. Lopez-Bertoni, H., Kozielski, K.L., Rui, Y., Lal, B., ***Vaughan, H.J.***, Wilson, D.R., Mihelson, N., Eberhart, C.G., Laterra, J. and Green, J.J., 2018. Bioreducible Polymeric Nanoparticles Containing Multiplexed Cancer Stem Cell Regulating miRNAs Inhibit Glioblastoma Growth and Prolong Survival. *Nano letters*, *18*(7), pp.4086-4094.
9. Kozielski, K.L., Ruiz-Valls, A., Tzeng, S.Y., Guerrero-Cázares, H., Rui, Y., Li, Y., ***Vaughan, H.J.***, Gionet-Gonzales, M., Vantucci, C., Kim, J. and Schiapparelli, P., 2019. Cancer-selective nanoparticles for combinatorial siRNA delivery to primary human GBM in vitro and in vivo. *Biomaterials*.

*These authors contributed equally

Patents

1. Green, J.J., Pomper, M.G., Zamboni, C.G., ***Vaughan, H.J.*** and Minn, I., Johns Hopkins University, 2020. *Transcriptionally targeted and cpg-free plasmid for theranostic gene therapy*. U.S. Patent Application 16/589,647.

Awards and Recognition

- Principal Investigators Meeting: NCI Alliance for Nanotechnology in Cancer Outstanding Poster Award

- Ruth L. Kirchstein F31 NIH National Research Service Award Fellowship, National Cancer Institute (2020-present)

- NIH Cancer Nanobiotechnology Training Center Fellowship recipient (2017)

- Pathways in Technology Early College High Schools at Dunbar Mentor (2016-present)

- NSF GRFP Honorable Mention (2016)

Oral Presentations and Posters

1. ***Vaughan, H.J.,*** Zamboni, C.G.; Radant, N.P.; Bhardwaj P.; Mease, R.C.; Pomper, M.G.; Green, J.J.; Polymeric Nanoparticles for Transcriptionally Targeted Theranostic Gene Delivery to Hepatocellular Carcinoma. Presentation. (2020). American Society for Cell and Gene Therapy Annual Meeting, Boston, MA (Virtual)
2. ***Vaughan, H.J.,*** Sarker, R.; Rui Y.; Zachos N. C.; Donowitz M.; Green J. J.; Polymer-Peptide Nanoparticle Targets Intracellular NHE3 Transporter Implicated in Diarrhea. Presentation. (2019) Biomedical Engineering Society Annual Meeting, Philadelphia, PA
3. ***Vaughan, H.J.***, Zamboni C.G.; Radant N.P.; Bhardwaj P.; Francisco D.H.; Green J.J.; Polymer Nanoparticles for Secreted TRAIL Cancer Therapy. Presentation. (2019) Society for Biomaterials Annual Meeting, Seattle, WA
4. ***Vaughan, H.J***., Zamboni C.G.; Pomper M.G.; Green J.J.; Poly(beta-amino ester) Nanoparticles for Therapeutic Gene Delivery to Hepatocellular Carcinoma. Poster. (2018) NIH/NCI Nano Alliance PI Meeting, Rockville, MD ***Outstanding Poster Award***

5. ***Vaughan, H.J***., Zamboni C.G.; Mease R.C.; Radant N.P.; Bhardwaj P.; Pomper M.G.; Green J.J.; Transcriptionally Targeted Biodegradable Polymeric Nanoparticles for Selective Theranostic Gene Delivery to Hepatocellular Carcinoma. Poster. (2018) Controlled Release Society Annual Meeting, New York, NY
6. ***Vaughan, H.J***., Zamboni C.G.; Mease R.C.; Radant N.P.; Bhardwaj P.; Pomper M.G.; Green J.J.; Transcriptionally Targeted Biodegradable Polymeric Nanoparticles for Selective Theranostic Gene Delivery to Hepatocellular Carcinoma. Poster. (2018) Johns Hopkins University Institute for Nanobiotechnology Mini Symposium, Baltimore, MD.

Abstracts

1. Kim J; Zamboni, C.G.; ***Vaughan, H.J***.; Wilson, D.R.; Green, J.J. High-throughput In Vivo Evaluation of Nanobiomaterial-mediated Tissue Targeting of Polymeric Gene Delivery Vectors Using DNA Barcodes. *Presentation.* (2017) Biomedical Engineering Society Annual Meeting, Phoenix, AZ
2. Kozielski, K.L.; Lopez-Bertoni, H.; Lal, B.; ***Vaughan, H.J.***; Laterra, J.; Green, J.J. MicroRNA delivery via poly(beta-amino ester) nanoparticles as a treatment for human glioblastoma. *Presentation*. (2016) 10th World Biomaterials Congress, Montreal, QC Canada.
3. Kozielski, K.L.; Lopez-Bertoni, H.; Lal, B.; ***Vaughan, H.J.***; Laterra, J.; Green, J.J. Environmentally triggered miRNA nanoparticles as a treatment for human glioblastoma. *Poster.* (2016)
4. Kozielski, K.L.; Lopez-Bertoni, H.; Lal, B.; ***Vaughan, H.J.***; Laterra, J.; Green, J.J. Environmentally triggered miRNA nanoparticles as a treatment for human glioblastoma. *Presentation*. (2015) US-Japan Symposium on Drug Delivery Systems, Lahaina, HI.
5. Kozielski, K.L.; Lopez-Bertoni, H.; Lal, B.; ***Vaughan, H.J.***; Laterra, J.; Green, J.J. Nanoparticles for miRNA Delivery as a Potent and Combinatorial Treatment for Glioblastoma. *Presentation.* (2015) Biomedical Engineering Society Annual Meeting, Tampa, FL.
6. Kozielski, K.L.; ***Vaughan, H.J.***; Kim, B.H.; Tzeng, S.Y.; Magraviti, A.M.; Wang, Y.; Guerrero-Cazares, H.; Quinones-Hinojosa, A.; Brem, H.; Tyler, B.; Green, J.J.: Poly(beta-amino ester) nanoparticles for selective and combinatorial delivery of siRNA and DNA to brain cancer. *Presentation*. (2015) 6th Annual Advanced Study Institute on Global Healthcare Challenges, Izmir, Turkey.
7. Kozielski, K.L.; ***Vaughan, H.J.***; Kim, B.H.; Tzeng, S.Y.; Guerrero-Cazares, H.; Quinones-Hinojosa, A.; Green, J.J.: Poly(beta-amino ester) nanoparticles for selective and combinatorial delivery of siRNA to brain cancer. *Presentation*. (2015) Society for Biomaterials, Charlotte, NC.
8. Kozielski, K.L.; ***Vaughan, H.J.***; Kim, B.H.; Tzeng, S.Y.; Guerrero-Cazares, H.; Quinones-Hinojosa, A.; Green, J.J.: Environmentally triggered nanoparticles for efficient and cancer-specific DNA and siRNA delivery to glioblastoma. *Presentation*. (2015) Johns Hopkins School of Medicine Neurooncology Monthly Research Meeting, Baltimore, MD.
9. Kozielski, K.L.; ***Vaughan, H.J.***; Kim, B.H.; Tzeng, S.Y.; Mangraviti, A.; Wang, Y.; Guerrero-Cazares, H.; Quinones-Hinojosa, A.; Brem, H.; Tyler, B.; Green, J.J. Poly(β-amino ester) nanoparticles for selective and combinatorial delivery of siRNA and DNA to brain cancer.

Poster. (2015) Johns Hopkins University Institute for Nanobiotechnology Annual Symposium, Baltimore, MD.

10. Kozielski, K.L.; ***Vaughan, H.J.***; Kim, B.; Tzeng, S.Y.; Guerrero-Cazares, H.; Quinones-Hinojosa, A.; Green, J.J.: Bioreducible nanoparticles for efficient and combinatorial siRNA delivery to primary human glioblastoma. *Presentation*. (2014) Johns Hopkins University Institute for Nanobiotechnology Mini Symposium, Baltimore, MD.

Research Experience

Johns Hopkins University Biomedical Engineering, Advisor: Dr. Jordan Green (2016-present)

- Developed DNA barcodes and qPCR methods for *in vivo* screening of polymer (PBAE) nanoparticles, resulting in a 5X increase in screening throughput

- With collaborators in Nuclear Medicine, co-invented a transcriptionally targeted CpG-free plasmid DNA for theranostic suicide gene expression, enabling liver cancer cell death and radiotracer accumulation

- Applied nucleic acid design principles to develop innovative cancer-targeted therapeutic plasmid DNAs, incorporating principles such as transcriptional targeting, codon optimization, and CpG-free sequences

- Designed and executed in vivo studies of candidate nanoparticles to assess biodistribution, transfection targeting, and anti-tumor efficacy and safety in a range of rodent liver tumor (hepatocellular carcinoma) models

- In the first therapeutic application of PBAE polymer nanoparticles for liver cancer, developed employed an engineered secretable TRAIL gene therapy, enabling >90% cancer cell death and

Duke University, Biomedical Engineering, Advisor: Dr. George Truskey (2014-2016)

- Created *in vitro* tissue engineered models of human vasculature to recapitulate structure and physiology of blood vessels

- Developed co-culture models to recapitulate interactions between endothelial cells and smooth muscle cells

- Used immunohistochemistry to verify adequate cellular adhesions and overall tissue morphology

- Developed a mechanical injury model to mimic endothelial trauma from catheter or stent placement

Johns Hopkins University Biomedical Engineering, Advisor: Dr. Jordan Green (Summer 2014)

- Optimized and characterized combinatorial delivery of siRNA and miRNA to human glioblastoma cells using PBAE nanoparticles

University of Maryland, Baltimore County, Biochemistry, Advisor: Dr. Michael Summers (Summer 2013)

- Performed *in vitro* transcription and RNA purification to support research to solve the structure of highly conserved 5' leader of HIV-1 genome by NMR

Extracurricular and Volunteer Experience

Pathways in Technology Early College High Schools (P-TECH) at Dunbar (2016-Present)

P-TECH is a national organization whose mission is to support high school students in achieving Associates degrees in high-demand technical fields while still in high school. As a P-TECH mentor in Baltimore, I supported a student from his freshman year of high school through graduation. This involved setting up regular one-on-one meetings, participating in career development workshops, and advising my student on his career trajectory and education as he pursues a degree in physical therapy.

BME Extramural Development in Graduate Education (EDGE) Director of Internships (2020-Present)

BME EDGE is a student-led organization dedicated to exposing students to non-academic careers and preparing them to excel in their chosen career path. Along with my co-director, I assisted PhD students in finding, applying to, and completing internships in biotech, pharma, consulting, and finance. In the 2020-2021 academic year, we placed 8 students in internships. We also built connections with companies in order to offer more opportunities in the future.

BME Application Assistance Program Volunteer (2020-2021)

I served as a mentor to a student from an underrepresented background applying to the BME PhD program. I met with the student to discuss her application, offered feedback on her materials, and provided support throughout the application process.

Teaching Assistant Experience

Cellular Engineering (2018, 2020)

This is an upper-level undergraduate and graduate course which focuses on principles and applications of cellular engineering, including modeling cellular processes, genetic engineering, and drug delivery. I held weekly office hours, graded homework and exams, and assisted the professors with course organization and structure.

Cell and Tissue Engineering Lab: Gene Delivery Lab Module (2018)

This is a laboratory-based course where students learn hand-on techniques related to cell and tissue engineering. I was responsible for preparing all lab materials, explaining transfection protocols, and answering student questions throughout the experiments.

Mentoring

Pranshu Bhardwaj (2016-2017)

Pranshu was an undergraduate student at Johns Hopkins University majoring in Cellular and Molecular Biology. I worked with Pranshu throughout his senior year He assisted with cloning, cell culture, and animal experiments in the lab. He is finishing his second year of medical school at University of Florida.

Nicholas Radant (2016-2019)

Nick was a Biomedical Engineering undergraduate student at Johns Hopkins University, and he worked in the lab with me for three years. During this time, he worked on several projects involving targeted gene delivery and treatment for liver cancer. He completed a postbaccalaureate program at NIH and is starting an MD/PhD at Marshall University.

David Francisco (2018-2019)

David is an undergraduate student at Johns Hopkins University majoring in Biomedical Engineering and Computer Science. David worked with me for his sophomore year optimizing cell culture and transfection protocols. Since this experience, he had the opportunity to work at the Max Planck institute in Germany and the Applied Physics Laboratory.

Laboni Hassan (2019-present)

Laboni is a Biomedical Engineering student at Johns Hopkins University. She worked with me in the lab for 2 years and assisted with several projects developing targeted therapeutics for liver cancer. She is graduating this spring and starting a Master’s program in Biomedical Engineering at Boston University starting Summer 2021.